Applications of Nanotubes in Electronic and Nanomechanical Devices

FINAL TECHNICAL REPORT

to

Office of Naval Research
Grant No. N00014-99-1-0252

by
Professor David Tomanek

Physics and Astronomy Department
Michigan State University
East Lansing, Michigan 48824

December 2002

REPORT DOCUMENTATION PAGE

Form Approved
OMB No. 0704-0188

1. REPORT DATE *(DD-MM-YYYY)*	2. REPORT DATE	3. DATES COVERED *(From - To)*
03-Dec-2002	Final Technical Report	15 Jan 1999 - 30 Sep 2002

4. TITLE AND SUBTITLE
Applications of Nanotubes in Electronic and Electromechanical Devices

5a. CONTRACT NUMBER

5b. GRANT NUMBER
N00014-99-1-0252

5c. PROGRAM ELEMENT NUMBER

6. AUTHOR(S)
David Tomanek

5d. PROJECT NUMBER

5e. TASK NUMBER

5f. WORK UNIT NUMBER

7. PERFORMING ORGANIZATION NAME(S) AND ADDRESS(ES)
Michigan State University
East Lansing, MI 48824-2320

8. PERFORMING ORGANIZATION REPORT NUMBER
61-3541

9. SPONSORING/MONITORING AGENCY NAME(S) AND ADDRESS(ES)
Office of Naval Research

10. SPONSOR/MONITOR'S ACRONYM(S)
ONR

11. SPONSORING/MONITORING AGENCY REPORT NUMBER

12. DISTRIBUTION AVAILABILITY STATEMENT
Unclassified/Unlimited

13. SUPPLEMENTARY NOTES

14. ABSTRACT

Using a combination of state-of-the-art computational techniques, the proposed research investigates the suitability of nanotubes for application in nanoscale devices. In view of the present and future Navy needs, the research focuses on applications utilizing the unusually high thermal and electrical conductivity, mechanical strength of nanotubes, as well as their potential for energy storage. Our research helps to better understand nanotube properties in case of chemically and structurally modified nanotubes consisting of carbon and boron nitride, including multi-wall systems and peapods, and addresses their hierarchical self-assembly. Emphasis is placed on addressing problems that currently hinder the production and utilization of nanotubes, including their separation by diameter and chirality, and the use of nanotubes to interconnect molecular electronics components among themselves and with present micron-size devices.

15. SUBJECT TERMS
Nanotechnology, Nanotubes, Devices, Transport, MEMS

16. SECURITY CLASSIFICATION OF:			17. LIMITATION OF ABSTRACT	18. NUMBER OF PAGES	19a. NAME OF RESPONSIBLE PERSON
a. REPORT	b. ABSTRACT	c. THIS PAGE			David Tomanek
U	U	U	UU		19b. TELEPONE NUMBER *(Include area code)* (517) 355-9702

Table of Contents

11. David Tománek, Electrical and Thermal Transport in Carbon Nanotubes. In *"Electronic Properties of Novel Materials - Molecular Nanostructures"*, Proceedings of the XIV International Winterschool in Kirchberg, Tyrol, March 2000, edited by Hans Kuzmany, Jörg Fink, Michael Mehring, and Siegmar Roth, pp. 338-343.

12. Petr Král, E. J. Mele, and David Tománek, Photogalvanic Effects in Heteropolar Nanotubes, Phys. Rev. Lett. **85**, 1512 (2000).

13. A. M. Rao, J. Chen, E. Richter, P. C. Eklund, R. C. Haddon, U. D. Venkateswaran, Y.-K. Kwon, and D. Tománek, Effect of van der Waals interactions on the Raman modes in single walled carbon nanotubes, Phys. Rev. Lett. **86**, 3895 (2001).

14. U. Kim, R. Pcionek, D.M. Aslam, and D. Tománek, Synthesis of high-density carbon nanotubes, Diamond and Related Materials **10**, 1947 (2001).

15. David Tománek, Thermal and electrical conductance of carbon nanostructures. In ``*Nanostructured Carbon for Advanced Applications*", Proceedings of the NATO Advanced Study Institute in Erice (Italy), July 2000, edited by G. Benedek, P. Milani, and V.G. Ralchenko.

16. Savas Berber, Young-Kyun Kwon, and David Tománek, Microscopic Formation Mechanism of Nanotube Peapods, Phys. Rev. Lett. **88**, 185502 (2002).

17. J. Gerard Lavin, Shekhar Subramoney, Rodney S. Ruoff, Savas Berber and David Tománek, Scrolls and Nested Tubes in Multiwall Carbon Nanotubes, Carbon **40**, 1123 (2002).

18. David Tománek, Mina Yoon, Jorge M. Pacheco, Gueorgui K. Gueorguiev, Steven W.D. Bailey, and Colin J. Lambert, Microscopic Switching of a Molecular Memory Device (submitted for publication).

19. Steven W.D. Bailey, David Tománek, Young-Kyun Kwon, and Colin J. Lambert, Giant magneto-conductance in twisted carbon nanotubes, Europhys. Lett. **59**, 75 (2002).

20. Koichiro Umemoto, Susumu Saito, Savas Berber, and David Tománek, Carbon foam: Spanning the phase space between graphite and diamond, Phys. Rev. B **64**, 193409 (2001).

21. Yoshiyuki Miyamoto, Susumu Saito, and David Tománek, Electronic inter-wall interactions and charge redistribution in multi-wall nanotubes, Phys. Rev. BR **65**, 041402 (2002).

22. A. Hassanien, M. Tokumoto, and D. Tománek, Imaging the interlayer interactions of multiwall carbon nanotubes using scanning tunneling microscopy and spectroscopy, Appl. Phys. Lett. **79**, 4210 (2001).

23. Petr Král, E.J. Mele, David Tománek, and Moshe Shapiro, Photo-Galvano-Mechanical Phenomena in Nanotubes. Proceedings of the XV International Winterschool in Kirchberg, Tyrol, March 2001, edited by Hans Kuzmany, Jörg Fink, Michael Mehring, and Siegmar Roth.

24. E.J. Mele, Petr Král, David Tománek, New Physics in Molecular Electronic and Molecular Optoelectronic Structures. Proceedings of the XV International Winterschool in Kirchberg, Tyrol, March 2001, edited by Hans Kuzmany, Jörg Fink, Michael Mehring, and Siegmar Roth.

25. A.V. Okotrub, V.V. Belavin, L.G. Bulusheva, V.A. Davydov, T.L. Makarova, D. Tománek, Electronic structure and properties of rhombohedrally polymerized C_{60}, J. Chem. Phys. **115**, 5637 (2001).

26. A.M. Rao, J. Chen, E. Richter, U. Schlecht, P.C. Eklund, R. C. Haddon, U. D. Venkateswaran, Y.-K. Kwon, and D. Tománek, Influence of Van Der Waals Interactions on the Raman Modes in Single Walled Carbon Nanotubes, Proceedings of the CARBON 2001 conference (submitted for publication).

27. Yoshiyuki Miyamoto, Savas Berber, Mina Yoon, Angel Rubio, and David Tománek, Onset of nanotube decay under extreme thermal and electronic excitations. Proceedings of the CNT'10 Conference in Tsukuba, Japan, October 3-5, 2001.

28. David Tománek, Mesoscopic origami with graphite: Scrolls, nanotubes, peapods. Physica B (2002).

29. David Tománek, Ballistic conductance in quantum devices: From organic polymers to nanotubes. Current Applied Physics **2**, 47 (2002).

30. David Tománek, Koichiro Umemoto, Susumu Saito, and Savas Berber, Hierarchical Assembly of Nanostructured Carbon Foam. Submitted to Molecular Crystals and Liquid Crystals.

31. Jin Choi, Yong-Hyun Kim, K. J. Chang, and David Tománek, Itinerant ferromagnetism in heterostructured C/BN nanotubes (submitted for publication).

32. A. Hassanien, A. Mrzel, M. Tokumoto, X. Zhao, Y. Ando, and D. Tománek, Scanning tunneling microscopy and spectroscopy of short multiwall carbon nanotubes, Mat. Res. Soc. Symp. Proc. Vol. **633**, A14.28.1 (2001).

Summary of Results

The suitability of nanotubes for application in nanoscale devices was studied using a combination of state-of-the-art computational techniques, The highlights of the research are the proposal for *a **"bucky-shuttle" memory device*** that was followed by the discovery of nanotube peapods. Our postulate of unprecedented ***thermal conductivity*** was followed by experimental confirmation. Studying the role of defects during structural transformations has led us to propose the use of ***defect engineering*** for hierarchical self-assembly of nanostructures.

Other problems addressed in this research include

- Design of a nanotube-based "bucky-shuttle" memory device, resulting in U.S. Patent Number 6,473,351
- Design of a nanotube-based laser driven atomic pump
- Discovery of fractional quantum conductance in carbon nanotubes
- Discovery of an orientational melting transition in carbon nanotube ropes
- Calculation of Electronic and Structural Properties of Carbon Nanohorns
- Studying the effect of inter-tube interactions on the Raman modes in single walled carbon nanotubes
- Synthesis of high-density carbon nanotubes
- Studying the microscopic formation mechanism of nanotube peapods
- Studying defect-induced structural transitions between scrolls and nested
- Proposing a magneto-conductance in twisted carbon nanotubes
- Proposing a new nano-material, a carbon foam that spans the phase space between graphite and diamond
- Study of electronic inter-wall interactions and charge redistribution in multi-wall nanotubes
- Studying the electronic structure and properties of rhombohedrally polymerized C_{60}
- Proposing a novel self-healing mechanism for defective nanotubes

"Bucky Shuttle" Memory Device: Synthetic Approach and Molecular Dynamics Simulations

Young-Kyun Kwon,[1] David Tománek,[1] and Sumio Iijima[2]
[1]*Department of Physics and Astronomy, and Center for Fundamental Materials Research, Michigan State University, East Lansing, Michigan 48824-1116*
[2]*NEC Corporation, Fundamental Research Laboratories, 34 Miyukigaoka, Tsukuba, Ibaraki 3058501, Japan*
(Received 23 October 1998)

Thermal treatment is reported to convert finely dispersed diamond powder to multiwall carbon nanocapsules containing fullerenes such as C_{60}. We investigate the internal dynamics of a related model system, consisting of a $K@C_{60}^{+}$ endohedral complex enclosed in a C_{480} nanocapsule. We show this to be a tunable two-level system, where transitions between the two states can be induced by applying an electric field between the C_{480} end caps, and discuss its potential application as a nonvolatile memory element. [S0031-9007(99)08484-7]

PACS numbers: 61.48.+c, 61.50.Ah, 73.61.Wp, 81.10.Aj

Carbon nanotubes [1,2], consisting of seamless and atomically perfect graphitic cylinders a few nanometers in diameter, have been synthesized in bulk quantities [3,4]. The unusual combination of their molecular nature and micrometer-size length [5,6] gives rise to uncommon electronic properties of these systems. Electrical transport measurements for individual nanotubes indicate that these systems may behave as genuine quantum wires [7], nonlinear electronic elements [8], or transistors [9]. Potential use of nanotube-based two-level systems for permanent data storage, discussed here, would significantly extend their range of application.

Here, we present evidence that unusual multiwall nanotube structures, such as the "bucky shuttle" [10], self-assemble from elemental carbon under specific conditions. Our molecular dynamics simulations indicate that the bucky shuttle shows an unusual dynamical behavior that suggests its use as a nanometer-sized memory element. We show that a nanotube memory would combine high switching speed, high packing density, and stability with nonvolatility of the stored data.

The system described in this study was produced by thermally annealing diamond powder of an average diameter of 4–6 nm which was prepared by the detonation method (Cluster Diamond, Toron Company Ltd.). The powder was heated in a graphite crucible in inert argon atmosphere at 1800 °C for 1 hour. This treatment transforms the diamond powder into graphitic nanostructures presented in transmission electron microscope images shown in Fig. 1. A large portion of this material consists of multiwall capsules with few layers, the smallest structures being fullerenes with a diameter close to that of C_{60}. In several cases depicted in Fig. 1, the enclosed fullerenes may move rather freely inside the outer capsule, like a bucky shuttle.

An enlargement of one of such structures in Fig. 1 is displayed in Fig. 2(a). Figure 2(b) illustrates a corresponding model, consisting of a C_{60} encapsulated in a C_{480} capsule. The energetics of the $C_{60}@C_{480}$ system is shown in Fig. 2(c). The ends of the outer capsule are halves of the C_{240} fullerene, the optimum structures to hold a C_{60} molecule at an interwall distance of 3.4 Å. These end caps connect seamlessly to the cylindrical portion of the capsule, a 1.5 nm long segment of the (10, 10) nanotube [3]. The interaction between the unmodified C_{60} molecule and the enclosing capsule is similar to that found in C_{60} crystals and nanotube bundles [3]; it is dominated by a van der Waals and a weak covalent interwall interaction that is proportional to the contact area between the constituents. An additional image charge interaction,

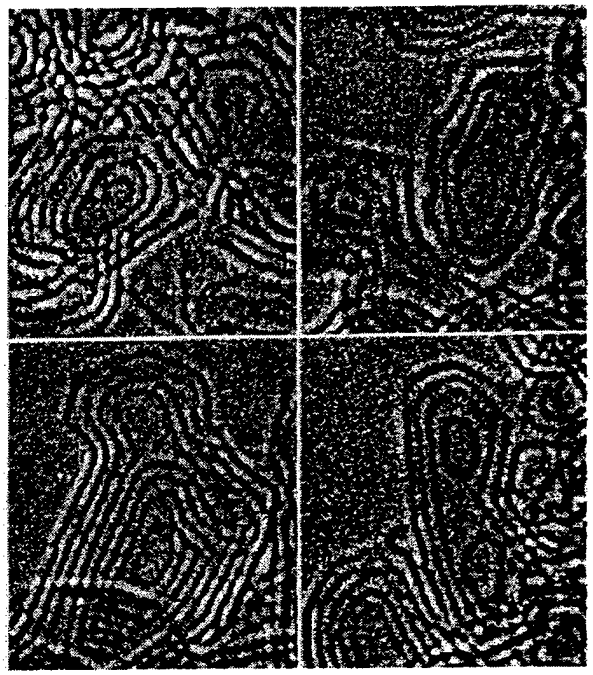

FIG. 1. Transmission electron microscope images depicting multiwall carbon structures that self-assemble during the thermal annealing of nanodiamond powder under the conditions described in this report. The smallest spherical structures are C_{60} molecules that are always found near the end of the capsule, where the attractive interwall interaction is strongest.

 0031-9007/99/82(7)/1470(4)$15.00

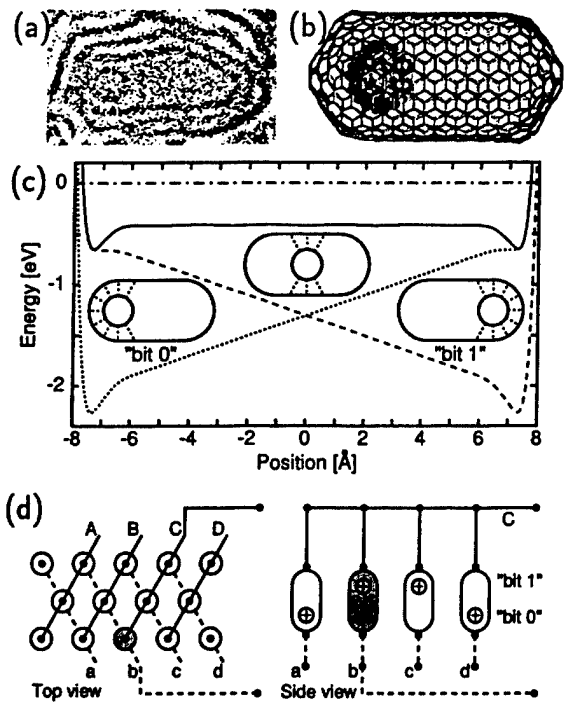

FIG. 2. (a) Enlargement of the upper-right section of the transmission electron microscope image in Fig. 1. (b) Structural model for an isolated $K@C_{60}^{+}@C_{480}$ bucky shuttle, with the $K@C_{60}^{+}$ ion in the "bit 0" position. (c) Potential energy of $K@C_{60}^{+}$ as a function of its position with respect to the outer capsule in zero field (solid line) and switching field $E_s = 0.1$ V/Å (dashed lines). The $K@C_{60}^{+}$ ion position, representing the information, can be changed by applying this switching field between the ends of the capsule. Energy zero corresponds to an isolated $K@C_{60}^{+}$ at infinite separation from the C_{480} capsule. (d) Schematic of a high-density memory board in the top and the side view. When a switching voltage is applied between conductors b and C, the corresponding bit information will be stored in the memory element bC at their intersection, shown shaded.

which is nearly independent of the C_{60} position, occurs if the C_{60} molecule carries a net positive charge, as we discuss below. Obviously, the van der Waals interaction stabilizes the C_{60} molecule at either end of the capsule, where the contact area is largest. This is reflected in the potential energy behavior in Fig. 2(c), and results in the likelihood of C_{60} being found near the ends of the capsule, as evidenced in Figs. 1 and 2(a). In the following, we will study the possibility of information storage in this two-level system.

Usefulness of this nanostructure for data storage implies the possibility to *write and read* information fast and reliably. Of equal importance is the capability to *address* the stored data efficiently, and the *nonvolatility* of the stored information.

In order to move the encapsulated C_{60} from one end of the capsule to the other (the molecular analog of writing) and to determine its position within the capsule (the molecular analog of reading) most efficiently, the C_{60} should carry a net charge. In the $K@C_{60}$ complex, which is known to form spontaneously under synthesis conditions in the presence of potassium, the valence electron of the encapsulated K atom is completely transferred to the C_{60} shell [11]. The C_{60} is likely to transfer the extra electron to the graphitic outer capsule, since the ionization potential of $K@C_{60}$ is smaller than the work function of graphite. The extra electron will likely be further transferred to the (graphitic) structure that holds this element in place. Since the enclosed K^+ ion does not modify the chemical nature of C_{60}, we will model the dynamics of the $K@C_{60}^{+}$ ion in the neutral C_{480} capsule by uniformly distributing a static charge of $+1e$ over the C_{60} shell.

The *writing process* corresponds to switching the equilibrium position of the C_{60}^{+} ion between the "bit 0" and the "bit 1" ends of the capsule in an applied electric field. This is best achieved if the connecting electrodes, supplying the bias voltage, are integral parts of the end caps, to reduce the field screening by the nanotube [12]. The energetics of C_{60}^{+} in the switching field $E_s = \pm 0.1$ V/Å, generated by applying a voltage of ≈ 1.5 V between the end caps, is displayed in Fig. 2(c). One of the local minima becomes unstable above a critical field strength, causing the C_{60}^{+} ion to move to the only stable position. The switching field $E_s = 0.1$ V/Å is small and will have no effect on the integrity of the carbon bucky shuttle, since graphitic structures disintegrate only in fields $E \gtrsim 3$ V/Å [13,14].

The information, physically stored in the position of the C_{60}^{+} ion within the capsule, can be *read nondestructively* by detecting the polarity of the capsule. An alternative *destructive read* process would involve measuring the current pulse in the connecting wires, caused by the motion of the C_{60}^{+} ion due to an applied probing voltage. The total charge transfer associated with the current pulse, which is one electron in our case, may be increased by connecting several capsules in parallel to represent one bit, and by using higher charged complexes such as $La@C_{82}^{2+}$.

When targeting high storage densities, the *addressability* of the stored information becomes important. One possible way to realize a high-density memory board is presented in Fig. 2(d). Maximum density is achieved by packing the nanotube memory elements like eggs in a carton. Rows of nanocapsules can be connected at the top and at the bottom by nanowire electrodes in such a way that a single memory element is addressed at their crossing point. Applying a switching voltage between two crossing electrodes [e.g., the bC pair in Fig. 2(d)] will generate a nonzero field only in the memory element labeled bC. As in the ferrite matrix memory, many memory elements can be addressed in parallel using such an addressing scheme. This arrangement applies both for the writing and the destructive reading processes described above, and allows for multiple bits to be written and read in parallel. In the latter case, the status of the memory element bC is inspected by applying a switching voltage between the electrode pair b, C and monitoring the current in these electrodes.

Unlike in presently used dynamic random access memory (DRAM) elements, where information has to be sustained by an external power source, the *nonvolatility of the stored information* results from a nonzero trap potential near the "bit 0" or "bit 1" end of the capsule. Thermal stability and nonvolatility of data depend on the depth of this trap potential, which in turn can be adjusted by changing the encapsulated fullerene complex. The calculated trap potential depth of ≈ 0.24 eV for the $K@C_{60}^+$ ion near the ends of the capsule in zero field suggests that stored information should be stable well beyond room temperature and require temperatures $T \gtrsim 3000$ K to be destroyed. Further improvement of the thermal stability could be achieved using higher-charged endohedral complexes containing divalent or trivalent donor atoms, such as $La@C_{82}$ discussed above.

To study the efficiency of the writing process, we performed a molecular dynamics simulation of the switching process from "bit 0" to "bit 1" in the microcanonical ensemble of the $C_{60}^+@C_{480}$ memory element. We used a parametrized linear combination of atomic orbitals (LCAO) total energy functional [15], augmented by long-range van der Waals interactions [16]. Our computationally efficient $O(N)$ approach to determine the forces on individual atoms [17] had been previously used with success to describe the disintegration dynamics of fullerenes [18] and the growth of multiwall nanotubes [19]. A time step of 5×10^{-16} s and a fifth-order Runge-Kutta interpolation scheme was used to guarantee a total energy conservation of $\Delta E/E \lesssim 10^{-10}$ between successive time steps.

The results of our simulation are shown in Fig. 3. Initially, the C_{60}^+ ion is equilibrated near the "bit 0" position. At time $t = 0$, a constant electric field of 0.1 V/Å is applied along the axis of the outer capsule. The originally stable "bit 0" configuration becomes unstable in the modified total energy surface, depicted in Fig. 2(c). The C_{60}^+ ion is subject to a constant acceleration to the right, and reaches the "bit 1" position only 4 ps later, as seen in Fig. 3(a). During this switching process, the potential energy lost by the C_{60}^+ ion is converted into kinetic energy, as seen in Fig. 3(b). Because of the small (albeit non-negligible) interaction between the encapsulated ion and the capsule, the kinetic energy gained initially occurs as rigid-body translational energy of the C_{60}^+ ion. A nearly negligible energy transfer into the internal degrees of freedom due to atomic-scale friction, manifested in a very small increase of the vibrational temperature in Fig. 3(c), is observed during this initial stage of the switching process.

The C_{60}^+ ion reaches the opposite end of the capsule, 4 ps after the switching field is applied, having gained 1.5 eV of net kinetic energy. This kinetic energy is too small to damage the capsule, as inelastic collisions involving C_{60} require energies exceeding 200 eV to occur [20]. Upon impact onto the enclosing capsule from the inside, a substantial fraction of this energy is converted into heat, thus increasing the vibrational temperature of

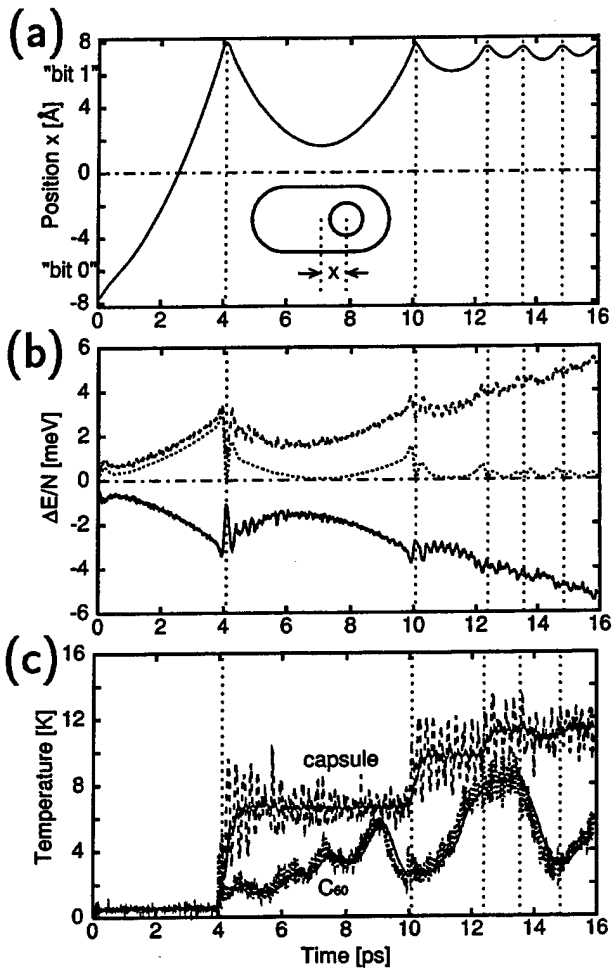

FIG. 3. Results of a molecular dynamics simulation of the switching process from "bit 0" to "bit 1", when a constant electric field of 0.1 V/Å is applied along the axis of the capsule. (a) Position of the $K@C_{60}^+$ ion with respect to the center of the enclosing C_{480} capsule as a function of time. (b) Changes in the potential energy (solid line) and kinetic energy (dashed line) in the laboratory reference frame as a function of time. The portion of the kinetic energy, corresponding to the translation of the enclosed $K@C_{60}^+$ ion with respect to the capsule (dotted line), is seen to decrease as the system temperature rises. The total energy (dash-dotted line) is conserved. All energies are given per atom. (c) Vibrational temperature of the enclosed $K@C_{60}^+$ ion (dotted line) and the enclosing capsule (dashed line) as a function of time. The solid lines are backward convolutions of the vibrational temperature values, using a Gaussian with a full-width at half maximum of 7.5×10^{-13} s.

the outer capsule by $\lesssim 10$ K and that of the C_{60}^+ ion by ≈ 2 K. Because of the high heat conductivity and melting temperature $T_M \lesssim 4,000$ K of graphitic nanostructures [18], this modest heat evolution is unlikely to cause any structural damage even at high access rates.

As seen in Fig. 3(b), the net kinetic energy of the encapsulated C_{60}^+ with respect to the outer capsule is significantly reduced during this collision. The C_{60}^+ bounces back towards the middle of the capsule, slowed down by the opposing electric field, and finally turns again towards

the "bit 1" end. Figure 3(c) indicates that thermal equilibration in the system after the collision is achieved stepwise. The step period of ≈ 1 ps results from the beats between the low-frequency quadrupolar deformation modes of the colder encapsulated C_{60}^+ ion and the hotter enclosing capsule, which have been excited during the quasielastic collision.

One or few oscillations of the C_{60}^+ ion inside the enclosing capsule, damped by transferring energy from macroscopic to internal degrees of freedom, are necessary to stabilize it in the new equilibrium "bit 1" position, with a kinetic energy not exceeding the depth of the trap potential. As seen in Fig. 3(b), this situation occurs ≈ 10 ps after the initial onset of the switching field, thus resulting in an ideal memory switching and access rate close to 0.1 THz. In the slower sequential mode, this translates into a data throughput rate of 10 Gbyte/s, 4 orders of magnitude faster than the data throughput rate of 4–5 Mbyte/s which is achieved presently in magnetic mass storage devices.

In order to further reduce the switching time, one may consider increasing the field to shorten the transfer time between the two states, keeping in mind that the damping process would be prolonged in such a case. Unlike in our model simulation, there is no need to apply a constant switching field during the entire bit flip process. A 0.5 ps pulse of a 0.1–0.5 V/Å field is found to suffice to detach the C_{60}^+ ion from its stable position and thus to change the memory state. This approach may be of particular use if an increase of the trap potential, due to a different fullerene complex, should be desirable.

Mass production of nanotube-based memory devices such as the one discussed here rely on the self-assembly of nanotubes and nanocapsules to ordered close-packed arrays. There has been encouraging evidence of such a self-assembly mechanism in the synthesis of free-standing nanotube ropes [3], aligned nanotube columns forming free-standing membranes [21], multiwall nanotube columns growing from a SiC(111) wafer [22], and most recently many C_{60} molecules inside long carbon nanotubes [23]. We also note that, since any double-wall nanocapsule with the enclosed structure shorter than the outer capsule behaves as a tunable two-level system, the functionality of the proposed nanoscale memory is basically independent of the exact size and shape of the encapsulated ion and the enclosing capsule.

In summary, we have shown that thermal treatment may convert finely dispersed diamond powder to multiwall carbon nanocapsules containing fullerenes such as C_{60}. Using molecular dynamics simulations, we investigated the internal dynamics of a related model system, consisting of a $K@C_{60}^+$ endohedral complex enclosed in a C_{480} nanocapsule. We showed this to be a tunable two-level system, where transitions between the two states can be induced by applying an electric field between the C_{480} end caps. This system, if considered as a memory element, would offer a combination of high switching speed, high density, nonvolatility of data, and relatively easy read/write access.

D. T. and Y. K. K. acknowledge fruitful discussions with R. E. Smalley and financial support by the Office of Naval Research.

[1] S. Iijima, Nature (London) **354**, 56 (1991).
[2] M. S. Dresselhaus, G. Dresselhaus, and P. C. Eklund, *Science of Fullerenes and Carbon Nanotubes* (Academic Press, San Diego, 1996).
[3] A. Thess, R. Lee, P. Nikolaev, H. Dai, P. Petit, J. Robert, C. Xu, Y. H. Lee, S. G. Kim, D. T. Colbert, G. Scuseria, D. Tománek, J. E. Fischer, and R. E. Smalley, Science **273**, 483 (1996).
[4] T. W. Ebbesen, Annu. Rev. Mater. Sci. **24**, 235 (1994).
[5] J. W. G. Wildöer, L. C. Venema, A. G. Rinzler, R. E. Smalley, and C. Dekker, Nature (London) **391**, 59 (1998).
[6] T. W. Odom, J.-L. Huang, P. Kim, and C. M. Lieber, Nature (London) **391**, 62 (1998).
[7] S. J. Tans, Michel H. Devoret, Hongjie Dai, Andreas Thess, Richard E. Smalley, L. J. Geerligs, and Cees Dekker, Nature (London) **386**, 474 (1997).
[8] M. Bockrath, David H. Cobden, Paul L. McEuen, Nasreen G. Chopra, A. Zettl, Andreas Thess, and R. E. Smalley, Science **275**, 1922 (1997).
[9] S. J. Tans, A. R. M. Verschueren, and C. Dekker, Nature (London) **393**, 49 (1998).
[10] For a review of the field of fullerenes and nanotubes, see B. I. Yakobson and R. E. Smalley, Am. Sci. **85**, 324 (1997).
[11] Y. S. Li and D. Tománek, Chem. Phys. Lett. **221**, 453 (1994).
[12] L. Lou, P. Nordlander, and R. E. Smalley, Phys. Rev. B **52**, 1429 (1995).
[13] S. G. Kim, Y. H. Lee, P. Nordlander, and D. Tománek, Chem. Phys. Lett. **264**, 345 (1997).
[14] Y. H. Lee, S. G. Kim, and D. Tománek, Chem. Phys. Lett. **265**, 667 (1997).
[15] D. Tománek and M. A. Schluter, Phys. Rev. Lett. **67**, 2331 (1991).
[16] Y.-K. Kwon, D. Tománek, Y. H. Lee, K. H. Lee, and S. Saito, J. Mater. Res. **13**, 2363 (1998).
[17] W. Zhong, D. Tománek, and G. F. Bertsch, Solid State Commun. **86**, 607 (1993).
[18] S. G. Kim and D. Tománek, Phys. Rev. Lett. **72**, 2418 (1994).
[19] Y.-K. Kwon, Y. H. Lee, S.-G. Kim, P. Jund, D. Tománek, and R. E. Smalley, Phys. Rev. Lett. **79**, 2065 (1997).
[20] H.-G. Busmann, Th. Lill, and I. V. Hertel, Chem. Phys. Lett. **187**, 459 (1991).
[21] G. Che, B. B. Lakshmi, E. R. Fisher, and C. R. Martin, Nature (London) **393**, 346 (1998).
[22] M. Kusunoki, J. Shibata, M. Rokkaku, and T. Hirayama, Jpn. J. Appl. Phys. **37**, L605 (1998).
[23] Brian W. Smith, Marc Monthioux, and David E. Luzzi, Nature (London) **396**, 323 (1998).

Laser-Driven Atomic Pump

Petr Král[1] and David Tománek[2]

[1]*Department of Physics, University of Toronto, 60 St. George Street, Ontario, Toronto M5S 1A7, Canada*

[2]*Department of Physics and Astronomy, and Center for Fundamental Materials Research, Michigan State University, East Lansing, Michigan 48824-1116*

(Received 31 August 1998)

We propose a laser-driven pump for atomic transport through carbon nanotubes. A two beam coherent control is used to inject carrier population into the lowest unoccupied nanotube bands, which is *anisotropic* in momentum space. The resulting electron current moves intercalated atoms along the tube. This system is a unique prototype of a single atom deposition machine which overcomes the loading problem of the scanning tunneling microscope. [S0031-9007(99)09502-2]

PACS numbers: 78.20.Jq, 61.48.+c, 66.30.Qa, 85.40.Ux

The demonstrated manipulation and deposition of individual atoms on surfaces with the tip of a scanning tunneling microscope (STM) [1,2] have opened a new era in nanotechnology. The STM enables us to study and modify nanostructures on the atomic scale [3,4] and to explore biomolecules [5]. The limitation of this technique to transport only single atoms prevents us from assembling larger structures. A "continuous STM" would offer a significant improvement here. Similar micromachines, commonly called "molecular motors" [6], can transport ions, atoms and molecules through membranes in biocells or along their tubular cytoskeleton [7].

The recently discovered nanotubes of carbon [8] and other materials [9] are formed with various diameters and chiralities, and their electronic structure varies from semiconducting to metallic [10–12]. The morphology of the hollow tubes provides an excellent possibility to create a nanometer-scale "fountain pen" (pump) with atomic filling. Isolated nanotubes can be filled [13] and nanotube ropes reversibly intercalated [14] during synthesis. The intercalated atoms usually condense into rather immobile aggregates [9,15]. To realize an atomic pump, a new mechanism is needed to move these atoms along the tubes, which could work similar to the mechanism of electron drag by hot carriers [16].

In applied dc electric fields, electromigration [17–19] has been shown to set atoms into motion. Partly ionized atoms are driven by the direct force F_d due to the external field that is locally modified at the atomic site, and by the wind force F_w caused by the reflection of conduction electrons from these atoms. Since F_d usually dominates F_w [18,19], generation of a force to set intercalated atoms into motion would require applying large dc biases, especially for atoms trapped at defects.

More efficient and qualitatively different driving could be realized if the atoms would take better advantage of the large unidirectional momenta and energy carried by the hot electrons. This type of driving can be realized in photovoltaic materials with no inversion symmetry, where a dc current of hot electrons can be generated by light. Only recently, a way has been shown to generate a net electric current by light in semiconductors [20,21], irrespective of their crystal symmetry. Generation of hot carriers with asymmetric population of momenta $\pm\mathbf{k}$, yielding such a current, was induced by quantum interference of one- and two-photon excitations with respective frequencies $2\omega_0$ and ω_0. The direction of the current is *coherently controlled* by the relative phase of the two laser beams. Since no special crystal symmetry is required, a current can be generated in the same way in isolated [22] and bundled [23] single-wall and multiwall carbon nanotubes with different geometrical and electronic structures. This current may displace an added atom in the nanotube, as schematically depicted in Fig. 1, by exerting on it the wind force F_w, due to the absorption of electron momenta. The direct force F_d, caused here by a local charge buildup due to electrons reflected from the atom, is much smaller than F_w.

Here we explore this idea of atomic driving in the (10, 10) carbon nanotube [24]. The model Hamiltonian,

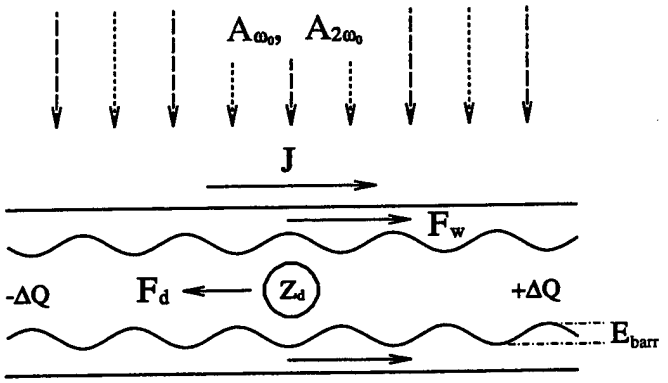

FIG. 1. Functional scheme of a nanotube-based atomic pump. Combined laser excitation at frequencies ω_0 and $2\omega_0$ induces a current J in the tube, which exerts the wind force F_w on an atom carrying the net charge Z_d. Reflected carriers build up a charge $\pm\Delta Q$, which generates a local field causing a direct force F_d to act on the atom. The atomic motion in the tube occurs on a potential energy surface with activation barriers E_{barr}.

0031-9007/99/82(26)/5373(4)$15.00

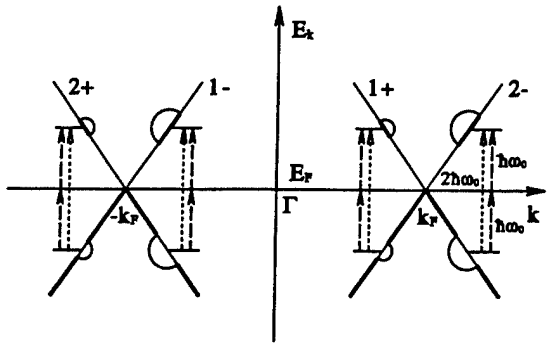

FIG. 2. Schematic of laser-induced one- and two-photon transitions at the respective energies $2\hbar\omega_0$ (long-dashed lines) and $\hbar\omega_0$ (dashed lines) between the crossing bands of a (10, 10) carbon nanotube. Because of coherent mixing of these processes connecting the same states, the generation at the right-hand side of the crossing points $\pm k_F$ exceeds that on the left-hand side, resulting in a nonzero current along the tube.

with bands crossing at E_F (see Fig. 2), is

$$H = \sum_{\alpha=\pm1,\pm2;k} \pm\hbar k v_F c^+_{\alpha,k} c_{\alpha,k} + H_{\text{el-tw}} - \frac{e}{c} A(t) \sum_k (v_{1\mp2\pm}(k) c^+_{1\mp,k} c_{2\pm,k} + \text{H.c.}) + \sum_k [V^s_{\text{at}}(k,\bar{k},t) c^+_{1\mp,k} c_{2\pm,\bar{k}} + \text{H.c.}] + H_{\text{el-at}}(t). \quad (1)$$

The summation over the wave vector k extends near the two Fermi points $\pm k_F$ in the one-dimensional Brillouin zone of the tube. $\bar{k}$ is center symmetric to k with respect to the closest $\pm k_F$. The index $\alpha = \pm1, \pm2$ denotes the bands, with the sign indicating the direction of the intraband velocity. $H_{\text{el-tw}}$ describes the scattering of electrons by twistons [25] and other excitations. The third term describes interband transitions; $A(t) = A_{\omega_0} e^{-i(\omega_0 t+\theta_{\omega_0})} + A_{2\omega_0} e^{-i(2\omega_0 t+\theta_{2\omega_0})}$ + c.c. is the component along the tube axis of the vector potential for the laser fields, and $v_{1\mp2\pm}(k) = \langle k, 1\mp | (-i\hbar/m_e)\nabla_{\text{axis}} | k, 2\pm\rangle$ are interband velocity matrix elements. The last two terms in Eq. (1) describe the scattering of electrons by the atom and the dynamical charge transfer to the atom.

The lowest bands of the (10, 10) tube near the Fermi points $\pm k_F$ are shown schematically in Fig. 2, with the populated regions for $E_k < E_F$ emphasized by thick lines. We show only the one- and two-photon transitions at the respective frequencies $2\omega_0$ and ω_0, connecting the same states; one-photon transitions at ω_0, not contributing to current, are neglected. Coherent mixing of the transition amplitudes for the one- and two-photon transitions can be controlled to yield different generation rates to the left and to the right of the Fermi points $\pm k_F$, symbolized by the different diameter of the half-circles, resulting in a nonzero current J.

In the rotating-wave approximation, the coherent sum of the one- and two-photon terms gives, for the effective generation field at k to the right of $\pm k_F$ [26],

$$\mathcal{A}_{\text{eff}}(k) = A_{2\omega_0} e^{-i\theta_{2\omega_0}} + \frac{\delta v(k)}{\hbar\omega_0} \frac{e}{c} (A_{\omega_0} e^{-i\theta_{\omega_0}})^2. \quad (2)$$

Only the crossing bands in Fig. 2 were included as *virtual* states in the two-photon part of Eq. (2) [26], where $\delta v(k) = 2v_F$ is the difference of the final (bands $1-$, $2-$) and initial (bands $2+$, $1+$) state velocities at k. The analogous expression for $\mathcal{A}_{\text{eff}}(\bar{k})$ at $\bar{k}$ to the left of $\pm k_F$ uses $\delta v(\bar{k}) = -2v_F$. Therefore, the amplitudes of $|\mathcal{A}_{\text{eff}}|$ at k and $\bar{k}$, and thus the generation rates there, can be different, and the resulting population imbalance of momenta near $\pm k_F$ creates a current. The direction and magnitude of this current are controlled by the phases θ_{ω_0}, $\theta_{2\omega_0}$ and the sign of the prefactor $\delta v(k)$, which is largely material independent. Consequently, the direction of the current that drives atoms in the pump can be controlled in single-wall and multiwall nanotubes or nanotube ropes.

The photogenerated current J, shown in Fig. 1, can be calculated from the Boltzmann equation in the relaxation time approximation [26,27]. In steady state it is given by

$$J = \frac{2e}{\hbar^2} \sigma_f^2 \tau_{\text{tr}}. \quad (3)$$

Here all bands in Fig. 2 and the two spin orientations are included, and τ_{tr} is the transport time in the tube. σ_f^2 is the product of the one- and two-photon terms in $(e/c)^2 |\mathcal{A}_{\text{eff}}(k)|^2$ and of $|v_{2-1+}(k)|^2$, yielding

$$\sigma_f^2 = \frac{4e^3 v_F}{c^3 \hbar\omega_0} |v_{2-1+}(k)|^2 A_{2\omega_0} (A_{\omega_0})^2 \cos(\delta\theta), \quad (4)$$

where the relative phase $\delta\theta = \theta_{2\omega_0} - 2\theta_{\omega_0}$ controls the direction of J. It is convenient to introduce the difference Δn in density of electrons traveling "right" and "left." Taking into account the contributions from all states near E_F, Δn is related to the current by $J = 4ev_F\Delta n$, which yields $\Delta n = \sigma_f^2 \tau_{\text{tr}}/(2\hbar^2 v_F)$.

To sustain atomic motion within the atomic pump, the force F due to the current J must be sufficiently large. Generation of such large forces F requires strong light intensities, excessively heating the tube. The absorbed power P depends in a linear way on the laser intensities I_{ω_0} and $I_{2\omega_0}$, whereas F is proportional to the product $I_{\omega_0} I_{2\omega_0}^{1/2}$. Therefore, the F/P ratio can be maximized using shorter laser pulses at higher intensities. The driving can also be increased by decreasing the frequency ω_0, since the factor $A_{2\omega_0}(A_{\omega_0})^2/\omega_0$ in Eq. (4) gives $\sigma_f^2 \propto \omega_0^{-4}$. In semiconducting nanotubes, one-photon absorption at ω_0 can be suppressed by tuning ω_0 in the gap, which changes the absorbed power dependence to $P \propto I_{\omega_0}^2$. Therefore, both I_{ω_0} and the ratio F/P can be sharply increased.

Our numerical estimates show that $I_{\omega_0} = I_{2\omega_0} = 100\ \text{kW/cm}^2$ at $\hbar\omega_0 = 100$ meV are reasonable values for these laser intensities. The interband velocity matrix elements are estimated to be $|v_{2-1+}(k)| \approx v_F \approx 1$ nm/fs [25,26], and the transport time due to scattering on

twistons is roughly $\tau_{tr} \approx 300/T[\mathrm{K}]$ ps. This value is based on the resistance of several ropes [25], extrapolated to a single tube. Then, using Eq. (4), we obtain $\sigma_f^2 = 0.47\ (\mathrm{meV})^2$. At $T = 300$ K, Eq. (3) yields the current $J = 0.38\ \mu$A and the electron density difference $\Delta n = 0.6 \times 10^{-3}\ \mathrm{nm}^{-1}$ in the empty tube.

When intercalated in a nanotube, atoms often become partly ionized. The close similarity between fullerenes, nanotubes, and graphite also suggests that the interaction energies between atoms and these sp^2 bonded systems are similar [28]. Therefore we use the potential energy barriers E_{barr} and net charges Z_d of atoms encapsulated in C_{60} [29] also for nanotubes. In the following, we consider Lithium atoms with $Z_d = +0.6e$ and $E_{barr} = 0.12$ eV. Calculations show that the tube band structure is not deformed much by the added atom. The chemical potential, however, shifts locally [15], thus attracting the delocalized transferred electrons and consequently screening the atom potential to a value V_{at}^s [30]. Further contribution to screening comes from the injected carriers that are also partly reflected by V_{at}^s [17]. In absence of experimental data, we assume $R \approx 0.1$ as a plausible value for the reflection coefficient of electrons on V_{at}^s.

This electron reflection generates a net wind force on the intercalated atom. The momentum transferred within a unit length l_0 of the tube is $\delta p/l_0 = (2\hbar\delta k)(4\Delta n)R = (8\hbar\omega_0/v_F)(\Delta n)R$, where $\delta k = k - \bar{k}$. Based on the parameter values determined above, the momentum transferred per unit time yields $F_w = (\delta p/l_0)v_F = (4\omega_0/\hbar v_F)\sigma_f^2\tau_{tr}R \approx 44\ \mu$eV/nm for the wind force and $F_w \propto T^{-1}$ for its temperature dependence. The effect of F_w on a partly ionized atom can be viewed as equivalent to a fictitious electric field, which in our case has a value $(e/Z_d)44$ V/mm.

Electrons reflected from the intercalated atom build up a local excess charge $\Delta Q_{\pm} \approx \pm 2e(\Delta n)l_{mfp}R$, separated about half of the mean-free path $l_{mfp} = v_F\tau_{tr}$ from the atom. Neglecting screening, the resulting dipole creates locally an electric field $E = -16e(\Delta n)R/l_{mfp}$. The Li atom carrying a charge $Z_d = +0.6e$ experiences a direct force $F_d = Z_dE = 8Z_de\sigma_f^2R/(\hbar v_F)^2 \approx -0.8\ \mu$eV/nm. Since the ratio $F_w/F_d = \hbar\omega_0\tau_{tr}v_F/2Z_de$ can be tuned to be very large ($\approx$58 here), our situation differs from the case of dc bias driving, where F_d dominates or is comparable to F_w both in bulk semiconductors [18] and metals [19].

The dynamics of the intercalated atom, as it diffuses along (across) the tube, is also influenced by the time dependence of $V_{at}^s(t)$ and $H_{el\text{-}at}(t)$. In the transition state of hopping, the atom may block the electron transport more efficiently, thus modifying R and consequently the net force $F = F_w + F_d$, and form new electron tunneling channels for transport. As these effects are very difficult to estimate quantitatively, we neglect them and evaluate the average drift velocity of the added atom using steady-state forces.

In the presence of the current J, the barriers for intersite hopping E_{barr} are shifted by the product of the net force on the atom F and the vector of length $l_t = 1.42$ Å that connects neighboring sites. Consequently, hopping rates towards left and towards right are given by $\nu_{L,R} = \nu_0 \exp[-(E_{barr} \pm Fl_t)/(k_BT)]$, where $\nu_0 = [(2E_{barr})/(m_{at}l_t^2)]^{1/2}$ is the atomic vibration frequency ($\nu_0 = 1.5 \times 10^{13}\ \mathrm{s}^{-1}$ for Li). This yields the drift velocity

$$\langle v_{at}\rangle = (\nu_L - \nu_R)l_t \approx \frac{2\nu_0 F l_t^2}{k_BT}\exp\left(-\frac{E_{barr}}{k_BT}\right). \quad (5)$$

The drift velocity $\langle v_{at}\rangle$ of the Li atom, given by Eq. (5), is shown in Fig. 3 as a function of temperature. It grows fast at low temperatures, reaches a maximum at $T \approx 700$ K, and then decreases slowly. At $T = 300$ K, $\langle v_{at}\rangle$ is more than 2 orders of magnitude smaller than the speed of broadening of the atom distribution by diffusion.

Exposure to the intense laser fields heats the nanotube, thus affecting the atomic transport. We estimate the average tube temperature T for laser pulses of duration t_p that repeat with a period of $t_{rep} = 1$ s. Assuming that in graphite radiation penetrates the topmost 30 layers, then a surface area s_1 of the tube should absorb the power $P = (I_{\omega_0} + I_{2\omega_0})(s_1/15)(t_p/t_{rep})$. Because of their mesoscopic nature, carbon nanotubes have limited emissivity in the long wavelength region. If approximated by a blackbody, power radiated out yields in steady state $P = \sigma T^4 s_1$, where $\sigma = 5.67 \times 10^{-8}\ \mathrm{W\,m^{-2}\,K^{-4}}$ is the Stefan-Boltzmann constant. For the above intensities, the dependence of the tube temperature $T = (2.35t_p[fs])^{1/4}$ K on the pulse length t_p is shown by the dashed line on the right-hand vertical scale of Fig. 3. The average atomic displacement during this laser pulse is $\langle x\rangle = \langle v_{at}\rangle t_p$. Thus $t_p = 15$-μs-long pulses raise the tube temperature to $T \approx 430$ K and cause displacements of $\langle x\rangle = 0.3\ \mu$m, comparable to the tube length.

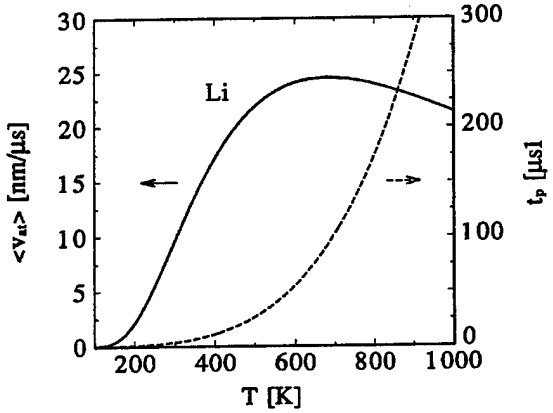

FIG. 3. The temperature dependence of the average drift velocity $\langle v_{at}\rangle$ of a Li atom in a nanotube is given by the solid line. The relationship between the tube temperature T and the duration t_p of the laser pulse (right-hand vertical scale) is given by the dashed line.

Electrons excited by laser to the energy $\hbar\omega_0 = 100$ meV above E_F may also scatter inelastically from the intercalated atom and thus "heat" it above the tube temperature T [31]. Assuming that the atom thermally equilibrates after each hop, which occurs statistically every $t_b = \exp(E_{\text{barr}}/k_BT)/\nu_0 = 7$ ps at $T = 300$ K, it can absorb several phonons of the energy $h\nu_0 \approx 58$ meV $\approx E_{\text{barr}}/2$. Its "temperature," thus raised by tens to hundreds of degrees Kelvin above T, enters into the exponent of the activation factor in Eq. (5). This causes a significant increase of the velocity $\langle v_{\text{at}} \rangle$, in particular at low T or in the case of stronger driving, and it can also dramatically improve atom detachment from various tube imperfections.

Large defects, such as bamboo closures within multiwall tubes, obviously block atomic transport and must be eliminated by destroying the corresponding nanotube section. Charge accumulating at the tube ends also acts as a defect by generating an additional direct force $\tilde{F}_d$ that drags positively charged atoms in the same direction as F_w. This charge is continuously released by electrons or ions entering and leaving the tube. Consequently, tube ends and other small defects act as a rather soft trap potential $V(x)$, yielding a distribution $\rho_{\text{at}}(x) \propto \exp[-V(x)/k_BT]$ of aggregated atoms. Thermal fluctuations of trapped atoms at the aggregate boundaries can be largely augmented by the absorption of phonons from hot electrons. The combined effect of atom detaching/driving by two laser beams might also be achieved if one laser beam (hot electron detaching) and a dc bias (driving by F_d) are applied to the nanotube.

In summary, we have proposed a molecular pump with a (carbon) nanotube body. Excitation of the nanotube by two laser beams in a coherent control scheme generates an electron current, which drives intercalated atoms by the wind force F_w. The temperature dependence of the drift velocity v_{at} for a Li atom shows a pronounced maximum at $\langle v_{\text{at}} \rangle \approx 25$ nm/μs. The detachment rate and the drift velocity of the atom can be enhanced by inelastic scattering of hot electrons. The pump can be used for a semicontinuous deposition of atoms on surfaces. Two beam irradiation of surfaces may also be used to locally control diffusion at surfaces [32] and inside layered or porous materials [33].

P. K. thanks J. E. Sipe for support provided by Photonics Research, Ontario, and D. T. acknowledges financial support from the Office of Naval Research under Grant No. N00014-99-1-0252.

[1] D. M. Eigler and E. K. Schweizer, Nature (London) **344**, 524 (1990).
[2] J. A. Stroscio and D. M. Eigler, Science **254**, 1319 (1991).
[3] I.-W. Lyo and Ph. Avouris, Science **253**, 173 (1991).
[4] M. F. Crommie, C. P. Lutz, and D. M. Eigler, Science **262**, 218 (1993).
[5] M. Böhringer *et al.*, Phys. Rev. B **57**, 4081 (1998).
[6] K. Svoboda *et al.*, Nature (London) **365**, 721 (1994); L. P. Faucheux *et al.*, Phys. Rev. Lett. **74**, 1504 (1995); R. D. Astumian, Science **276**, 917 (1997).
[7] V. A. Lombillo, R. J. Stewart, and J. R. McIntosh, Nature (London) **373**, 161 (1995).
[8] S. Iijima, Nature (London) **354**, 56 (1991).
[9] A. Rubio *et al.*, mtrl-th/9508011; A. Rubio, J. L. Corkill, and M. L. Cohen, Phys. Rev. B **49**, 5081 (1994).
[10] J. W. Mintmire, B. I. Dunlap, and C. T. White, Phys. Rev. Lett. **68**, 631 (1992).
[11] N. Hamada, S. Sawada, and A. Oshiyama, Phys. Rev. Lett. **68**, 1579 (1992).
[12] R. Saito *et al.*, Appl. Phys. Lett. **60**, 2204 (1992).
[13] P. M. Ajayan *et al.*, Phys. Rev. Lett. **72**, 1722 (1994).
[14] G. Gao, T. Cagin, and W. A. Goddard III, Phys. Rev. Lett. **80**, 5556 (1998); L. Grigorian *et al.*, Phys. Rev. Lett. **80**, 5560 (1998).
[15] Y. Miyamoto *et al.*, Phys. Rev. Lett. **74**, 2993 (1995).
[16] T. J. Gramila *et al.*, Phys. Rev. Lett. **66**, 1216 (1991); A.-P. Jauho and H. Smith, Phys. Rev. B **47**, 4420 (1993).
[17] R. S. Sorbello, Phys. Rev. B **39**, 4984 (1989).
[18] D. Kandel and E. Kaxiras, Phys. Rev. Lett. **76**, 1114 (1996).
[19] A. Lodder and J. P. Dekker, in *Stress Induced Phenomena in Metalliation*, edited by H. Okabayashi and P. S. Ho, AIP Conf. Proc. No. 418, (AIP, New York, 1998), p. 315–328 (cond-mat/9803172).
[20] G. Kurizki, M. Shapiro, and P. Brumer, Phys. Rev. B **39**, 3435 (1989).
[21] E. Dupont *et al.*, Phys. Rev. Lett. **74**, 3596 (1995); R. Atanasov *et al.*, Phys. Rev. Lett. **76**, 1703 (1996).
[22] J. W. G. Wildöer *et al.*, Nature (London) **391**, 59 (1998).
[23] Y.-K. Kwon, S. Saito, and D. Tománek, Phys. Rev. B **58**, R13 314 (1998).
[24] A. Thess *et al.*, Science **273**, 483 (1996).
[25] C. L. Kane *et al.*, cond-mat/9704117.
[26] P. Král and J. Sipe, in Proceedings of the ICPS24 Conference, Jerusalem, 1998 (to be published).
[27] P. Král, Phys. Rev. B **53**, 11 034 (1996).
[28] Y.-K. Kwon *et al.*, Phys. Rev. Lett. **79**, 2065 (1997).
[29] Y. S. Li and D. TománekChem. Phys. Lett. **221**, 453 (1994); *ibid.* **243**, 42 (1995).
[30] M. F. Lin and D. S. Chuu, Phys. Rev. B **55**, 4996 (1997).
[31] K. S. Ralls, D. C. Ralph, and R. A. Buhrman, Phys. Rev. B **40**, 11 561 (1989).
[32] I. Derényi, Ch. Lee, and A.-L. Barabási, Phys. Rev. Lett. **80**, 1473 (1998).
[33] S. Furusawa, T. Suemoto, and M. Ishigame, Phys. Rev. B **38**, 12 600 (1988).

ELSEVIER

Diamond and Related Materials 10 (2001) 1947–1951

DIAMOND AND RELATED MATERIALS

www.elsevier.com/locate/diamond

Synthesis of high-density carbon nanotube films by microwave plasma chemical vapor deposition

U. Kim[a,*], R. Pcionek[a], D.M. Aslam[a], D. Tománek[b]

[a] *Department of Electrical and Computer Engineering, Michigan State University, East Lansing, MI 48824, USA*
[b] *Department of Physics and Astronomy, Michigan State University, East Lansing, MI 48824, USA*

Received 1 August 2000; accepted 19 January 2001

Abstract

Nanotubes with diameters ranging from 20 to 400 nm and densities in the range of 10^8–10^9 cm^{-2}, produced on metal-coated silicon by microwave plasma chemical vapor deposition, show various shapes depending upon: (i) growth conditions; and (ii) pre- or post-growth treatment of the samples. Presence of nitrogen in the growth or pre-growth atmosphere increases the density and vertical growth rate of nanotubes. The growth rate on an iron-coated substrate is higher than on a nickel-coated substrate. A cleaning procedure, consisting of ultrasonic treatment of nanotubes in methanol, is demonstrated.

Keywords: Carbon nanotube; Microwave plasma chemical vapor deposition (MPCVD)

1. Introduction

Since their discovery [1] using arc discharge evaporation, carbon nanotubes have been the subject of numerous investigations [2–6] because of their unique electronic and mechanical properties. A precise control of the fabrication method including patterning is required for potential applications in electronics [7,8], field emission displays [9–12], biomedical devices and nanoelectromechanical systems (NEMS) [13]. Aligned carbon nanotubes have been obtained using chemical vapor deposition (CVD) on flat substrates [4], and by pyrolysis of acetylene on cobalt within a nano-channel alumina template [14]. Bower et al. [15] showed that aligned carbon nanotubes can be grown perpendicular to the local substrate surface, regardless of the surface tilt or shape, using microwave plasma CVD (MPCVD). The alignment is induced by the electrical self-bias field imposed on the substrate surface from the plasma environment.

In the present study, we make use of the many control parameters accessible in an MPCVD reactor to selectively grow nanotubes with particular morphologies. Similar to all other nanotube synthesis techniques, incorporation of defects cannot be avoided during the growth. A post-growth cleaning process is usually required before using the nanotubes in device structures. In this article, we report: (i) a uniform, high-density growth; and (ii) a cleaning procedure for carbon nanotubes.

2. Experimental

The flexibility of the MPCVD system, which permits a contamination-free processing and a modification of plasma shape through tuning of the cavity, allows syn-

* Corresponding author. Tel.: +1-517-353-6329; fax: +1-517-353-1980.
E-mail address: kimungsi@egr.msu.edu (U. Kim).

0925-9635/01/$ - see front matter
PII: S0925-9635(01)00384-3

thesis of a wide variety of carbon allotropes, ranging from nano-diamond [16] to nanotubes. Nanotubes in the present study are fabricated by MPCVD using iron (Fe) or nickel (Ni) as transition metal catalysts on titanium coated silicon substrates. A thin film of Ni (100 nm) is sputter deposited, or ferric nitrate [$Fe(NO_3)_3$] dissolved in methanol is coated (100–300 nm) on the substrate. Typical parameters varied in this study are: (i) growth temperature (450–850°C), growth time (0.5–120 min) and atmosphere ($N_2/H_2/CH_4$), and (ii) pre- and post-growth treatment (N_2/H_2). Scanning electron microscopy (SEM) and transmission electron microscopy (TEM) are used to characterize nanotube properties such as diameter, length, orientation, uniformity and density.

3. Results and discussion

Fig. 1 shows an overview of nanotube structures grown under varying deposition parameters as detailed in Table 1. A very uniform growth is achieved at temperatures between 650 and 750°C. Both vertical and horizontal growth of nanotubes was observed. A pre-growth treatment in nitrogen plasma enhances vertical growth. As shown in Fig. 1a, clusters are formed on top of the nanotubes during deposition at 650°C. The diameters of tubes grown under these conditions are in the range of 20–100 nm, implying multi-wall nanotubes. Energy-dispersive spectroscopy (EDS) indicates the presence of carbon in these clusters. Increasing the deposition temperature to 750°C reduces the size of these clusters, but increases the diameter of the tubes to 100–400 nm as shown in Fig. 1b. We interpret this diameter increase by improved growth kinetics at higher temperatures, in agreement with the conclusions of Thess et al. [2]. As seen in Fig. 1c, the build-up of clusters is strongly suppressed if nanotubes are grown by placing the metal-coated substrate upside down, leaving a gap between the growing surface and the substrate holder. In this case, tubes are grown downward and the plasma has to reach the growing surface. At the growth temperature of 650°C, the tube lengths are found to increase from approximately 1 μm to 50

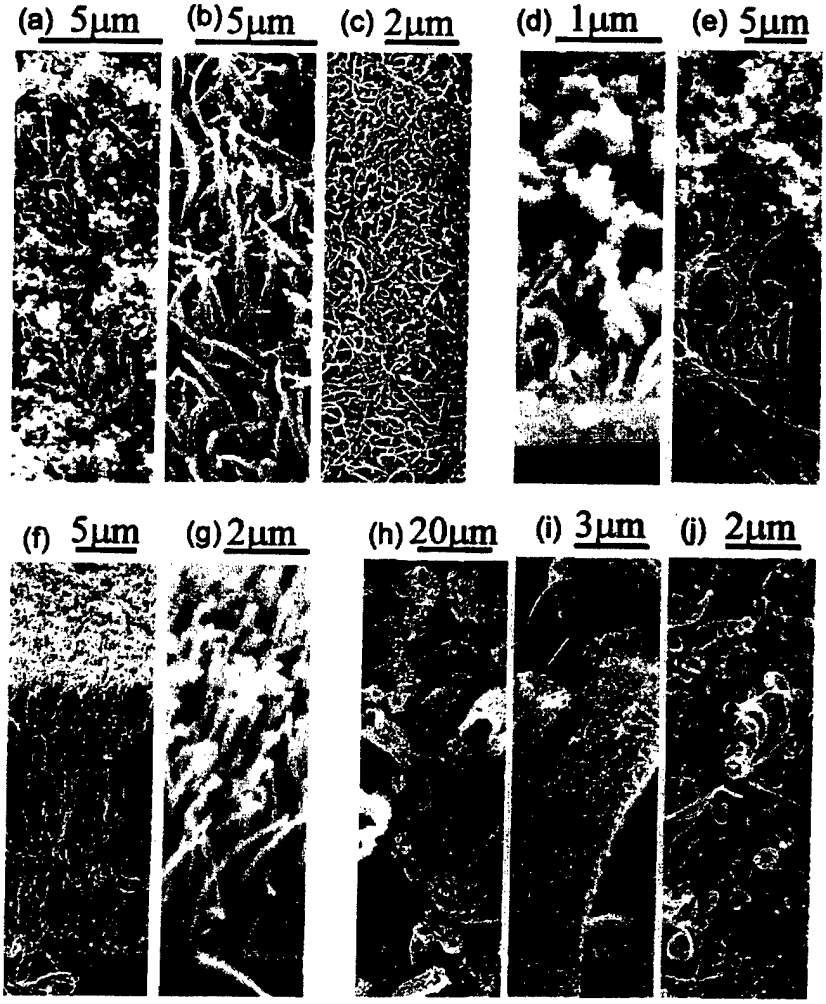

Fig. 1. Scanning electron microscopy (SEM) images of carbon nanotube films grown under the conditions described in Table 1.

Table 1
Growth conditions and tube diameters shown in Fig. 1

Specimen	Growth parameters				Tube diameter (nm)
	Temp. (°C)	Growth time (min)	Reaction gases	Substrate	
Fig. 1a	650	15		Fe/Ti/Si	20–100
Fig. 1b	750	15		Fe/Ti/Si	100–400
Fig. 1c	650	15		Si/Ti/Fe	30–50
			H_2 (90 sccm)		
Fig. 1d	650	0.5		Fe/Ti/Si	20–100
			N_2 (10 sccm)		
Fig. 1e	650	120		Fe/Ti/Si	20–100
			CH_4 (6 sccm)		
Fig. 1f	650	15		Fe/Ti/Si	20–100
Fig. 1g	650	15		Ni/Ti/Si	60–100
Fig. 1h,i,j	650	15		Fe/etched Ti/Si	20–80

μm, if the growth time is increased from 30 s to 120 min, as seen in Fig. 1d,e. The tube diameter is not affected by the growth time. Also in this case, terminating clusters can be clearly seen. In another experiment, the effect of Fe and Ni as a catalyst was investigated, while keeping the growth parameters the same. Although the growth on Fe or Ni yields similar ranges of diameters, density and orientation (vertical or horizontal), the growth rate is faster for Fe than that for Ni, consistent with the higher catalytic activity of Fe. Morphology of nanotube films grown on Fe and Ni is shown in Fig. 1f,g, respectively.

Different nanotube shapes can be obtained if the substrate is etched using different acids before applying the Fe coating (Fig. 1h–j). This treatment, leading to a very thin (20–80 nm) layer of Fe coating, can be used to create 'macaroni' shapes with a hollow core, which appear to be woven out of very fine nanotubes, as seen in Fig. 1i. This technique has the potential of creating different types of 'fibers' made of nanotubes.

Transmission electron microscopy (TEM) was used for accurate measurements of the tube diameter. As seen in Fig. 2a,b, TEM images of nanotubes grown at 650°C show two distinct features, namely a straight hollow and a repeating arrowhead shape. For straight hollow tubes, the width of hollow region is in the range of 11–55 nm, with a wall thickness in the range of 20–38 nm depending on the tube diameter. The tip of the arrowhead is in the range of 8–12 nm, while the wide side of arrowhead is in the range of 15–30 nm. It is interesting to know that the average tube diameter is different from the hollow structures. The tubes with a straight hollow core are approximately 20 nm larger in diameter than the ones with an arrowhead shape. The tip of the tubes is tapered and closed. The black spots on the walls seem to be the structural defects generated during growth.

As shown in Fig. 3, patterned substrates are used to deposit nanotubes selectively. The substrate is treated in H_2/N_2 plasma at 650°C for 5 min, followed by exposure to CH_4.The growth lasts for 15 min. SEM observations indicate that the alignment and orientation of nanotubes in Fig. 3 are uniform across the deposited area.

In addition to the above observed structures, we report two new findings based on our experiments, namely the etching of nanotubes by plasma and post-growth detachment of the carbon clusters from the tubes. For growth temperatures in the range of 800–900°C, etching of carbon nanotubes was observed. At the lower end of this range, tubes grown during short growth times (less than 5 min) can be etched if longer growth times (greater than 15 min) are used.

Previously reported purification methods [17,18], designed to remove clusters and other undesirable structures from the nanotube material, involve laborious steps such as refluxing, centrifugation, sedimentation

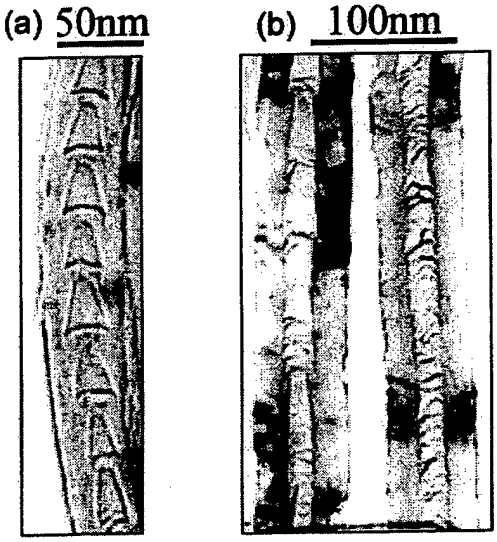

Fig. 2. Transmission electron microscopy (TEM) images of carbon nanotube films grown under various conditions.

and filtration, or boiling in an acid bath. We have demonstrated an alternate, less laborious way to purify CVD grown nanotubes, which involves treatment of as-grown nanotubes in methanol in an ultra-sonic bath for 15 min. Tubes cleaned in this way, shown in Fig. 4, become free of the cluster residue. We find that CVD-grown nanotubes adhere well to the substrate, thus suggesting their application as field electron emitters. It may be pointed out that an ultrasonic cleaning procedure has also been reported for single-wall nanotubes grown by laser-vaporization [19].

4. Conclusions

A comparison between the growth conditions described in Table 1 and the nanotube morphologies of Fig. 1 suggests that the higher temperature used to synthesize the sample in Fig. 1b yields tubes that are fatter and straighter. At lower temperatures, associated with the system depicted in Fig. 1j, the commonly forming pentagon–heptagon defects cannot be annealed easily, causing the tubes to bend. We note that nanotube coils, when anchored firmly in a substrate, could be used to make strong interconnects between surfaces [20], in vague analogy with the Velcro® closure, thus harnessing the unusually high tensile strength of 30 GPa found in carbon nanotubes [21].

In summary, we report formation of dense carbon nanotube films with different morphologies that were synthesized by varying the conditions in a MPCVD reactor. We found optimum growth in presence of an iron catalyst and nitrogen in the atmosphere. A cleaning procedure, consisting of ultrasonic treatment of nanotubes in methanol, has been found to efficiently remove any amorphous residue formed during the synthesis.

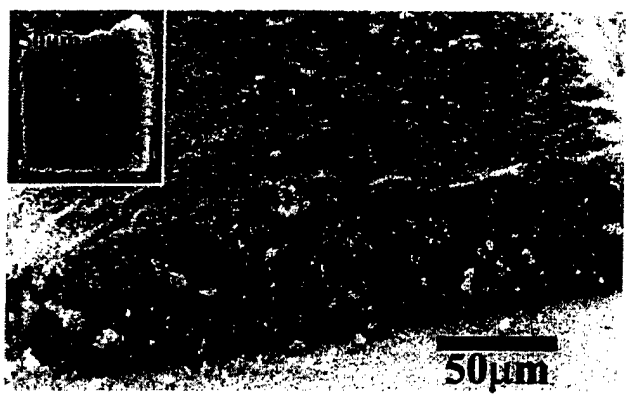

Fig. 3. SEM micrographs show the patterned nanotubes (250 × 250 μm^2).

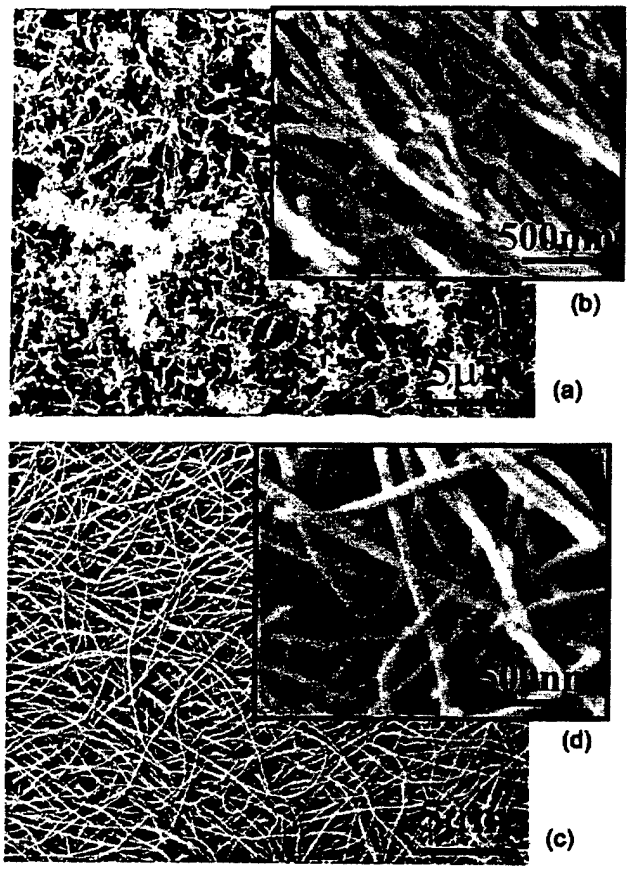

Fig. 4. SEM images of as-grown nanotube films (a and b) and films that have been subjected to ultrasonic treatment in methanol (c and d), resulting in removal of carbon clusters.

Acknowledgements

Financial support for this research has been provided by NASA Grant Number NAG5-9276. D.T. acknowledges financial support from ONR/DARPA under Grant Number N00014-99-1-0252.

References

[1] S. Iijima, Nature (London) 354 (1991) 56.
[2] A. Thess, R. Lee, P. Nikoaev et al., Science 273 (1996) 483.
[3] W.Z. Li, S.S. Xie, L.X. Qian et al., Science 274 (1996) 1701.
[4] Z.F. Ren, Z.P. Huang, J.W. Xu et al., Science 282 (1998) 1105.
[5] L.C. Qin, D. Zhou, A.R. Krauss, D.M. Gruen, Appl. Phys. Lett. 72 (1998) 3437.
[6] X. Xu, G.R. Brandes, Appl. Phys. Lett. 74 (1999) 2549.
[7] C. Dekker, Physics Today, May (1999) 22.
[8] P. Poncharal, Z.L. Wang, D. Ugarte, W.A. de Heer, Science 283 (1999) 1513.
[9] W. Zhu, C. Bower, O. Zhou, G. Kochanski, S. Jin, Appl. Phys. Lett. 75 (1999) 873.
[10] K.A. Dean, B.R. Chalamala, J. Appl. Phys. 85 (1999) 3832.
[11] Y. Saito, K. Hamaguchi, R. Mizushima et al., Appl. Surf. Sci. 146 (1999) 305.
[12] P.G. Collins, A. Zettl, Phys. Rev. 55 (1997) 9391.
[13] D. Srivastava, Nanotechnology 8 (1997) 186.
[14] J. Li, C. Papadopoulos, J. Xu, M. Moskovits, Appl. Phys. Lett. 75 (1999) 367.

[15] C. Bower, W. Zhu, S. Jin, O. Zhou, Appl. Phys. Lett. 77 (2000) 830.
[16] G.S. Yang, M. Aslam, K.P. Kuo, D.K. Reinhard, J. Asmussen, J. Vac. Sci. Technol. B 13 (1995) 1030.
[17] J. Liu, A.G. Rinzler, H. Dai et al., Science 280 (1998) 1253.
[18] L. Forro, J.P. Salvetat, J.M. Bonard et al., in: D. Tománek, R.J. Enbody (Eds.), Science and Application of Nanotubes, Kluwer Academic/Plenum Publishers, New York, 2000.
[19] K.B. Shelimov, R.O. Esenaliev, A.G. Rinzler, C.B. Huffman, R.E. Smalley, Chem. Phys. Lett. 282 (1998) 429.
[20] Micro-Fastening System and Method of Manufacture. U.S. patent application of D. Tománek, Richard J. Enbody, Young-Kyun Kwon.
[21] M.F. Yu, B.S. Files, S. Arepalli, R.S. Ruoff, Phys. Rev. Lett. 84 (2000) 5552.

Electronic structure and properties of rhombohedrally polymerized C_{60}

A. V. Okotrub, V. V. Belavin, and L. G. Bulusheva
Institute of Inorganic Chemistry SB RAS, pr. Ak. Lavrentieva 3, Novosibirsk 630090, Russia

V. A. Davydov
Veretschagin Institute of High Pressure Physics, Troitsk 142092, Moscow Region, Russia

T. L. Makarova
Ioffe Physico-Technical Institute, St. Petersburg 194021, Russia

D. Tománek
Department of Physics and Astronomy, Michigan State University, East Lansing, Michigan 48824-1116

(Received 23 May 2001; accepted 9 July 2001)

The valence electronic structure of rhombohedrally polymerized C_{60}, synthesized at 6 GPa and 725 °C, has been studied using x-ray emission spectroscopy. The C $K\alpha$ spectrum of the polymer was found to differ from that of the C_{60} fullerite especially in the high-energy region. The observed spectra were compared to densities of states, calculated using a tight-binding approximation for three two-dimensional hexagonal C_{60} networks, distinguished by the nature of intermolecular bonding. Theoretical spectra of the polymers agree well with experiment and indicate that changes in the valence band of C_{60} upon polymerization are mainly due to the formation of intermolecular bonds, and only to a negligible degree due to a distortion of the C_{60} cage. Rotation of C_{60} within the hexagonal layer changes dramatically the electronic properties of the polymer from a semiconducting behavior for the structure with 66/66 connections to a metallic behavior for a layer containing C_{60} molecules that are linked through 56/65 bonds. The occurrence of the latter configuration may explain the observed metalliclike in-plane conductivity of the rhombohedral phase of C_{60}. [DOI: 10.1063/1.1398079]

I. INTRODUCTION

The rhombohedral phase of the C_{60} fullerene is formed under pressures ranging from 5 to 8 GPa and in the temperature range of 700–1000 °C.[1] The solid is characterized by an anisotropy of bonding. The interaction between polymerized layers has van der Waals character and each C_{60} molecule of a layer is bonded to its six neighbors by twelve equatorial atoms.[2,3] The formation of four-membered rings between molecules is evident from ^{13}C NMR studies on the rhombohedral phase.[4] The C_{60} fullerene has two symmetry-independent bonds: one is shared by two hexagons (66-bond, sometimes called a "double" bond) and another separates a hexagon from a pentagon (65-bond, sometimes called a "single" bond). Hence, a cycloaddition of C_{60} may develop through 66/66, 66/56, 56/56, and 56/65 intermolecular bonding. For the $(C_{60})_2$ dimer, the former configuration has been predicted by quantum-chemical calculations to be the most energetically stable.[5,6]

The covalent bonding between C_{60} molecules considerably changes the electronic structure and properties of the solid. Density functional (LDA) and tight-binding calculations of the rhombohedral phase and its two-dimensional layer found the fundamental gap to be narrower and the band dispersion to be larger in comparison to bulk C_{60} fullerite, a molecular solid.[7,8] The presence of 56-bonding in the hexagonal network was considered to explain semimetal properties of the rhombohedral solid.[8] Furthermore, increase of the π conjugations between C_{60} molecules could lead to the transition in the metallic state.[9] Electrical properties of the rhombohedral polymer were found to be strongly dependent on the temperature of polymerization.[10] In the polymerized plane, the conductivity increases with increasing the preparation temperature up to a metalliclike behavior.

The purpose of the present work is to investigate the electronic structure of rhombohedrally polymerized C_{60} using x-ray emission spectroscopy and the tight-binding method. The x-ray emission arises as the result of electron transitions from valence shell to a previously created core vacancy. Due to dipole selection rules and localization of the core orbital, _α spectrum characterizes the distribution of C $2p$ electrons in the valence band of a compound. Recently, the changes in the valence band of C_{60} films upon photopolymerization have been studied by photoelectron spectroscopy using He I (Ref. 11) and Mg $K\alpha$ (Ref. 12) excitations. The valence electronic structure of the polymerized C_{60} films was found to be almost the same as that of the pristine films. A shift of the spectrum toward lower binding energies and a broadening of bands was shown to be caused by the increased size of the conjugated π-electron system.[11] The presence of six-coordinated C_{60} molecules in the rhombohedral polymer could have a similar effect on the electronic structure. The interpretation of the spectral features and study of the electronic properties of the polymers are performed by considering differently arranged hexagonal networks of C_{60} in the calculations.

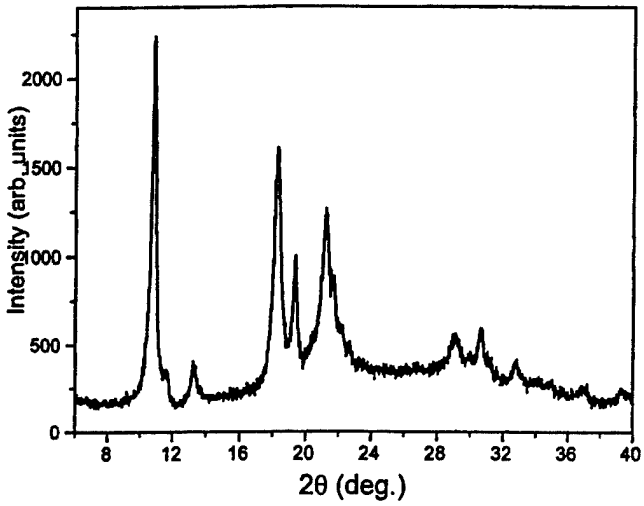

FIG. 1. X-ray diffraction spectrum of rhombohedrally polymerized C_{60}.

II. EXPERIMENT

The rhombohedral C_{60} polymer was prepared in a Toroid-type high-pressure apparatus from fullerene powder of 99.9% purity, produced by Term USA, Berkeley, CA. The fullerite sample was heated rapidly up to 725 °C at a constant pressure of 6 GPa. The details of the sample preparation procedure were published earlier.[13]

The x-ray diffraction pattern of the sample as produced (Fig. 1) indicates the formation of a practically pure rhombohedral phase of C_{60}, with the lattice parameters $a = 9.20$ Å and $c = 24.61$ Å.

The x-ray emission spectra of the C_{60} molecular solid and the rhombohedrally polymerized C_{60} were recorded with a "Stearat" spectrometer, using the ammonium biphtalate (NH_4AP) single crystal as a crystal-analyzer. This crystal has a nonlinear reflection efficiency, which is corrected by the procedure described elsewhere.[14] The samples were deposited on a copper substrate and cooled down to liquid nitrogen temperature in the vacuum chamber of the x-ray tube with a copper anode ($U = 6$ kV, $I = 0.5$ A). The x-ray transition energies, displayed in Fig. 3, were obtained with an absolute accuracy of ±0.15 eV and a spectral resolution of 0.4 eV.

III. THEORY

Three two-dimensional polymers with different intermolecular bonds (Fig. 2) were constructed. Each molecule in polymer I is connected to six neighbors by a [2+2] cycloaddition of 66-bonds. Hexagonal packing of C_{60} molecules linked by 65-bonds results in the 65/56 configuration (polymer II), where each pentagon adjacent to a four-membered ring is opposite to a hexagon. Polymer III can be imagined as an insertion of misoriented molecules in polymer I. The central C_{60} molecule of the fragment depicted in Fig. 2(c) is linked by 65-bonds to 66-bonds of the neighboring molecules. The portion of 66-bonding molecules in the polymerized layer is twice that of the misoriented molecules. A unit cell of polymers I and II contains one molecule, whereas a unit cell of polymer III holds three molecules.

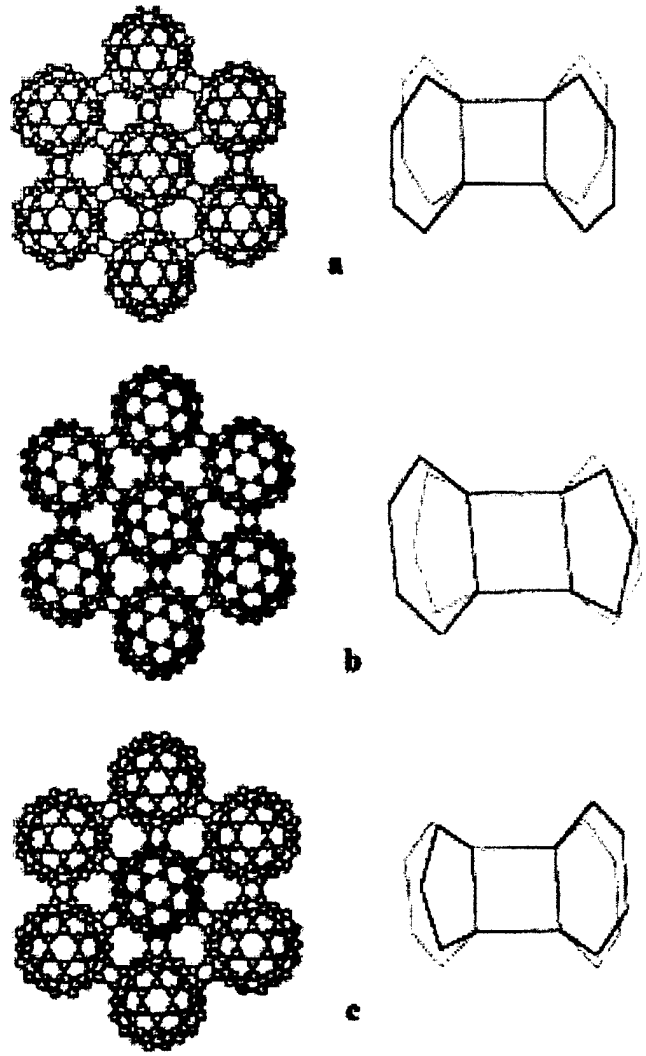

FIG. 2. Structural models describing the bonding within rhombohedrally polymerized C_{60}. (a) Polymer I with 66/66 bonding, (b) polymer II with 65/56 bonding, and (c) polymer III, characterized by 65 edges of the central molecule being adjacent to 66 edges of neighboring molecules. Changes in the orientation of the fullerenes are emphasized by different levels of shading.

The geometry of the polymer fragments (Fig. 2) was optimized by the molecular mechanic MM+ force field.[15] The relaxed intermolecular bonds in 66/66, 65/56, and 65/66 configurations have a length of 1.582 Å, 1.594 Å, and 1.608 Å, characteristic of covalent bonds in sp^3 hybridized carbon systems. The atomic coordinates of the central molecule in the fragments were used to calculate the electronic band structure of the polymers. For polymer III, the atomic coordinates of the two neighboring 66-bonded molecules were used in addition. The resulting values of a translation vector for polymers I, II, and III are equal to 9.19 Å, 9.17 Å, and 9.26 Å, which is in good agreement with the experimentally determined lattice parameter of 9.2 Å.

The polymers were calculated using an empirical tight-binding Hamiltonian that was especially parameterized to reproduce the features in the x-ray fluorescence spectra of fullerenes.[16] For these calculations, 132 k points were chosen in the irreducible part of the Brillouin zone. The intensity of x-ray transitions was computed as a sum of the squared tran-

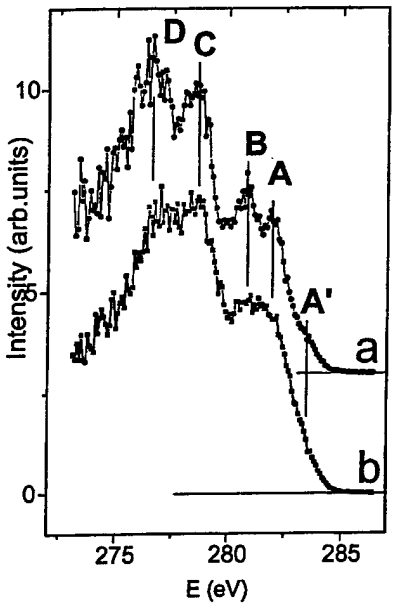

FIG. 3. Observed C $K\alpha$ spectra of (a) the C_{60} molecular solid, fullerite, and (b) rhombohedrally polymerized C_{60}.

sition coefficients, corresponding to the contribution of the C $2p$-atomic orbitals (AOs) to the particular molecular orbital (MO). The C $K\alpha$ intensity profile, shown in Fig. 4, was further convoluted with a 0.5 eV Lorenzian function and plotted in a scale of the one-electron energies of the occupied MOs. Total energies of the polymers were derived using a carbon–carbon interaction potential[17] with somewhat changed parameters.[16]

IV. RESULTS AND DISCUSSION

The $\_\alpha$ spectra of the C_{60} fullerite and the rhombohedral C_{60} polymer are displayed side-by-side for comparison in Fig. 3. Due to the reflection peculiarities of the crystal analyzer used, the C $K\alpha$ intensity can be reliably measured only in the region from 285 eV to 275 eV. The fullerite spectrum exhibits four well-developed maxima, which are in good agreement with spectra recorded on spectrometers with diffraction gratings, using synchrotron radiation.[18,19] The weak intermolecular interactions in fullerite have only a slight effect on the density of states.[20] This permits us to correlate the energy bands to the molecular levels of C_{60} and, hence, to interpret the C $K\alpha$ spectrum on the basis of calculations of the free molecule. A detailed analysis of the fullerite spectrum has been performed in Ref. 21. The high-energy maxima A and B correspond to the radially directed π-like MOs, whereas the maxima C and D are mainly formed by σ-like MOs. The shoulder A′ is a nondiagrammatic line caused by the reemission of C $1s$ electrons excited into the lowest unoccupied MO (LUMO) of C_{60}.[19] Formation of covalent intermolecular bonding in the rhombohedral C_{60} polymer noticeably changes the $\_\alpha$ spectral profile [Fig. 3(b)]. First, the gaps between the maxima A, B and between the maxima C, D nearly disappear, and the $\_\alpha$ spectrum of the polymer shows two broad maxima: an intense split maximum around 277.5 eV and a high-energy maximum at 281 eV. Second, all spectral lines move towards the high-energy

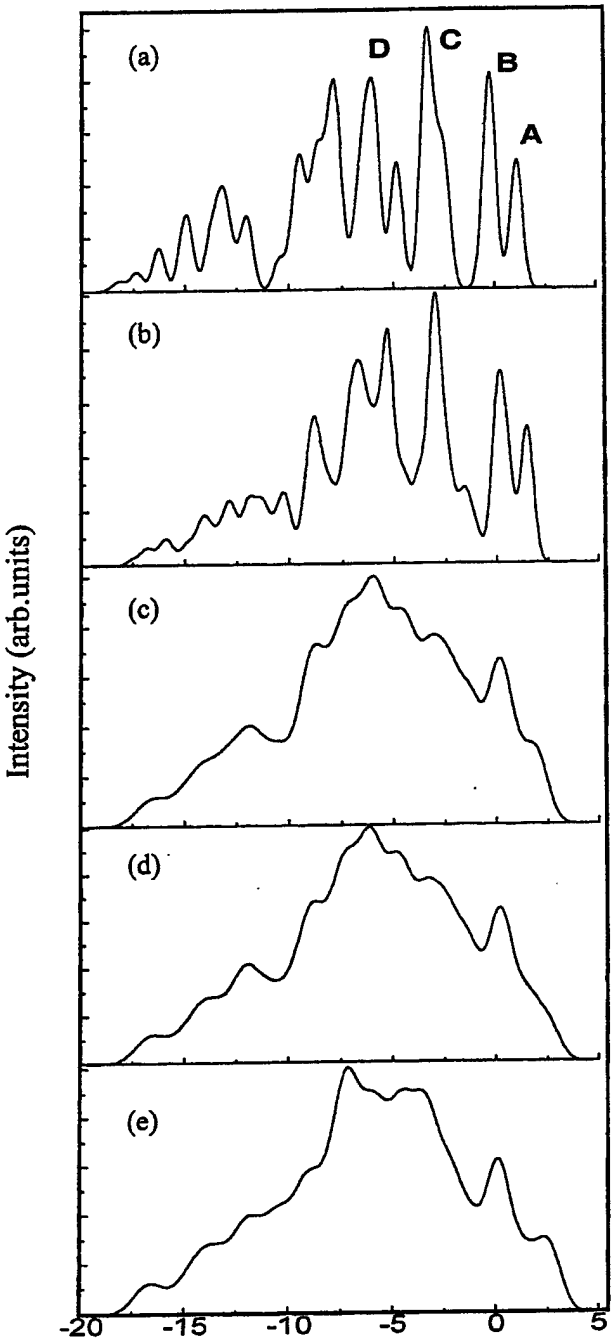

FIG. 4. Calculated C $K\alpha$ emission spectra for (a) the icosahedral C_{60} molecule, (b) the distorted C_{60} cage taken from the 66/66 layer, (c) polymer I, (d) polymer III, and (e) polymer II. The spectral lines were convoluted with a 0.5 eV Lorenzian function.

region with respect to the molecular solid. The observed effects may be caused by a distortion of the C_{60} cage in the polymer and/or by the formation of new intermolecular bonds.

Figure 4 demonstrates the change of the theoretical $\_\alpha$ spectrum of the free C_{60} molecule due to polymerization. Maxima in the spectrum of the icosahedral molecule [Fig. 4(a)] were labeled in accordance with those in the experimental spectrum of fullerite. The calculated spectrum, plotted for a distorted C_{60} that is isolated from 66/66 layer, keeps the basic maxima [Fig. 4(b)]. Splitting of MOs that were initially degenerate in the icosahedral C_{60} results in a broad-

ening and a shift of the spectral maxima. The main effect of the interactions between C_{60} molecules in the polymer is on the _α profile [Figs. 4(c)–4(e)]. Compared to the theoretical spectra of C_{60}, those of polymerized C_{60} are characterized by a significant broadening of the high-energy maxima A and B and their shift towards the Fermi level. Furthermore, one can see an increase in the electronic density of states between the maxima. These tendencies are observed in all theoretical spectra, although the spectra of polymers I and III, which are similar in appearance, differ from the spectrum of polymer II in the intensities and positions of the features. Therefore, to decide which is the most preferable arrangement of a hexagonally polymerized C_{60} layer, based only on a comparison between theoretical and experimental $CK\alpha$ spectra, seems not to be feasible. Actually, the electronic density of states in the vicinity of the Fermi level[8] is much more sensitive to the local structure than the distribution of $C\,2p$ valence electrons in the solid.

The energy band dispersion of the calculated polymers along high-symmetry lines in the Brillouin zone of the hexagonal lattice is shown in Fig. 5. The polymer I has an indirect 0.81 eV gap between the top of the valence band (marked as T point) and the bottom of the conduction (K point). A previous calculation of the 66/66 layer with different atomic positions, based on the same quantum-chemical scheme, had provided the gap value of 0.57 eV,[16] thus demonstrating the strong effect of geometry on the width of the fundamental gap. Nevertheless, the basic features in the density of states in a wide energy interval are practically the same for both structures. The character of the band dispersion near the Fermi level is also similar. In particular, the highest occupied and lowest unoccupied bands are doubly degenerate in the point.

Significant changes in the electronic band structure of hexagonal layer occur when C_{60} molecules are connected by 56-bonds [Fig. 5(b)]. The conductance and valence bands meet at the _ point, indicating metallic properties of polymer II. Compared to the 66/66 configuration, the electronic structure of polymer II is characterized by increasing the width of the lowest branch of the conduction band and shifting the top of the valence band towards the higher energy. Both of these effects reveal an enhancement of the intermolecular overlap of π-type states. To analyze the possible reasons for such an enhancement, the electron density associated with the LUMO was drawn for the fragments of polymer I, II (Fig. 6). Let us focus our attention on the charge distribution within the cavity in-between the linked molecules. The π-electron overlap is negative in polymer I, whereas it is positive in polymer II. We conclude that it is the interaction within the C_{60} layer across the intermolecular space, which most likely enhances the electron conductivity in the two-dimensional layer of polymer II. Two basic differences in the molecular arrangement within the layer of polymers I, II seem to play a major role in their properties. First, the C_{60} unit cell in polymer I belongs to the D_{3d} symmetry, whereas that of polymer II is of S_6 symmetry; thus also the symmetry of the wave functions is different. Actually, as seen in Fig. 6, the LUMO shown for the three-molecule fragment of polymer I has one node and that of polymer II has three nodes. The second

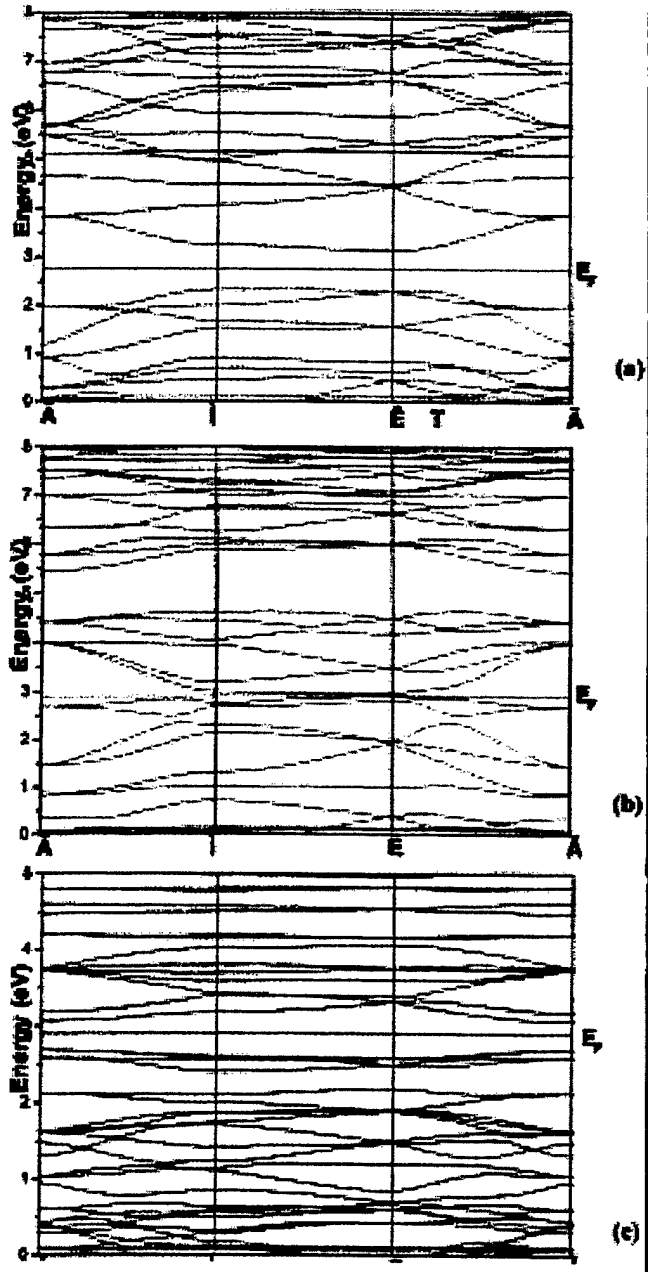

FIG. 5. Electronic band structure of (a) polymer I, (b) polymer II, and (c) polymer III.

difference distinguishing between the polymers is the position of the nearest threefold coordinated atoms within the neighboring molecules. These atoms form vertices of pentagons or hexagons in polymers I and II. In polymer I, such atoms are much further separated from the equator of the central C_{60} than in polymer II. Consequently, the radially directed π-type orbitals interact more effectively in polymer II.

Polymer III contains C_{60} cages of the two orientations present in polymers I and II. According to the band structure calculation, this polymer is a semiconductor. A direct band gap at the _ point is about 0.38 eV wide. The insertion of "misoriented" C_{60} molecules into the 66/66 layer in a ratio of 1:2 narrows the gap to practically half its value. The rather small band dispersion near the top of the valence and bottom of the conduction band reflects a smaller degree of interac-

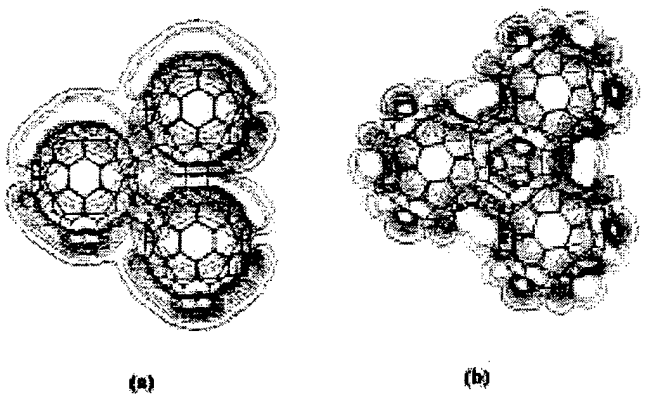

FIG. 6. Electronic charge density associated with crystal states derived from the lowest unoccupied molecular orbitals for fragments of (a) polymer I with 66/66 connections, and (b) polymer II with 65/56 connections within the layer.

tion within the π electron system in the 65/66 configuration than in the other geometries considered. Furthermore, we can also see an increased separation between the top of the valence and bottom of the conduction bands near the _ point in the Brillouin zone of polymer III. The relative position of atoms belonging to 66-connected molecules of polymer I and 65-connected molecules of polymer II, distinctly different from polymer III, and the longer intermolecular bonds in polymer III decrease the π-like orbital overlap through the cavities. Inspection of Figs. 5(a) and 5(b) reveals that the upper branches of the valence band of polymer II are located at a higher energy than those of polymer I. The appearance of these π-states in the electronic structure of polymer III explains the observed band gap narrowing in comparison to the 66/66 configuration. The large spacing between the top four occupied bands and deeper lying bands supports our interpretation that the π-states are rather localized in comparison to the other bands. Polymer III is also less stable than the other polymers and may be considered as an intermediate structure between the more stable configurations of polymers I and II.

V. SUMMARY

Our study of the electronic structure of rhombohedrally polymerized C_{60} using x-ray emission spectroscopy revealed changes in the density of occupied C $2p$-states with respect to fullerite, the C_{60}-based molecular solid. Upon polymerization, the main features of the C $K\alpha$ spectrum were found to broaden and shift towards higher binding energies. To interpret the experimental results, we calculated the electronic spectra of hexagonal C_{60} layers using an empirical tight-binding approach. The calculations considered three configurations, with neighboring molecules connected by 66/66, 65/56, and 65/66 bonds. Comparison between the calculated spectra revealed that the differences between the polymer phase and a free C_{60} molecule are similar to the differences between the experimental spectra of polymerized C_{60} and the molecular solid. The intermolecular interactions in the polymer were found to play a primary role in determining the electronic structure and properties of rhombohedrally polymerized C_{60}. Insertion of misoriented C_{60} molecules in the 66/66 layer reduces the fundamental gap by one half, and the gap disappears completely in the polymer containing molecules connected by 65/56 intermolecular bonds. The formation of a specific bond between neighboring C_{60} molecules is primarily caused by the geometric configuration in the pristine solid. At the onset of the polymerization process in an ordered layer, the 66-bond of one molecule faces a hexagon of the neighboring molecule. Furthermore, the 66/66 configuration is energetically preferable. Thus, formation of a 66/66 connected layer is favored both on kinetic and energetic grounds. Under particular conditions, however, which may involve temperature gradients or imperfect packing, polymers might form that involve other configurations. Our produced samples of rhombohedrally polymerized C_{60} have a polycrystalline structure that may be caused by spatially varying intermolecular connections. Our electronic structure calculations of the different polymers indicate that the occurrence of regions containing 65/56 bonded molecules within a 66/66 connected hexagonal layer may cause variations of in-plane conductivity.

ACKNOWLEDGMENTS

This work was financially supported by the INTAS (Project No. 00-237) and the Russian scientific and technical program "Current directions in condensed matter physics" within the project "Fullerenes and atomic clusters" (Project No. 98055).

[1] B. Sundqvist, Adv. Chem. Phys. **48**, 1 (1999).
[2] G. Oszlanyi and L. Forro, Solid State Commun. **93**, 265 (1995).
[3] M. Nunez-Regueiro, L. Marques, J-L. Hodeau, O. Bethoux, and M. Perroux, Phys. Rev. Lett. **74**, 278 (1995).
[4] C. Goze, F. Rachdi, L. Hajji, M. Nunez-Regueiro, L. Marques, J-L. Hodeau, and M. Mehring, Phys. Rev. B **54**, R3676 (1996).
[5] D. L. Strout, R. L. Murry, C. Xu, W. C. Eckhoff, G. K. Odom, and G. E. Scuseria, Chem. Phys. Lett. **214**, 576 (1993).
[6] J. Kurti and K. Nemeth, Chem. Phys. Lett. **256**, 119 (1996).
[7] S. Okada and S. Saito, Phys. Rev. B **59**, 1930 (1999).
[8] C. H. Xu and G. E. Scuseria, Phys. Rev. Lett. **74**, 274 (1995).
[9] K. Harigaya, Chem. Phys. Lett. **242**, 585 (1995).
[10] T. L. Makarova, P. Scharff, B. Sundqvist, M. E. Gaevski, E. Olsson, V. A. Davydov, A. V. Rakhmanina, and L. S. Kashevarova, Carbon (to be published).
[11] A. Ito, T. Morikawa, and T. Takahashi, Chem. Phys. Lett. **211**, 333 (1993).
[12] J. Onoe, A. Nakao, and K. Takeuchi, Phys. Rev. B **55**, 10051 (1997).
[13] V. A. Davydov, L. S. Kashevarova, A. V. Rakhmanina, V. Agafonov, H. Allouchi, R. Ceolin, A. V. Dzyabchenko, V. M. Senyavin, and H. Szwarc, Phys. Rev. B **58**, 14786 (1998).
[14] V. D. Yumatov, A. V. Okotrub, and L. N. Mazalov, Zh. Strukt. Khim. **26**, 59 (1985).
[15] N. L. Allinger, J. Am. Chem. Soc. **99**, 8127 (1977).
[16] V. V. Belavin, L. G. Bulusheva, A. V. Okotrub, and D. Tomanek, J. Phys. Chem. Solids **61**, 8127 (2000).
[17] C. H. Xu, C. Z. Wang, C. T. Chan, and K. M. Ho, J. Phys.: Condens. Matter **4**, 6047 (1992).
[18] J. Kawai and M. Motoyama, Phys. Rev. B **47**, 12988 (1993).
[19] J.-H. Guo, P. Glans, P. Skytt, N. Wassdahl, J. Nordgren, Y. Luo, H. Agren, Y. Ma, T. Warwick, P. Heimann, E. Rotenberg, and J. D. Denlinger, Phys. Rev. B **52**, 10681 (1995).
[20] S. Saito and A. Oshiyama, Phys. Rev. Lett. **66**, 2637 (1991).
[21] A. V. Okotrub and L. G. Bulusheva, Fullerene Sci. Technol. **6**, 405 (1998).

Carbon foam: Spanning the phase space between graphite and diamond

Koichiro Umemoto,[1] Susumu Saito,[1] Savas Berber,[2] and David Tománek[1,2,*]
[1]*Department of Physics, Tokyo Institute of Technology, 2-12-1 Oh-okayama, Meguro-ku, Tokyo 152-8551, Japan*
[2]*Department of Physics and Astronomy, and Center for Fundamental Materials Research, Michigan State University, East Lansing, Michigan 48824-1116*

(Received 25 May 2001; published 19 October 2001)

We study an unusual class of carbon structures, based on rigidly interconnected segments of graphite. The resulting foamlike systems cover the structural phase space extending from hexagonal diamond to graphite. Related to the most stable phases of carbon, these hybrid systems show an unusually high structural stability at low mass densities. Our density-functional calculations indicate that carbon foam is metallic, stable, and structurally rigid.

DOI: 10.1103/PhysRevB.64.193409 PACS number(s): 61.48.+c, 68.70.+w, 81.05.Tp, 71.20.−b

With the apparently ever-expanding plethora of stable structures, including fullerenes and nanotubes,[1] elemental carbon continues to amaze the scientific community. In search of structural rigidity and toughness competing with that of diamond and graphite, hybrid structures containing sp^2 and sp^3 bonded carbon have been discussed in the literature.[2–7] Here we study and theoretically characterize an unusual system which combines the shear rigidity of diamond with the open structure, low mass density, and an even higher stability of graphitic carbon.[8] We also propose a way to synthesize the new carbon foam using self-assembly on stepped single-crystal surfaces as a template.

The structure studied, shown schematically in Fig. 1(a), is conceptually based on interconnected graphite strips. The resulting periodic three-dimensional (3D) network, depicted in Fig. 1(c), is structurally reminiscent of a foam. The long open channels are formed by terraces in the layered structure. These terraces are formed of graphitic strips that are interconnected in a seamless manner. The primitive orthorhombic conventional unit cell of a particular foam structure, containing 64 atoms, is depicted in Fig. 1(b). This figure also illustrates the use of three- and fourfold coordinated carbon atoms in the construction of carbon foam.

The rigidity of the foam structure depends on the area density of bonds in the c direction that connect the terraces in the ab plane. By construction, these bonds are formed by providing atoms within the graphitic ab layers with additional neighbors in the c direction, thus locally converting sp^2 to sp^3 hybridized carbon atoms. The unit cell in the b direction can be as short as 2.46 Å, the separation between the parallel sides of the graphitic hexagons. In this case, the structure contains chains aligned with the b axis, consisting of carbon atoms that are fourfold coordinated prior to relaxation. Increasing b yields a structure of interconnected graphite strips, wavy both in the a and b directions, that eventually becomes indistinguishable from graphite as $b\rightarrow\infty$.

Keeping b at its minimum value near 2.46 Å and reducing the terrace width in the a direction to zero, the structure reduces to a network of fourfold coordinated carbon atoms, namely that of hexagonal diamond or wurtzite. Increasing a, on the other hand, yields a structure which, in the $a\rightarrow\infty$ limit, is that of layered graphite.

The size of the unit cell is determined by the number of carbon atoms in the ab plane; the equilibrium value of c depends on the predominant type of hybridization and ranges between the interlayer spacings of diamond and graphite. In other words, with the flexibility of independently adjustable values of a and b, we have a system that continuously spans the structural phase space between diamond and graphite, the most stable phases of elemental carbon.

To describe the structural and electronic properties of carbon foam, we use the local-density approximation (LDA) within the framework of the density-functional theory.[9,10] We adopt the Ceperley-Alder exchange-correlation potential in the LDA,[11] and use norm-conserving pseudopotentials[12] with the Kleinman-Bylander separable approximation.[13] We use a plane-wave basis set with a cutoff energy of 50 Ry and eight special k-points to sample the full Brillouin zone of the foam. The geometry is optimized using the conjugate gradient approach.[14]

For the system depicted in Fig. 1, the optimized lattice parameters are $a_{opt}=16.44$ Å, $b_{opt}=9.58$ Å, and $c_{opt}=3.28$ Å. We find the intralayer bond lengths to be close to the graphite value of 1.42 Å, and the interlayer distance to be only slightly smaller than the graphite value of 3.35 Å. During the optimization process, we observe an intriguing structure relaxation especially near the sites labeled sp^3 in Figs. 1(a) and (b). These atoms sacrifice one of their four neighbor bonds, characterizing an initial sp^3 hybridization, and bind strongly to only three neighbors with strong sp^2 bonds. Accordingly, the system of π electrons acquires a 3D metallic character, as will be discussed later.

Our total-energy calculations indicate that the foam is almost as stable as graphite and diamond, the most stable allotropes of carbon. We find the cohesive energy of the foam with 64 atoms per unit cell to be smaller by 0.13 eV/atom than that of graphite (or the equally stable diamond). The foam is more stable by 0.31 eV/atom than the isolated C_{60} molecule, and similarly stable as carbon nanotubes. Consequently, we expect the new carbon foam to remain stable once it is synthesized.

With 64 atoms in the unit cell, the above optimized unit-cell size translates into a mass density of only $\rho=2.48$ g/cm^3. This value is nearly as low as that of graphite,

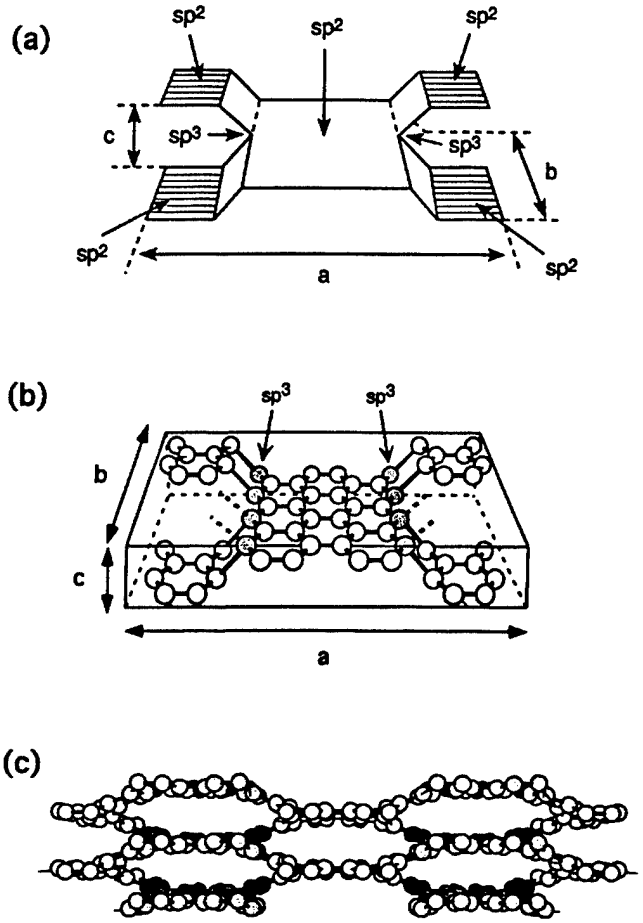

FIG. 1. Structural description of carbon foam. (a) Schematic illustrating the structural relationship between carbon foam and layered graphite. (b) Conventional orthorhombic unit cell of carbon foam, holding 64 atoms. Unit-cell variations are possible by changing the number of carbon atoms along the a and b axes. Initially fourfold coordinated sp^3 atoms are gray shaded, and the initial bond direction to their fourth neighbors is indicated by the dashed lines. (c) Perspective view of the 3D foam lattice structure, based on the above unit cell.

$\rho = 2.27$ g/cm^3. In spite of its low density, the foam material shows an unusually high stiffness along all three axes.

Due to the structural similarity with graphite, we find the elastic stiffness of foam along the b axis $c_b = c_{22} = 9.42$ Mbar close to the very high in-layer stiffness of graphite, $c_{11} = 12.3$ Mbar. This value also lies close to that of diamond, for which our elastic response calculations give $c_{11} = 11.29$ Mbar, in close agreement with previously observed[15] and calculated[16] values. The reduced stiffness of carbon foam along the a direction, $c_a = c_{11} = 9.02$ Mbar, is a consequence of the scissorslike instability in that direction.

As expected for a rigidly interconnected 3D lattice, the predicted value $c_c = c_{33} = 0.82$ Mbar in the foam is significantly higher than the graphite value $c_c = 0.34$ Mbar. The predicted bulk modulus of carbon foam, with $B = 0.79$ Mbar, lies in between the values $B = 0.33$ Mbar of graphite and $B = 4.69$ Mbar for diamond.

The structural rigidity of carbon foam results from strong covalent bonds along all spatial directions. In particular, the strong bonds in the c direction resemble the sp^2 intralayer bonds of graphite. The bonding integrity throughout the structure is reflected in delocalization of the charge density in the ab and ac plane, shown in Fig. 2.

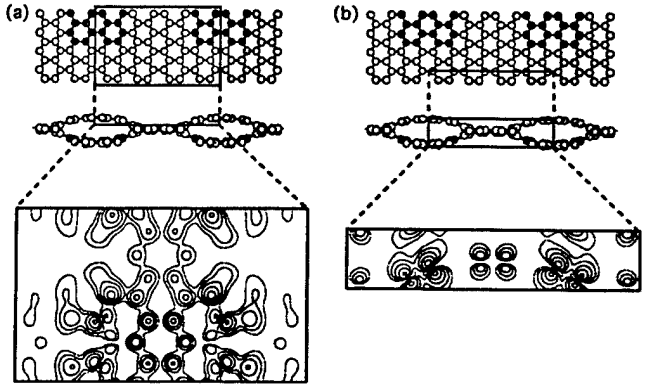

FIG. 2. Contour plot of the charge density associated with states close to the Fermi level. The plot covers a charge density range between 2.0×10^{-4} electrons/a.u.^{3} and 3.2×10^{-3} electrons/a.u.^{3}, with contour lines representing twice the values at adjacent contours. The sp^2 character of covalent bonds is shown in (a) in the ac plane and in (b) in the ab plane, close to the terrace.

The possibility of metallic conduction along the graphitic strips in carbon foam had been suggested based on Hückel calculations.[8] To investigate the degree of metallic behavior, we show the band dispersion along high-symmetry lines in the primitive orthorhombic unit cell in Fig. 3. We find the band dispersion within the ab plane, i.e., along the $\Gamma - X$ and $\Gamma - Y$ directions, to be large and comparable to the dispersion of a graphitic monolayer, reflecting the strong sp^2 bonding. Since our particular unit cell holds more carbon atoms in the a direction than in the b direction, the dispersion along $\Gamma - Y$ is larger than along $\Gamma - X$. The band dispersion along the $\Gamma - Z$ direction is somewhat larger than that of layered graphite, due to the rigid bonds in the c direction. Our 64-atom unit cell holds 256 valence electrons, and we find that the 128th and the 129th bands cross the Fermi level along the $\Gamma - Y$, $\Gamma - Z$, and the $Y - T$ lines.

The electronic density of states of carbon foam, displayed in the right panel of Fig. 3, is reminiscent of graphite, reflecting the structural similarity of the two structures. The system is metallic, with the nonvanishing value of the density of states at the Fermi level $N(E_F) = 1.0$ states/eV/spin, similar to other previously discussed sp^2 lattices.[4]

A possible way to synthesize carbon foam may be achieved by directed assembly on a templated substrate. Recently, graphitic strips have been synthesized by hydrocarbon decomposition on stepped transition metal or metal carbide surfaces, such as Pt(557), Ni(557), or TiC(557).[17] Whereas hydrocarbons such as benzene graphitize on the flat terraces, the more active step sites have been shown to break the graphitic bonds, thus separating the graphitic overcoating into disconnected strips. We postulate that under conditions where graphite layers still remain intact, such a separation into strips may be suppressed. Due to the stronger local bending of the still intact overlayer near the steps, the strained segments become more reactive. With more than

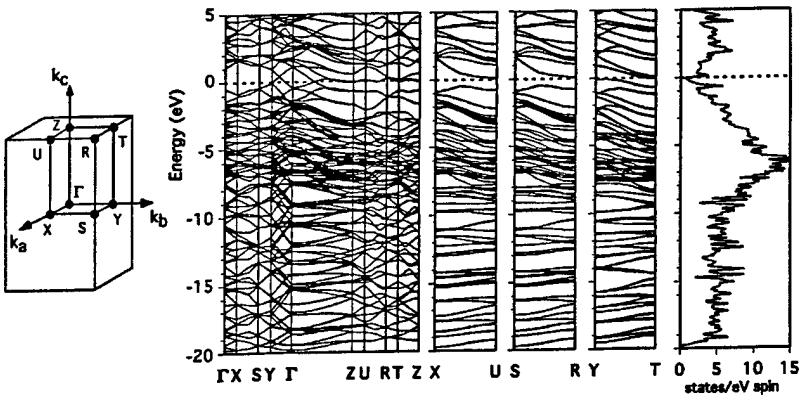

FIG. 3. Electronic band dispersion along high-symmetry lines in the Brillouin zone of the graphitic structure of Fig. 1. The schematic drawing of the Brillouin zone shows the labeling of high-symmetry points. The corresponding density of states is shown in the right panel. The energy reference is the Fermi level.

one graphitic overlayer, the initially layered structure, reminiscent of wavy graphite, may reconnect to a foamlike structure. Bonding arrangements, reminiscent of those illustrated in Fig. 1(c), also likely exist in defective graphite. In that case, however, the channels are likely to become very irregular, inducing significant strain to the lattice.

We would like to emphasize that the structural motif of the carbon foam introduced here is also easily extended to other layered systems, such as boron nitride. It is also conceivable to construct a hybrid foam material consisting of alternating graphite and BN layers. A decoration or substitution of the originally sp^3 sites by elements such as Si, with a different preferential bonding arrangement, may also be used to modify the interlayer spacing. In any case, the high porosity and accessibility of the foam structures suggests their potential for the absorption and storage of hydrogen or alkali metals for fuel cell or battery applications.

In summary, we studied an unusual class of structures, based on rigidly interconnected segments of graphitic carbon. The resulting foamlike systems cover the structural phase space extending from hexagonal diamond to graphite. Related to the most stable phases of carbon, these hybrid systems show an unusually high structural stability at low mass densities. Our density-functional calculations indicate that carbon foam should be metallic, stable, and structurally rigid.

S.S. acknowledges support under the Grant-in-Aid for Science Research Priority Area "Fullerenes and Nanotubes" by the Ministry of Education of Japan, JSPS RFTF96P00203, and the Nissan Science Foundation. D.T. acknowledges financial support by the Office of Naval Research and DARPA under Grant No. N00014-99-1-0252 and the hospitality of Tokyo Institute of Technology where this research was performed.

*Corresponding author. Email address: tomanek@pa.msu.edu

[1] For recent reviews, see *Science and Application of Nanotubes*, edited by David Tománek and Richard Enbody (Kluwer, New York, 2000); M. S. Dresselhaus, G. Dresselhaus, and P. C. Eklund, *Science of Fullerenes and Carbon Nanotubes* (Academic Press, San Diego, 1996).

[2] R. Hoffman, T. Hughbanks, M. Kertesz, and P. H. Bird, J. Am. Chem. Soc. **105**, 4831 (1983).

[3] A. Y. Liu, M. L. Cohen, K. C. Hass, and M. A. Tamor, Phys. Rev. B **43**, 6742 (1991).

[4] A. Y. Liu and M. L. Cohen, Phys. Rev. B **45**, 4579 (1992).

[5] J. L. Corkill, A. Y. Liu, and M. L. Cohen, Phys. Rev. B **45**, 12 746 (1992).

[6] H. R. Karfunkel and T. Dressler, J. Am. Chem. Soc. **114**, 2285 (1992).

[7] N. Park and J. Ihm, Phys. Rev. B **62**, 7614 (2000).

[8] A hybrid carbon structure similar to ours was originally postulated by A. T. Balaban, D. J. Klein, and C. A. Folden, Chem. Phys. Lett. **217**, 266 (1994).

[9] P. Hohenberg and W. Kohn, Phys. Rev. **136**, B864 (1964).

[10] W. Kohn and L. J. Sham, Phys. Rev. **140**, A1133 (1965).

[11] J. P. Perdew and A. Zunger, Phys. Rev. B **23**, 5048 (1981); D. M. Ceperley and B. J. Alder, Phys. Rev. Lett. **45**, 566 (1980).

[12] N. Troullier and J. L. Martins, Phys. Rev. B **43**, 1993 (1990).

[13] L. Kleinman and D. M. Bylander, Phys. Rev. Lett. **48**, 1425 (1982).

[14] O. Sugino and A. Oshiyama, Phys. Rev. Lett. **68**, 1858 (1992).

[15] H. J. McSkimin and P. Andreatch, Jr., J. Appl. Phys. **43**, 985 (1972); **43**, 2944 (1972).

[16] A. Fukumoto, Phys. Rev. B **42**, 7462 (1990).

[17] M. Terai, N. Hasegawa, M. Okusawa, S. Otani, and C. Oshima, Appl. Surf. Sci. **132**, 876 (1998); E. Rokuta, Y. Hasegawa, A. Itoh, K. Yamashita, T. Tanaka, S. Otani, and C. Oshima, Surf. Sci. **428**, 97 (1999).

PHYSICAL REVIEW B, VOLUME 65, 041402(R)

Electronic interwall interactions and charge redistribution in multiwall nanotubes

Yoshiyuki Miyamoto,[1] Susumu Saito,[2] and David Tománek[3]
[1]*Fundamental Research Laboratories, NEC Corporation, 34 Miyukigaoka, Tsukuba, 305-8501, Japan*
[2]*Department of Physics, Tokyo Institute of Technology, 2-12-1 Oh-okayama, Meguro-ku, Tokyo 152-8551, Japan*
[3]*Department of Physics and Astronomy, Michigan State University, East Lansing, Michigan 48824-1116*
(Received 9 October 2001; published 28 December 2001)

Using density functional theory, we calculate the charge redistribution incurred upon forming multiwall carbon nanotubes, or by sandwiching initially isolated single-wall nanotubes between graphene layers. In these systems, we observe a significant charge transfer between the π electron system of the tube walls and a newly formed interlayer state. We discuss the direction of charge flow in terms of the interlayer hybridization and work function differences in the composite systems.

DOI: 10.1103/PhysRevB.65.041402 PACS number(s): 61.48.+c, 71.20.Tx, 73.61.Wp, 81.05.Tp

Carbon nanotubes[1] have attracted much attention from the viewpoints of science and technological applications because of their unique electronic and mechanical properties. Prior to experimental confirmation, it was predicted that a single-wall nanotube (SWNT) can be either semiconducting or metallic, depending on its helical pitch and diameter.[2,3] Whereas the conductance behavior of SWNTs can be basically understood based on the electronic structure of a graphene monolayer, there is no such simple relationship to planar graphite for the band structure and density of states of narrow SWNTs. There, the large curvature of the walls causes a hybridization between the σ^* and π^* electron systems which are decoupled in graphite. As a consequence, all SWNTs with a diameter below 7 Å have been predicted to be metallic, independent on their helical pitch.[4]

Further modifications in the electronic structure are introduced due to interwall interaction in multiwall nanotubes (MWNTs). Interest in these systems is rising due to recent synthesis of double-wall nanotubes (DWNTs) by fusion of fullerenes encapsulated in SWNTs.[5,6] Due to low density of states at the Fermi level and close proximity of van Hove singularities, even a minute charge redistribution in nanotubes may significantly modify their conducting and superconducting behavior.[7,8] Drastic effects due to charge transfer are expected in nanotube-based electronic devices.[7] In double-wall nanotubes, theoretical studies have addressed the effect of interwall interactions on the equilibrium geometry[9] and electronic structure.[10] So far, there have been no self-consistent calculations that would focus on the electrostatic potential and charge distribution in nanotubes with multiple walls.

Here we show that the presence of an interwall interaction in DWNTs modifies the electronic states close to the Fermi level, thus revealing the atomic arrangement within both walls to scanning tunneling microscopy (STM)[11] and resonant Raman spectroscopy.[12] Our self-consistent calculations also indicate that, depending on the diameter of the individual tubes, there is a charge transfer that shifts the energy bands by up to 0.3 eV, a significant value in device physics. We find the charge transfer to occur not only from one tube to another, but also to a newly formed interwall state. This state, reminiscent of the interlayer state found in graphite,[13] may affect the conductivity of DWNTs.[14]

Due to the local curvature and rehybridization between the σ^* and π^* states, we suspect the work function of nanotubes to be higher than that of graphite. This appears to be confirmed by the direction of charge flow in a system consisting of nanotubes sandwiched between graphene sheets. Unfortunately, the potential in DWNT systems, consisting of pairs of (n,n) "armchair" nanotubes, is different from that of the isolated SWNT components. The direction of charge flow may then not be correlated with SWNT work function differences. The importance of the self-consistent potential is emphasized by the lack of correlation between the work function and tube diameter, when judged by charge transfer only.

In this work, we have performed first-principles calculations using density functional theory within the local density approximation (LDA). For the LDA exchange-correlation potential, we used the Perdew-Zunger functional[15] fitted to the Ceperley-Alder results.[16] Soft nonlocal pseudopotentials[17] in the separable form[18] were used to express interactions between valence electrons and ions. A plane wave basis set with a kinetic cutoff energy of 40 Ry was used to expand the Bloch valence wave functions. In the three-dimensional periodic lattice used in our calculation, we used hexagonal unit cells with the c axis parallel to the tube axis. The unit cell size was chosen to keep the distance between the walls of adjacent tubes at 7 Å, to prevent wave function overlap between neighboring cells. To perform the momentum space integration for DWNTs, we sampled the first quasi-1D Brillouin zone by $18k$ points. In the following, we focus mainly on the (5,5)@(10,10) double-wall nanotube, consisting of a (5,5) inside the (10,10) nanotube. We also find this system convenient for the sake of simple comparison with previous calculations.[9,10] We also investigated charge redistribution profiles in other systems, namely (4,4)@(9,9), (4,4)@(10,10), (4,4)@(11,11), (5,5)@(11,11), (6,6)@(11,11), and (6,6)@(12,12) double-wall nanotubes.

When computing the electronic structure of (5,5)@(10,10) nanotubes, we considered two different geometries, one of them symmetric and the other one asymmet-

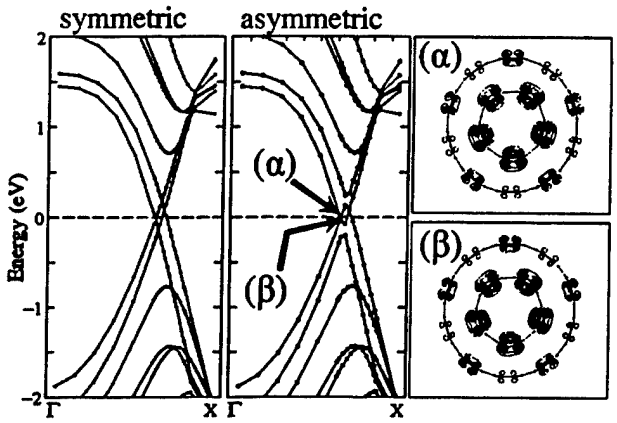

FIG. 1. One-dimensional electronic band structure of the (5,5)@(10,10) double-wall nanotube in the symmetric (left) and asymmetric (middle) configuration. The position of E_F=0 eV is shown by the dashed line. The energy position of pseudogap states α and β, lying 0.03 eV above and below E_F of the asymmetric (5,5)@(10,10) nanotube, is indicated by arrows in the middle panel. The two rightmost panels are contour maps of the charge density associated with these states. The contour plots are shown in a plane containing the atoms, normal to the tube axis. The minimum contour values shown are set to be common.

ric. In both cases the tubes are coaxial. In the symmetric geometry the two nanotubes maintain the common fivefold symmetry. In the asymmetric geometry, which was also considered in Ref. 10, the fivefold symmetry is broken by first rotating the (5,5) nanotube by 3° from the symmetric orientation and then shifting it axially by half a lattice constant. Figure 1 shows the computed band structures of the symmetric and asymmetric (5,5)@(10,10) nanotubes, which resemble those obtained by the tight-binding (TB) method.[10] In the symmetric (5,5)@(10,10) system, four bands cross near the Fermi level. In the asymmetric case, band crossing is not allowed, causing the formation of four pseudogaps in the density of states. Since TB and LDA give similar band structures, the subtle differences in the charge distribution and character of wave functions close to E_F have been missed for a long time. While the inter-layer hybridization opens up pseudogaps in the electronic structure, it also modifies the character of the corresponding wavefunction near E_F, as shown in the rightmost panels of Fig. 1, and hence is likely to affect the conductivity of multiwall nanotubes.[14]

The eigenstate characteristics near E_F of the asymmetric (5,5)@(10,10) nanotubes are displayed in the rightmost panels of Fig. 1 as contour maps of the corresponding charge densities. The state labeled α is located 0.03 eV above E_F, whereas the β state lies 0.03 eV below E_F. These eigenstates are close to the pseudogap region and are predominatly formed by the π orbitals of the inner (5,5) nanotube. Meanwhile, tails of these wave functions extend out to the region occupied by the outer (10,10) nanotube, where they reflect the atomic arrangement of the inner tube. We therefore expect that STM and STS spectra for very small bias voltages, which sample a very narrow energy region around E_F, can provide information about the atomic structure and relative orientation in multiwall nanotubes.[11] This rather subtle effect, confined mainly to the pseudogap region very close to E_F, has been apparently overlooked in previous simulations of STM images of multiwalled nanotubes that were performed for larger bias voltages.[19,20]

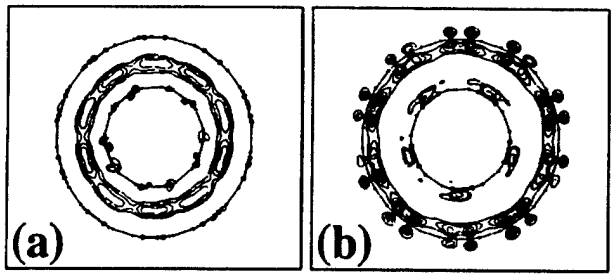

FIG. 2. Contour maps of the accumulated (a) and depleted (b) charge densities within the asymmetric (5,5)@(10,10) nanotube. The contour plots are shown in a plane containing the atoms, normal to the tube axis. The minimum contour values shown are set to be common.

Next we discuss the self-consistent charge redistribution in the (5,5)@(10,10) DWNT. Figure 2(a) displays the accumulated and 2(b) the depleted charge in the asymmetric (5,5)@(10,10) nanotube with respect to the superposition of isolated (5,5) and (10,10) nanotubes. We find it intriguing that the charge transfer does not mainly occur from one tube to another, but rather from the outer (10,10) tube to the intertube region. We find this behavior not to depend on the tube orientation, and to occur for the symmetric (5,5)@(10,10) arrangement as well. We found the amount of charge transfer of 0.09 electrons per period, corresponding to sixty carbon atoms within a 2.46 Å long axial tube segment, to be considerable. The (10,10) nanotube therefore can be viewed as being hole doped by the inner (5,5) nanotube. A very similar charge transfer is also seen in a hypothetical situation, in which arrays of (10,10) nanotubes are sandwiched in-between graphene sheets, as shown in Fig. 3(a).

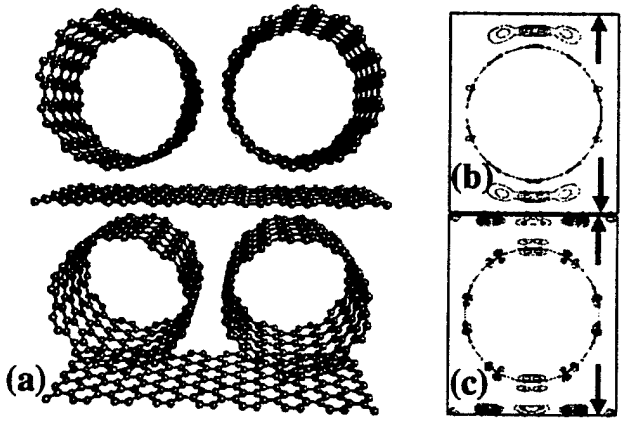

FIG. 3. (a) Perspective view of the atomic arrangement for arrays of (10,10) nanotubes sandwiched between graphene layers. The interwall distance is 3.47 Å between the tubes and 3.34 Å between the tubes and graphene layers. Contour maps of the accumulated (b) and depleted (c) charge densities of the system. The position of the graphene layers is indicated by arrows. The contour plots are shown in a plane containing the atoms, normal to the tube axes. The minimum contour values shown are set to be common.

The character of the state which accommodates the extra charge is very similar to the interlayer state found in graphite.[13] The charge redistribution within this system, shown in Figs. 3(b) and 3(c), is determined by subtracting superposed charge densities of neutral, isolated (10,10) nanotubes and graphene monolayers from the total charge density of the bulk system. As shown in Figs. 3(b) and 3(c), the depleted charge stems from the π electron system of the graphene layers. This result is consistent with the intuitive interpretation that the work function of nanotubes is higher than that of graphite, as confirmed by recent photoemission data.[21] Recently, a similar charge redistribution profile has also been discovered in "peapods," consisting of fullerene chains encapsulated in nanotubes.[22]

Similar charge accumulations in the interwall region were also found in (4,4)@(9,9),(4,4)@(10,10),(4,4)@(11,11), and (6,6)@(11,11) double-wall nanotubes. Among these, the (6,6)@(11,11) DWNT shows a π-electrons depletion of the outer (11,11) nanotube, same as the (5,5)@(10,10) nanotube. On the other hand, in other (4,4)@(n,n) pairs, with n ranging from 9 to 11, the charge depletion occurs in the *inner* (4,4) nanotube. As for the (5,5)@(11,11) and (6,6)@(12,12) nanotubes, the direction of the charge transfer is unclear. Thus we conclude that the direction of charge flow does not simply follow an ordering scheme based on tube diameters, not even for the same helical pitch.

In general, the direction of charge transfer between two weakly interacting systems is determined by the difference of their work functions. An intriguing question is, whether the intertube interaction in multiwall tubes can be considered weak enough to allow the extrapolation of work functions for isolated single-wall tubes.

For solid surfaces, the asymptotic form of the self-consistent potential in the direction normal to the surface was used to determine the work function in a periodic array of slabs.[23] As we show in Fig. 4, the self-consistent potential V_{tot} of the dilute periodic lattice of (5,5)@(10,10) nanotubes does not converge sufficiently fast the intertube region to allow a similar work function extrapolation. This slow convergence is chiefly due to the asymptotic behavior of the Hartree and local-ionic potentials which diverge logarithmically with increasing distance from charged cylindrical objects.[24] Due to the even smaller interwall than intertube distance in DWNTs, the changes in the crystal potential due to the presence of the other tube and the interwall interaction are likely to significantly modify the potential of the individual tubes, making extrapolations of their work function in this geometry even more difficult. We believe that the calculation of accurate work function values for nanotubes of a given diameter and helical pitch is nontrivial, since it requires considering a very large vacuum region away from the tube. We should also note that, in reality, a finite length of nanotubes must affect their work function.

Since the charge flow in a multiwall system is not simply correlated with the work function difference of the individual tubes, we seek in the following to explain its origin in terms of the interwall hybridization. These considerations have to take into account not only the curvature-induced changes in the π electron system of the tubes, but also their interaction

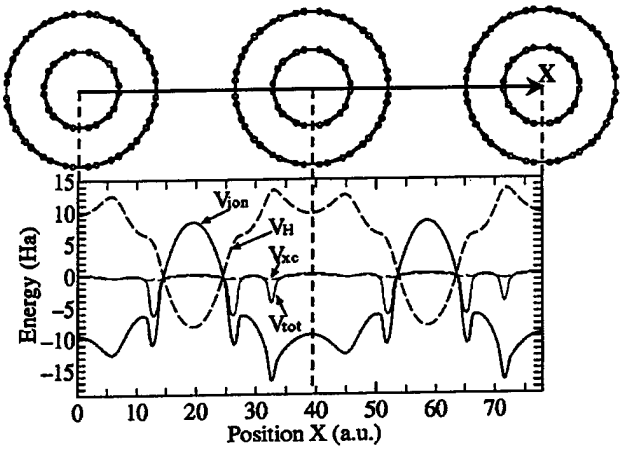

FIG. 4. Profiles of the self-consistent potentials along a line connecting the nearest-neighbor (5,5)@(10,10) double-wall nanotubes in the periodic lattice. V_{tot} stands for the total, V_H for the Hartree, V_{ion} for the ionic, and V_{xc} for the exchange-correlation potential in the lower panel. The contribution of the nonlocal part of the pseudopotentials is not shown. The corresponding atomic positions within the symmetric (5,5)@(10,10) nanotube and the line used to display the potential profiles is given in the upper panel.

with the newly formed interwall state. Our calculations indicate that in planar hexagonal graphite, there is no charge flow into the interlayer region.[25] We conclude that the involvement of the interwall state in the charge redistribution is closely related to the curvature of the tube walls.

As shown in previous calculations,[4] the tube wall curvature causes a σ^*-π^* hybridization which is suppressed by symmetry in planar graphite monolayers. We expect that the modified $\sigma(*)$ and $\pi(*)$ system of electrons will interact with the interlayer state. The degree of rehybridization within the MWNT system, as compared to graphite, depends not only on the curvature of the individual tubes, but even more importantly on the interwall distance and the atomic registry between adjacent walls. Judging from very similar charge redistributions found for the symmetric and asymmetric (5,5)@(10,10) DWNTs, the chirality and diameter of the individual tubes matter more than relative tube orientations. It is difficult to pinpoint the dominant eigenstates responsible for the charge transfer into the interwall region, since the charge redistribution has contributions from many eigenstates, some of them far below E_F. Also, there appears to be a significant hybridization between these deep states and the interlayer state.[22]

The possibility of hole doping of composite systems containing nanotubes and fullerenes without halogen or other impurity atoms, as predicted for the (10,10) nanotube within the (5,5)@(10,10) double-wall system, opens new possibilities for engineered electronic devices. Recently, hole doping was shown to significantly increase the superconducting transition temperature T_C of supported fullerene layers.[26] We expect that hole doping will modify the conductivity of nanotubes, and may even lead to higher T_C values for nanotube-based superconductors.

Finally, we briefly address the exfoliation energy in MWNTs. Due to the curvature-induced reactivity increase,

we expect that the energy to separate nested nanotubes should exceed the exfoliation energy of graphite (0.054 eV/atom experimental,[27] 0.025 eV/atom theoretical.[28]) Our value of 0.07 eV per unit cell containing sixty atoms in total lies significantly lower. We suspect that the present k point sampling, even though finer than in previous work,[9] is still not sufficient enough to probe the density of states in the vicinity of the Fermi level in (5,5)@(10,10) nanotubes with sufficient accuracy. We believe that a precise determination of the exfoliation energy of nanotubes will involve a very dense k point mesh probing the eigenstates near E_F.

In summary, we calculated the self-consistent charge density and potential profiles for double-wall nanotubes, considering constituent tubes of various chiralities, and for single-wall nanotubes sandwiched between graphene layers. We found that the atomic structure of the inner tube modifies the charge density associated with states near E_F even outside the outer tube, so that it can be probed by STM. A significant amount of charge, originating mainly from the π electron system of the tubes and graphite layers, is transferred mainly into a new interwall state, related to the interlayer state of graphite. The associated hole doping, occurring in individual tubes, will affect their conducting and possibly superconducting behavior. Our results indicate that the work function of nanotubes is larger than that of graphite, and that work function differences between single-wall tubes cannot be deduced easily from the charge transfer in double-wall systems.

All calculations were performed on the SX4 supercomputer system at the NEC Tsukuba Laboratories. This work was performed under the management of Frontier Carbon Technology supported by NEDO. This work was also supported by Grant-in-Aid for Scientific Research, Priority Area (#402) by Ministry of Education of Japan, JSPS RFTF96P00203 and Nissan Science Foundation (S.S.); ONR and DARPA under Grant No. N00014-99-1-0252 (D.T.).

[1] S. Iijima, Nature (London) **354**, 56 (1991).
[2] N. Hamada, S. Sawada, and A. Oshiyama, Phys. Rev. Lett. **68**, 1579 (1992).
[3] R. Saito, M. Fujita, G. Dresselhaus, and M.S. Dresselhaus, Appl. Phys. Lett. **60**, 2204 (1992).
[4] X. Blase, L.X. Benedict, E.L. Shirley,and S.G. Louie, Phys. Rev. Lett. **72**, 1878 (1994).
[5] B.W. Smith and D.E. Luzzi, Chem. Phys. Lett. **321**, 169 (2000).
[6] S. Bandow, M. Takizawa, K. Hirahara, M. Yudasaka, and S. Iijima, Chem. Phys. Lett. **337**, 48 (2001).
[7] François Léonard and J. Tersoff, Phys. Rev. Lett. **83**, 5174 (1999).
[8] M. Kociak, A.Yu. Kasumov, S. Guéron, B. Reulet, I.I. Khodos, Yu.B. Gorbatov, V.T. Volkov, L. Vaccarini, and H. Bouchiat, Phys. Rev. Lett. **86**, 2416 (2001).
[9] J.-C. Charlier and J.-P. Michenaud, Phys. Rev. Lett. **70**, 1858 (1993).
[10] Y.K. Kwon and D. Tománek, Phys. Rev. B **58**, R16 001 (1998).
[11] A. Hassanien, M. Tokumoto, and D. Tománek, Appl. Phys. Lett. (to be published).
[12] A. Jorio, R. Saito, J.H. Hafner, C.M. Lieber, M. Hunter, T. McClure, G. Dresselhaus, and M.S. Dresselhaus, Phys. Rev. Lett. **86**, 1118 (2001).
[13] N.A.W. Holzwarth, S.G. Louie, and S. Rabii, Phys. Rev. B **26**, 5382 (1982), and references therein.
[14] Stefano Sanvito, Young-Kyun Kwon, David Tománek, and Colin J. Lambert, Phys. Rev. Lett. **84**, 1974 (2000).
[15] J.P. Perdew and A. Zunger, Phys. Rev. B **23**, 5048 (1981).
[16] D.M. Ceperley and B.J. Alder, Phys. Rev. Lett. **45**, 566 (1980).
[17] N. Troullier and J.L. Martins, Phys. Rev. B **43**, 1993 (1991).
[18] L. Kleinmann and D.M. Bylander, Phys. Rev. Lett. **48**, 1425 (1982).
[19] A. Rubio, Appl. Phys. A: Mater. Sci. Process. **68**, 275 (1999).
[20] Ph. Lambin, V. Meunier, and A. Rubio, Phys. Rev. B **62**, 5129 (2000).
[21] S. Suzuki, C. Bower, Y. Watanabe, and O. Zhou, Appl. Phys. Lett. **76**, 4007 (2000).
[22] S. Okada, S. Saito, and A. Oshiyama, Phys. Rev. Lett. **86**, 3835 (2001).
[23] See, for example, J.R. Chelikowsky, Phys. Rev. B **16**, 3618 (1977).
[24] We have reset the $\mathbf{G}=0$ component of both V_{ion} and V_H to zero in Fig. 4, which corresponds to a uniform energy shift.
[25] The charge flow in bulk graphite was investigated in analogy to the procedure used for nanotubes, by subtracting the superposed charge densities of graphene monolayers from the total charge density of graphite. In hexagonal graphite with AB stacking, we observed only a minute charge transfer between the two inequivalent atoms. The direction of the charge transfer, involving the π electron system, was towards the atom facing neighboring atoms in the adjacent layers.
[26] J.M. Schön, Ch. Kloc, and B. Batlogg, Nature (London) **406**, 702 (2000); *ibid.*, **408**, 549 (2000).
[27] L.A. Girifaloco and R.A. Ladd, J. Chem. Phys. **25**, 693 (1956).
[28] M.C. Schabel and J.L. Martins, Phys. Rev. B **46**, 7185 (1992).

J. Mater. Res. 13Γ2363 (1998).

Do carbon nanotubes spin when bundled?

Young-Kyun Kwon and David Tománek
Department of Physics and Astronomy, Michigan State University, East Lansing, Michigan 48824-1116

Young Hee Lee
Department of Physics and Astronomy, Michigan State University, East Lansing, Michigan 48824-1116
Department of Physics and Semiconductor Physics Research Center, Jeonbuk National University, Jeonju 561-756, Korea

Kee Hag Lee
Department of Physics and Astronomy, Michigan State University, East Lansing, Michigan 48824-1116
Department of Chemistry, WonKwang University, Iksan, Chonbuk 570-749, Korea

Susumu Saito
Department of Physics, Tokyo Institute of Technology, 1-12-1 Oh-okayama, Meguro-ku, Tokyo 152, Japan
(Received 5 February 1998; accepted 15 May 1998)

Using *ab initio* and parametrized techniques, we determine the equilibrium structure of an ordered "bundle" of (10,10) carbon nanotubes. Due to the small inter-tube interaction and lattice frustration, we predict a very soft libration mode to occur at $\nu \approx 12$ cm^{-1}. This mode is predicted to disappear above the orientational melting temperature which marks the onset of free tube rotations about their axis. We discuss the effect of the weak inter-tube coupling and orientational disorder on the electronic structure near the Fermi level.

PACS numbers: 61.48.+c, 61.50.Ah, 73.61.Wp

I. INTRODUCTION

Among carbon based materialsΓfullerenes (such as the C_{60} "buckyball" [1]) and nanotubes [2] have received much attention recently due to their high structural stability and interesting electronic properties. Structurally rigid [3] and highly conducting [4] "ropes" of carbon nanotubes are the molecular counterparts of carbon fibers [5].

Perfectly spherical C_{60} molecules are known to spin freely at room temperature [6] when crystallized to a solid [7]. One may wonderΓwhether the cylindrical single-wall (10Π0) carbon nanotubes [5]Γthe abundant species [4Β9] among single-wall tubesΓ could also rotate relatively freely when forming well-ordered bundlesΓ the "ropes" [4]. ^{13}C nuclear magnetic resonance experiments on solid C_{60} [6] have shown that it is only below $T \approx 260$ K that the free C_{60} rotation is hindered by the asphericity of the inter-molecular potentialΓdue to the discrete atomic positions. In bundles of nanotubesΓwe expect the barrier for rotation to be even lower due to the frustration introduced by triangular packing of tubes that have a D_{10h} symmetry and due to orientational dislocations caused by local twists along the tube axis. Due to their large moment of inertiaΓnanotubes are not expected to spin as fast as the C_{60} molecules. Nevertheless Γit is useful to study the soft librational motion of nanotubes and their transition to relatively free tube rotationsΓmarking the onset of orientational disorder in nanotube "ropes".

Electronic states involved in the superconducting behavior of the alkali-doped C_{60} solid derive from this molecule's degenerate lowest unoccupied t_{1u} molecular orbital [10] that extends to an ≈0.5 eV wide band due to the inter-C_{60} interactionsΓwhich in turn depend on the molecular orientation [10Π1]. SimilarlyΓinteractions between carbon nanotubes in "ropes"Γwhich depend on the mutual orientation of adjacent tubesΓare expected to affect states at the Fermi level to an important degree. This point is especially intriguingΓsince recent calculations suggested that small deformations may open up a gap at E_F in *isolated* conducting nanotubes [12]. HenceΓ we expect our results to be of consequence for the conducting behavior of these systems [13].

In the followingΓwe present theoretical evidenceΓsupported by recent experimental dataΓabout an orientational melting transition in "ropes" consisting of (10Π0) nanotubes. We find that even at relatively low temperaturesΓthe hindrance of tube rotations due to discrete atomic positions in the tube walls should lose its significance. This should mark the onset of relatively free rotation or twisting motion about the tube axes. We find that bundling up of nanotubes to "ropes" is accompanied by an ≈7% increase in the density of states near the Fermi level $N(E_F)$Γalmost independent of tube orientation. The inter-tube interaction gives rise to an additional band broadening by ≈0.2 eVΓwhich would significantly diminish the effect of minute tube distortions

on states near E_FΓpredicted for individual tubes [12].

II. THEORY

To investigate the possibility of rotations in a bundle of nanotubes and their effect on the electronic structure of the systemΓwe first optimize the geometry of an ordered nanotube latticeΓthe "rope"Γusing the density functional formalism within the local density approximation (LDA). Our plane-wave code [14] uses an energy cutoff of 50 RydbergsΓdescribes carbon atoms using soft nonlocal pseudopotentials [15] within a separable approximation [16]Γ and uses the Ceperley-Alder exchange-correlation potential [17] as parametrized by Perdew and Zunger [18]. This basis had been successfully used to optimize the lattice constant of the C_{60} solid [19] and related systems [20]. Due to the large size of the basis setΓthat contains nearly 200Ⅱ000 plane wavesΓwe restrict our sampling of the irreducible part of the Brillouin zone to 4 k-points when determining the optimum inter-tube spacing and the equilibrium tube geometry.

III. RESULTS AND DISCUSSION

The interatomic distances in the tubesΓ optimized within the LDAΓare $d_{CC} = 1.397$ Å for bonds perpendicular to the tube axis ("double" bonds) and $d_{CC} = 1.420$ Å for the other ("single") bonds. The weak inter-tube interaction in the "rope"Γshown in Fig. 1(a)Γcauses only very small radial deformation ("buckling") of the tubes with an amplitude of $\Delta R \approx 0.03$ Å. As shown in Fig. 1(a)Γthe calculated equilibrium inter-tube separation $a_{e,th} = 16.50$ Å lies only 2.8% below the observed value $a_{e,expt} = 16.95 \pm 0.34$ Å [4]. We also observe a significant decrease of radial tube deformations ("buckling") from $\Delta R \approx 0.03$ Å to ≈ 0.004 Å as the inter-tube spacing in the "rope" increases by a mere 2.8% from the theoretical equilibrium value $a_{e,th} = 16.50$ Å. Suppression of this radial deformationΓwhich is likely linked to the ability of individual tubes to spin freelyΓshould effectively cause an increase of the equilibrium inter-tube spacing a_e at the orientational melting temperature. HenceΓthe 2.8% difference between the observed and calculated value of a_e may be partly due to the factΓthat the value observed at room temperature [4] $a_{e,expt}$ was compared to the calculated zero-temperature value $a_{e,th}$.

Even though the agreement between the calculated and observed inter-tube spacing is very good for a partly Van der Waals system by standards of *ab initio* calculationsΓwe try to understand the minor deviations by calculating the optimized geometry of hexagonal graphite in Figs. 1(b) and (c) using the very same basis. Our results for the energy dependence on the inter-layer separation cΓ

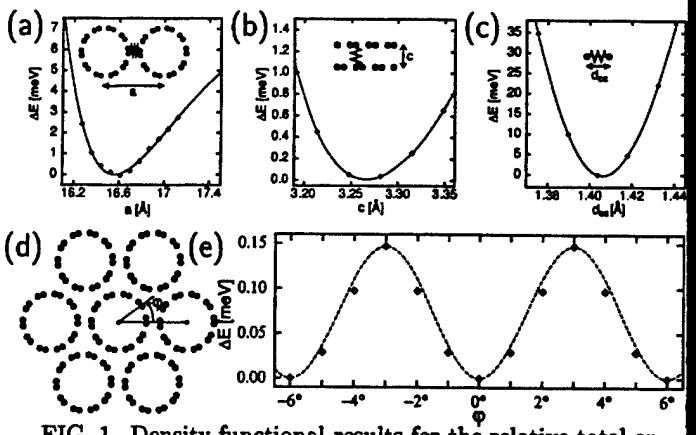

FIG. 1. Density functional results for the relative total energy ΔE of (a) a "rope" of (10,10) carbon nanotubes as a function of the inter-tube spacing a, (b) hexagonal graphite as a function of interlayer spacing c, and (c) hexagonal graphite as a function of the bond length d_{CC}. (d) Schematic end-on view of the "rope" structure, depicting the tube orientation angle φ. (e) Dependence of the "rope" energy ΔE on the orientation angle φ of individual nanotubes. All energies are given per atom.

presented in Fig. 1(b)Γshow that also this value is underestimated by 2.4% when compared to the experimental value. Similar to the tubesΓthe interatomic distance in graphite is underestimated by only 0.8% with respect to the experimental value.

We found the k-point sampling used in the LDA calculation sufficient to describe the details of intra-tube and general features of inter-tube interactions. This interaction depends not only on the inter-tube separation aΓ but also the tube orientation angle φΓdefined in Fig. 1(d). The relatively coarse k-point gridΓused in the LDA studyΓ was found not to be adequate to describe the minute effect of tube rotations on the inter-tube hybridization and the density of states near E_F. ThereforeΓwe performed a parametrized calculation of these quantities using 102Ⅱ00 k-points in the irreducible Brillouin zone for the "rope" lattice and 800 k-points for the tube. Our tight-binding parametrizationΓwhich has been used previously to describe superconductivity in bulk C_{60} [10]Γis based on LDA electronic structure results [21] and hence should describe correctly the covalent part of the interaction.

These resultsΓin good agreement with the LDA data presented in Fig. 1(a)Γ indicate that nanotubes gain $\Delta E_b \approx 9$ meV per atom when bunching up to a "rope". The calculated dependence of the binding energy ΔE on the tube orientation φ is comparably weakΓas shown in Fig. 1(e). Due to the high degree of frustration in a system of tubes with D_{10h} symmetry that are bundled to a triangular latticeΓ we find $\Delta E(\varphi)$ to be periodic in φΓ with a period $\Delta\varphi = 6°$ and an activation barrier for rotation of $\Delta E \lesssim 0.15$ meV per atom [22]Γin good agreement with our LDA results for the equilibrium tube

orientation and the rotational barrier of $\Delta E \approx 0.3$ meV per atom. At the relatively large equilibrium separation $d_w \approx 3.4$ Å between the walls of neighboring nanotubes the repulsive part of the interaction depends only weakly ($\Delta E \lesssim 0.07$ meV) on the tube orientation angle φ. We conclude that $\Delta E(\varphi)$ is dominated by the small changes in hybridization between neighboring nanotubes.

At very low temperatures we expect nanotubes to perform mostly librational motion in the shallow potential wells. We should think of tube librations or rotations within the "rope" as of a twisting motion of tube segments rather than a spinning motion of rigid tubes. Approximating the periodic but strongly anharmonic potential $\Delta E(\varphi)$ by the sinusoid shown in Fig. 1(e) we estimate the libration frequency to lie at $\nu \approx 12$ cm^{-1}. This soft mode lies close to the observed (but not identified) infrared modes of the "rope" at $\nu \approx 15, 22, 40$ cm^{-1} [23]. The librational mode should be infrared silent if the E-field were parallel to a perfect bundle of (10,10) nanotubes. This is however not the case in real samples where all nanotube orientations coexist exposing most of the tubes to a nonzero E-field component normal to their axis. Also the majority of rope samples have recently been reported to contain a large fraction of *chiral* (n,m) nanotubes with a diameter close to that of the achiral (10, 10) tubes [24,25]. While the potential energy surface and hence the libration frequency should be very similar the infrared coupling to the low-frequency modes could be significantly enhanced in this case.

An infinitely rigid and straight nanotube when part of an ordered "rope" has only two degrees of freedom namely for axial and angular motion. Even though the activation barrier *per atom* for any of these motions may be small the relevant quantity in this case is the infinitely high barrier for the entire rigid tube that would lock it in place. In the other extreme of a straight zero-rigidity tube composed of independent atoms 0.15 meV/atom activation barrier for rotation would give rise to an orientational melting transition at $T_{OM} \approx 2$ K.

A more realistic estimate of the onset of orientational disorder must consider that nanotube "ropes" when synthesized are far from being straight over long distances [4]. As suggested by the potential energy surface for this mode in Fig. 1(e) a local twist by $\varphi > 3°$ results in the nanotube switching locally from one equilibrium orientation to another. Formally by mapping the orientational coordinate φ onto the position coordinate x this process can be described using the Frenkel-Kontorova model used to describe dislocations in strained one-dimensional lattices. Under synthesis conditions at tempeartures exceeding 1,000 K we expect substantial finite twists to occur in *free* nanotubes which are associated with strictly zero energy cost over an infinte length. Upon condensation to a bundle in an attempt to optimize the inter-wall interaction while minimizing the torsion energy orientational dislocations are frozen in at an energy cost of only ≈ 0.17 meV per atom in a ≈ 150 Å long strained region [26] as compared to an optimized straight bundle of nanotubes. Taking a straight zero-rigidity tube as a reference we expect T_{OM} to increase from the 2 K value with increasing rigidity. Presence of orientational dislocations on the other hand should lower the activation barrier for tube rotations thus lowering T_{OM} and possibly compensating the effect of nonzero rigidity.

There are two indications that onset of orientational disorder may occur below room temperature. First the infrared modes of the "rope" at $\nu \approx 15, 22, 40$ cm^{-1} some of which may be librations have been reported to disappear at $T \approx 30 - 180$ K [23]. The second indication is the transition from nonmetallic to metallic character of the nanotubes occurring near 50 K [13] which in our interpretation arises from subtle changes of the electronic density of states near E_F in presence of increasing orientational disorder to be discussed below. This is more closely related to the recently proposed mechanism for the temperature dependence of resistivity due to inter-tube hopping near defects [27] than temperature-induced changes in the weak localization of electrons on individual tubes [28].

Our results for the electronic structure of an isolated tube and that of the "rope" are presented in Fig. 2. The irreducible Brillouin zone of the triangular tube lattice shown in Fig. 2(a) collapses to the $\Gamma - A$ line as the inter-tube separations increase in a system of separating tubes. In this case the Fermi momentum occurs at the point Δ_F. On the other hand when nanotubes are bundled in the "rope" lattice the Fermi point Δ_F expands to a Fermi surface in the hexagonal Brillouin zone that is normal to the $\Gamma - A$ line. This Fermi surface shows a small corrugation induced by the inter-tube interaction.

Inter-tube interactions in the "rope" cause substantial changes in the electronic states that are also reflected in the density of states. Our results presented in Figs. 2(b) and (c) indicate that upon bunching of tubes to a "rope" the density of states near the Fermi level increases by $\approx 7\%$ from 1.4×10^{-2} states/eV/atom in tubes to 1.5×10^{-2} states/eV/atom in "ropes". We find $N(E)$ near E_F to be nearly independent of the tube orientation angle φ suggesting that states close to the Fermi level do not couple significantly to tube librations in this marginally metallic system [4,13]. This is similar to the situation in the doped C_{60} solid [29] where librations also do not play an important role in the superconducting behavior induced by electron-phonon coupling.

An intriguing effect linked to orientational order within the "rope" is the appearance of a pseudo-gap near E_F in the density of states as seen in Fig. 2(c). Occurrence of this pseudo-gap in "ropes" of (10,10) nanotubes has independently been confirmed in Ref. [30]. This feature results from breaking the D_{10h} tube symmetry by the triangular lattice and should be less significant in the highly symmetric ordered lattice of (6,6) nanotubes

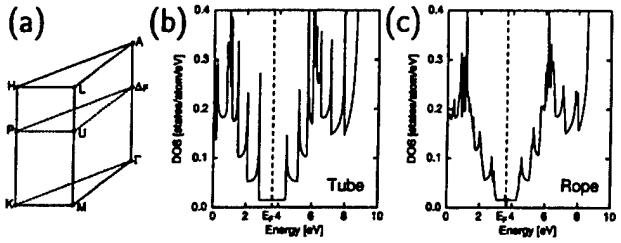

FIG. 2. (a) Irreducible part of the hexagonal Brillouin zone of a nanotube crystal, the "rope". Density of states of (b) an isolated nanotube and (c) a nanotube crystal, the "rope". Dashed lines indicate the position of the Fermi level E_F.

[31]. We expect that in presence of orientational disorder caused in particular by the twisting motion of (10$\bar{1}$0) nanotubes in the "rope" at $T > T_{OM}$ the Brillouin zone should collapse to a point. The resulting reduction of the pseudo-gap should mark the onset of metallic behavior of the "ropes" as discussed above.

IV. CONCLUSIONS

We used *ab initio* and parametrized techniques to determine the orientational ordering in a "bundle" of (10$\bar{1}$0) carbon nanotubes and its effect on the electronic properties. The weak inter-tube interaction and lattice frustration results in a very soft libration mode that occurs at $\nu \approx 12$ cm^{-1}. Due to the small activation barrier for rotation we predict this mode to disappear at very low temperatures marking the onset of orientational melting of tubes in the "rope". We suggest that the orientational melting transition in the tube lattice should be accompanied by a significant possibly discontinuous increase of the equilibrium inter-tube spacing a_e. The inter-tube coupling introduces an additional band dispersion of $\lesssim$0.2 eV and opens up a pseudo-gap of the same magnitude at E_F. The pseudo-gap is expected to be significantly reduced in a lattice showing strong orientational disorder marking the onset of metallic behavior.

ACKNOWLEDGMENTS

We acknowledge useful discussions with Richard E. Smalley and John E. Fischer about nanotube conductivity and with Steven G. Louie about the origin of the pseudo-gap. Y.H.L. acknowledges financial support by the LG Yonam Foundation and the Korea Science and Engineering Foundation (KOSEF; Grant Number KOSEF94-0501-11) and partial support by the Semiconductor Physics Research Center at Jeonbuk National University. K.H.L. acknowledges financial support by the Korean Ministry of Education (Grant Number BSRI96-3438). S.S. acknowledges A. Oshiyama for providing the LDA program used in this work. He also would like to thank for the support by the Ministry of Education Science and Culture of Japan The Murata Science Foundation and the Japan Society for the Promotion of Science (Project number 96P00203). The LDA calculation was partly performed at the Computer Center of the Institute for Molecular Science.

REFERENCES

[1] H.W. Kroto, J.R. Heath, S.C. O'Brien, R.F. Curl, and R.E. Smalley, Nature **318**, 162 (1985).

[2] S. Iijima, Nature **354**, 56 (1991).

[3] M.M.J. Treacy, T.W. Ebbesen, and J.M. Gibson, Nature **381**, 678 (1996).

[4] A. Thess, R. Lee, P. Nikolaev, H. Dai, P. Petit, J. Robert, C. Xu, Y.H. Lee, S.G. Kim, D.T. Colbert, G. Scuseria, D. Tománek, J.E. Fischer, and R.E. Smalley, Science **273**, 483 (1996).

[5] For an overview of the rapidly developing field of carbon nanotubes, see M.S. Dresselhaus, G. Dresselhaus, and P.C. Eklund, *Science of Fullerenes and Carbon Nanotubes*, (Academic Press Inc., 1996 San Diego), and references therein.

[6] C.S. Yannoni, R.D. Johnson, G. Meijer, D.S. Bethune, and J.R. Salem, J. Phys. Chem. **95**, 9 (1991); R. Tycko, R.C. Haddon, G. Dabbagh, S.H. Glarum, D.C. Douglass, and A.M. Mujsce, J. Phys. Chem. **95**, 518 (1991).

[7] W. Krätschmer, L.D. Lamb, K. Fostiropoulos, and D.R. Huffman, Nature **347**, 354 (1990).

[8] P. Nikolaev, A. Thess, A.G. Rinzler, D.T. Colbert, and R.E. Smalley, Chem. Phys. Lett. **266**, 422 (1997).

[9] Young Hee Lee, Seong Gon Kim, and David Tománek, Phys. Rev. Lett. **78**, 2393 (1997).

[10] M. Schluter, M. Lannoo, M. Needels, G.A. Baraff, and D. Tománek, Phys. Rev. Lett. **68**, 526 (1992).

[11] Susumu Saito and Atsushi Oshiyama, Phys. Rev. Lett. **66**, 2637 (1991).

[12] C.L. Kane and E.J. Mele, Phys. Rev. Lett. **78**, 1932 (1997).

[13] J.E. Fischer, H. Dai, A. Thess, R. Lee, N. Hanjani, D.L. Dehaas, and R.E. Smalley, Phys. Rev. B **55**, R4921 (1997).

[14] O. Sugino and A. Oshiyama, Phys. Rev. Lett. **68**, 1858 (1992).

[15] N. Troullier and J.L. Martins, Phys. Rev. B **43**, 1993 (1991).

[16] L. Kleinman and D.M. Bylander, Phys. Rev. Lett. **48**, 1425 (1982).

[17] D.M. Ceperley and B.J. Alder, Phys. Rev. Lett. **45**, 566 (1980).

[18] J.P. Perdew and A. Zunger, Phys. Rev. B **23**, 5048 (1981).

[19] J.H. Weaver, J.L. Martins, T. Komeda, Y. Chen, T.R. Ohno, G.H. Kroll, N. Troullier, R.E. Haufler, and R.E. Smalley, Phys. Rev. Lett. **66**, 1741 (1991).

[20] S. Okada and S. Saito, Phys. Rev. B **55**, 4039 (1997).
[21] D. Tománek and Michael A. Schluter, Phys. Rev. Lett. **67**, 2331 (1991).
[22] Rather than using a a fixed cutoff distance in our parametrized scheme, which would cause artifacts in the energy due to a changing neighbor map during tube rotations, we obtained the potential energy surface by carefully integrating over energy differences due to small rotations, during which the neighbor map was kept fixed.
[23] W. Holmes, J. Hone, P.L. Richards, and A. Zettl, Bull. Am. Phys. Soc. **43**, 629 (1998).
[24] J.W.G. Wildöer, L.C. Venema, A.G. Rinzler, R.E. Smalley, and C. Dekker, Nature **391**, 59 (1998).
[25] T.W. Odom, J.-L. Huang, P. Kim, and C.M. Lieber, Nature **391**, 62 (1998).
[26] Y.-K. Kwon and D. Tománek (in preparation).
[27] A.B. Kaiser, G. Düsberg, and S. Roth, Phys. Rev. B **57**, 1418 (1998).
[28] L. Langer, V. Bayot, E. Grivei, J.-P. Issi, J.P. Herremans, C.H. Olk, L. Stockman, C. Van Haesendonck, and Y. Bruynseraede, Phys. Rev. Lett. **76**, 479 (1996).
[29] C. Christides, D.A. Neumann, K. Prassides, J.R.D. Copley, J.J. Rush, M.J. Rosseinsky, D.W. Murphy, R.C. Haddon, Phys. Rev. B **46**, 12088 (1992).
[30] P. Delaney, H.J. Choi, J. Ihm, S.G. Louie, and M.L. Cohen, Nature **391**, 466 (1998).
[31] J.-C. Charlier, X. Gonze, and J.-P. Michenaud, Europhys. Lett. **29**, 43 (1995).

QUANTUM TRANSPORT IN INHOMOGENEOUS MULTI-WALL NANOTUBES

S. Sanvito[1,2,3], Y.-K. Kwon[3], D. Tománek[3], and C.J. Lambert[1]

[1]*School of Physics and Chemistry, Lancaster University, Lancaster, LA1 4YB, UK*
[2]*DERA, Electronics Sector, Malvern, Worcs. WR14 3PS, UK*
[3]*Department of Physics and Astronomy, and Center for Fundamental Materials Research, Michigan State University, East Lansing, Michigan 48824-1116*

INTRODUCTION

Carbon nanotubes[1,2] are narrow seamless graphitic cylinders, which show an unusual combination of a nanometer-size diameter and millimeter-size length. This topology, combined with the absence of defects on a macroscopic scale, gives rise to uncommon electronic properties of individual single-wall nanotubes[3,4], which depending on their diameter and chirality, can be either metallic, semiconducting or insulating[5–7].

In this paper we focus attention only on metallic nanotubes and in particular on the so-called "armchair" nanotubes. An armchair nanotube is a graphite tube in which the hexagon rows are parallel to the tube axis. If n is the number of carbon dimers along the nanotube circumference the tube will be labeled as (n, n) nanotube. One of the most important properties of the armchair nanotubes is that they behave like a mono-dimensional metal and this is directly connected with their structure. The electronic wave-length in fact is quantized around the circumference of the tube because of the periodic boundary conditions. This gives rise to mini-bands along the tube axis and the tube is metallic or insulating whether or not one or more mini-bands cross the Fermi energy. In the case of armchair nanotubes two mini-bands along the tube axis cross the Fermi energy[8], therefore, according to scattering theory[9], the conductance is expected to be $2G_0$, where $G_0 = 2e^2/h \approx (12.9\ \mathrm{k}\Omega)^{-1}$ is the quantum conductance. Direct evidence of the de-localization of the wave function along the tube axis has been already shown[10,11], while a direct measurement of the conductance quantization for single-wall nanotubes is still missed (for an introduction to electronic transport in carbon nanotubes see reference 12).

The situation for multi-wall nanotubes is rather different. A multi-wall nanotube consists of several single-wall nanotubes inside one another, forming a structure reminiscent of a "Russian doll". A section of a double-wall (5,5)@(10,10) armchair nanotube is presented in figure 1.

Recent measurements[13] of the conductance in multi-wall nanotubes have raised a significant controversy due to the observation of unexpected conductance values and of ballistic transport at temperatures far above room temperature. In these experiments

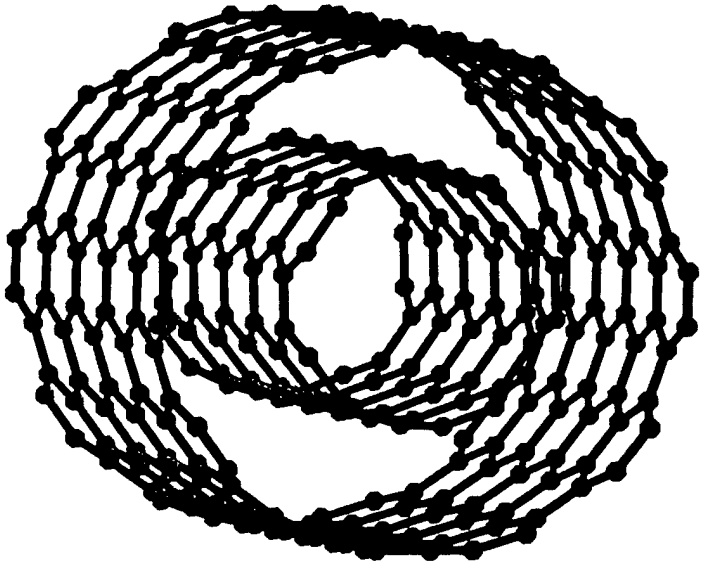

Figure 1: Section of a (5,5)@(10,10) "armchair" nanotube.

several multi-wall nanotubes are glued to a gold tip, which acts as the first electrode, with a colloidal silver paint. The second electrode is made by a copper bowl containing mercury, which provides a gentle contact with the nanotube. The tip is lowered into the mercury and the two-probe conductance is measured as a function of the immersion depth of the tubes into the mercury. The main feature of the experiments is that at room temperature the conductance shows a step-like dependence on the immersion depth, with a value of $0.5\,G_0$ for low immersion and $1\,G_0$ when the tip is further lowered. The value of $0.5\,G_0$ usually persists for small immersion depths ($\leq$ 40nm) and is completely absent in some samples, while the value $1\,G_0$ is found for very long immersion depths, up to 0.5μm. Nevertheless some anomalies have been found with conductances of $0.5\,G_0$ lasting for more than 500nm[13].

While the ballistic behavior up to high temperature can be explained by the almost complete absence of backward scattering[14], the presence of such conductance values is still not completely understood. In the absence of inter-tube interactions, if one assumes that m of the nanotubes forming the multi-wall nanotube are metallic and in contact with both the electrodes, then a conductance of $2mG_0$ is expected for the multi-wall nanotube. This means that even in the extreme case in which only one tube is metallic and in contact with the electrodes a conductance of $2G_0$ must be measured. Therefore the values $0.5\,G_0$ and $1\,G_0$ are largely unexpected. One possible explanation, provided by the authors of the experiments, is that only the outermost tube is responsible for the transport and that the anomalous conductance is the result of scattering to impurities. Nevertheless both these hypothesis may be challenged. The first is based on the assumption that, since mercury does not wet the innermost tubes, it does not provide an efficient electrical contact with the innermost part of the multi-wall nanotube. This may not be the case because the interaction between the different walls may be large and the motion of electrons across the structure efficient. As far as the second hypothesis concerns, it has been shown recently[15] that disorder averages over the tube's circumference, leading to an electron mean free path that increases with the nanotube diameter. Therefore single impurities affect transport only

weakly, particularly in the nanotube forming the outermost shell, which has the largest diameter.

In this paper we address these puzzling measurements and show that the structural properties of multi-wall nanotubes can explain their peculiar transport. The electronic band structure of multi-wall carbon nanotubes[16–18], as well as single-wall ropes[19,20] is now well documented. More recently, it has been shown that pseudo-gaps form near the Fermi level in multi-wall nanotubes[18] due to inter-wall coupling, similar to the pseudo-gap formation in single-wall nanotube ropes[19,20]. Here we demonstrate that the unexpected transport properties of multi-wall nanotubes arise from the inter-wall interaction. This interaction may not only block some of the quantum conductance channels, but also redistribute the current non-uniformly over the individual tubes. When only the outermost tube is in contact with one of the voltage/current electrodes, then this forms a preferred current path and, because of inter-tube interaction, the conductance of the whole system will typically be smaller than $2G_0$.

The paper is organized as follows. In the next section we will briefly describe a general scattering technique to compute the transport properties of finite systems attached to semi-infinite contacts, both described by a tight-binding Hamiltonian. In the following section we will discuss the transport in infinite multi-wall nanotubes and understand which are the effects of the inter-tube interaction both on the dispersion and on the wave-function of the tube. Then we present the results for transport properties of inhomogeneous multi-wall nanotubes, giving an explanation of the experiments of reference 13. In this part we will consider different scenarios about the structure of the electrical contacts. At the end we will make some final remarks.

GENERAL SCATTERING TECHNIQUE

To determine transport properties of finite multi-wall nanotubes, we combine for the first time, a tight-binding parameterization determined by *ab-initio* calculations for simpler structures[21], with a scattering technique developed recently for magnetic multilayers[22,23]. The use of a tight-binding model is justified by the necessity to deal with a system comprising a large number of degrees of freedom. This parameterization has been used to describe detailed electronic structure and total energy differences of systems with unit cells which are too large to handle accurately by *ab-initio* techniques. The electronic structure and superconducting properties of the doped C_{60} solid[24], the opening of a pseudo-gap near the Fermi level in a rope consisting of (10,10) nanotubes[20] and in (5,5)@(10,10) double-wall nanotubes[18] are some of the problems successfully tackled by this technique. The band structure energy functional is augmented by pairwise interactions describing both the closed-shell interatomic repulsion and the long-range attractive van der Waals interaction. This reproduces correctly the interlayer distance and the C_{33} modulus of graphite. Independent checks of this approach can be carried out by realizing that the translation and rotation of individual tubes are closely related to the shear motion of graphite. We expect that the energy barriers in tubes lie close to the graphite value which, due to the smaller unit cell, is easily accessible to *ab-initio* calculations[25].

The scattering technique that we used have been recently employed in studies of giant magnetoresistance[22,23] and ferromagnetic/superconductor structures[26]. It yields the quantum-mechanical scattering matrix S for a phase-coherent system attached to external reservoirs. The rôle of the reservoirs is to inject and collect incoherent electrons into the scattering region. The energy-dependent conductance $G(E)$ in the

zero-temperature limit is computed by evaluating the Landauer-Büttiker formula[27]

$$G(E) = \frac{2e^2}{h} T(E) \,, \tag{1}$$

where $T(E)$ is the total transmission coefficient evaluated at the energy E (E_F in the case of zero-bias). The formula of equation (1) provides an exact relation between the conductance of a system and its scattering properties.

The transmission coefficient is evaluated using a scattering technique that combines a real space Green function calculation for the incoherent leads and a Gaussian elimination (ie "decimation") algorithm for the scattering region. A general scheme of the technique is presented in figure 2, where we indicate how a transport problem can be mapped onto a quantum mechanical scattering problem.

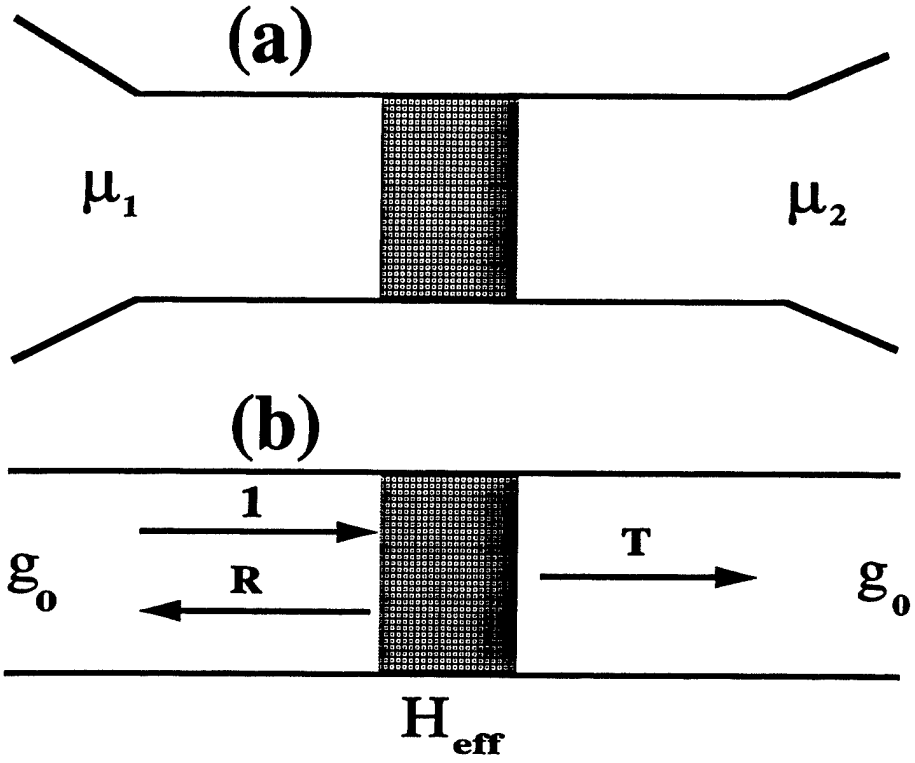

Figure 2: Scheme of the scattering calculation. The system (a) consists in two reservoirs with chemical potentials μ_1 and μ_2 separated by a scattering region. The problem is mapped by using the Landauer-Büttiker formalism onto a quantum mechanical scattering problem (b). The incoming scattering channels in the leads are calculated through the surface Green function g_0. The effective coupling matrix H_{eff} is computed by "decimating" the internal degrees of freedom of the scattering region. The total transmission T and reflection R coefficients are then calculated by solving exactly the Dyson's equation and by using a generalization of the Fisher-Lee relations.

Suppose the total Hamiltonian H for the whole system (nanotubes plus external leads) can be written

$$H = H_{\text{L}} + H_{\text{L-NT}} + H_{\text{NT}} + H_{\text{NT-R}} + H_{\text{R}} \,, \tag{2}$$

where H_{L} and H_{R} describe respectively the semi-infinite left-hand side and right-hand side lead, $H_{\text{L-NT}}$ and $H_{\text{NT-R}}$ are the coupling matrices between the leads and the nanotube and H_{NT} is the Hamiltonian of the nanotube. In what follows we will consider the leads themselves to be carbon nanotubes, whose number of walls depends on the position of the electrical contacts. This is justified when the transport bottleneck is

formed by the nanotubes and not to the metal-nanotube contacts. As far as we know detailed *ab-initio* analysis of metal/nanotube interaction is still not available.

The surface Green function g_0^S of the leads are calculated by numerically evaluating the general semi-analytic formula given in reference 22. One of the key-points of such a calculation is to compute the scattering channels in the leads. Suppose z to be the direction of the transport and the Hamiltonian of the leads to be an infinite matrix of trigonal form with respect to such a direction, with the matrices H_0 and H_1 respectively in the diagonal and off-diagonal positions. Therefore the dispersion relation for electrons in a Bloch state

$$\psi_z = \frac{1}{v_k^{1/2}} e^{ikz} \phi_k \tag{3}$$

and moving along z with unit flux can be written as

$$(H_0 + H_1 e^{ik} + H_{-1} e^{-ik} - E)\phi_k = 0\,, \tag{4}$$

where v_k is the group velocity corresponding to the state (3) and $H_{-1} = H_1^\dagger$ ($H_0 = H_0^\dagger$). Note that the matrices H_0 and H_1 describe respectively the interaction within a unit cell and the interaction between adjacent cells. If a unit cell possesses M degrees of freedom, these matrices will be $M \times M$ matrices. Moreover ϕ_k is a M dimensional column vector which describes the transverse degrees of freedom of the Bloch-function. The Green function in the leads is constructed by adding up states of the form of equation (3) with k both real and imaginary, which means that the dispersion relation (4) must be solved for real energies in the form $k = k(E)$. This is the opposite to what is usually computed by ordinary band structure theory where one is interested in finding all the real energies $E = E(k)$ for a chosen real k-vector. Moreover in the calculation of $k = k(E)$ instead of solving the equation

$$\det\left(H_0 + H_1 e^{ik} + H_{-1} e^{-ik} - E\right) = 0\,, \tag{5}$$

which involves the use of a root tracking algorithm in the complex plane, we map the problem onto an eigenvalue problem by defining the matrix $\mathcal{H}$

$$\mathcal{H} = \begin{pmatrix} -H_1^{-1}(H_0 - E) & -H_1^{-1}H_{-1} \\ \mathcal{I} & 0 \end{pmatrix}\,, \tag{6}$$

where $\mathcal{I}$ is the $M \times M$ identity matrix. The eigenvalues of $\mathcal{H}$ are the roots e^{ik} and the upper half of the eigenvectors of $\mathcal{H}$ are the corresponding eigenvectors ϕ_k.

The second part of the calculation involves computing an effective coupling matrix between the surfaces of the scattering region. Note that the purpose of a scattering technique is to calculate the S matrix between electrons in the leads. Therefore one is not interested in information regarding the internal degrees of freedom of the scattering region, but only in the resulting coupling between the external interfaces. This can be achieved by reducing the matrix $H_{\text{L-NT}} + H_{\text{NT}} + H_{\text{NT-R}}$ to an effective coupling matrix H_{eff}. Suppose the total number of degrees of freedom of the Hamiltonian $H_{\text{L-NT}} + H_{\text{NT}} + H_{\text{NT-R}}$ is N, and the number of degrees of freedom of the lead surfaces M. One can eliminate the $i = 1$ degree of freedom (not belonging to the external surfaces) by reducing the $N \times N$ total Hamiltonian to an $(N-1) \times (N-1)$ matrix with elements

$$H_{ij}^{(1)} = H_{ij} + \frac{H_{i1}H_{1j}}{E - H_{11}}\,. \tag{7}$$

Repeating this procedure l times we obtain the "decimated" Hamiltonian at l-th order

$$H_{ij}^{(l)} = H_{ij}^{(l-1)} + \frac{H_{il}^{(l-1)}H_{lj}^{(l-1)}}{E - H_{ll}^{(l-1)}}\,, \tag{8}$$

and finally after $N - M$ times, the effective Hamiltonian

$$H_{\text{eff}}(E) = \begin{pmatrix} H^*_{\text{L}}(E) & H^*_{\text{LR}}(E) \\ H^*_{\text{RL}}(E) & H^*_{\text{R}}(E) \end{pmatrix} . \tag{9}$$

In the equation (9) the matrices $H^*_{\text{L}}(E)$ and $H^*_{\text{R}}(E)$ describe the intra-surface couplings respectively in the left-hand side and right-hand side surfaces, and $H^*_{\text{LR}}(E)$ and $H^*_{\text{RL}}(E)$ describe the effective coupling between these surfaces. From the above equations it is clear that only matrix elements coupled to the eliminated degree of freedom are redefined. This exact recursive technique therefore turns out to be very efficient in the case of short-range interaction like the nearest neighbors tight-binding model considered here. Two important considerations must be made. Firstly we note that both the Green function calculation and the "decimation" require a fixed energy. Once this has been set the calculation is exact and does not use any approximation. Secondly the calculation of the Green function is completely decoupled by the calculation of the effective Hamiltonian for the scatterer. This can allow very efficient numerical optimizations, particularly in the study of disordered systems[28].

Once both the surface Green function of the leads g^{S}_0 and the effective coupling Hamiltonian $H_{\text{eff}}(E)$ are computed then the total Green function G^{S} for the whole system (leads plus scattering region) are easily calculated by solving the Dyson's equation

$$G^{\text{S}}(E) = [(g^{\text{S}}_0(E))^{-1} - H_{\text{eff}}]^{-1} . \tag{10}$$

Finally the scattering matrix elements are extracted from G^{S} by using a generalization of the Fisher-Lee relations[29].

For the case of leads made by carbon nanotubes a final observation must be considered. The unit cell along the axis of the nanotube comprises two atomic planes, and since the hopping matrix between sequential unit cells H_1 is therefore singular, the dispersion relation cannot be calculated by using the equation (6). We avoid this complication by projecting out the non-coupled degrees of freedom between sequential cells before calculating the scattering channels. This has been done by using the "decimation" technique described above.

CONDUCTANCE IN MULTI-WALL NANOTUBES

For an homogeneous system $T(E)$ assumes integer values corresponding to the total number of open scattering channels at energy E. For individual (n, n) "armchair" tubes, this integer is further predicted to be even[8], with a conductance of $2G_0$ near the Fermi level. As an example, our results for the conductance $G(E)$ and the density of states of the $(10, 10)$ nanotube are shown in Fig. 3.

The main feature of an "armchair" nanotube is its true mono-dimensional metallic behavior. Note that the density of state shows mono-dimensional van Hove singularities which are due to the presence of dispersion-less mini-bands. This is reflected in the energy-dependent conductance which shows a typical step-like behavior. Such steps appear whenever the energy crosses a new mini-band, and therefore correspond to the van Hove singularities in fig 3a. It is crucial to note that in an infinite system every scattering channel gives the same contribution G_0 to the conductance independently from its dispersion and group velocity. The situation is rather different in an inhomogeneous system, where the scattering of electrons from low dispersion to high dispersion bands of different materials, can give rise to strong backward scattering and therefore

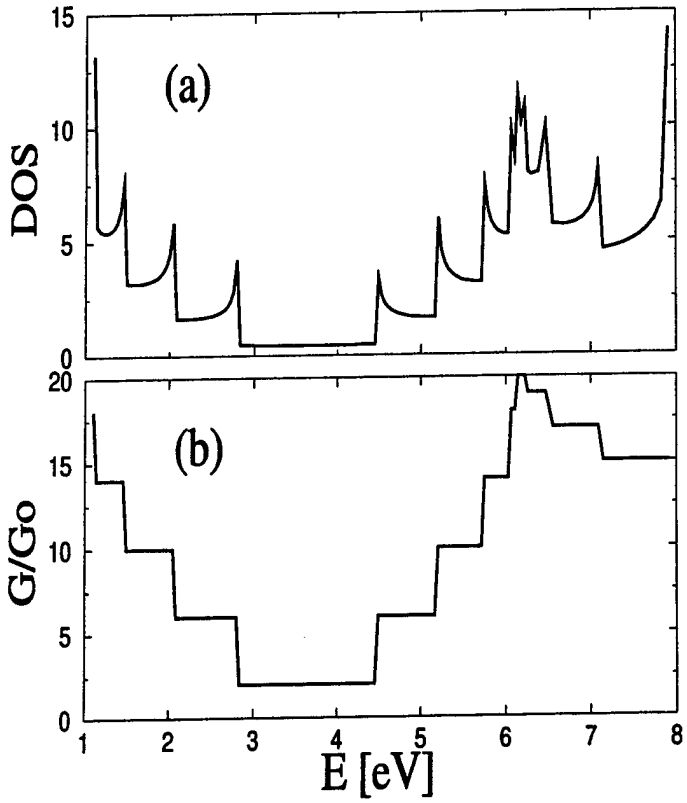

Figure 3: Single-wall (10,10) nanotube. (a) Local density of states. (b) Conductance as a function of energy. The Fermi level lies at 3.65 eV.

to a reduction of the conductance[22,23,28]. At the Fermi energy of an "armchair" nanotube (in this case $E_F = 3.65$ eV) only two scattering channels are present resulting in a conductance $2G_0$, which remains constant in an energy interval of approximately 1.5eV.

Consider now multi-wall nanotubes. As observed in the introduction, in the absence of inter-tube interactions, different tubes behave as conductors in parallel and the conductances are simply additive. Therefore, since the position of the Fermi energy does not change with the tube diameters we expect a conductance $2mG_0$ for a multi-wall nanotubes comprising m walls. Note also that the width of the energy region around the Fermi energy where the conductance is $2G_0$, depends only weakly on the tube diameters. The situation changes drastically when inter-tube interaction is switched on. In figures 4 and 5 we present the density of states and the conductance respectively for a (10,10)@(15,15) and for a (5,5)@(10,10)@(15,15) multi-wall nanotube.

In the figures we restricted the energy window to the region where the single-wall armchair nanotubes present conductances of $2G_0$. The main feature of both the figures is the presence of pseudo-gaps[18] which lower the conductance from the expected value $2mG_0$. In the case of a double-wall nanotube, this results in two regions where the conductance passes from $4G_0$ to $2G_0$, while in triple-wall nanotube the values $6G_0$, $4G_0$ and $2G_0$ are possible. Nevertheless both these results are still not consistent with the experimental observations of $1G_0$ and $0.5G_0$[13].

It is important to note that the presence of energy pseudo-gaps does not only lowers the conductance but also gives rise to two important effects. First it changes drastically the dispersion of the mini-bands close to the gaps. At the edge of the gaps in fact the dispersion passes from a linear to an almost dispersion-less parabolic-like structure. This is shown in figure 6 where we present the band structure along the

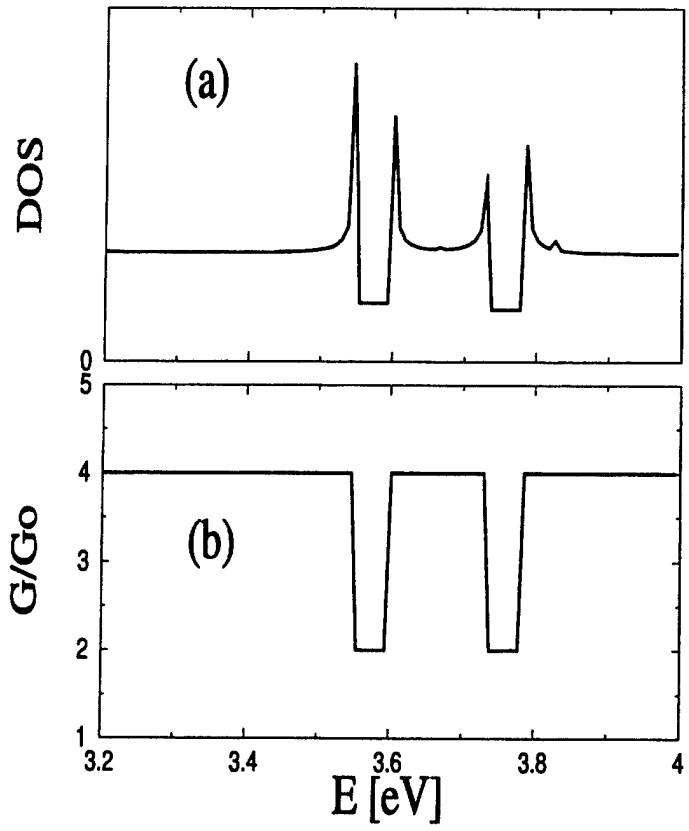

Figure 4: (a) Local density of states for a double-wall (10,10)@(15,15) nanotube. (b) Conductance as a function of energy.

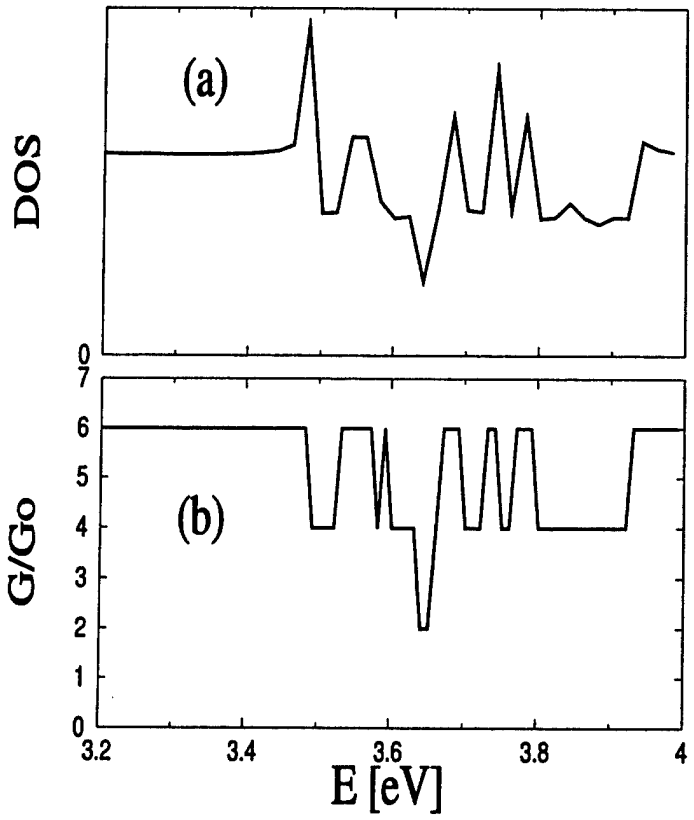

Figure 5: (a) Local density of states for a triple-wall (5,5)@(10,10)@(15,15) nanotube. (b) Conductance as a function of energy.

direction of the tube axis for a double-wall (10,10)@(15,15) nanotube (b) together with the band structure of a single-wall (15,15) nanotube.

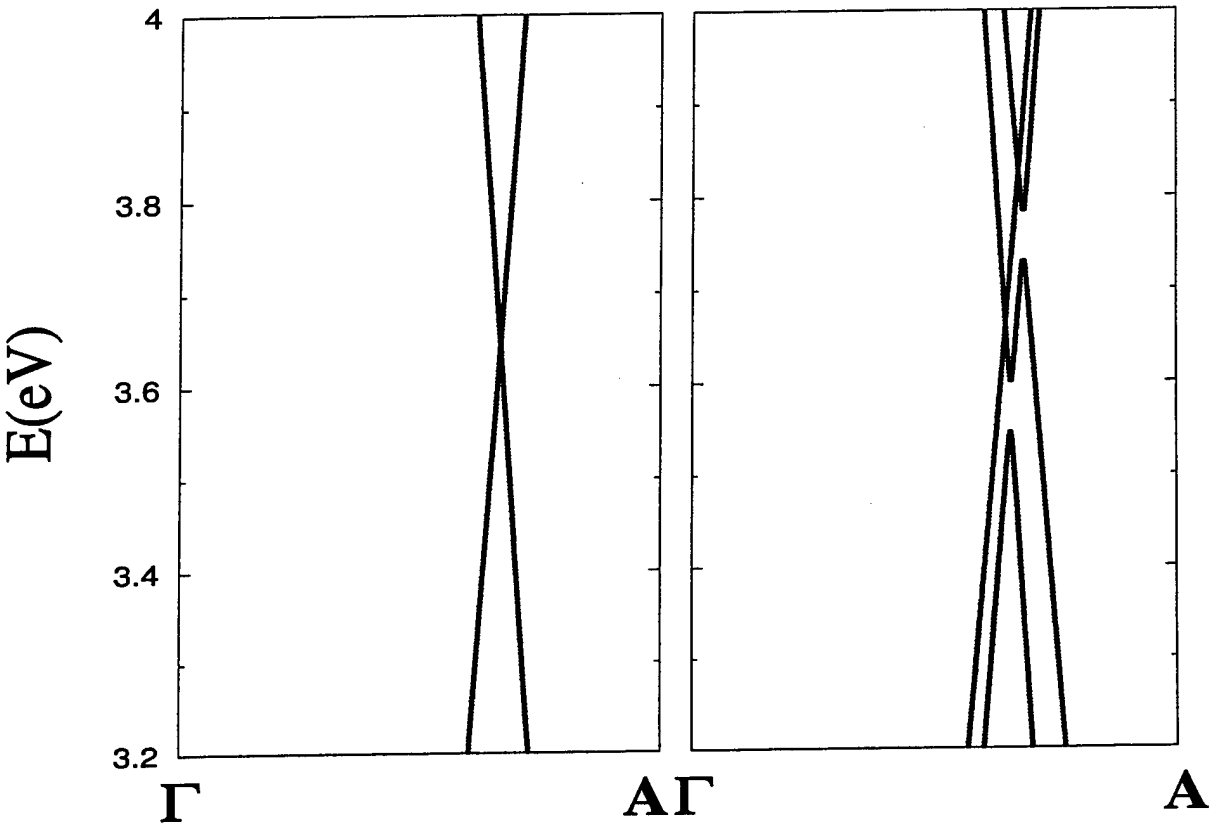

Figure 6: (a) Band structure along the tube axis for a (15,15) nanotube, with $E_F = 3.65$ eV. (b) Band structure along the tube axis for a (10,10)@(15,15) nanotube.

Secondly the amplitude of the wave-function across the nanotubes changes. Far from the gaps, where the effects of the inter-tube interaction are weak, the wave-function is expected to have a uniform distribution across the different walls composing the nanotube. This is what is found in the case of non-interacting walls, whereas in the vicinity of a pseudo-gap, the distribution changes dramatically and the amplitude may be enhanced along some walls and reduced along some others. To demonstrate this effect in figure 7 we present the partial conductance across the two walls composing a (10,10)@(15,15) nanotube and across the three walls composing a (5,5)@(10,10)@(15,15) nanotube. The partial conductance is defined as the projection of the total conductance for an infinite multi-wall tube onto the degrees of freedom describing the individual walls. From the figure it is very clear that the amplitude of the wave-function (which is proportional to the partial conductance) is not uniform across the structure and depends critically on the energy.

Both the change in the dispersion and the non-uniform distribution of the amplitude of the wave-function across the tubes have drastic effects on the transport of heterogeneous systems, because it creates strong inhomogeneities along the structure, and therefore strong backward scattering. This aspect, which occurs in a multi-wall nanotube when one of the innermost walls closes, will be discussed in the next section.

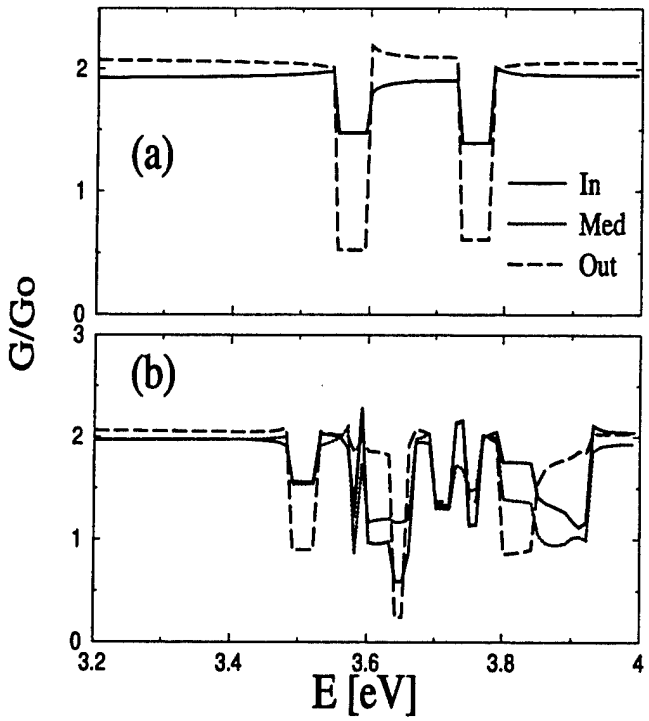

Figure 7: Partial conductance of (a) (10,10)@(15,15) and (b) (5,5)@(10,10)@(15,15) nanotube. The solid line, dotted and dashed lines represent the partial conductance respectively onto the innermost, the medium (only in the case of (5,5)@(10,10)@(15,15)) and the outermost tube. Note that within the pseudo-bandgaps the conductance does not distribute uniformly onto the different tubes.

TRANSPORT IN INHOMOGENEOUS MULTI-WALL NANOTUBES

In this section we will use the ideas developed above to describe the experiments of reference 13. Note that for inhomogeneous systems, where multi-wall nanotubes are contacted to the voltage/current probes, the conductance quantization in unit of $2G_0$ which we found also for multi-wall nanotube in presence of inter-wall interaction is evidently violated and fractional values of the conductance are allowed. One of the difficulties of the experiments, which use gold as one electrode and mercury as the other, is that not all tubes make contact with the electrodes. We have considered two different scenarios and have found that agreement with the experiments is obtained when we assume that only the outermost tube is in contact with the gold electrode, whereas the number of walls in contact with the mercury depends on the depth at which the tube is immersed into the liquid. This latter assumption may seem surprising, because the mercury does not wet the inner tubes. Nevertheless we believe that at equilibrium, the inter-tube interaction allows a uniform distribution of the chemical potential across the cross-section of the whole structure and therefore in the linear-response regime, the scattering problem reduces to a semi-infinite single-wall nanotube (the one in direct contact with gold) attached to a scattering region in which a variable number of walls are present (see fig.8a). Moreover a close analysis of the inter-tube matrix elements shows that these are of the same order of magnitude as the intra-wall ones. This means that electron transport between different walls may be efficient, as well as the electron feeding of the innermost walls from the electrons reservoirs.

Consider first the case in which only the outermost tube makes contact with the gold electrode. We argue that the step-like dependence of the conductance on the immersion depth is due to the fact that the scattering region makes contact with the

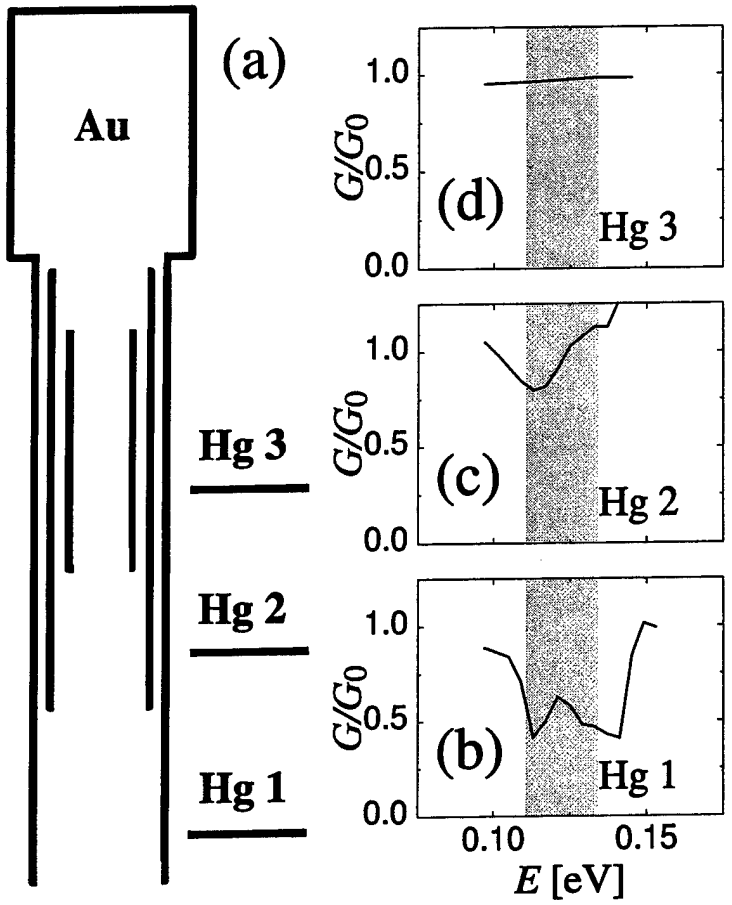

Figure 8: (a) Schematic geometry of the system in which only the outermost tube is contacted with the gold electrode for different immersion depths. (b)-(d) Conductance as a function of energy for the system of (a) at the immersion depths Hg1, Hg2, and Hg3. E is given with respect to E_F of the pristine (undoped) nanotube.

mercury reservoir via a multi-wall semi-infinite nanotube whose number of walls varies and depends on the immersion of the structure. For small immersion depths (such as Hg1 in fig.8a), only the outermost tube is in contact with mercury, because it is the only one with an end below the mercury level. A further lowering of the gold tip (to depths such as Hg2 and Hg3 in fig.8a) will sequentially place more inner walls into electrical contact with the mercury, thereby changing the conductance. We notice that the conductance of such a structure cannot be larger than that of the single-wall nanotube, which is the only tube in contact with the gold electrode.

In figure 8b we present the conductance as a function of energy for the inhomogeneous structure described in figure 8a. In all three cases, the simulated structure makes contact with the upper Au reservoir via a (15,15) nanotube, which forms the upper external lead, whereas the lower external lead contacting the Hg comprises either a single, double or triple-wall nanotube. The solid curve corresponds to a structure formed from a 200 atomic plane (AP) (5,5)@(10,10)@(15,15) triple-wall region, below which is attached to a 200 AP (10,10)@(15,15) double-wall region. The ends of the outer (15,15) nanotube are connected to semi-infinite (15,15) nanotubes, which form the external leads. The dashed curve corresponds to a structure formed from a 200 AP (5,5)@(10,10)@(15,15) triple-wall region. The upper end of the outer tube attached to a semi-infinite (15,15) nanotube, which forms the external lead contacting the Au reservoir. The lower end of the (10,10) and (15,15) nanotubes continue to infinity, and form a (10,10)@(15,15) external contact to the Hg reservoir. Finally the dot-dashed

line shows the conductance of a (5,5)@(10,10)@(15,15) nanotube, which at the lower end makes direct contact with the Hg and at the upper end, the outer tube continues to infinity, thereby forming a (15,15) external contact to the Au reservoir. These situations correspond to immersion of the tube into the mercury at positions Hg1, Hg2 and Hg3 respectively, where either one wall and two walls are in electrical contact with the mercury.

In all the simulations, the ends of the finite-length tubes are left open and we do not include capping layers. We believe that the capping layers are not crucial to the description of the transport properties of inhomogeneous multi-wall nanotubes, since these are mainly determined by the mis-match of wave-vectors between different regions. Figure 8b shows clearly that in an energy window of about 0.05eV (indicated by vertical dashed lines), the conductance for the first structure is approximately $0.5G_0$, while for the latter two is of order $1G_0$. Note that such energy window is two times larger than the bias used in the experiments and also much larger than room temperature. This suggests that these results are quite robust and will survives both at room temperature and moderate biases. This remarkable result is in excellent agreement with the recent experiments of reference 13.

The scattering in such an inhomogeneous structure arises from the reasons pointed out in the previous section. In the energy window considered in fact the infinite (5,5)@(10,10)@(15,15) presents a large pseudo-gap with conductance $4G_0$. We therefore expect that at both the interfaces of the (5,5)@(10,10)@(15,15) region with respectively the (10,10)@(15,15) region and the (15,15) tube, the mismatch of either the transverse components of the wave-function ϕ_k and the longitudinal k-vectors will be large. This gives rise to the strong suppression of the conduction observed in the experiments. In figure 9 we present the conductance as a function of immersion depth in mercury for the structure described above. The conductance is calculated at zero-temperature in the zero bias limit and the energy has been set in the middle of the marked region of figure 8a (3.825eV). Note again that the agreement with the curve of experiments of reference 13 is very good.

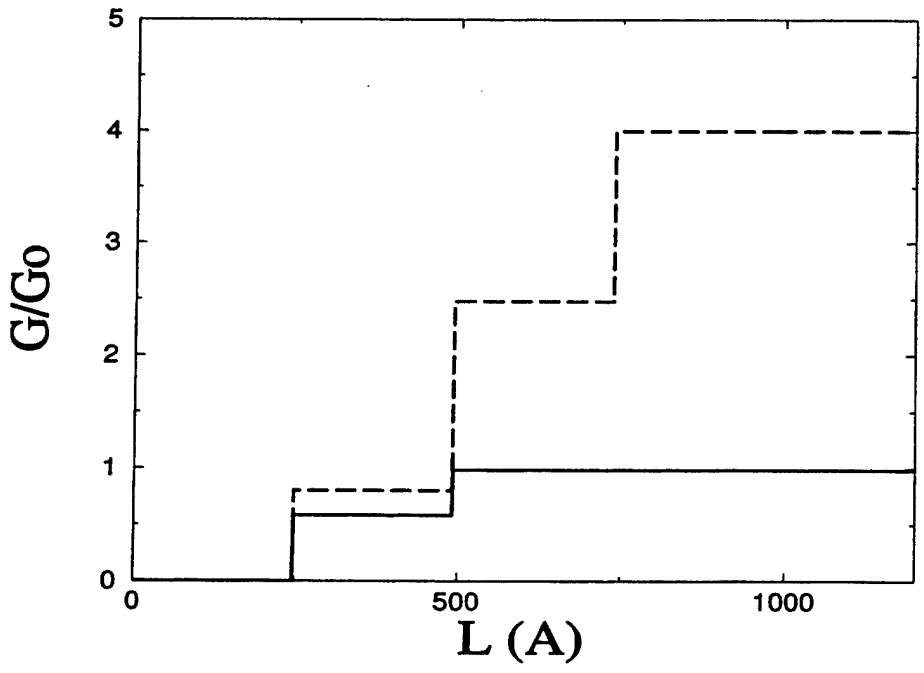

Figure 9: Conductance as a function of immersion depth. The solid curve corresponds to the structure of figure 8a and the dashed curve to that of figure 10a.

We now consider a second possible scenario, in which three tubes are in direct contact with the gold electrode. In this case the electrons are fed from gold into the structure directly along all the tubes. This contact can be simulated by a semi-infinite (5,5)@(10,10)@(15,15) nanotube with uniform chemical potential across the tubes. The structure considered is presented in figure 10a. In this case the upper bound of the conductance is no longer fixed by the single-wall tube to be $2G_0$ but can be as large as $6G_0$ and depends on the number of walls contacting the mercury. In figure 10b we show the conductance as a function of energy respectively for a 200 AP (10,10)@(15,15) nanotube sandwiched between a (15,15) and a (5,5)@(10,10)@(15,15) nanotube leads, for (10,10)@(15,15) nanotube lead in contact with a (5,5)@(10,10)@(15,15) nanotube lead, and for an infinite (5,5)@(10,10)@(15,15) nanotube. This again corresponds to the different levels of immersion Hg1, Hg2 and Hg3 in (Fig. 10a). Note that in the case in which the (5,5)@(10,10)@(15,15) nanotube is in direct contact with both the gold and the mercury electrodes its conductance corresponds to the number of opening scattering channels for the infinite triple-wall system.

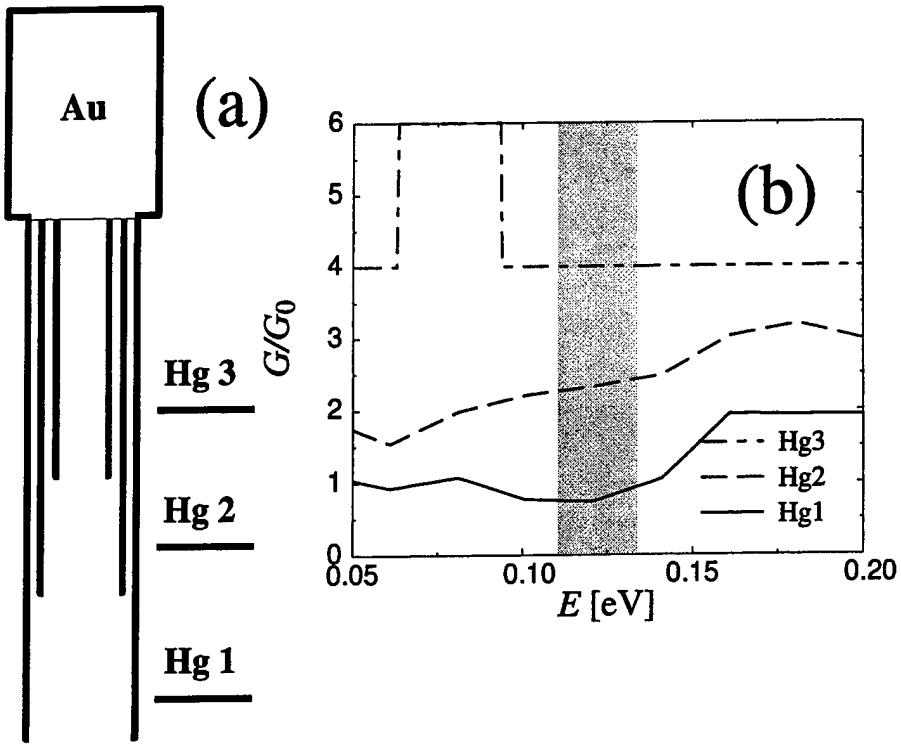

Figure 10: (a) Schematic geometry of the system in which three tubes tubes are contacted with the gold electrode for different immersion depths. (b) Conductance as a function of energy for the system of (a). E is given with respect to E_F of the pristine (undoped) nanotube.

Figure 10 shows that when all three tubes are electrically connected to the gold electrode, a much larger increase in the conductance occurs when a new wall is lowered below the mercury level, although this is still smaller than the value of $2G_0$, obtained for completely isolated tubes. In this case, corresponding to the different value of the immersion depth, we expect the conductance to be respectively $1G_0$, $2G_0$ and $4G_0$.

The large difference between the transport of the structures in figures 8a and 10a is therefore crucially dependent on the number of tubes which make a direct contact with the gold electrode. At the moment a complete description of the nanotube/metal interface is not available, although it will deserve further investigation both experimentally and theoretically.

CONCLUSIONS

To conclude we have presented a fully quantum scattering technique which yields the S matrix of inhomogeneous multi-wall nanotubes. We have shown that the inter-tube interaction drastically modifies transport, not only by opening pseudo-gaps close to the Fermi energy, but also by redistributing the amplitude of the transverse component of the wave-function across the multi-wall structure. These effects, when combined together, form a convincing explanation of puzzling experiments in which non-integer values of conductance have been found in multi-wall nanotubes[13]. To arrive at this quantitative description of the experiments, we have explored several possibilities regarding on the nature of the nanotube/metal interfaces. Only those calculations in which the outermost tube is in direct contact with the gold electrode showed good agreement with the experiments.

ACKNOWLEDGEMENTS

This work has been done in collaboration with the group of Prof. J.H. Jefferson at DERA Malvern, who is kindly acknowledged. SS acknowledges also the financial support by the DERA and the MSU-CMPT visitor fund. YKK and DT acknowledge financial support by the Office of Naval Research under Grant Number N00014-99-1-0252.

REFERENCES

1. S. Iijima, Nature **354**, 56 (1991).
2. For a general review, see M.S. Dresselhaus, G. Dresselhaus, and P.C. Eklund, *Science of Fullerenes and Carbon Nanotubes* (Academic Press Inc., 1996 San Diego), and references therein.
3. S. Iijima and T. Ichihashi, Nature **363**, 603 (1993).
4. D.S. Bethune, C.H. Kiang, M.S. de Vries, G. Gorman, R. Savoy, J. Vazquez, R. Beyers, Nature **363**, 605 (1993).
5. J.W. Mintmire, B.I. Dunlap, and C.T. White, Phys. Rev. Lett. **68**, 631 (1992).
6. R. Saito, M. Fujita, G. Dresselhaus, and M.S. Dresselhaus, Appl. Phys. Lett. **60**, 2204 (1992).
7. N. Hamada, S. Sawada, and A. Oshiyama, Phys. Rev. Lett. **68**, 1579 (1992).
8. L. Chico, L.X. Benedict, S.G. Louie and M.L. Cohen, Phys. Rev. B **54**, 2600 (1996), W. Tian and S. Datta, *ibid.* **49**, 5097 (1994), M.F. Lin and K.W.-K. Shung, *ibid.* **51**, 7592 (1995).
9. R. Landauer, Phil. Mag. **21**, 863 (1970).
10. S.J. Tans, M.H. Devoret, H. Dai, A. Thess, R.E. Smalley, L.J. Geerligs, C. Dekker, Nature **386**, 474 (1998).
11. M. Bockrath, D. H. Cobden, P. L. McEuen, N. G. Chopra, A. Zettl, A. Thess, R. E. Smalley Science **275**, 1922 (1997).
12. C. Dekker, Physics Today May 1999, 22 (1999).
13. S. Frank, P. Poncharal, Z.L. Wang, and Walt A. de Heer, Science **280**, 1744 (1998).
14. T. Ando, T. Nakanishi, J. Phys. Soc. Jpn. **67**, 1704 (1998).
15. C.T. White, T.N. Todorov, Nature **393**, 240 (1998).

16. Riichiro Saito, G. Dresselhaus, and M.S. Dresselhaus, J. Appl. Phys. **73**, 494 (1993).
17. Ph. Lambin, L. Philippe, J.C. Charlier, and J.P. Michenaud, Comput. Mater. Sci. **2**, 350 (1994).
18. Young-Kyun Kwon and David Tománek, Phys. Rev. B **58**, R16001 (1998).
19. P. Delaney, H.J. Choi, J. Ihm, S.G. Louie, and M.L. Cohen, Nature **391**, 466 (1998).
20. Young-Kyun Kwon, Susumu Saito, and David Tománek, Phys. Rev. B **58**, R13314 (1998).
21. D. Tománek and Michael A. Schluter, Phys. Rev. Lett. **67**, 2331 (1991).
22. S. Sanvito, C.J. Lambert, J.H. Jefferson, A.M. Bratkovsky, Phys. Rev. B **59**, 11936 (1999).
23. S. Sanvito, C.J. Lambert, J.H. Jefferson, A.M. Bratkovsky, J. Phys. C: Condens. Matter. **10**, L691 (1998).
24. M. Schluter, M. Lannoo, M. Needels, G.A. Baraff, and D. Tománek, Phys. Rev. Lett. **68**, 526 (1992).
25. J.-C. Charlier, X. Gonze, and J.-P. Michenaud, Europhys. Lett. **28**, 403 (1994); M.C. Schabel and J.L. Martins, Phys. Rev. B **46**, 7185 (1992).
26. F. Taddei, S. Sanvito, C.J. Lambert, J.H. Jefferson, Phys. Rev. Lett. **82**, 4938 (1999).
27. M. Büttiker, Y. Imry, R. Landauer, S. Pinhas, Phys. Rev. B **31**, 6207 (1985).
28. S. Sanvito, C.J. Lambert, J.H. Jefferson, to appear in Phys. Rev. B, and also cond-mat/9903381
29. C.J. Lambert, V.C. Hui, S.J. Robinson, J. Phys. C: Condens. Matter. **5**, 4187 (1993).

Orientational Melting in Carbon Nanotube Ropes

Young-Kyun Kwon and David Tománek

Department of Physics and Astronomy, and Center for Fundamental Materials Research, Michigan State University, East Lansing, Michigan 48824-1116

(Received 24 August 1999)

Using Monte Carlo simulations, we investigate the possibility of an orientational melting transition within a "rope" of carbon nanotubes. When twisting nanotubes bundle up during the synthesis, orientational dislocations or twistons arise from the competition between the anisotropic intertube interactions, which tend to align neighboring tubes, and the torsion rigidity that tends to keep individual tubes straight. We map the energetics of a rope containing twistons onto a lattice gas model and find that the onset of a free "diffusion" of twistons, corresponding to orientational melting, occurs at $T_{OM} \gtrsim 160$ K.

PACS numbers: 61.48.+c, 61.50.Ah, 73.61.Wp, 81.10.Aj

Since their first successful synthesis in bulk quantity [1], "ropes" of single-wall carbon nanotubes have been in the spotlight of nanotube research. Recent experimental data indicate that carbon nanotube ropes exhibit an unusual temperature dependence of conductivity [2], magnetoresistance [3], and thermoelectric power [4]. Several physical phenomena have been suggested to cause the intriguing temperature dependence of conductivity behavior, such as twistons [5], orientational melting [6,7], weak localization [8], and Kondo effect [3]. The opening of a pseudogap near E_F in a bundle composed of (10, 10) tubes has been postulated to result from breaking the D_{10h} tube symmetry by the triangular lattice [6,9].

Nanotubes [10] and C_{60} "buckyball" molecules [11,12] are similar inasfar as their interaction is weakly attractive and nearly isotropic when condensing to a solid. The small anisotropy of the C_{60} intermolecular potential drives the solid to an orientationally ordered simple-cubic lattice with four molecules per unit cell at low temperatures [13]. Only at $T \gtrsim 249$ K does the C_{60} solid undergo a transition to a face-centered cubic lattice. As confirmed by ^{13}C nuclear magnetic resonance [14], this is an order-disorder phase transition, with C_{60} molecules spinning freely and thus becoming equivalent above 249 K. Unlike the C_{60} solid, very little is known about the equilibrium structure of bundled nanotubes beyond the fact that they form a triangular lattice [1]. In particular, nothing is known about the equilibrium orientation of the tubes within a rope. More intriguing still is the possibility of an orientational melting transition associated with the onset of orientational disorder within a rope.

In the following, we calculate the potential energy surface and the orientational order of straight and twisted tubes within a rope. We further postulate that realistic nanotube ropes contain orientational dislocations that have been frozen in as the tubes formed ropes at a finite temperature, the same way as dislocations are known to form in crystals. We map the energetics of a rope with dislocations onto a lattice gas model and find that the onset of orientational disorder, corresponding to a free axial diffusion of twistons, should occur at $T_{OM} \gtrsim 160$ K in ropes containing various types of nanotubes.

In order to determine the orientational order and the rotational motion of tubes in a rope, we need to describe both the intertube interaction and the torsional strain within the individual tubes. Since the anisotropic part of the intertube interaction in a rope is weak and local, it can be well described by pairwise intertube (*not* interatomic) interactions. To describe the interaction between tubes in a rope as a function of their orientation, we use the parametrized linear combination of atomic orbitals (LCAO) formalism with parameters determined by *ab initio* results for simpler structures [15]. This technique has been successfully used to explain superconductivity arising from interball interactions in the doped C_{60} solid [16], the opening of a pseudogap near E_F in a (10, 10) nanotube rope [6,7], and the opening and closing of four pseudogaps during the librational motion of a (5,5)@(10, 10) double-wall tube [17]. The total energy functional consists of a nonlocal band structure energy term and of pairwise interatomic interactions describing both the closed-shell repulsion and the long-range van der Waals attraction. A smooth cutoff function [18] has been implemented to keep the total energy continuous as the neighbor topology changes while tubes rotate. This energy functional correctly reproduces the exfoliation energy, the interlayer distance, and the C_{33} modulus of hexagonal (AB) graphite, as well as the energy barrier for interlayer sliding, corresponding to the energy difference between AB and AA stacked graphite.

To determine the interaction between a pair of aligned (n, n) nanotubes, we first define the orientational angles φ_1 and φ_2 for these tubes by the azimuthal angle of the center of a particular bond with respect to the connection line between adjacent nanotube axes, as shown in Fig. 1(a). For each (φ_1, φ_2) pair, we calculate the intertube interaction using a fine mesh of 800 k points sampling the one-dimensional irreducible Brillouin zone. Because of the high symmetry of the system, the interaction energy $\Delta E(\varphi_1, \varphi_2)$ is periodic in φ_1 and φ_2, with a period $\Delta\varphi = 360°/n$. With the simple variable

0031-9007/00/84(7)/1483(4)$15.00

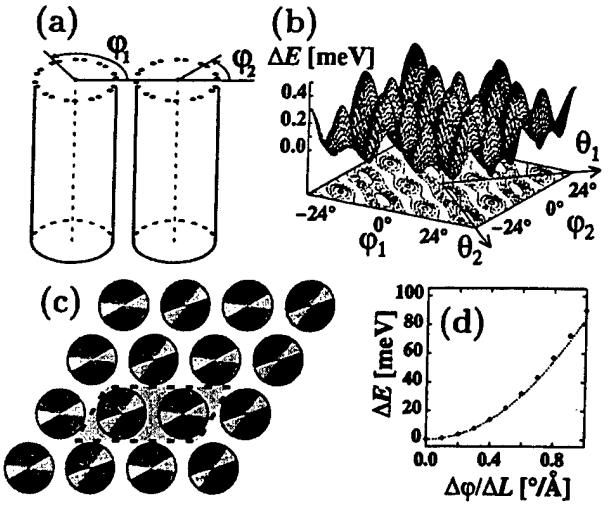

FIG. 1. (a) Definition of the orientational angles φ_1 and φ_2 of two aligned nanotubes. (b) Interaction energy *per atom* between two (10, 10) carbon nanotubes at equilibrium distance as a function of the tube orientations. (c) Top view of the equilibrium structure of bundled interacting nanotubes, with a two-tube unit cell. (d) Torsion energy *per atom* within an individual (10, 10) nanotube.

transformation $\theta_1 = \varphi_1 + \varphi_2$ and $\theta_2 = \varphi_1 - \varphi_2$, the interaction energy ΔE can be simply expanded in harmonic functions of θ_1 and θ_2, with the same period $\Delta\theta = 360°/n$. The resulting potential energy surface, displayed in Fig. 1(b) for a pair of (10, 10) nanotubes, shows a maximum corrugation of only $\Delta E_{max} \approx 0.5$ meV/atom.

The equilibrium geometry of bundled (10, 10) nanotubes can be found by optimizing the total energy E with respect to the orientations of all individual tubes [19]. Because of the high level of orientational frustration in a triangular lattice of (10, 10) nanotubes with D_{10h} symmetry, the potential energy surface $E(\varphi_1, \varphi_2, \ldots)$ is very complex. We determine the global minimum of $E(\varphi_1, \varphi_2, \ldots)$ by applying the Metropolis Monte Carlo algorithm to an infinite system of straight nanotubes in a $(2 \times 2), (4 \times 4), \ldots, (8 \times 8)$, superlattice, with unit cells containing between 4 and 64 nanotubes. Independent of the unit cell size, we find that the global energy minimum corresponds to a two-dimensional oblique lattice with two tubes per unit cell, shown in Fig. 1(c). In equilibrium, the orientations φ_1, φ_2 of the two tubes within this unit cell satisfy the condition $\theta_1 = \varphi_1 + \varphi_2 = 12°$ and $\theta_2 = \varphi_1 - \varphi_2 \approx \pm 9.71°$ within the range $-18° \leq \theta < +18°$.

Even though the energy barrier $\Delta E \lesssim 0.5$ meV per atom for a free rotation in a pair of tubes, shown in Fig. 1(b), appears small, the barrier to rotate an entire tube, that is completely straight and rigid, is unsurmountable. In the following, we postulate that tube rotations in a rope are still possible in view of the finite, albeit large value of the tube torsion constant. To determine the torsional strain within an isolated, twisted (10, 10) tube, we combined the LCAO method mentioned above with the recursion technique [20]. This approach has been used success to describe the dynamics of fullerene melting [21] growth of multiwall nanotubes [22], and the dynami a "bucky-shuttle" memory device [23]. Our calculat shown in Fig. 1(d), suggest that the torsional ener harmonic up to a strain of $\Delta\varphi/\Delta L \approx 1°/\text{Å}$. Within harmonic regime, the torsional energy *per atom* ca well represented by the expression $\Delta E = \kappa(\Delta\varphi/\Delta$ with $\kappa \approx 2.58 \times 10^{-2}$ meV/(rad^2/Å^2). Since the n ber of atoms in the tube is proportional to the total length ΔL_{tot}, the total torsional energy of the tub inversely proportional to the total tube length for a g total twist angle $\Delta\varphi_{tot}$, and hence becomes vanishi small for a long tube.

To study the possibility of orientational melting nanotube rope, we first consider an unrealistic model tem of bundled (10, 10) tubes consisting of torsio decoupled axial segments of 20 atoms, resembling "rings" or "disks." The interaction between two adja disks in neighboring tubes is the value ΔE of Fig. multiplied by the number of atoms in the disk. Abs of axial coupling makes this system equivalent to a dimensional triangular lattice of disks with one (orie tional) degree of freedom per disk. Results of Monte C simulations of orientational melting in (2×2), $(4 \times$ and (6×6) superlattices with 4, 16, and 36 such t per unit cell, respectively, are shown in Fig. 2. To en proper phase space sampling even at low temperat each data point represents an ensemble average taken $\gtrsim 10^5$ Monte Carlo steps *per degree of freedom*. Re for the temperature dependence of the total energy pe gree of freedom, shown in Fig. 2(a), suggest that an entational melting transition should occur at $T_{OM} \approx 5$ This transition becomes more pronounced with increa unit cell size in the superlattice. The sharp peak in temperature dependence of the corresponding specific data, shown in Fig. 2(b), suggests this phase transitio

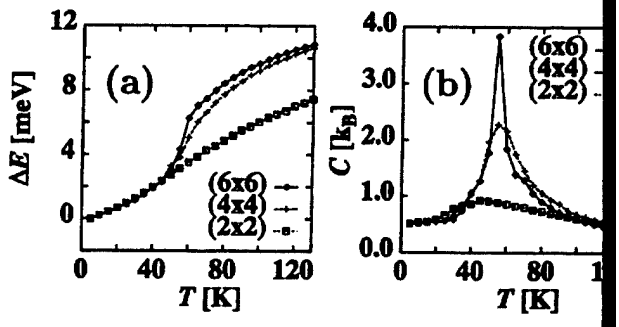

FIG. 2. Temperature dependence of (a) the total energy and (b) the specific heat C *per degree of freedom* in m $(m \times m)$ superlattices of interacting (10, 10) nanotubes *zero torsional rigidity*. Each nanotube is modeled by a c of torsionally decoupled, rigid segments ("disks") contai twenty atoms, each representing one orientational degre freedom. In this model system, orientational melting oc at $T \gtrsim T_{OM} \approx 55$ K.

be of first order. At low and at high temperatures, the specific heat per degree of freedom approaches the classical value $C = 0.5k_B$.

To address orientational melting in a realistic (10, 10) nanotube rope, we add the proper torsional coupling between the disks, according to our results in Fig. 1(d). Monte Carlo simulations analogous to those described above showed no indication that initially straight nanotubes would start to perform a "ratcheting twisting motion," corresponding to orientational melting in the rope, up to 4000 K when individual nanotubes should disintegrate structurally. We have also found that the large mass and high bond stiffness essentially inhibit any global or local axial sliding motion within the rope below this high structural melting temperature.

The key to the understanding of orientational melting is to consider the energetics and dynamics of orientational dislocations in the system. Consider two nanotubes which, under synthesis conditions, show a total twist $\Delta\varphi_{\text{tot}} \gtrsim 36°$ over the entire tube length, at the negligible cost in total energy of $\approx$0.1 eV for a 100 μm long tube. As these tubes bundle up during annealing, at least two orientationally aligned domains form within the tube pair, separated by an orientational dislocation. Similar twists of up to 1°/nm, associated with such orientational dislocations, have been recently observed by electron diffraction in nanotube ropes [24]. Such solitons may move rather freely along the tube axes, but cannot be annihilated if the paired tubes are infinitely long, or if they bundle up to a double torus [25].

The equilibrium geometry of these frozen-in twistons is given by the competition between the anisotropic intertube interactions, which tend to align neighboring tubes, and the torsion rigidity that tends to keep individual tubes straight. The formation of twistons is a general phenomenon that is independent of tube chirality. The energetics and dynamics of twistons is well represented by mapping the Frenkel-Kontorova model onto the orientational degrees of freedom of a triangular lattice of chains. In bundled (10, 10) nanotubes, the orientation $\varphi(z)$ of individual tube layers near the dislocation is well reproduced by the function $\varphi(z) = \varphi_0 + \Delta\varphi\{1 + \exp[(z - z_0)/w]\}^{-1}$, with the typical values $\Delta\varphi \approx 36°$ and $w \approx 30$ Å. Such dislocations, which can be either left or right handed, show a total twist of 36° that extends across a very long tube segment of $\approx$250 Å in the axial direction, thus resulting in a very small twisting deformation of only $\approx$0.18° per tube layer.

The energy cost of $\Delta E \approx 5$ eV to create such a twiston, given by the energy difference between ropes containing one or no dislocation, is relatively high. Whereas this energy makes a spontaneous creation of twistons or left-/right-handed twiston pairs within a rope unlikely even at high temperatures, there are only two other scenarios to change their total number. Twistons could "slide off" the end, thus negligibly modifying the total number of twistons in very long ropes. The other scenario involves the annihilation of left-/right-handed twiston pairs which is most likely to occur just after synthesis, as no activation energy is often associated with this process. Since the number of left- and right-handed twistons is likely to differ, the dynamics will eventually be dominated by the remaining twistons of one handedness. For the pairs of left-/right-handed twistons separated by large distances, presence of orientational dislocations in adjacent tubes will impose an activation barrier onto its annihilation and reduce the probability of this process.

In the following, we thus focus our attention on a system with a constant number of twistons of the same handedness and the onset of their mobility. The dynamics of the entire system is limited to a subspace of the configurational space, where the number of twistons on each tube is fixed. We notice that the axial motion of a twiston corresponds to a finite tube rotation in that given segment, and that the energetics of a rope containing twistons can be mapped onto a lattice gas model of twistons moving along individual tubes. The small potential energy barriers associated with an "up"- and a "down"-moving twiston passing each other in adjacent tubes depend on the orientation of the other surrounding tubes, and are evaluated by the total energy expression above. We correlate the onset of orientational melting in the rope with depinning and a completely free "diffusion" of twistons within the tubes.

Results of a Monte Carlo simulation for the orientational melting transition in a (10, 10) nanotube rope containing twistons are presented in Fig. 3. We consider a (6×6) superlattice of nanotubes with a fixed number of orientational dislocations on each tube. The energy of this system is given by the positions of these twistons within each periodically repeated unit cell containing 36 tubes with 5000 layer segments discretizing the axial direction. This system with nominally 180 000 degrees of freedom is mapped onto a lattice gas of twistons in the following way. Out of the 36 tubes per unit cell, we select twelve nonadjacent tubes, each containing a single twiston that can move axially. The remaining tubes in the unit cell have eight such orientational dislocations frozen in. Their positions are equally spaced over the tube axes, but axially offset in adjacent tubes.

The temperature dependence of the total energy of this classical system, shown in Fig. 3(a), shows a slope that is initially small close to $T = 0$, then becomes large within the temperature range $0 < T \lesssim 500$ K, and finally becomes small. The corresponding specific heat data, shown in Fig. 3(b), begin with the classical value $C = 0.5k_B$ at low temperatures and peak at $T_{\text{OM}} \gtrsim 160$ K. We have observed that ropes consisting of different types of tubes, such as (10, 10) and (9, 9), with different numbers of twistons, show a very similar behavior in spite of their significantly different ground state geometries and potential energy surface topologies. The nature of the orientational melting transition at T_{OM} is illustrated in Fig. 3(c). The two snapshots of the geometry, taken at $T = 500$ K,

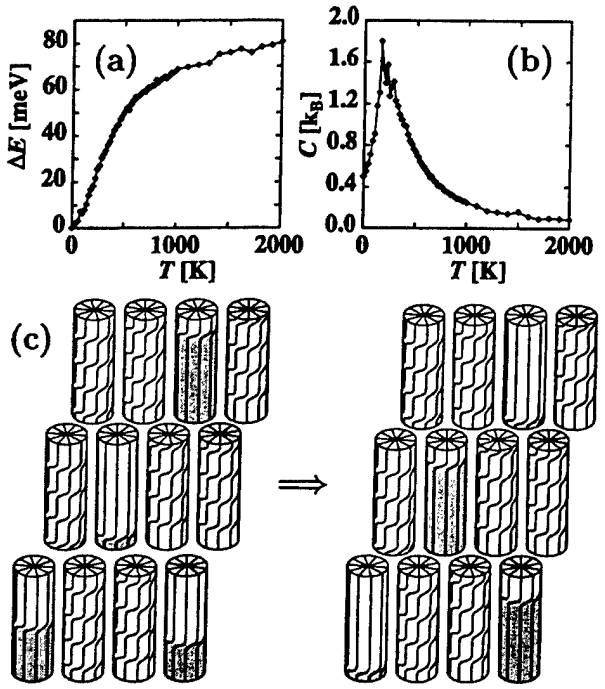

FIG. 3. Temperature dependence of (a) the total energy ΔE and (b) the specific heat C *per degree of freedom* in a realistic rope consisting of interacting tubes of finite rigidity. (c) Illustration of the microscopic process of orientational melting in an exaggerated perspective. The two views depict the position of orientational dislocations at different points in time at $T = 500$ K. The axial motion of the twistons, indicating orientational melting, is highlighted by the changing grey-shaded sections in four of the tubes.

indicate that above $T \approx T_{OM}$, frozen-in twistons become depinned and diffuse relatively freely along the tube axes, as indicated by the changing gray-shaded sections in the tubes. Since these twistons are important scattering centers for electrons, their depinning may significantly affect the transport in these one-dimensional systems at $T \approx T_{OM}$ that may play the role of T^* in Ref. [2].

In summary, using Monte Carlo simulations, we have investigated the possibility of an orientational melting transition within a "rope" of carbon nanotubes. We postulate that during the synthesis, as twisting nanotubes bundle up, orientational dislocations or twistons arise from the competition between the anisotropic intertube interactions, which tend to align neighboring tubes, and the torsion rigidity that tends to keep individual tubes straight. We have mapped the energetics of a (10, 10) nanotube rope containing such twistons onto a lattice gas model and find that the onset of a free "diffusion" of twistons, corresponding to orientational melting, should occur at $T_{OM} \gtrsim 160$ K.

We acknowledge fruitful discussions with Marcel den Nijs and Jean S. Chung. This work was supported by the Office of Naval Research and DARPA under Grant No. N00014-99-1-0252.

[1] A. Thess *et al.*, Science **273**, 483 (1996).
[2] R. S. Lee *et al.*, Nature (London) **388**, 255 (1997); J. E. Fischer *et al.*, Phys. Rev. B **55**, R4921 (1997).
[3] G. T. Kim *et al.*, Phys. Rev. B **58**, 16 064 (1998).
[4] J. Hone *et al.*, Phys. Rev. Lett. **80**, 1042 (1999); M. L. Tian *et al.*, Phys. Rev. B **58**, 1166 (1998).
[5] C. L. Kane *et al.*, Europhys. Lett. **41**, 683 (1998).
[6] Young-Kyun Kwon, Susumu Saito, and David Tománek, Phys. Rev. B **58**, R13 314 (1998).
[7] Young-Kyun Kwon *et al.*, J. Mater. Res. **13**, 2363 (1998).
[8] M. S. Fuhrer *et al.*, Solid State Commun. **109**, 105 (1999).
[9] P. Delaney *et al.*, Nature (London) **391**, 466 (1998).
[10] S. Iijima, Nature (London) **354**, 56 (1991).
[11] H. W. Kroto *et al.*, Nature (London) **318**, 162 (1985).
[12] W. Krätschmer *et al.*, Nature (London) **347**, 354 (1990).
[13] P. A. Heiney *et al.*, Phys. Rev. Lett. **66**, 2911 (1991).
[14] C. S. Yannoni *et al.*, J. Phys. Chem. **95**, 9 (1991); R. Tycko *et al.*, *ibid.* **95**, 518 (1991).
[15] D. Tománek and M. A. Schluter, Phys. Rev. Lett. **67**, 2331 (1991).
[16] M. Schluter *et al.*, Phys. Rev. Lett. **68**, 526 (1992).
[17] Young-Kyun Kwon and David Tománek, Phys. Rev. B **58**, R16 001 (1998).
[18] We use the Fermi-Dirac expression $\{1 + \exp[(d - d_c)/d_w]\}^{-1}$, with $d_c = 3.87$ Å and $d_w = 0.2$ Å, as a smooth cutoff function of distance d for both the hopping integrals and pairwise interactions.
[19] We define the orientation φ_i of tube i in the rope with respect to the x axis, taken as one of the bond directions $\mathbf{d}_{ij}$ to its adjacent tube j. To determine the interaction of this tube with any of its other five neighboring tubes k, the orientational angles φ_i and φ_k need to be incremented by a multiple of 12° to account for the bond rotation from $\mathbf{d}_{ij}$ to $\mathbf{d}_{ik}$ in the triangular lattice.
[20] W. Zhong, D. Tománek, and G. F. Bertsch, Solid State Commun. **86**, 607 (1993).
[21] S. G. Kim and D. Tománek, Phys. Rev. Lett. **72**, 2418 (1994).
[22] Young-Kyun Kwon *et al.*, Phys. Rev. Lett. **79**, 2065 (1997).
[23] Young-Kyun Kwon, David Tománek, and Sumio Iijima, Phys. Rev. Lett. **82**, 1470 (1999).
[24] Annick Loiseau (private communication).
[25] R. Martel, H. R. Shea, and Ph. Avouris, Nature (London) **398**, 299 (1999).

Microscopic Formation Mechanism of Nanotube Peapods

Savas Berber, Young-Kyun Kwon,* and David Tománek

Department of Physics and Astronomy, Michigan State University, East Lansing, Michigan 48824-1116

(Received 11 January 2002; published 18 April 2002)

Using molecular dynamics calculations, we investigate the absorption of a C_{60} molecule in a (10, 10) nanotube either through the open end or a large defect in the tube wall as possible scenarios for the hierarchical self-assembly of $(C_{60})_n$@(10, 10) "nano-peapods." We find the absorption through a defect to be significantly more efficient than the end-on absorption. This process occurs most likely within a narrow launch velocity range for the fullerene that agrees well with the observed optimum temperature window for peapod formation.

DOI: 10.1103/PhysRevLett.88.185502 PACS numbers: 61.48.+c, 68.70.+w, 81.05.Tp

A new type of self-assembled hybrid structures called "nano-peapods," consisting of fullerene arrays inside single-wall carbon nanotubes, have recently been reported [1–6]. Potential uses of nano-peapods range from nanometer-sized containers for chemical reactions [4] to data storage [7], and possibly high temperature superconductors [8]. Even though the encapsulation of fullerenes (such as C_{60}) in nanotubes is favorable on energetic grounds [7,9,10] and occurs rapidly by exposing nanotubes to sublimed fullerenes [1–5], virtually nothing is known about how the fullerenes enter the nanotubes when forming the nano-peapods.

A statistical mechanics approach, which considers only the initial and final states, describes only the equilibrium state after an infinite time [10]. It can say nothing about the likelihood of fullerene encapsulation in a finite time, as it ignores any activation barriers along the reaction path. Only trajectory calculations based on the complex potential energy surface of the system can provide detailed answers about the dynamics and intermediate steps involved in the formation of nano-peapods.

An important current controversy involves the questions, whether fullerenes enter through the open ends of perfect nanotubes or whether defects in the wall play an important role as entry channels. The extremely high filling ratio of up to 100% [5] appears hard to achieve even within a few days if the only entry channels are the two open ends of each tube. In such a case, the fullerene kinetics is limited and even a single impurity may block an entry channel. On the other hand, only a few openings in the tube walls have been observed in high-resolution transmission electron microscopy (HRTEM) images [11]. Another important question, which a statistical approach cannot answer, is whether the encapsulation process, be it through an open end or through a defect, occurs directly from the gas phase or involves a diffusive motion along the wall.

Here, we present a large-scale simulation for the entry of a C_{60} molecule into a (10, 10) carbon nanotube via different scenarios, illustrated in Fig. 1. We consider the encapsulation through the open end of a free-standing nanotube [Fig. 1(a)] and through the open end of a nanotube bundle [Fig. 1(b)]. These scenarios are compared to the C_{60} entry through a defect, in our model a large opening in the nanotube wall [Fig. 1(c)] [12]. Formation of such large defects may occur, we believe, during the harsh purification process that is a necessary prerequisite for peapod formation [4]. By assuming that the C_{60} adsorbs on the wall prior to encapsulation, we take advantage of the enhanced probability of the fullerene to find an entry channel into a nanotube within the lower-dimensional phase space probed by the C_{60} diffusing along the wall, as compared to a fullerene in the gas phase. Our calculations elucidate not only which of these processes is most likely but also the optimum temperature window for the peapod formation.

We calculate the potential energy of the fullerene-nanotube system using an electronic Hamiltonian that was used successfully to describe the formation of multiwall nanotubes [13] and the dynamics of a "bucky-shuttle" device [7]. This approach describes accurately not only the covalent bonding within the graphitic substructures but also the modification of the fullerene-nanotube interaction due to the interwall interaction and possibly the presence of unsaturated bonds at defect sites or tube edges [14]. We find the use of an electronic Hamiltonian to be required in this system, as analytical bond-order potentials do not describe the rehybridization at defect sites and tube ends with sufficient precision. Once the quantum nature of the interatomic interactions has been taken into account, the trajectories of the heavy carbon atoms are described reliably in a classical manner.

In Fig. 1 we present schematic views of the encapsulation scenarios together with the calculated potential energy surfaces in the x-y plane that contains the tube axes, the center of the C_{60} molecule, and the defect. The tube structures underlying the potential energy surfaces have been globally optimized. They reflect the relaxation at the open end of the tube and the edges of a large defect in the tube wall, representing an extended vacancy formed during the harsh purification process [15].

When following an "optimum" trajectory starting outside the tube, a C_{60} molecule may first physisorb on the outer wall, thus gaining $\approx$0.07 eV. Our energy contour plots in Fig. 1 suggest that the fullerene diffuses virtually freely along the tube wall. Since the adsorption potential

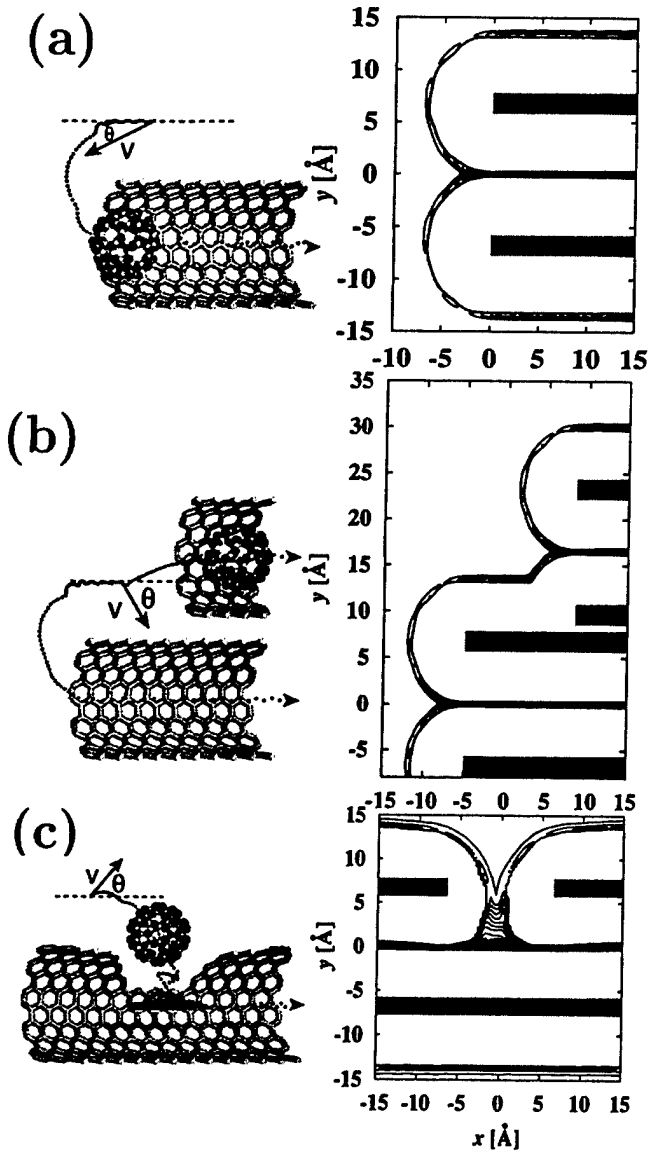

FIG. 1. Perspective views (left panels) and potential energy surfaces (right panels) for the encapsulation of a C_{60} molecule in a (10, 10) nanotube under different scenarios. The dotted lines indicate possible C_{60} trajectories, characterized by the launch velocity v and launch angle θ with respect to the tube axis. The potential energy surfaces are shown in the x-y plane containing the center of the fullerene and the tube axis x. Adjacent energy contours are separated by 0.01 eV; the position of the tube walls is indicated by the solid gray areas. The scenarios involve C_{60} encapsulation through (a) the open end of an isolated (10, 10) nanotube, (b) the open end of bundled (10, 10) nanotubes, and (c) a large opening in the (10, 10) nanotube wall, centered in the x-y plane.

is relatively shallow, the fullerene's angular velocity along the perimeter is limited by requiring the centrifugal force not to exceed a critical value for radial detachment. Consequently, the fullerene should follow a near-axial helical trajectory within a narrow 1D channel in the x-y plane during its diffusive motion along the tube surface. Because of the large inertia of the C_{60} molecule and the absence of corrugations along the potential energy surface, virtually no rotations are excited as the fullerene slides along the tube wall. Upon entering the nanotube, the C_{60} gains an additional 0.36 eV [16].

The absence of activation barriers for all fullerene encapsulation scenarios depicted in Fig. 1 is surprising for two reasons. First, it suggests that the strong attraction to the undercoordinated atoms at the tube or defect edges does not trap the fullerene, but only modifies the entry channel without hindering the encapsulation [14]. Second, it leaves the origin of the observed optimum temperature of ≈400 °C for C_{60} encapsulation an open question.

The likelihood of C_{60} encapsulation depends on its initial conditions and the topology of the entire potential energy surface, as suggested by the sample trajectories in Fig. 1. In our molecular dynamics simulations, we initially placed the C_{60} molecule at equilibrium radial distance from the tube. We then calculated C_{60} trajectories in the x-y plane using time steps of 5×10^{-16} s, by varying the launch speed v from 0–300 m/s in 1 m/s increments and the launch angle θ with respect to the tube axis from $-90°$ to $+90°$ in 1° increments. The calculation of all 54 000 trajectories for each encapsulation pathway would not be computationally feasible without approximations. We described the fullerene-nanotube interaction by the potential energy surfaces presented in Fig. 1, thus implying that both the C_{60} and the nanotube are structurally rigid.

For each set of initial conditions, we found that the ultimate outcome of each trajectory regarding encapsulation is decided within less than 10^6 time steps. We also found that all physically interesting phenomena occur within a velocity range between 50–200 m/s, the lower bound marking the onset of C_{60} mobility along the tube. The upper end of this range corresponds to high temperatures, at which fragmentation and tube fusion are to be expected. Consequently, we will discuss the encapsulation under the specific scenarios within this velocity range.

The outcome of the encapsulation process through the end of an isolated nanotube, depicted in Fig. 1(a), is shown in Fig. 2. The scatter diagram of Fig. 2(a) condenses the information of all trajectories regarding encapsulation. A black mark denotes a trajectory with a launch velocity and angle that leads to encapsulation, such as that shown in Fig. 2(b). Similarly, a white field marks failed encapsulation, such as depicted in the trajectory of Fig. 2(c). Consequently, the fraction of the dark area is proportional to the probability of encapsulation. The scatter diagram, dominated by white color, suggests that encapsulation through the open end of an isolated nanotube should be very rare. The main reason is the relatively narrow and shallow channel in the potential energy surface of Fig. 1(a), which the fullerene must follow to reach the inside of the tube. At very low velocities, the fullerene gets trapped in one of the shallow potential energy wells outside the tube wall. At too high velocities, on the other hand, the C_{60} is incapable of following the tight "U turn" in the potential energy surface, as illustrated in Fig. 2(c).

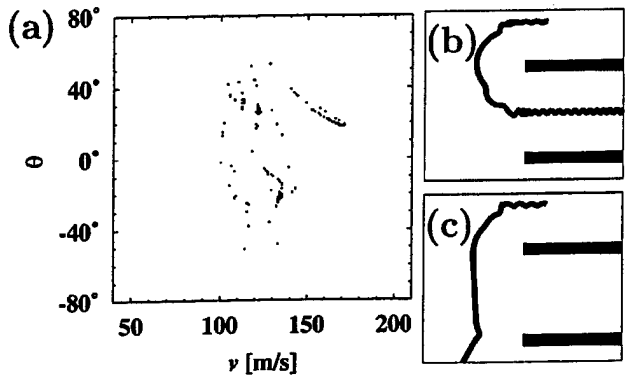

FIG. 2. (a) Scatter diagram showing the probable outcome of a C_{60} encapsulation through the open end of an isolated (10, 10) nanotube, as a function of the fullerene launch velocity v and launch angle θ. Only initial conditions leading to a successful encapsulation are marked in black in the scatter diagram. A sample successful encapsulation trajectory is depicted in (b), and an unsuccessful trajectory in (c).

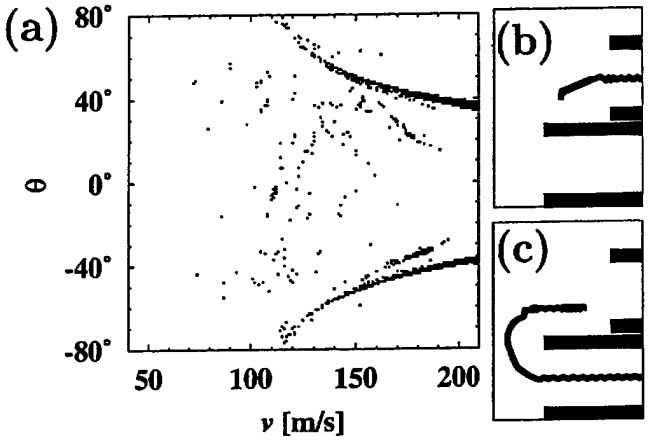

FIG. 3. Scatter diagram analogous to Fig. 2, but for bundled (10, 10) nanotubes. Sample trajectories describing successful encapsulation are depicted in (b) and (c).

In view of the low estimated probability of encapsulation through the end of an isolated tube, we considered next the analogous process at the end of a nanotube bundle, consisting of (10, 10) tubes with an interwall separation of 3.4 Å, depicted in Fig. 1(b). As suggested by the two successful trajectories in the left panel of Fig. 1(b), the more complex potential energy surface for this system increases the number of entry channels, thus enhancing the probability of encapsulation. The results of our trajectory calculations, summarized in the scatter diagram of Fig. 3(a), indeed show a somewhat higher encapsulation probability as compared to the single-tube scenario. In comparison to Fig. 2(a), we observe two solid dark regions for velocities beyond $\approx$150 m/s and $\theta \approx \pm 40°$. These regions correspond to trajectories that first follow the wall of one tube and continue inside the neighboring tube, as shown in Fig. 2(b). This new channel is relatively narrow due to the "S" shape of the tube-fullerene interaction potential well, shown in the right-hand panel of Fig. 1(b). As in the case of an isolated tube, trajectories involving a "U turn", depicted in Fig. 3(c), form an additional entry channel, responsible for the rare encapsulation events in the remaining region of the scatter diagram. We conclude that, even in the case of a bundle, the probability of encapsulation through the end is rather low.

The outcome of the encapsulation process through a large opening in the side wall of the (10, 10) nanotube, depicted in Fig. 1(c), is shown as a scatter diagram in Fig. 4(a). In comparison to Figs. 2(a) and 3(a), the dark area in the scatter diagram of Fig. 4(a) is substantially larger, yielding a 30-fold increase of the cross section for the C_{60} entry. In the following, we focus on the encapsulation through the large wall opening as the most likely process leading to peapod formation.

The scatter diagram of Fig. 4(a) shows a complex pattern consisting of large areas corresponding to the C_{60} entering the tube. Among these events, we have marked those trajectories leading to a definitive encapsulation, as depicted in Fig. 4(b), in red. The "green" and "blue" trajectories, shown in Figs. 4(c) and 4(d), involve a temporary entry of the C_{60} molecule into the tube. In that case, after multiple scattering events, the fullerene may eventually escape in the backward ("green event") or the forward direction ("blue event"). Since such multiple scattering processes are chaotic, the blue and green events are homogeneously intermixed rather than separated into specific regions in Fig. 4(a).

To interpret the complex pattern in the scatter diagram of Fig. 4(a), we took a closer look at the individual trajectories. For launch velocities below 50 m/s, the C_{60} becomes trapped in one of the local minima and never reaches the

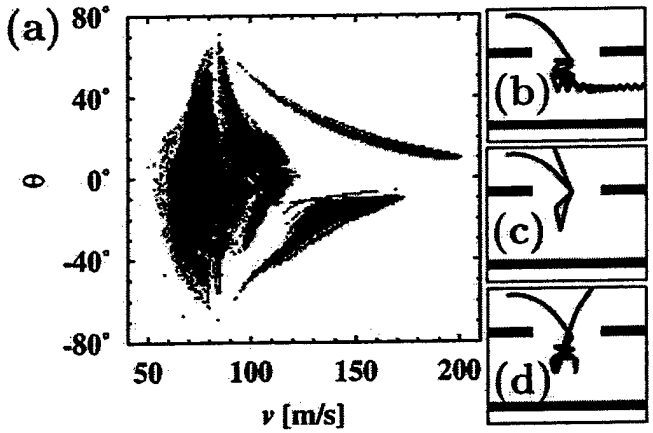

FIG. 4 (color). (a) Scatter diagram showing the probable outcome of a (10, 10) encapsulation through a large opening in the wall of a (10, 10) nanotube. Initial conditions that do not lead to encapsulation are marked in white. Those leading to encapsulation, with a sample trajectory shown in (b), are marked in red. Initial conditions and corresponding trajectories involving a temporary entry of the fullerene into the tube are shown in green if the final velocity has a negative x component (c) and in blue if the final velocity has a positive x component (d).

defect. The highest probability of a successful encapsulation with an axial launch ($\theta = 0°$) is achieved at velocities ranging from 50 m/s $\lesssim v \lesssim$ 120 m/s. Axial launches with velocities exceeding $\approx$120 m/s overshoot the hole. C_{60} encapsulation is still possible for fast launches, but requires large launch angles and involves one or several radial reflections off the wall, as shown schematically in Fig. 1(c). For a given nonzero launch angle, the largest launch velocity allowing the fullerene to enter the tube involves a straight trajectory with no radial reflections. This is the case for the trajectories depicted in Figs. 4(b)–4(d), for launch angles $\theta \approx 10°$ and $v \lesssim 200$ m/s. At lower launch velocities, a radial reflection from the tube wall causes the fullerene to overshoot the hole. As the velocity is reduced further, the point of first radial reflection is shifted closer to the launch site, allowing the fullerene to successfully enter the nanotube again. At a constant launch angle such as $\theta = 40°$, we can distinguish up to seven alternating regions associated with "successful" and "unsuccessful" trajectories. Each of these contiguous regions in Fig. 4(a) can be characterized by the number of radial reflections between the launch site and the hole edge.

Maybe our most important result is the finding that, in the absence of inelastic scattering, the probability of successful encapsulation ("red" events) is largest in the velocity range between 80–120 m/s and almost independent of the launch angle θ. This suggests that not the launch direction but rather the kinetic energy of the C_{60} molecule decides the outcome. In view of the restricted motion of the C_{60} molecule along the tube surface, which reduces the number of degrees of freedom, we find that this velocity window translates into a kinetic temperature of the C_{60} close to 400 °C.

It is remarkable that the optimum temperature for peapod formation, as predicted by our calculation, falls into the observed temperature range from (350–450) °C [4]. Previous explanations of this optimum temperature window were based only on plausibility arguments suggesting a low C_{60} mobility at low temperatures and a closure of the wall defects or fullerene fusion [17] under annealing conditions. We believe that the quantitative agreement between theory and observation also provides indirect evidence that the microscopic encapsulation mechanism involves defects in the tube wall.

Our assumption that the microscopic degrees of freedom are decoupled from the macroscopic motion of the C_{60} molecule gained us 5 orders of magnitude in computing efficiency. Clearly, the possibility of energy transfer between the macroscopic and microscopic degrees of freedom introduces a damping mechanism. This new inelastic channel could convert some of the green and blue trajectories, depicted in Fig. 4, into successful encapsulation events, thus further increasing the cross section for C_{60} encapsulation.

In summary, we studied the microscopic formation mechanism of $(C_{60})_n$@ (10,10) peapods by considering the fullerene entry through an extended vacancy in the wall and the open end of isolated or bundled tubes. Our total energy calculations indicate that the encapsulation process does not involve activation barriers. Extensive molecular dynamics simulations, performed under the different scenarios as a function of the C_{60} launch velocity and direction, indicate that the most likely encapsulation occurs through a large opening in the tube wall, within a narrow range of launch velocities that agrees well with the experimentally observed temperature window. Increasing concentration of defects will improve the encapsulation efficiency up to the point where, due to a significant fraction of atoms missing or displaced, the tubes lose their structural integrity.

This work was partly supported by the Korean IMT-2000 "Molecular Logic Devices" and the BK21 program.

*Present address: Nanomix, Inc., 1295A 67th Street, Emeryville, California 94608.

[1] B. W. Smith, M. Monthioux, and D. E. Luzzi, Nature (London) **396**, 323 (1998).
[2] B. Burteaux *et al.*, Chem. Phys. Lett. **310**, 21 (1999).
[3] B. W. Smith, M. Monthioux, and D. E. Luzzi, Chem. Phys. Lett. **315**, 31 (1999).
[4] B. W. Smith and D. E. Luzzi, Chem. Phys. Lett. **321**, 169 (2000).
[5] K. Hirahara *et al.*, Phys. Rev. Lett. **85**, 5384 (2000).
[6] J. Sloan *et al.*, Chem. Phys. Lett. **316**, 191 (2000).
[7] Y.-K. Kwon, D. Tománek, and S. Iijima, Phys. Rev. Lett. **82**, 1470 (1999).
[8] Robert F. Service, Science **292**, 45 (2001).
[9] L. A. Girifalco, M. Hodak, and R. S. Lee, Phys. Rev. B **62**, 13104 (2000).
[10] M. Hodak and L. A. Girifalco, Phys. Rev. B **64**, 035407 (2001).
[11] M. Monthioux *et al.*, Carbon **39**, 1251 (2001).
[12] We propose that what has been interpreted as harmless "amorphous overcoating" of perfect single-wall nanotubes in HRTEM images may indeed represent defective nanotube segments with openings large enough to let a fullerene pass through.
[13] Y.-K. Kwon *et al.*, Phys. Rev. Lett. **79**, 2065 (1997).
[14] Because of their enhanced reactivity, unsaturated edges form a stronger bond with the fullerenes than edges saturated with hydrogen or other elements. It is conceivable that fullerenes could get trapped near vacancies that are smaller or comparable in size with the fullerene.
[15] We consider a defect formed by removing 76 atoms from the wall, with a diameter of $\approx$13.6 Å, just large enough to permit an unhindered entry of a C_{60} molecule.
[16] Susumu Okada, Susumu Saito, and Atsushi Oshiyama, Phys. Rev. Lett. **86**, 3835 (2001).
[17] S. Bandow *et al.*, Chem. Phys. Lett. **337**, 48 (2001).

Stability, electronic structure and reactivity of the polymerized fullerite forms

V.V. Belavin

Novosibirsk State Technical University, av.Karla Marksa 20, Novosibirsk 630092, Russia

L.G. Bulusheva and A.V. Okotrub

Institute of Inorganic Chemistry SB RAS, av. Ak.Lavrenteva 3, Novosibirsk 630090, Russia

D. Tomanek

Department of Physics and Astronomy, Michigan State University, East Lansing, MI 48824-1116, USA

A study of band structure, stability and electron density distribution from selected crystal orbitals of polymerized C_{60} forms was carried out. Linear chain, tetragonal and hexagonal layers, and three-dimensional polymer with a simple cubic lattice were calculated using an empirical tight-binding method. The hopping parameters were chosen to fit a theoretical X-ray emission spectrum of C_{60} to the experimental one. Our results indicate that all calculated polymers are semiconductors with the smallest energy gap for hexagonal structure. Though the molecules C_{60} are linked by strong covalent bonds, the crystal orbitals characterized by the electron density localization on an individual carbon cage are separated in the electronic structure of polymers. The suggestions about reactivity of the one-dimensional and two-dimensional tetragonal polymers were made from the analyses of crystal orbitals accompanied with the highest occupied (HO) and lowest unoccupied (LU) bands. The polymerized C_{60} forms were found to be less stable than an icosahedral fullerene molecule.

Introduction

At ambient conditions solid C_{60} is a molecular crystal, in which the molecules are orientationally disordered while their centers of mass form a regular face-centered-cubic (fcc) lattice. At higher temperature and pressure the fullerite C_{60} is polymerized forming the various crystal structures depending upon the synthetic conditions [1-5]. Treatment of the fullerite in the pressure range below 8 GPa and at temperatures about 750 K results in the formation of linear C_{60} chains along the (110) direction of the original fcc lattice leading to an orthorhombic phase. Increasing the temperature provides an additional intermolecular bonding in either (111) or (100) planes, and the synthesis of a rhombohedral or a tetragonal phase. These phases have a two-dimensional structure with the interlayer distance of 9.8 Å [2, 3]. Above about 8 GPa very hard, three-dimensional polymeric structures are formed [6].

Studies by IR-, NMR and Raman spectroscopy showed the lowering in symmetry of the fullerene molecules and the presence of sp^3 intermolecular bonds in the polymerized C_{60} structures.

The molecules C_{60} are linked with each other by [2+2] cycloaddition mechanism forming a four-membered ring between the neighbors [7-9]. Strong covalent bonding between the cages and, as a consequence, the reduction of number of π-electrons in C_{60} change the electronic properties of the fullerite. So, the bands in the photoemission spectrum of polymerized C_{60} film are shifted toward the Fermi level [10] decreasing the energy gap relative to that for the fullerite. At present, the techniques of producing the polymeric phase in the pure form and the quantities, sufficient for an experimental research of their electronic properties, are still developing. In this connection a study of the electronic structure of polymers by quantum chemistry is very important for prediction of their possible properties and applications.

From tight-binding calculation a linear C_{60} chain has been found to be semiconductive with a finite band gap of 1.148 eV and almost pure σ-type intermolecular bonding [11]. Assuming the weak van der Waals interlayer interaction in the rhombohedral and tetragonal polymers a theoretical prediction on stability and conducting properties of these phases have been made by the result of tight-binding calculation of a single layer [12]. Different number of intermolecular covalent bonds in the tetragonal and rhombohedral structures was found to cause the distinction of band gap values, which were estimated to be 1.2 and 1.0 eV respectively. The investigation of the electronic structure of the three-dimensional rhombohedral C_{60} polymer has been carried out in [13] using the local-density approximation (LDA). The phase was found to be indirect semiconductor with band gap of 0.35 eV. Although the LDA generally underestimates the energy gap, the difference between the rhombohedral and fcc C_{60}, about 0.7 eV, correlates well with the result of tight-binding calculations [12].

The goal of present contribution is to study the electronic band structure, stability and chemical bonding of the C_{60} solids within the framework of a uniform quantum-chemical approach. All polymers known to date: one-dimensional, two-dimensional tetragonal, two-dimensional hexagonal and three-dimensional cubic structures are considered. The polymers are calculated using an empirical tight-binding method, which was specially parameterized to reproduce correctly the electronic density of states (DOS) in the valence band of fullerenes C_{60} and C_{70}.

Computational details

Using an empirical tight-binding approach to study of electronic structure of any compound it is necessary to choose matrix elements for correct description of the interelectronic interactions. As the fullerite is an allotropic form of carbon, the parameters obtained by fitting the band structure of bulk graphite were used as the initial ones [14]. These parameters were checked against the X-ray fluorescence spectra of fullerites C_{60} and C_{70} [15].

An X-ray emission arises as a result of electron transitions from valence shell of a compound to core-located vacancies. Since these transitions are governed by the dipole selection rules, CKα spectrum corresponds essentially to the density of states of carbon 2p electrons. The theoretical CKα spectra of C_{60} and C_{70} were plotted by the results of tight-binding calculations of the fullerenes molecules. A comparison between the experimental spectrum of fullerite and the theoretical spectrum of free molecule is possible because of the weakness of intermolecular interactions in the solids, as evident from the insignificant band dispersion in the fullerite C_{60} [16]. The intensity of a separate spectral line was calculated as a sum of squared modules of the coefficients with which 2p-atomic orbitals (AO) contribute in the molecular orbital (MO). For each occupied MO the calculated contribution is represented as a line, which position on the energy scale within the Koopmans' theorem gives the one-electron energy of corresponding MO. The resulting spectral profile was obtained by broadening the vertical lines by a 0.3-eV full-width-at-half-maximum Gaussian function.

Comparison between the experimental CKα spectra of fullerites C_{60} and C_{70} and the theoretical spectra of molecules calculated with the parameters set [14] is shown in Fig. 1(a, b). The theoretical spectral profiles do not correlate with the experimental ones in the one-electron energy region bellow 0. The reasons of such discrepancy were found from the analysis of calculation results to be inadequate interaction of the π-electrons and the underestimating of s- and p-states hybridization of in the cage fullerene molecules. The hopping parameters $V_{pp\pi}$ and $V_{sp\sigma}$, which are responsible for these interactions, were fitted to the best agreement between the theoretical and experimental X-ray spectra of C_{60}. The spectrum of C_{60} molecule, calculated with a set of parameters E_s = -3.65 eV, E_p = 3.65 eV, $V_{ss\sigma}$ = -3.63 eV, $V_{sp\sigma}$ = 4.50 eV, $V_{pp\sigma}$ = 5.38 eV, $V_{pp\pi}$ = -3.04 eV, reasonably reproduces the number of main spectral features, their relative intensities and energy separations in the experimental spectrum (Fig. 1(c)). Using the new parameter set we calculated the CKα spectrum of C_{70} molecule. Quite well agreement between experimental and theoretical spectra for this compound (Fig. 1(d)) confirms the ability of chosen parameters to correctly describe the electron interactions in fullerenes molecules. These parameters would be expected to take into account the specificity of cage carbon structures such as spatial peculiarities and electronic states of atoms.

The total energy of the carbon systems was calculated as:

$$E_{tot} = E_{bs} + E_{rep}, \qquad (1)$$

where E_{bs} is the sum of electronic eigenvalues over all occupied electronic states and E_{rep} is a short-ranged repulsive energy. The electronic eigenvalues are obtained by solving the empirical tight-

binding Hamiltonian, the off-diagonal elements of that $V_{ss\sigma}$, $V_{sp\sigma}$, $V_{pp\sigma}$, and $V_{pp\pi}$ were scaled with interatomic separation r as a function $s(r)$. The repulsive energy E_{rep} was calculated using the expressions given in [17]:

$$E_{rep} = \sum_i f\left(\sum_j \phi(r_{ij})\right) \tag{2}$$

where $\phi(r_{ij})$ is a pairwise potential between atoms i and j, and f is a functional expressed as a 4th-order polynomial. The pairwise potential $\phi(r)$ and scaling function $s(r)$ are parametrically expressed by [18]:

$$\phi(r) = \phi_0 \cdot (d_0 / r)^m \cdot \exp\left(m \cdot \left(-(r/d_c)^{m_c} + (d_0/d_c)^{m_c}\right)\right) \tag{3}$$

$$s(r) = (r_0 / r)^n \cdot \exp\left(n \cdot \left(-(r/r_c)^{n_c} + (r_0/r_c)^{n_c}\right)\right) \tag{4}$$

The change of $V_{sp\sigma}$ and $V_{pp\pi}$ values required of the re-parameterization of these functions. The parameters were chosen by fitting the dependence of cohesive energy versus nearest-neighbor interatomic separation for graphite and diamond [18]. The resulting parameters for the functions $\phi(r)$ and $s(r)$ and the polynomial coefficients are given in Table 1. Using these parameters gave the bond lengths of 1.542 and 1.446 Å in diamond and graphite at equilibrium. These values satisfactorily correlate with the experimental ones 1.546 and 1.420 Å respectively.

Electronic DOS was calculated by a histogram method, in which an energy interval is split into the cells with width of ΔE, and number of states N_i is computed in each of the cells. The integration over the irreducible wedge of the Brillouin zone was done using 36 k points and 0.1-eV Gaussian broadening.

Results and discussion

One-dimensional, two-dimensional tetragonal and hexagonal polymers of C_{60} are depicted in Fig. 2. The neighboring fullerene cages are linked by the four-membered rings from carbon atoms at a fusion between two hexagons of a molecule. Each C_{60} molecule in the polymeric chain is connected to two neighbors and belongs to symmetry point group D_{2h}. In the tetragonal and hexagonal layers each individual molecule having 4 or 6 neighbors belongs to the symmetry point group D_{2h} or D_{3d} respectively. Three-dimensional cubic polymer was constructed by the attachment of two C_{60} molecules in perpendicular direction to the tetragonal layer. The atomic coordinates in the distorted carbon cages were obtained from the results of geometry optimization of a linear trimer $(C_{60})_3$ by quantum-chemical semiempirical PM3 method [19]. A unit cell of the polymeric chain is the central C_{60} fragment of the trimer. The geometry of this fragment has the most deviation

from an icosahedral one near the four-membered rings. Conserving this deviation near each linking ring the atomic coordinates for other polymers were generated according to the point group symmetry of C_{60} cage in a unit cell. An intramolecular bond length of 1.55 Å taken also from [19] is characteristic for the carbon compounds in the sp^3-hybridization.

Linear C_{60} chain

Molecular orbitals of the icosahedral C_{60} may be divided into two types: radial ρ-orbitals directed towards the center of the carbon cage and tangential τ-orbitals aligned with the local normal of the cage surface. According to the results of calculation using various quantum-chemical methods, the highest occupied MO (HOMO) of fullerene is a fivefold degenerated orbital with h_u symmetry and the lowest unoccupied MO (LUMO) is a threefold orbital with t_{1u} symmetry. These MOs are ρ-type orbitals. Distortion of the fullerene molecule during polymerization changes its electronic structure. The energy levels of icosahedral C_{60} and the C_{60} fragment isolated from the linear chain are compared in Fig. 3. A deviation from the icosahedral structure causes the splitting of the degenerated MOs and, therefore, the energetic broadening of ρ- and τ-orbital blocks. The splitting depends on the extent of molecular distortion.

The covalent bonding of the C_{60} cages in the polymeric chain results in the dispersion of energy levels (Fig. 3(c)). The characteristic peculiarity of the polymer valence band is the presence of two groups, A and B, of crystal orbitals (CO) accompanied with the bands having very little dispersion. The pattern of electron density distribution for one of such COs is depicted in Fig. 4. Electronic density from this ρ-type orbital is mainly localized on twelve hexagons of carbon cage, while on the atoms providing the intermolecular bonding it is practically equal to zero. The number of similar localized COs may be suggested to depend on the extent of C_{60} cage distortion and the crystal structure of a polymer.

According to the band structure calculation, the linear C_{60} chain is a semiconductor. A direct band gap at the Γ point is about 2.180 eV; therefore, the polymer chain formation narrows the icosahedral C_{60} HOMO-LUMO gap by 0.921 eV. The HO and LU bands of C_{60} chain are not degenerate. Width of the LU band is about 0.125 eV indicating a small value of the transfer integral of ρ-electrons along the polymer chain. As the LU band is separated from higher states by 0.131 eV, the electron doping of the one-dimensional C_{60} polymer will make a single-band conducting system. Analysis of the electron density distribution from the COs accompanied with the HO and LU bands (Fig. 5) can predict the reactivity of C_{60} polymer. The atomic size is proportional to the sum of squared coefficients with which carbon AOs participate in the CO formation. The higher electron density on atoms 1, 2 for the HO and 3, 4 for the LU crystal orbitals will result in the further attachment of C_{60} molecules to the double bonds with formation of the two-dimensional tetragonal polymer.

Two-dimensional tetragonal polymer

The calculated band structure of the two-dimensional tetragonal polymer near the Fermi level is shown along the symmetric directions of the square Brillouin zone (Fig. 6). The top of the valence band is found to be at the center of the Brillouin zone and the bottom of the conduction band is at the M point. The fundamental energy gap between these band extremes is 1.852 eV. The LU band in the tetragonal polymer is separated from higher states as that in the polymer chain, though its dispersion increases up to 0.286 eV indicating the stronger intramolecular overlapping of ρ-electrons. Two blocks of COs (A and B) characterized by the localization of electron density on the individual C_{60} cages are positioned in the energy interval from 2 to 0 eV. Increasing the neighboring molecules in the tetragonal polymer reduces the total number of localized orbitals in the valence band near the Fermi level compared to the linear C_{60} chain.

Structure of the frontier COs is schematically shown in Fig. 7. Both orbitals are characterized by the higher electron density on the central double bonds of a C_{60} fragment. Therefore, we expect the attachment of the additional fullerene molecules to the tetragonal structure along z direction in the chosen coordinate system (Fig. 6.) with the formation of three-dimensional cubic polymer. Low electronic density on atoms 3 and 4 explains the small dispersion along the XM direction for the highest branch of the valence band.

Cubic polymer

The consideration of the three-dimensional cubic polymer after the two-dimensional tetragonal is caused by the increasing of a coordination number within the same point group symmetry of the C_{60} fragment. In the cubic polymer the C_{60} cage being D_{2h} symmetric have the greatest number of neighbors. The band structure calculation shows that the cubic polymer has a direct energy gap of 2.235 eV at M point of the Brillouin zone (Fig. 8). Increasing the neighbors up to six in the polymer extends the energy gap by 0.05 and 0.38 eV in comparison with the one-dimensional and two-dimensional tetragonal structure, respectively.

The formation of covalent bonds along the additional direction enhances the intramolecular overlapping of ρ-electrons and, therefore, their energy broadening. As a consequence the energy dispersion of the LU band increases up to 0.956 eV and, furthermore, all the unoccupied states form one continuous conduction band. Electronic structure of the cubic polymer is characterized by the further narrowing of the energy interval in which the higher occupied bands are positioned. Among these bands only two small-dispersed bands (A and B) are selected. The fifth and sixth neighbors in the cubic polymer are attached to the bonds shared by the central hexagons, that remains in the structure of the C_{60} fragment only 8 slightly deformed hexagons. The ρ-electronic density is localized on these small sections (Fig. 9), while in the one-dimensional and two-dimensional

tetragonal polymers the ρ-electrons are distributed on the areas composed of 6 adjacent hexagons. Spatial separation of the ρ-electrons in the cubic polymer reduces their intermolecular interaction that results in the narrowing of the higher occupied bands distribution.

Two-dimensional hexagonal polymer

Among considered polymeric structures the two-dimensional hexagonal polymer is the most intriguing because of the high-symmetry C_{60} fragment is strongly distorted around the molecular equator due to the formation of 12 covalent bonds. The band structure of the hexagonal polymer is shown in Fig.10. The polymer has indirect 0.577 eV gap between the extremes at K and T points. This value is minimal in the series of calculated C_{60} polymers. The LU and HO bands are twofold-degenerated in the center of the Brillouin zone. The bands of the polymer show considerable dispersion along all symmetry directions. Only one small-dispersed band near 0 eV can be selected. The electronic density from the CO corresponding to this band is localized on the areas composed of 4 adjacent hexagons from the top and bottom parts of the C_{60} fragment (Fig. 11). The ρ-electrons of the COs accompanied with the HO and LU bands were found to localize on the tops of the slightly deformed pentagons. The C_{60} fragments in the hexagonal layer are closely packed that makes it possible to the intermolecular interaction of ρ-electrons through the small tetragonal cavities. It is the reason of the large dispersion of the HO and LU bands along the ΓK direction of the Brillouin zone.

Analysis of electronic density of states

The calculated electronic DOS for the icosahedral C_{60} molecule and the polymerized C_{60} structures are compared in Fig. 12. The electron distribution near the Fermi level is the most interesting. The feature A in the DOS of C_{60} molecule originates from the HOMO of h_u symmetry and the feature B corresponds to two lower energy orbitals having h_g and g_g symmetry. From the icosahedral molecule to the hexagonal polymer the intensity of these features is gradually decreased. The feature A is considerably broadening, while the width and intensity of the feature B are less varying. The two-dimensional hexagonal polymer is characterized by the most noticeable changes of these features, that is due to the largest change of ρ-system of the icosahedral C_{60} when a hexagonal layer is formed. This considerable change is also the cause of the smallest energy gap between the bands, which density forms the feature A and B, and the deeper occupied bands. The feature A and B in the electronic DOS are associated with the bands from the blocks A and B, therefore, the decreasing of their intensities reflects the reduction of the number of localized

orbitals. The localization of electron density from the higher occupied COs on the individual C_{60} cage of the cubic polymer gives the intense feature near the Fermi level.

The population analyses have shown that the intermolecular bonds in the C_{60} polymers are almost pure σ-bonding. The orbitals providing the σ-bonding between carbon cages are positioned in the depth of valence band about of 8-9 eV below the Fermi level. The examples of such type COs in the one-dimensional and hexagonal polymers are given in Fig. 13. Two orbitals, which are differed by a sign of the AOs overlapping in the four-membered ring, are divided in the electronic structure of the linear C_{60} chain. As evident from Fig. 13(a), radially directed AOs form the ρ-type orbital. In the electronic structure of the tetragonal polymer there are COs providing the σ-bonding between molecules or simultaneously along the both crystallographic directions (x, y) or along a particular one. The intermolecular σ-bonding COs of the hexagonal polymer can be as pure ρ-type orbitals (Fig. 13(b)) so a combination of radial and tangential AOs (Fig. 13(c)). Through the former orbital, the AOs of the atoms composing the four-membered rings have the positive overlapping between molecules and negative overlapping on the other directions. The latter CO being completely bonding is energy deeper orbital.

Energy of the polymeric structures

The calculated HO-LU band gap and energies E_{tot}, E_{bs}, and E_{rep} for the polymerized fullerite forms are compared with those for free C_{60} molecule in Table 2. The total energy of each of the considered polymeric structure is higher than that of the fullerene molecule. With increasing the neighbors in a polymer its total energy increases, except that for the three-dimensionally polymerized C_{60}. Analysis of the E_{bs} and E_{rep} values shows that the less stability of the hexagonal polymer compared to the cubic one is caused by the stronger short-range repulsion in the former structure. Actually, the more closely packing of the C_{60} cages in the hexagonal layer than in any plane of the cubic structure leads to the additional interactions, in particular, the intermolecular ρ-electron overlapping. The change of the total energy with the polymerization correlates with the change of the HO-LU band gap: than the band gap is smaller that the polymer is less stable.

Conclusion

The tight-binding method was parameterized to correct reproducing the 2p-electron density distribution in the valence band of the fullerite C_{60} and C_{70}. The determined parameters can be used later for the electronic structure calculation of various cage carbon compounds. Using new parametric scheme a systemic study of electronic band structure of four polymerized phases of C_{60}, which are known to day, was carried out. For the tetragonal and rhombohedral phases only one

layer was calculated assuming the insignificant influence of van der Waals interactions between layers on the electronic energy bands and crystal orbitals.

Polymerization of fullerene C_{60} results in the narrowing of HOMO-LUMO gap that is caused by the splitting of degenerated MOs of the icosahedral C_{60} due to its distortion and the formation of intermolecular bonds. All considered polymers were found to be semiconductive with the smallest band gap for the two-dimensional hexagonal polymer and the largest one for the cubic polymer. A change of the band gap with the number of neighbors and the type of their connection in the polymer correlates with the calculated total energy values. The polymerized fullerite forms were found to be less stable than free C_{60} molecules. Among the polymers the linear C_{60} chain is characterized by the greatest energy stability.

Near the Fermi level the ρ-type crystal orbitals, which electronic density is localized on individual C_{60} cages, were revealed for all calculated polymers. The number of such orbitals decreases when the number of neighbors and the extent of C_{60} fragment distortion increase. The σ-bonding between C_{60} molecules was found to provide by the crystal orbitals located about of 8-9 eV below the Fermi level. Furthermore, due to the small-size cavities in the hexagonal layer, intermolecular interactions are also provided by the highest ρ-orbitals. The analyses of the frontier orbitals in the polymeric chain and the tetragonal structure showed the further attachment of fullerene molecules should result in the formation of the tetragonal and cubic polymer, respectively.

Acknowledgments

This work was financially supported by the Russian scientific and technical program «Fullerenes and Atomic Clusters» (Projects No.5-1-98), and Federal Directed Program «Integration», grant K0042.

References

[1] Y. Iwasa, T. Arima, R.M. Fleming, T. Siegrist, O. Zhou, R.C. Haddon, L.J. Rothberg, K.B. Lyons, H.L. Carter Jr., A.F. Hebard, R. Tycko, G. Dabbagh, J.J. Krajewski, G.A. Thomas, T. Yagi, Science, 264 (1994) 1570.

[2] M. Nunez-Regueiro, L. Marques, J.-L. Hodeau, O. Bethoux, M. Perroux, Phys. Rev. Lett., 74 (1995) 278.

[3] G. Oszlanyi, L. Forro, Solid State Commun., 93 (1995) 265.

[4] L. Marques, J.-L. Hodeau, M. Nunez-Regueiro, M. Perroux, Phys. Rev., B54 (1996) R12633.

[5] V.D. Blank, S.G. Buga, N.R. Serebryanaya, V.N. Denisov, G.A. Dubitsky, A.N. Ivlev, B.N. Mavrin, M.Yu. Popov, Phys. Lett., A205 (1995) 208.

[6] P.-A. Persson, U. Edlund, P. Jacobsson, D. Johnels, A. Soldatov, B. Sundqvist, Chem. Phys. Lett., 258 (1996) 540.

[7] C. Gonze, F. Rachdi, L. Hajji, M. Nunez-Rugueiro, L. Marques, J.-L. Hodeau, M. Mehring, Phys. Rev., B54 (1996) R3676.

[8] A.M. Rao, P.C. Eklund, J.-L. Hodeau, L. Marques, M. Nunez-Regueiro, Phys. Rev., B55 (1997) 4766.

[9] B. Sundqvist, Physica, B265 (1999) 208.

[10] A. Ito, T. Morikawa, T. Takahashi, Chem. Phys. Lett., 211 (1993) 333.

[11] K. Tanaka, Yu. Matsuura, Y. Oshima, T. Yamabe, Y. Asai, M. Tokumoto, Solid. State Commun., 93 (1995) 163.

[12] C.H. Xu, G.E. Scuseria, Phys. Rev. Lett., 74 (1995) 274.

[13] S. Okada, S. Saito, Phys. Rev. B55 (1977) 4039.

[14] D. Tomanek, S.G. Louie, Phys. Rev., B37 (1988) 8327.

[15] A.V. Okotrub, L.G. Bulusheva, Fullerene Science and Technology, 6 (1998) 405.

[16] S. Saito, A. Oshiyama, Phys. Rev. Lett., 66 (1991) 2637.

[17] L. Goodwin, A.J. Skinner, D.G. Pettifor, Europhus. Lett., 9 (1989) 701.

[18] C.H. Xu, C.Z. Wang, C.T. Chan, K.M. Ho, J. Pys.: Condens. Matter 4 (1992) 6047.

[19] A.V. Okotrub, L.G. Bulusheva, Yu.V. Shevstov, L.N. Mazalov, O.A. Gudaev, V.K. Malinovskii, Phys. Low-Dim. Struct., 5/6 (1997) 103.

Figure captions

Fig. 1. Comparison of the theoretical CKα spectra (profile 1) of C_{60} and C_{70} calculated with the old (a, b) and new (c, d) parametric set with the experimental X-ray spectra (profile 2) of the fullerite C_{60} (a, c) and C_{70} (b, d).

Fig. 2. The fragments of linear C_{60} chain (a), two-dimensional tetragonal (b) and hexagonal (c) polymers.

Fig. 3. Energy levels of the icosahedral C_{60} molecule (a), the distorted C_{60} cage from the linear polymer (b), and the band structure of the liner C_{60} polymer (c). The small-dispersed occupied bands are marked by A and B.

Fig. 4. Schematic structure of the crystal orbital (a) corresponding to the small-dispersed band of the linear C_{60} chain, the electron density from such type orbital are mainly localized on dashed hexagons (b).

Fig. 5. Schematic representation of the frontier occupied (a) and unoccupied (b) orbitals of the linear C_{60} chain. A circle size correlates with the 2p-AO participation in the construction of a given MO.

Fig. 6. Calculated band structure of the tetragonal polymer. The small-dispersed bands near the Fermi level are marked by A and B. Also is shown the Brillouin zone corresponding to the C_{60} monolayer.

Fig. 7. Schematic representation of the frontier occupied (a) and unoccupied (b) orbitals of the tetragonal C_{60} polymer. A circle size correlates with the 2p-AO participation in the construction of a given MO.

Fig. 8. Calculated band structure of the three-dimensional C_{60} polymer. The first Brillouin zone of the simple cubic lattice is also shown.

Fig. 9. Schematic representation of the crystal orbitals accompanied by the band, which are marked by A and B in the Fig. 8. The hexagons, on which the electron density is localized, are dashed.

Fig. 10. Calculated band structure of the hexagonal C_{60} polymer around the Fermi level. The two-dimensional Brillouin zone is also shown.

Fig. 11. Schematic representation of crystal orbital accompanied by the small-dispersed band from the electronic structure of the hexagonal polymer. The electronic density from this orbital is localized on the dashed hexagons.

Fig. 12. Calculated electronic density of states for icosahedral C_{60} molecule (a), linear C_{60} chain (b), two-dimensional tetrahedral (c) and hexagonal (d) polymers, three-dimensional C_{60} polymer (e).

Fig. 13. The examples of the crystal orbitals providing σ-bonding between neighboring C_{60} cages in the liner polymer (a) and the hexagonal layer (b, c).

Table 1. Parameters for the functions $s(r)$, $\phi(r)$ and coefficients of the polynomial $f(x)$.

n	n_c	r_c (Å)	r_0 (Å)	
2.0	6.5	2.18	1.536	
ϕ_0 (eV)	m	m_c	d_c (Å)	d_0 (Å)
4.165	4.203	8.185	2.105	1.640
c_0	c_1	c_2	c_3	c_4
-2.590	0.572	-1.789×10^{-3}	2.353×10^{-5}	-1.242×10^{-7}

Table 2. Energetic characteristics of icosahedral C_{60} molecule and the polymerized fullerite forms: the calculated HO-LU band gap (E_g), total (E_{tot}), electronic (E_{bs}) and repulsive (E_{rep}) energy.

Structure	E_g(eV)	E_{rep}(eV/atom)	E_{bs}(eV/atom)	E_{tot}(eV/atom)
icosahedral C_{60}	3.101	12.175	-28.265	-16.090
linear chain	2.180	11.607	-27.612	-16.005
tetragonal layer	1.852	11.171	-27.093	-15.922
hexagonal layer	0.577	11.468	-27.119	-15.651
cubic	2.235	10.842	-26.707	-15.865

Coherent control of photocurrents in graphene and carbon nanotubes

E. J. Mele
Department of Physics and Laboratory for Research on the Structure of Matter, University of Pennsylvania, Philadelphia, Pennsylvania 19104

Petr Král
Department of Physics, University of Toronto, Toronto, Ontario M5S 1A7, Canada

David Tománek
Department of Physics and Astronomy, Michigan State University, East Lansing, Michigan 48824
(Received 3 September 1999)

Coherent one-photon (2ω) and two-photon (ω) electronic excitations are studied for graphene sheets and for carbon nanotubes using a long-wavelength theory for the low-energy electronic states. For graphene sheets we find that a coherent superposition of these excitations produces a polar asymmetry in the momentum space distribution of the excited carriers with an angular dependence that depends on the relative polarization and phases of the incident fields. For semiconducting nanotubes we find a similar effect which depends on the square of the semiconducting gap, and we calculate its frequency dependence. We find that the third-order nonlinearity, which controls the direction of the photocurrent is robust for semiconducting tubes and vanishes in the continuum theory for conducting tubes. We calculate corrections to these results arising from higher-order crystal-field effects on the band structure and briefly discuss some applications of the theory.

I. INTRODUCTION

The magnitude and direction of photocurrents in semiconductors are ordinarily controlled using applied bias voltages. Interestingly the direction of a photocurrent in a semiconductor can also be controlled without bias voltages through phase coherent control of the incident optical fields. In a typical experiment an initial and final state are simultaneously coupled using two coherent excitations: one photon excitation at frequency 2ω and two photon excitation at frequency ω. The coherent superposition of these two excitations can lead to a polar asymmetry in the momentum space distribution of the excited photocarriers and therefore to a net photocurrent. The effect has been discussed theoretically[1,2] and observed experimentally in photoyield from atoms[3] and for photocurrents in semiconductors.[4] Recently, two of us have proposed that for carbon nanotubes this effect could provide directional control of a photocurrent along the tube axis[5] and even suggests a novel method for biasing the diffusion of ionic species which intercalate within the nanotubes.

In this paper, we study the excitations that lead to this effect both for graphene sheets and for carbon nanotubes. In both these systems the low-energy electronic properties relevant to most solid state effects are determined by an interesting feature of the band structure. The isolated graphene sheet has only an incipient Fermi surface; it is actually a zero gap semiconductor where the conduction and valence bands meet at precise points in momentum space. The carbon nanotube is a cylindrical tubule formed by wrapping a graphene sheet and for metallic tubes the "zero gap" feature manifests itself in a peculiar doubling of the low energy electronic spectrum with "pairs" of forward and backward moving excitations at both k_F and $-k_F$.[6] In either case, the low-energy electronic spectra are described by a two-component Dirac Hamiltonian.[6]

In this paper, we develop the theory of phase coherent one- and two-photon excitation within this model. The application to the graphene sheet turns out to be a useful pedagogical model, which is unusual for a semiconductor and nicely illustrates the origin of phase coherent control of photocurrents for a graphene derived system. For graphene it is inappropriate to analyze the third-order nonlinearity by analogy with the third-order response in atomic systems, as has been done previously for semiconductors.[4] Instead, we find that the third-order response probes the rather unique geometry of the extended low-energy electronic eigenstates which occur within the graphene sheet. The application of the model to a carbon nanotube shows, interestingly, that the third-order nonlinearity is suppressed for excitations between the lowest subbands of any conducting nanotube and vanishes completely for transitions between the lowest subbands of a conducting "armchair" tube, but it is nonzero and robust for the gapped subbands of a semiconducting tube. In fact, the effects we calculate are significantly stronger for semiconducting nanotubes than for a conventional semiconductor. In principle this effect might be used to distinguish conducting and semiconducting tubes in a compositionally mixed sample. Other possible applications of the idea will be discussed later in the paper.

In this paper, we briefly review the effective mass theory for the graphene sheet in Sec. II. In Secs. III and IV, we derive the interaction terms in the long-wavelength theory, which couple the electrons to time varying electromagnetic fields and present a calculation of the coherent third-order nonlinear optical excitations using this model. Section V applies the results to study the third-order response of an isolated infinite graphene sheet. In Sec. VI, we use the theory to

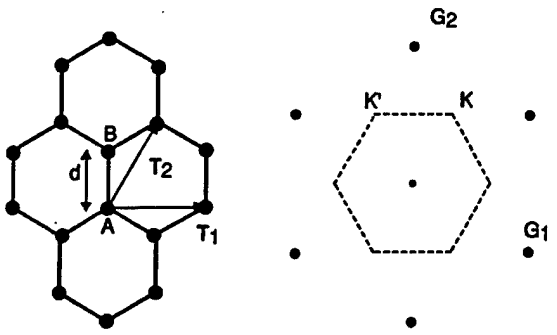

FIG. 1. Direct and reciprocal space structures of the graphene lattice. The primitive cell contains two sublattice sites labeled A and B in the left panel. The right panel shows the first star of reciprocal-lattice vectors and the first Brillouin zone. The long-wavelength theory expands the electronic Hamiltonian for momenta near the K and K' points at the Brillouin-zone corners.

study third-order effects for conducting and semiconducting carbon nanotubes. A discussion and some applications of the results are presented in Sec. VII.

II. EFFECTIVE MASS THEORY

In this section, we briefly review the effective mass description of the low-energy electronic states. The theory is developed for an ideal graphene sheet, a section of which is shown in Fig. 1. The primitive cell of this structure contains two atoms, labeled A and B in the figure. The lattice is unchanged after a translation by any combination of the two primitive translations vectors

$$\vec{T}_1 = a(1,0),$$

$$\vec{T}_2 = a\left(\frac{1}{2}, \frac{\sqrt{3}}{2}\right), \tag{1}$$

where the bond length $d = a/\sqrt{3}$. We introduce a pair of primitive translation vectors for the reciprocal lattice $\vec{G}_i$ such that $\vec{G}_i \cdot \vec{T}_j = 2\pi\delta_{ij}$, yielding

$$\vec{G}_1 = \frac{4\pi}{\sqrt{3}a}\left(\frac{\sqrt{3}}{2}, -\frac{1}{2}\right)$$

$$\vec{G}_2 = \frac{4\pi}{\sqrt{3}a}(0,1) \tag{2}$$

which generate a triangular lattice in reciprocal space.

The critical points $K(K')$ are important to our discussion, and they occur at the corners of the Brillouin zone of this reciprocal lattice at the positions

$$K = \frac{1}{3}(\vec{G}_1 + 2\vec{G}_2) = \frac{4\pi}{3a}\left(\frac{1}{2}, \frac{\sqrt{3}}{2}\right),$$

$$K' = \frac{1}{3}(-\vec{G}_1 + \vec{G}_2) = \frac{4\pi}{3a}\left(-\frac{1}{2}, \frac{\sqrt{3}}{2}\right). \tag{3}$$

The "bonding" and "antibonding" π electron bands meet precisely at these $K(K')$ points in reciprocal space. This band touching is required by symmetry for this system and it is correctly described by the simplest model for e propagation within the graphene sheet which is a binding model in which the hopping of an electron b neighboring sites is set by a single energy, t. Thus, w

$$h_{\mu\nu} = \langle \phi_\mu | H | \phi_\nu \rangle = t \quad \text{(nearest-neighbor } \mu\nu\text{)}$$

$$= 0 \quad \text{(otherwise)}.$$

Working in the sublattice basis and at crystal mome we have the Hamiltonian

$$H(\vec{k})$$

$$= t\begin{pmatrix} 0 & 1 + e^{-i\vec{k}\cdot\vec{T}_2} + e^{-i\vec{k}\cdot(\vec{T}_2 - \vec{T}_1)} \\ 1 + e^{i\vec{k}\cdot\vec{T}_2} + e^{i\vec{k}\cdot(\vec{T}_2 - \vec{T}_1)} & 0 \end{pmatrix}$$

If we set $\vec{k} = \vec{K} + \vec{q}$ and expand the Hamiltonian for we obtain the long-wavelength Hamiltonian

$$H_K(\vec{q}) = \frac{\sqrt{3}ta}{2}\begin{pmatrix} 0 & q_x + iq_y \\ q_x - iq_y & 0 \end{pmatrix} = \hbar v_F \vec{\sigma}^* \cdot \vec{q}$$

where $\vec{\sigma}$ are the 2×2 Pauli matrices. A similar ex near the K' point yields

$$H_{K'} = -\hbar v_F \vec{\sigma} \cdot \vec{q}.$$

Identifying each of the critical points with the index α $\alpha = 1$ denotes the K point and $\alpha = -1$ denotes the K' these Hamiltonians can be rotated into diagonal for the unitary operators

$$U_\alpha(\vec{q}) = \frac{1}{\sqrt{2}}\begin{pmatrix} 1 & 1 \\ -\alpha e^{-i\alpha\theta} & \alpha e^{-i\alpha\theta} \end{pmatrix},$$

where $\theta = \tan^{-1}(q_y/q_x)$. Thus,

$$U_\alpha^\dagger(\vec{q}) H_\alpha(\vec{q}) U_\alpha(\vec{q}) = \hbar v_F \begin{pmatrix} -|q| & 0 \\ 0 & |q| \end{pmatrix},$$

so that Eqs. (6) and (7) describe pairs of bands that c linearly away from the critical K and K' points. No that $H_\alpha(\vec{q}) = H^*_{-\alpha}(-q)$ as expected. Equations (6) and the unitary rotations in Eq. (8) provide the appr description of all the low energy electronic excitati quired for this problem.

III. GRAPHENE-FIELD INTERACTION HAMILTO

In this section we collect several results we need scribe the coupling of electrons described by Eqs. (6) to the electromagnetic potentials. For a particle of ch interacting with the electromagnetic vector potential scalar potential Φ the momentum and energy are sh $\rightarrow \vec{p} - Q\vec{A}/c$ and $E \rightarrow E - Q\Phi$.[7] Thus, the interaction tonian that couples the Dirac particle to the time vector potential (A_x, A_y) is

$$H_{\alpha,int} = -\alpha v_F Q(A_x\sigma_x - \alpha A_y\sigma_y)/c.$$

This interaction operator can also be obtained by calculating the velocity operator from the commutator of the position operator with the unperturbed Hamiltonian:

$$\vec{v}_\alpha = \frac{i}{\hbar}[H_\alpha, \vec{r}] \tag{11}$$

and therefore

$$\vec{v}_\alpha = \alpha v_F(\sigma_x, -\alpha\sigma_y) \tag{12}$$

so that $H_{\alpha,int} = -\vec{j}_\alpha \cdot \vec{A}/c$.

It is useful to rotate the interaction Hamiltonian (10) into the band basis using the unitary operators in Eq. (8). To do this we write $\hat{q} = (q_x, q_y)/|\vec{q}|$ and compute $H^b_{\alpha,int} = U^\dagger_\alpha(\hat{q}) H_{\alpha,int}(\hat{q}) U_\alpha(\hat{q})$ giving

$$H^b_{\alpha,int}(\hat{q},\vec{A}) = \frac{ev_F}{c}\begin{pmatrix} -\hat{q}\cdot\vec{A} & -i\alpha\hat{z}\cdot(\hat{q}\times\vec{A}) \\ i\alpha\hat{z}\cdot(\hat{q}\times\vec{A}) & \hat{q}\cdot\vec{A} \end{pmatrix}. \tag{13}$$

This demonstrates that the coupling between the Bloch electrons and the vector potential depends on the angle between $\vec{v}$ and $\vec{A}$ and that the interband matrix elements [which are the off-diagonal terms in Eq. (13)] vanish when the two are collinear. Indeed, $H_\alpha(\vec{q})$ and $H_{\alpha,int}(\hat{q},\vec{A})$ commute along these special lines in reciprocal space, so that interband transitions are forbidden along this trajectory. This peculiar feature can be traced to the absence of a mass term in the effective Hamiltonians in Eqs. (6) and (7) which would ordinarily mix the plane-wave solutions to Eqs. (6) and (7) and thereby allow interband transitions by coupling with the long-wavelength current operator. When $\vec{v}$ and $\vec{A}$ are not collinear interband transitions are allowed and the transition amplitudes are fixed by the mismatch in their orientations in the graphene plane. This has interesting consequences for coherent control of nonlinear optical processes in the nanotubes, as we show below.

IV. NONLINEAR OPTICAL EXCITATIONS

In this section, we present a calculation of the transition probabilities for the third-order nonlinear optical excitations among the electronic states given by the models in Secs. II and III. We introduce time varying fields of the form

$$\vec{A}(\vec{r},t) = \vec{A}_\omega e^{-i\omega t + i\phi_1} + \vec{A}_{2\omega} e^{-2i\omega t + i\phi_2} + \text{c.c.} \tag{14}$$

and study the response of the system to third order in these exciting fields. Asymmetries in the photocurrent are controlled by the coherent excitation of electrons from an initial state to a final state by one photon (2ω) and by two one photon (ω) processes. The coherent mixing of these two processes is studied by evolving the density matrix to third order in the exciting fields and isolating the terms proportional to $A_\omega A_\omega A_{-2\omega}$.

It is convenient to study the time evolution of the one particle density matrix $\rho = \langle \Psi^\dagger(\vec{r})\Psi(\vec{r}')\rangle$. The Hamiltonian for our system is $H_\alpha + H_{\alpha,int}$ and we work in the Heisenberg representation so that

$$\frac{d\rho}{dt} = \frac{i}{\hbar}[H_{\alpha,int}(t), \rho], \tag{15}$$

where H_α is the free particle Hamiltonian and $H_{\alpha,int}(t) = e^{iH_\alpha t} H_{\alpha,int} e^{-iH_\alpha t}$. In the band basis the density matrix in the initial state has the form

$$\rho_0 = \rho(t=-\infty) = \begin{pmatrix} 1 & 0 \\ 0 & 0 \end{pmatrix} \tag{16}$$

since only the negative energy states of the Hamiltonians (6) and (7) are initially occupied.

We expand the density matrix order by order in the exciting fields

$$\rho(t) = \rho_0 + \rho_1 + \rho_2 + \rho_3 + \cdots. \tag{17}$$

Integrating Eq. (17) to first order in the applied fields gives

$$\rho_1 = \frac{iev_F}{\hbar c}\begin{pmatrix} 0 & F_1(t) \\ -F_1^*(t) & 0 \end{pmatrix}, \tag{18}$$

where

$$\begin{aligned} F_1(t) = {} & \frac{\alpha\hat{z}\cdot(\hat{q}\times\vec{A}_\omega)e^{-i(\Delta+\omega)t+i\phi_1}}{-\Delta-\omega-i\delta} \\ & + \frac{\alpha\hat{z}\cdot(\hat{q}\times\vec{A}_{-\omega})e^{-i(\Delta-\omega)t-i\phi_1}}{-\Delta+\omega-i\delta} \\ & + \frac{\alpha\hat{z}\cdot(\hat{q}\times\vec{A}_{2\omega})e^{-i(\Delta+2\omega)t+i\phi_2}}{-\Delta-2\omega-i\delta} \\ & + \frac{\alpha\hat{z}\cdot(\hat{q}\times\vec{A}_{-2\omega})e^{-i(\Delta-2\omega)t-i\phi_2}}{-\Delta+2\omega-i\delta}, \end{aligned} \tag{19}$$

where $\Delta = 2v_F q$ and δ is a positive infinitesimal.

The second-order terms ρ_2 include the lowest-order changes to the occupation probabilities which can be induced with excitation by the ω or the 2ω fields

$$\begin{aligned} (\dot{\rho}_2)_{22} = -(\dot{\rho}_2)_{11} = {} & \frac{2\pi e^2 v_F^2}{\hbar^2 c^2}[|\alpha\hat{z}\cdot(\hat{q}\times\vec{A}_\omega)|^2\delta(\Delta-\omega) \\ & + |\alpha\hat{z}\cdot(\hat{q}\times\vec{A}_{2\omega})|^2\delta(\Delta-2\omega)] \end{aligned} \tag{20}$$

as well as oscillating nonlinear off-diagonal coherence terms

$$(\rho_2)_{12} = -\frac{ie^2 v_F^2}{\hbar^2 c^2} F_2(t). \tag{21}$$

Anticipating the situation $2\omega \approx \Delta$, the most important contribution to $F_2(t)$ has the form

$$F_2(t) = \frac{(\hat{q}\cdot\vec{A}_{-\omega})(\alpha\hat{z}\cdot\hat{q}\times\vec{A}_{-\omega})e^{-i(\Delta-2\omega)t-2i\phi_1}}{(-\Delta+\omega-i\delta)(-\Delta+2\omega-i\delta)}. \tag{22}$$

The second-order coherence term in Eq. (22) leads to a transition rate, which is third order in the applied fields and is the source of the polar asymmetry of the photocurrent,

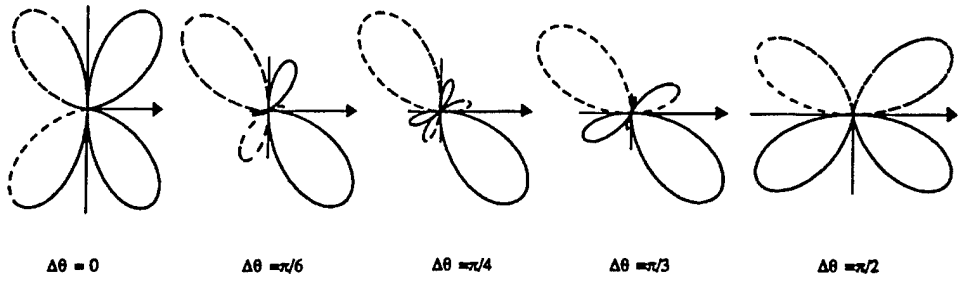

FIG. 2. Angular distributions of the transition rates given by Eq. (23). In each panel the $\vec{A}_\omega$ is polarized along the horizontal direction (th direction of the arrow in each plot) and $\Delta\theta$ is the angle between the $\vec{A}_{2\omega}$ and $\vec{A}_\omega$ fields. The polar plot gives the transition rate as a functio of the angle of the Bloch wave vector $\hat{q}$ with respect to the direction of $\vec{A}_\omega$. These angular distributions are superimposed on the angula distribution for the direct transition rate, which is given by the second term in Eq. (20). The solid curves correspond to $(\dot{\rho}_3)_{22}>0$, dashe curves to $(\dot{\rho}_3)_{22}<0$ when $\cos(\phi_2-2\phi_1)>0$.

$$(\dot{\rho}_3)_{22}=\frac{8\pi e^3 v_F^3}{\Delta\hbar^3 c^3}\mathrm{Re}[(\alpha\hat{z}\cdot\hat{q}\times\vec{A}_{2\omega})(\hat{q}\cdot\vec{A}_{-\omega})$$

$$\times(\alpha\hat{z}\cdot\hat{q}\times\vec{A}_{-\omega})e^{i(\phi_2-2\phi_1)}]\delta(\Delta-2\omega). \quad (23)$$

Equation (23) contains a factor of two from the sum over the (physical) spins. Equation (23) presents the main result of the paper. It shows that the transition rate depends on the polarization and phases of both exciting fields and the Bloch wave vector $\vec{q}$. We will explore the consequences of the geometric structure of this result for the graphene sheet and for carbon nanotubes in the following two sections. For the moment, we note that the result is odd in the direction of the Bloch wave vector $\hat{q}$ and even in the critical point index α (it depends on α^2) and therefore the symmetry breaking nonlinearity is nonzero after integration over the full Brillouin zone.

V. APPLICATION TO GRAPHENE

In this section, we apply the formalism developed in Sec. III to study the coherent optical control of photocurrents for a single-graphene sheet. The model nicely illustrates the selection rules which apply in this geometry, and the results can be extended to analyze the more complex situation for the nanotube, which will be presented in Sec. VI.

We note that both Eqs. (20) and (23) contain terms that describe transitions from the valence to the conduction band at the frequency $2\omega=\Delta$. Equation (20) is the ordinary linear absorption in the material. Interestingly, we see that the angular distribution of the excited photocarriers is not isotropic but rather follows a $\sin^2\phi$ dependence with respect to the polarization of the exciting radiation. Nevertheless, this angular distribution has even parity and thus does not produce a net current. On the other hand, Eq. (23) gives an angular distribution that breaks the inversion symmetry of the graphene sheet. The symmetry breaking is actually implicit in the coherent superposition of the exciting fields. We will estimate the prefactors to compare the relative strengths of these terms for accessible laboratory fields later in the paper; for the moment we note that the nonlinear terms in Eq. (23) typically contribute $\approx 10^{-3}$ of the total transition rate, and thus the induced anisotropy while nonzero (and we believe measurable) is a subtle effect.

The angular distribution in Eq. (23) is controlled by the relative polarizations and phases of the incident $\vec{A}_\omega$ and $\vec{A}_{2\omega}$ fields. Figure 2 displays polar plots of the angular distribu tions for the situation where the amplitudes are in phase [i.e. $\vec{A}_\omega$ and $\vec{A}_{2\omega}$ in Eq. (14) are presumed to be real] for variou incident polarizations. Note that the underlying electroni dispersion relations are completely isotropic in the linearize theory, and thus only the relative polarization of the tw exciting fields is relevant for the interference pattern. In al cases $\vec{A}_\omega$ is taken to be polarized along the horizontal direc tion shown by the arrow in the plots. In each plot, we ob serve a node in the current distribution along this direction This follows from the symmetry of $H^b_{\alpha,inl}$ in Eq. (13), whic shows that interband coupling is prohibited for $\hat{q}$ parallel t $\vec{A}$. Nonetheless, the situation for collinear ω and 2ω excita tion clearly shows the asymmetry between the "forward" and "backward" distribution of the photocurrent. The situa tion is more interesting when the exciting fields are noncol linear. We observe that the angular distribution develops "three lobe" structure. Ultimately, when the exciting field area mutually orthogonal, we recover the "two lobe" patter with the angular distribution rotated by $\pi/2$ with respect t the polarization of the incident ω field. It is useful to quan tify the anisotropy of the distribution by calculating the av erage polarization of the net photocurrent $\langle\cos\phi\rangle$ and $\langle\sin\phi$ averaged over this distribution. One finds

$$\langle\cos\phi\rangle=\frac{1}{2}\cos\theta$$

$$\langle\sin\phi\rangle=-\frac{1}{2}\sin\theta \quad (24$$

so that when the 2ω field is tipped by an angle θ with respec to the ω field, the photocurrent is oriented in the direction $-\theta$. Finally, the "sign" of the effect is determined by th relative phases of the two exciting fields. Note that the phas delays ϕ_1 and ϕ_2 in the exciting fields of Eq. (14) modulat the transitions rates[4] in Eq. (23) in the combination

$$(\dot{\rho}'_3)_{22}\rightarrow(\dot{\rho}_3)_{22}\cos(\phi_2-2\phi_1). \quad (25$$

This does not change the qualitative features of the angula distribution but it can modify both its magnitude and it overall sign.

Thus the angular distribution in the collinear case $\Delta\theta=0$ can be reversed by advancing the phase of the ω fields by $\pi/2$.

VI. APPLICATION TO NANOTUBES

A. Low-Energy Theory for Semiconducting Tubes

In this section, we apply the formalism of Sec. III to study phase coherent control of a photocurrent on a carbon nanotube. The essential complication is that the wrapped structure of the nanotube quantizes the allowed crystal momenta so that the transition rate automatically contain an intrinsic anisotropy. Nevertheless, the formalism developed in Sec. III can be extended to include this situation.

We first define the geometry for the single-wall nanotube. The nanotube is a cylinder formed by wrapping a graphene sheet and the wrapping can be defined by the graphene superlattice translation vector around the tube waist. We adopt the primitive vectors of Eq. (1) as a basis and represent the superlattice translation $\vec{T}_{MN}$ as

$$\vec{T}_{MN}=M\vec{T}_1+N\vec{T}_2=\left(M+\frac{N}{2},\frac{\sqrt{3}N}{2}\right)a. \tag{26}$$

It is useful to define two unit vectors defining the longitudinal and azimuthal directions within the graphene plane

$$\hat{e}_l=(\cos\theta_c,\sin\theta_c)$$

$$\hat{e}_a=(-\sin\theta_c,\cos\theta_c), \tag{27}$$

where $\theta_c=\cos^{-1}(M+N/2)/(\sqrt{M^2+N^2+MN})$ is the chiral angle of the tube. The wrapping of the tube quantizes the allowed momenta along the azimuthal direction $\vec{k}\cdot\hat{e}_a=2\pi n/(a\sqrt{M^2+N^2+MN})$ while the electrons obey free particle boundary conditions along the tube direction and the longitudinal component $\vec{k}\cdot\hat{e}_l$ can take any value.[8–10] Thus, the loci of allowed momenta are "lines" in reciprocal space. These lines need not intersect the critical K and K' points, which are used as a reference for the long-wavelength theory. To determine the mismatch between the allowed crystal momenta and the K and K' point wave functions we resolve the Bloch wave vector at K and K' into its longitudinal and azimuthal components. We find

$$K_\alpha=\frac{4\pi}{3a}\left(\frac{\alpha}{2},\frac{\sqrt{3}}{2}\right) \tag{28}$$

and

$$K_\alpha\cdot\hat{e}_a=\frac{2\pi}{3a}\left[\frac{2\alpha M+N(3+\alpha)}{2\sqrt{M^2+N^2+MN}}\right], \tag{29}$$

which lies along the locus of allowed wave vectors when $2\alpha M+(3+\alpha)N=6n$. One third of the (M,N) tubes satisfy this condition, and for the remaining two thirds of the tubes the $K(K')$ momenta are mismatched to the kinematically allowed momenta by a minimum amount

$$\Delta_\alpha=\frac{2\pi}{3a\sqrt{M^2+N^2+MN}}(-1)^{\mathrm{mod}(\alpha(N-M),3)}. \tag{30}$$

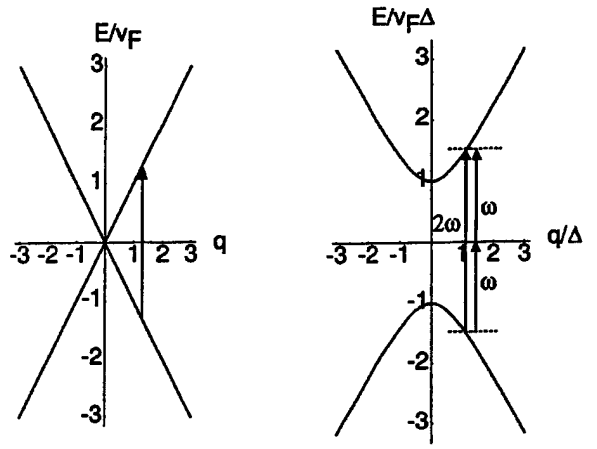

FIG. 3. Optical excitation between lowest subbands of a conducting tube (left panel) are forbidden in the long-wavelength theory. They are allowed for a semiconducting tube (or for the gapped subbands of a conducting tube) as shown on the right. Δ denotes the crystal momentum mismatch between the valence and conduction band states and the $K(K')$ points of the graphene sheet. The right-hand panel illustrates one- and two-photon excitations, which interfere to produce a polar asymmetry in the photocurrent.

Representing the "reduced" Bloch wave vector with the complex number $\tilde{q}=q_x+iq_y=qe^{i\theta_c}$ and the momentum mismatch by $\tilde{\Delta}_\alpha=i\Delta e^{i\theta_c}$ after a rotation of the coordinate system by the chiral angle θ_c (so that the x axis runs parallel to the tube length) the Hamiltonians in Eqs. (6) and (7) can be written

$$H_\alpha(q)=\hbar v_F\begin{pmatrix}0 & \alpha q+i\Delta_\alpha\\ \alpha q-i\Delta_\alpha & 0\end{pmatrix}. \tag{31}$$

Note that in Eq. (31) $H_\alpha(q)=H^*_{-\alpha}(-q)$. The spectrum is now $E(q)=\pm\sqrt{q^2+\Delta^2}$ and the Hamiltonian is diagonalized with the unitary transformation

$$U_\alpha(q)=\frac{1}{\sqrt{2}}\begin{pmatrix}1 & 1\\ -\alpha e^{-i\alpha\gamma} & \alpha e^{-i\alpha\gamma}\end{pmatrix}, \tag{32}$$

where $\gamma=\tan^{-1}(\Delta/q)$. This is the rotation identified in Eq. (8) for the unfolded graphene sheet with Δ playing the role of the y component of the momentum. With this identification the interaction Hamiltonian for the nanotube analogous to Eq. (13) in the band basis is

$$H^b_{\alpha,int}(q,A)=\frac{ev_FA}{c}\frac{1}{\sqrt{q^2+\Delta^2}}\begin{pmatrix}-q & i\alpha\Delta\\ -i\alpha\Delta & q\end{pmatrix}. \tag{33}$$

Note that the off-diagonal terms which describe the amplitudes for interband transitions depend explicitly on the size of the semiconducting backscattering gap Δ and vanish for the lowest subbands of a conducting nanotube as shown in Fig. 3.

Thus, when the exciting fields are collinear and directed along the tube direction the third-order transition rate is

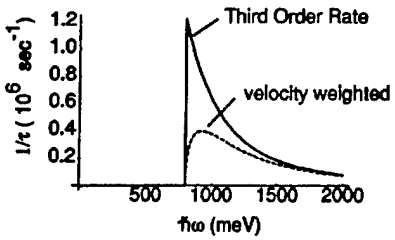

FIG. 4. Frequency dependence of the third-order transition rate leading to anisotropy of the photocurrent. The solid curve gives the transition rate of Eq. (30) as a function of the exciting frequency $\hbar\omega$. To display the spectra we have taken a semiconducting gap $\hbar v_F\Delta = 800$ meV and normalized the incident intensity so that $|A| = 10^{-9}$ T-m at all frequencies. The dashed curve is the transition rate weighted by the final state velocity. Band-edge states are strongly scattered by the mass term and do not contribute effectively to the photocurrent.

$$(\dot{\rho}_3)_{22} = \frac{4\pi\alpha^2 e^3 v_F^6}{\hbar^2 c^3 \omega^4} \Delta^2 q \,\mathrm{Re}\,(A_{2\omega} A_{-\omega} A_{-\omega} e^{i(\phi_2 - 2\phi_1)}) \times \delta[2E(q) - 2\hbar\omega]. \tag{34}$$

Equation (34) is the origin of the asymmetry discussed in Ref. 5. We note that the result depends on the square of the magnitude of the gap Δ and it vanishes for transitions between the lowest subbands of a conducting tube. The result is odd in the reduced momentum q which produces an asymmetry between forward and backward moving photocarriers. The third-order transition rate is very small for high exciting frequency since the high-energy electrons are very weakly backscattered through the mass term in Eq. (31) and behave essentially as free particles. These properties are displayed in Fig. 4 which shows the third-order transition rate between two bands of a semiconducting tube as a function of the exciting frequency. It is interesting to note that the expected divergence in the one dimensional density of states at threshold is exactly canceled by the momentum prefactor q in Eq. (34) and thus the spectrum shows only a steplike singularity at the threshold. Thus, the transition probability for right- and left-moving photocarriers jumps discontinuously across the critical point at $q = 0$. Note however that the states near the band gap have no group velocity and cannot contribute to the photocurrent so the velocity weighted transition rate (which is more relevant to this application) goes to zero at threshold. This is shown by the dashed curve in Fig. 4. The results in Fig. 4 show the nonlinear injection rate for a perfect defect free semiconducting tube. A slowly varying impurity potential (long range disorder in the notation of Ref. 12) can produce an additional channel for backscattering and will therefore further suppress the group velocity for electronic states near the band edges. In the presence of disorder, we therefore expect an additional rounding of the current injection rate, similar to that shown as the dashed curve in Fig. 4. The range and strength of this suppression will depend sensitively on the details of the long-range impurity potential. The results of Fig. 4 are insensitive to this additional backscattering deeper into the particle-hole continuum.

B. Crystal-field effects for conducting tubes

Equation (34) gives the third-order nonlinear response in the long-wavelength limit where we can linearize the electronic bands around the critical $K(K')$ points. Corrections to this result can be obtained in an expansion in qa and physically arise from crystal-field ("trigonal warping") effects in the underlying band structure. The most significant such corrections occur for conducting tubes. Equation (34) gives a vanishing transition rate for excitations between the lowest bands of a conducting tube and trigonal warping of the band structure of the graphene sheet provides a mechanism to "turn on" these transitions even for conducting tubes. Thus a third-order nonlinear response is symmetry allowed for the lowest subbands of a conducting nanotube, though it strictly vanishes in the long-wavelength limit we have discussed so far.

To investigate the trigonal warping effects we rederive the interaction Hamiltonian without adopting the effective mass representation. To do this we note that in the presence of a vector potential $\vec{A}$ the Hamiltonian (5) is perturbed through the Peierls substitution $\vec{k} \to \vec{k} - (Q/c)\vec{A}$. Therefore, we can calculate the current operator using $j_\mu = -\partial H/\partial A_\mu = (Q/c)\partial H/\partial k_\mu$. In the site representation the Hamiltonian has only off-diagonal elements, so we can write

$$H_{int} = -\frac{e}{c}\vec{A}\cdot\begin{pmatrix} 0 & \nabla_k t(\vec{k}) \\ \nabla_k t^*(\vec{k}) & 0 \end{pmatrix}. \tag{35}$$

We also note that the Hamiltonian is diagonalized with the unitary transformation:

$$U(\vec{k}) = \frac{1}{\sqrt{2}}\begin{pmatrix} 1 & 1 \\ -\dfrac{t^*(\vec{k})}{|t(\vec{k})|} & \dfrac{t^*(\vec{k})}{|t(\vec{k})|} \end{pmatrix}, \tag{36}$$

which is the discrete lattice analog of the continuum result in Eq. (8). Thus, we can rotate the interaction Hamiltonian into the band basis according to $U^\dagger(\vec{k}) H_{int}(\vec{k}) U(\vec{k})$, which gives

$$H^b_{int}(\vec{k}) = -\frac{e}{c}\frac{A_\mu}{|t(k)|}\begin{pmatrix} -\mathrm{Re}\,(t^*\partial_{k_\mu} t) & i\,\mathrm{Im}\,(t^*\partial_{k_\mu} t) \\ -i\,\mathrm{Im}\,(t\partial_{k_\mu} t^*) & \mathrm{Re}\,(t^*\partial_{k_\mu} t) \end{pmatrix}. \tag{37}$$

Explicit evaluation of the matrix elements in Eq. (36) for a general chiral nanotube is complicated. *In general*, one may have interband matrix elements between lowest subbands of a conducting tube [which are the off-diagonal terms in Eq. (37)]; albeit with greatly reduced magnitudes—the scale of these matrix elements is typically $\approx 10^{-2}$ the scale for the matrix elements in Eq. (31), which are produced by the mass term in the linearized theory for a semiconducting tube. An important exception to this rule for conducting tubes occurs for the armchair (M,M) tubes. Then one finds that $t(k) = e^{2\pi i/3}[1 + 2\cos(k_x a)]$ for propagation in the lowest subbands of the tube, and we have

$$[t^*(k_x)\partial_k t(k_x)]/|t(k_x)| = ta\,\mathrm{sgn}\,[1 + 2\cos(k_x a)]\sin(k_x a). \tag{38}$$

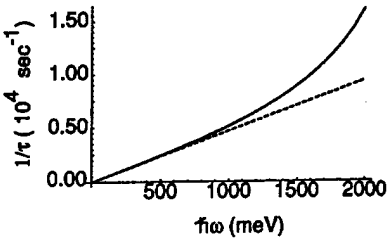

FIG. 5. Frequency dependence of the third-order transition rate involving the lowest subbands of a conducting zigzag tube, which produce an anisotropy of the photocurrent. The dashed curve uses a linear dispersion relation for the electronic states with the matrix elements computed using the lattice theory of Eq. (37). The normalization of the incident fields is the same as for the results of Fig. 4 so that the rates can be directly compared (note the vertical scale change). These interband excitations are symmetry forbidden in the Dirac theory but become weakly allowed in the presence of crystal-field effects on the low-energy electronic states. For a conducting tubes third-order transitions between the gapped subbands provide a much stronger nonlinear third-order response, as shown in Fig. 4.

Thus, near the critical points the diagonal elements of the velocity operator are $\pm v_F$ and the off-diagonal components vanish *everywhere*. Note that this occurs because of a tube symmetry; the armchair tube retains a mirror plane, which contains the tube axis so that the two lowest subbands of the conducting tube can be indexed as even or odd under reflection through this mirror plane. The vector potential along the tube axis is even under the mirror reflection and cannot couple even and odd subbands. On the other hand, for a zigzag tube one has $t(k)=e^{ik_y a/\sqrt{3}}(1+e^{-i\sqrt{3}k_y a/2})$. This vanishes for $k_y=2\pi/\sqrt{3}a$ which corresponds to a "face" of the Brillouin zone in Fig. 1. Thus, one finds for the conducting zigzag tube

$$(t^*\partial_k t)/|t| = \frac{ta\left[\frac{i}{\sqrt{3}}\cos^2(\sqrt{3}ka/4)\right]-\left[\frac{\sqrt{3}i}{2}\cos(\sqrt{3}ka/4)e^{\sqrt{3}ik_y a/4}\right]}{|\cos(\sqrt{3}ka/4)|}. \tag{39}$$

Therefore, near the crossing point $k_y=(2\pi/\sqrt{3}a)+q$ one finds

$$(t^*\partial_k t)/|t| \approx \frac{\sqrt{3}ta}{2}\left(1-i\frac{qa}{2\sqrt{3}}+\cdots\right). \tag{40}$$

Thus, the diagonal matrix elements of the velocity operator [the real part of Eq. (39)] are constant $[v_F(1+\mathcal{O}(qa))^2]$ while the off-diagonal elements (the imaginary part) vanish proportional to qa near the Fermi points. This implies that the product of the matrix elements in the third-order transition rate vanish as $(qa)^2$ for the conducting zigzag tube. This changes both the magnitude and the frequency dependence of the third-order transition rate. We obtain

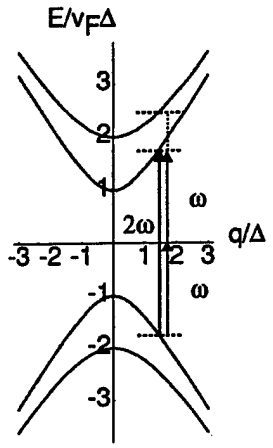

FIG. 6. Interfering excitations when the ω field is polarized perpendicular to the tube and the 2ω field is polarized along the tube direction. The 2ω field excites transitions between subbands with the same azimuthal quantum numbers. The ω field excites transitions with $\delta m=\pm 1$.

$$(\dot{\rho}_3)_{22}=\frac{\pi e^3 v_F}{12\hbar^2 c^3}a^2\omega\,\mathrm{sgn}(q)\,\mathrm{Re}\,(A_{2\omega}A_{-\omega}A_{-\omega} \times e^{i(\phi_2-2\phi_1)})\,\delta[2(|t(q)|-\hbar\omega)]. \tag{41}$$

The result is plotted in Fig. 5 using the same normalization as in Fig. 4 for comparison (note the scale change). One finds that the transition rate vanishes linearly in frequency, and is suppressed by $\approx 10^{-2}$ with respect to the interband transition rate for a semiconducting tube. This reflects the fact that at low-energy the effects of trigonal warping are relatively small compared to the backscattering from the mass term in the low-energy Hamiltonian for a semiconducting tube. We note that calculations of the frequency dependence of the resonant Raman cross section for conducting tubes[11] show a strong enhancement of the cross section near the first interband threshold, also demonstrating the suppression of interband transition matrix elements between the lowest conducting subbands in these structures.

Figure 5 presents *only* the results for excitations coupling the lowest subbands of a conducting tube. Transition rates between gapped subbands are described by Eq. (34) so that the transition rate displayed in Fig. 4 should be superposed on these results. This situation calculated for a zigzag tube illustrates the generic behavior for a general (M,N) tube if one wishes to calculate beyond the linearized theory. Analogous results for arbitrary chiral tubes can be obtained by direct evaluation of the matrix elements in Eq. (37).

C. Noncollinear fields

This treatment can be extended to include the situation where the exciting fields are not collinear. Interestingly, this does not change the qualitative frequency dependence shown in Fig. 4, although the prefactor is altered for noncollinear fields.

We will consider only the case where the exciting fields are orthogonal, since any incident field can be resolved into its longitudinal (along the tube) and transverse (perpendicular to the tube) components. We observe that for a field perpendicular to the tube axis we have allowed interband tran-

sitions only when the azimuthal quantum number m changes by ± 1 since the vector potential A "seen" in the tangent plane of the tube is $\vec{A}\cdot\hat{\phi}=A\cos\phi$ where $\hat{\phi}$ is a unit vector that circulates counterclockwise around the tube waist. For the graphene sheet this is equivalent to introducing a spatially varying vector potential with wavevector $1/R$ where R is the tube radius. Thus, the third-order nonlinear process we are seeking is symmetry forbidden if $\vec{A}_{2\omega}$ has a transverse polarization (the lowest subbands have the same azimuthal quantum numbers.) However, it is possible to have the situation shown in Fig. 6, where $\vec{A}_{\omega}$ is perpendicular to the tube axis, and $\vec{A}_{2\omega}$ is polarized along the tube direction. Here the virtual intermediate state for the two-photon process is provided by a higher azimuthal subband.

This reduces the strength of the effect, but not the overall frequency dependence, which is controlled by dispersion of the lowest azimuthal subband that is accessed to second order in $\vec{A}_{\omega}$.

We modify the interaction Hamiltonian Eq. (33) for the situation where the exciting radiation is polarized perpendicular to the tube direction. In the "site" basis one finds that the interaction Hamiltonian for this polarization is

$$H^{s}_{\alpha,int}=\frac{ev_FA}{c}\begin{pmatrix}0 & -i\\ i & 0\end{pmatrix}, \tag{42}$$

where $A=A(y)=A_0\cos(y/R)$. The y dependence implies that this interaction couples subbands with a difference in azimuthal quantum numbers m such that $\delta m=\pm 1$ and we will explicitly consider only the two low-energy pairs of subbands as shown in Fig. 6, which we label 1 and 2. The Hamiltonian in Eq. (42) can now be rotated into the band basis using the unitary rotations of Eq. (32) in the combination $H^{b}_{\alpha,int}=U_2^{\dagger}(q)H^{s}_{\alpha,int}U_1(q)$, which gives

$$H^{b}_{\alpha,int}=\frac{ev_FA}{c}e^{i(\gamma_2-\gamma_1)/2}\begin{pmatrix}\sin[\alpha(\gamma_1+\gamma_2)/2] & i\cos[\alpha(\gamma_1+\gamma_2)/2]\\ -i\cos[\alpha(\gamma_1+\gamma_2)/2] & \sin[\alpha(\gamma_1+\gamma_2)/2]\end{pmatrix}. \tag{43}$$

Thus, the second-order coherence term [analogous to Eq. (22) for the graphene sheet] is

$$(\rho_2)_{12}=-\frac{ie^2v_F^2A_{\omega}^2}{\hbar^2c^2}\frac{\alpha^2\sin(\gamma_1+\gamma_2)e^{-i(\Delta-2\omega)t}}{[-E_2(q)-E_1(q)+\omega-i\delta][-2E_1(q)+2\omega-i\delta]}. \tag{44}$$

The coherence factor appearing in Eq. (44) can be re-expressed in terms of the Hamiltonian parameters

$$\sin(\gamma_1+\gamma_2)=\frac{q(\Delta_2-\Delta_1)}{E_2(q)E_1(q)}, \tag{45}$$

where $E_m(q)=\sqrt{q^2+m^2\Delta^2}$ and Δ is the lowest gap of the semiconducting tube. Note that the effect vanishes for $\Delta_1=\Delta_2$, i.e. between subbands of the same azimuthal symmetry. The second-order coherence factor leads to the symmetry breaking third-order transition rate

$$(\dot{\rho}_3)_{22}=\frac{4\pi\alpha^2e^3v_F^3}{\hbar^3c^3\omega^4}\frac{(\Delta_2-\Delta_1)\Delta_1qE_1}{E_2}\mathrm{Re}(A_{2\omega}A_{-\omega}A_{-\omega}\times e^{i\phi_2-2i\phi_1})\delta[2(E(q)-\hbar\omega)], \tag{46}$$

which has exactly the same frequency dependence as the result of Eq. (34).

VII. DISCUSSION

Third-order phase coherent control of photocurrents have been studied and demonstrated for semiconductors [e.g., GaAs (Refs. 2, 3, and 13)] and since the effects calculated for carbon nanotubes are strongest for semiconducting tubes, it is appropriate to compare these effects. We find that the predicted effects are significantly stronger in nanotubes than for conventional semiconductors. This occurs because of the larger carrier velocities and the longer carrier relaxation times that are expected for the nanotubes. For carbon nanotubes this is particularly interesting since this third-order nonlinearity provides a method for current injection without contacts. It has proven experimentally difficult to fabricate low-resistance electrical contacts with carbon nanotubes by conventional submicron lithographic methods.

For an incident intensity $S=10^2$ kW/cm^2 the electric field amplitude $E=8.5\times10^5$ V/m$\approx10^6$ V/m. At an optical frequency $\omega=10^{15}$ s^{-1} this corresponds to a vector potential amplitude $|A|\approx10^9$ T−m (which is the value used in obtaining the results in Figs. 4 and 5). Then we find that the typical carrier injection rate $dn/dt\approx10^6$ s^{-1} per unit cell. For hot photoexcited carriers the relaxation rate is presumed to be dominated by phonon emission, for which we estimate a carrier relaxation time $\tau\approx1$ ps so the steady state distribution gives $\bar{n}\approx10^{-6}$ carriers per tube unit cell (note that the unit cell contains typically 40–60 carbon atoms around the tube circumference). Summing over the electron and hole contributions to the photocurrent and over the two electronic branches (K and K') we obtain an induced current $I\approx$ 0.4 nA, or an effective current density $J\approx260$ μA/μm^2. This is $10-10^2$ larger than the induced density predicted for third order transitions between the valence and conduction bands in GaAs.[13] The enhancement is due mainly to the relatively large carrier velocity for the carbon nanotubes, and the larger estimated carrier relaxation times. For conducting tubes this enhancement is partially offset by the *small* interband matrix

elements between the lowest subbands of conducting tubes; for a conducting zigzag tube we estimate the photocurrent density $J \approx 5\ \mu A/\mu m^2$ under the same assumptions, a value which is comparable to that found for conventional semiconductors.[13] We note that even with these long carrier relaxation times, one should be able to achieve a steady state distribution during a 100-ns incident pulse. For conducting nanotubes one has the additional difficulty of resolving this signal over a background free carrier density $\bar{n}_b \approx 10^{-5}$ produced by ordinary one-photon excitation between the lowest subbands [first term in Eq. (20)]. Since this is a "nonpolar" contribution, i.e., it does not contribute to the photocurrent, the nonlinear contribution can be identified, in principle.

The angular distributions calculated for interband excitations in graphene sheets show a similar structure to the angular dependence calculated for the third-order rate for transitions from the heavy-hole band to the conduction band in GaAs.[13] In both cases the net induced current is polarized along the direction of the exciting field, but the current distribution is peaked *away* from the field direction. The high symmetry of the graphene sheet provides an additional interesting degree of freedom, namely control of the direction of the injected current by controlling the *relative* polarizations of the incident fields, as displayed in Fig. 2. It would be very interesting to carry out experiments on graphite (either bulk or thin films) to verify the predicted angular dependence. Quantitative studies of the magnitude of the effect would be very useful as a probe of the scattering processes which control the dynamics of hot photoexcited carriers in these systems. We note that previous experiments on GaAs have observed the third-order nonlinearity, but with an amplitude that is an order of magnitude smaller than predicted theoretically.

For carbon nanotubes, one can anticipate at least three interesting applications of this phenomenon. First, as noted above, the method provides a means for current injection without electrical contacts. The absence of "low resistance" contacts on carbon nanotubes has often made it difficult to explore low-energy transport phenomena in these systems.[14–16] A particularly interesting experiment would be to use the third-order nonlinearity to produce a steady state separation of charge in a carbon nanotube rope or mat. In this state the "driving force," which produces a photocurrent via the third-order nonlinearity would be balanced by the internal electric field produced by charge separation (in an open circuit condition). The relaxation of this charge distribution after the driving fields are turned off directly measures the conductivity *along* the pathways for charge motion in the system. Thus measurement of the transient relaxation after pulsed excitation would provide an interesting probe of the microscopic conductivity in this structurally heterogeneous system. Second, one can imagine applications that make use of the enhancement of the effect on semiconducting tubes (and its suppression in conducting tubes) to isolate semiconducting and conducting species in compositionally mixed samples. Finally, momentum transfer from the photoexcited carriers to intercalated ionic species can be used in principle to bias the diffusion of atomic or molecular species in the current carrying state. This effect requires *in addition* an asymmetry between the amplitudes for backscattering electrons and holes from the dopant species. This interesting application has been discussed in Ref. 5 using a simple model for the momentum transfer.

ACKNOWLEDGMENTS

We thank C. L. Kane for helpful comments about this problem. Work at Penn was supported by the DOE under Grant No. DE-FG02-84ER45118 and by the NSF under Grant No. DMR 98-02560. Work at Toronto was supported by Photonics Research, Ontario.

[1] G. Kurizki, M. Shapiro, and P. Brumer, Phys. Rev. B **39**, 3435 (1989).
[2] R. Anatosov, A. Haché, J. L. P. Hughes, H. M. van Driel, and J. E. Sipe, Phys. Rev. Lett. **76**, 1703 (1996).
[3] Y-Y. Yin, C. Chen, D. S. Elliot, and A. V. Smith, Phys. Rev. Lett. **69**, 2353 (1992).
[4] E. Dupont, P. B. Corkum, H. C. Liu, M. Buchanan, and Z. R. Wasilewski, Phys. Rev. Lett. **74**, 3596 (1995).
[5] P. Král and D. Tománek, Phys. Rev. Lett. **82**, 5373 (1999).
[6] C. L. Kane and E. J. Mele, Phys. Rev. Lett. **78**, 1932 (1997).
[7] M. O. Scully and M. Suhail Zubairy, *Quantum Optics* (Cambridge University Press, Cambridge, 1997), Chap. 5.
[8] J. W. Mintmire, B. I. Dunlap, and C. T. White, Phys. Rev. Lett. **68**, 631 (1992).
[9] N. Hamada, S. Sawada, and A. Oshiyama, Phys. Rev. Lett. **68**, 1579 (1992).
[10] R. Saito, M. Fujita, G. Dresselhaus, and M. S. Dresselhaus, Appl. Phys. Lett. **60**, 2704 (1992).
[11] E. Richter and K. R. Subbaswamy, Phys. Rev. Lett. **79**, 2737 (1997).
[12] P. L. McEuen, M. Bockrath, D. H. Cobden, Y. G. Yoon, and S. G. Louie, cond-mat/9906055 (unpublished).
[13] P. Král and J.E. Sipe, Phys. Rev. B (in press).
[14] A. Bezryadin, A. R. M. Verschuren, S. J. Tans, and C. Dekker, Phys. Rev. Lett. **80**, 4036 (1998).
[15] Ph. Avouris and R. Martel, *Physics and Chemistry of Nanostructured Materials* (Taylor & Francis, London, 1999).
[16] A. Bachtold *et al.*, Nature (London) **397**, 673 (1999).

Photogalvanic Effects in Heteropolar Nanotubes

Petr Král,[1] E. J. Mele,[2] and David Tománek[3]

[1]*Department of Chemical Physics, Weizmann Institute of Science, 76100 Rehovot, Israel*

[2]*Department of Physics, Laboratory for Research on the Structure of Matter, University of Pennsylvania, Philadelphia, Pennsylvania 19104*

[3]*Department of Physics and Astronomy, and Center for Fundamental Materials Research, Michigan State University, East Lansing, Michigan 48824-1116*

(Received 18 January 2000)

We show that an electrical shift current is generated when electrons are photoexcited from the valence to conduction bands on a BN nanotube. This photocurrent follows the light pulse envelope and its symmetry is controlled by the atomic structure of the nanotube. We find that the shift current has an intrinsic quantum mechanical signature in which the chiral index of the tube determines the direction of the current along the tube axis. We identify the discrete lattice effects in the tangent plane of the tube that lead to an azimuthal component of the shift current. The nanotube shift current can lead to ultrafast optoelectronic and optomechanical applications.

PACS numbers: 72.40.+w, 61.48.+c, 78.20.Jq, 85.40.Ux

Recent progress in synthesis of nanometer scale materials has led to the discovery of $B_xC_yN_z$ nanotubes. They can be formed in nearly homogeneous ordered structures [1,2] or in multiwall hybrid structures with alternating BN and C compositions [3]. These materials differ fundamentally from the structurally similar carbon nanotubes by being *noncentrosymmetric* (NCS) and *polar*. This opens the possibility for accessing a new class of photovoltaic effects at the molecular scale.

Photovoltaic effects in NCS materials are often based on an asymmetric generation of hot carriers at momenta $\pm\mathbf{k}$ leading to a so-called "ballistic photocurrent" [4–6]. In polar NCS materials, photoexcitation across the band gap with polarized light also produces the so-called electrical "shift current" [7–9]. Microscopically this originates from a net displacement of charge in the unit cell due to light induced interband transitions ($\mathbf{J}_e$), intraband relaxation ($\mathbf{J}_s$), and (radiative) transitions to the original bands ($\mathbf{J}_r$). In bulk materials, the excitation component $\mathbf{J}_e$ usually prevails.

We show that *unpolarized light* can induce a shift current $\mathbf{J}_e$ in polar NCS nanotubes, with a direction along the tube axis which is determined by the chiral index of the tube. We find that this effect has an essentially quantum mechanical origin, where the *sign* of the current along the tube axis is controlled by the phase matching of electronic Bloch waves around the tube circumference. The discrete lattice structure controls the azimuthal component of this current and thus produces a net *helical current* on the tube. These photoeffects can lead to an assortment of new optoelectronic, optomechanical, and magnetic applications, and interesting extensions to ring structures [10] and heterojunctions [11]. We should stress that the photoeffects we discuss here are found at nonlinear order in the exciting fields, and are therefore physically distinct from chiral currents tilted with respect to the tube axis, predicted in dc bias driven chiral BN nanotubes [12] or chiral stretched C nanotubes [13,14].

A flat BN sheet has a honeycomb lattice with the B and N occupying alternate sublattices as shown in Fig. 1. The physics of the shift current can be understood qualitatively by considering the response of this 2D network of bonds to normally incident polarized light. The valence states are polarized towards the N sites and the conduction states towards the B sites. For vertically polarized (y-polarized) incident light the response of the system is dominated by the bonds which produce a net y-polarized current. For horizontally (x-polarized) incident light, the bonds with a nonzero horizontal component dominate, but these also produce a net y-polarized current. Note that excitation with an unpolarized incident field *cannot* produce a net current on this lattice since it has a threefold symmetry. However, this symmetry is removed when the sheet is wrapped into a cylindrical nanotube where the physics should be dominated by excitations with the field polarized along the tube axis. Depending on the wrapped structure of the tube, we anticipate an intrinsic photocurrent which can flow along the tube, around the tube, or in a chiral pattern on the tube surface.

These ideas can be quantified by developing a quantum mechanical model which generalizes our long wavelength theory for a nonpolar carbon nanotube [15] to the heteropolar lattice. We work in a basis of Bloch orbitals $\Phi_{k\alpha}(r) = e^{ik\cdot r}\sum_n e^{-ik\cdot(r-R_n-\tau_\alpha)}\phi_{n\alpha}/\sqrt{N} = e^{ik\cdot r}U_{k\alpha}$ where $\alpha = \pm 1$ denotes the two sublattices occupying sites at τ_α in the nth unit cell. We study the states near the conduction and valence band edges at the K and K' points of the Brillouin zone shown in Fig. 1. A long wavelength Hamiltonian for these states is obtained by an expansion in small crystal momenta around these points, and yields in our two component basis ($\hbar = 1$)

 0031-9007/00/85(7)/1512(4)$15.00

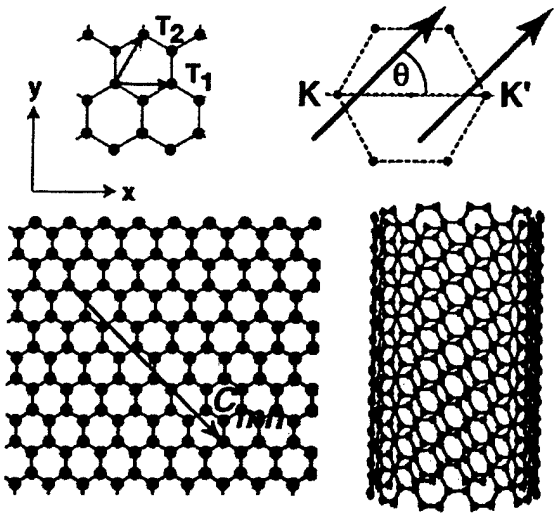

FIG. 1 (color). Planar BN forms a honeycomb lattice with B and N occupying alternate sites (upper left). A BN tube is formed by wrapping the sheet through the translation vector C_{mn} (lower left) quantizing the transverse crystal momenta. The upper right-hand panel shows two representative lines of allowed momenta for a tube with a nonzero chiral index $\nu = \mathrm{mod}(m - n, 3)$ and chiral angle θ. The lower right panel shows the structure for the nonchiral armchair (10, 10) wrapping of the BN sheet.

$$H_\lambda(\Delta, k, \delta_\lambda) = \begin{pmatrix} \Delta & \lambda v_F(k - i\delta_\lambda) \\ \lambda v_F(k + i\delta_\lambda) & -\Delta \end{pmatrix}, \tag{1}$$

where $\lambda = \pm 1$ is an index which labels an expansion around the K or K' points. The Hamiltonian in Eq. (1) is parametrized by three energies: a symmetry breaking site diagonal potential Δ, the kinetic energy $v_F k$ for motion along the tube, and the kinetic energy $v_F\delta$ due to the quantization of the transverse momentum around the circumference of the tube. On a cylindrical tube with lattice constant a and primitive lattice translation vectors in its tangent plane $T_1 = a(1, 0)$ and $T_2 = a(1/2, \sqrt{3}/2)$ (Fig. 1) it is conventional to index the lattice structure by two integers m and n which define a superlattice translation vector $C_{mn} = mT_1 + nT_2$. The transverse momenta on an (m, n) tube are quantized to the values $\delta_N = \delta_0 + 2\pi N/|C_{mn}|$ where $\delta_0 = 2\pi\,\mathrm{sgn}(\nu)/3|C_{mn}|$, depending on the sign of the chiral index of the tube, $\nu = \mathrm{mod}(n - m, 3)$. In Eq. (1) $\delta_\lambda = \lambda\delta_N$.

The eigenvectors of H in Eq. (1) are

$$g_v = \begin{pmatrix} ue^{-i\phi/2} \\ -ve^{i\phi/2} \end{pmatrix} \frac{e^{i\theta_{vk}}}{\sqrt{2}}; \qquad g_c = \begin{pmatrix} ve^{-i\phi/2} \\ ue^{i\phi/2} \end{pmatrix} \frac{e^{i\theta_{ck}}}{\sqrt{2}}, \tag{2}$$

where $E = \sqrt{v_F^2(k^2 + \delta_\lambda^2) + \Delta^2}$, $\phi = \tan^{-1}(\delta_\lambda/\lambda k)$, $u = \sqrt{(E - \Delta)/E}$, and $v = \sqrt{(E + \Delta)/E}$. In the rest of this paper we will set the Fermi velocity $v_F = 1$ so that energies and momenta are measured in the same units. Equation (2) explicitly includes a gauge function θ_{mk} since the overall phase of the Bloch function is not fixed, and our calculation will require differentiation with respect to k. The Bloch eigenfunctions of our problem are expressed as the product of three factors $\psi_{km}(r) = e^{ik\cdot r}\sum_\alpha g_{m\alpha}(k)U_{k\alpha}(r)$.

We extend the model Hamiltonian in Eq. (1) to include coupling of electrons to the oscillating optical fields $\mathbf{E}(t) = \mathbf{E}e^{-i\omega t} + \text{c.c.}$ through the dipole operator [8,9] $H_{\mathrm{int}} = -e\mathbf{E}(t)\cdot\mathbf{r}$. For a field polarized along the tube direction the matrix elements of the dipole operator between band eigenstates m and m' at crystal momenta k and k' are expressed using a formulation due to Blount [16]

$$r_{m'm}(k', k) = \langle\psi_{k'm'}|r|\psi_{km}\rangle = -i\langle\psi_{k'm'}|\partial_k|\psi_{km}\rangle + i\delta(k - k')\sum_{\alpha\beta}\delta_{\alpha\beta}g^*_{m'\beta}(k')\partial_k g_{m\alpha}(k). \tag{3}$$

The second term on the right-hand side of (3) forms the connection $\xi_{m'm} = ig^*_{m'}(k)\cdot\partial_k g_m(k)$ due to the k dependence of the eigenstates in (2) [17].

In general the shift current $\mathbf{J}$ can be expressed in terms of the band off-diagonal matrix elements of the velocity operator $\mathbf{v}_{\beta\alpha}$ ($\mathbf{v} = i[H, \mathbf{r}]$), and the band off-diagonal term in the density matrix $\rho_{\alpha\beta}$, calculated to second order in the exciting fields $\mathbf{E}$, as follows [7–9]:

$$\mathbf{J} = 2e\sum_{m\neq n}\int\frac{dk}{2\pi}\mathbf{v}_{mn}(k)\rho_{nm}(k) = \mathbf{J}_e + \mathbf{J}_s + \mathbf{J}_r. \tag{4}$$

We focus on the component of the excitation current J_e *along the tube direction.* After evaluating the sum in (4), we arrive at the transparent result

$$J_e = 2e\int\frac{dk}{2\pi}\dot{f}_{cv}(k)R_{cv}(k) \approx e\dot{n}\mathcal{R}. \tag{5}$$

Here $\dot{f}_{cv}(k)$ is the transition rate at wave vector k, and the *shift vector* $R_{cv}(k)$ is given by

$$R_{cv}(k) = \partial_k\theta_{vc}(k) + \xi_{cc}(k) - \xi_{vv}(k) \tag{6}$$

with $\xi_{vc}(k) = |\xi_{vc}(k)|e^{i\theta_{vc}(k)}$. The shift vector $R_{cv}(k)$ is invariant under the gauge transformations $\exp(i\theta_{mk})$ and we will evaluate it in a gauge with $\partial_k\theta_{mk} = 0$.

For an incident electric field polarized along the tube direction, interband excitations are allowed only between band states with the same transverse momentum δ. For transitions between the lowest two azimuthal subbands ($N = 0$) using the eigenfunctions in Eq. (2) we find

$$\xi_{vc}(k) = \frac{-1}{2}uv\left(\frac{\Delta}{E^2 - \Delta^2}\partial_k E + i\partial_k\phi\right), \tag{7}$$

which gives the off-diagonal contribution in Eq. (6)

$$\partial_k\theta_{vc} = \partial_k\tan^{-1}\left(\frac{-\delta\sqrt{\delta^2 + \Delta^2 + k^2}}{k\Delta}\right). \tag{8}$$

The diagonal elements in Eq. (6) are

$$\xi_{mm}(k) = ig_m^\dagger\cdot\partial_k g_m = \mp\frac{\Delta}{2E}\left(\frac{\delta}{\delta^2 + k^2}\right), \tag{9}$$

where the sign is negative for valence states and positive for conduction states. Combining Eqs. (8) and (9) we obtain the shift vector

$$R_{cv}(k) = \frac{2\delta\Delta}{(\delta^2 + k^2)\sqrt{\delta^2 + \Delta^2 + k^2}}. \quad (10)$$

Comparison with Eq. (9) shows that the shift current [Eq. (5)] opposes the direction of the ground state polarization of the tube.

This shift vector is odd in the symmetry breaking potential Δ and *odd in the transverse momentum* δ. Therefore, two BN tubes with nearly the same wrapped lattice structure but *opposite* chiral indices ν exhibit reversed ground state polarizations and opposite shift currents. Armchair BN nanotubes with wrapping indices (m, m) have chiral index $\nu = 0$ and do not exhibit a longitudinal shift current [as shown in the middle panel in Fig. 2 for the (5,5) tube]. Zigzag BN tubes with wrapping indices $(m, 0)$ can be grouped into three families with positive, negative, or zero shift currents distinguished by the sign of the chiral index ν [an example for the (8,0) tube with $\nu = -1$ is in the left panel of Fig. 2]. It is important to notice that an isolated flat BN sheet has a threefold symmetry axis perpendicular to the BN plane and therefore it has zero electric polarization in its tangent plane, by symmetry. Thus it has no shift current for excitations at the band edge. The nonzero shift vector in Eq. (10) when $k \to 0$ is a remarkable long wavelength quantum mechanical effect that reveals the quantization of the transverse momentum on the wrapped tube.

The shift current J_e in Eq. (5) is determined by the average shift vector $\mathcal{R}$, describing the change of polarity in the excitation, and by the carrier injection rate $\dot{n}$. The BN bond has significant ionic character with [18] $2\Delta \approx 4$ eV. This gives for excitations near the band edge, $k \to 0$, a shift vector with a magnitude $\mathcal{R} \approx 0.06$ nm for a (17,0) tube. For an incident intensity $S = 100$ kW/cm^2 we can also obtain the interband excitation rate; we estimate that $\dot{n} \approx 70\ \text{nm}^{-1}\,\mu\text{s}^{-1}$ produces a net electronic shift current of $J_e \approx 0.67$ pA. This value is slightly larger than what one obtains for excited bulk polar semiconductors. Opposing shift currents on different walls of a coaxial multiwall tube can reduce the macroscopic current, but cannot eliminate it except for rare high symmetry concentric lattice structures. We also expect that the recombination current J_r will oppose J_e since both currents rely on optical transitions with longitudinal polarization. However, this should not prevent the observation of J_e using pulsed laser excitation since the time scale for J_r is of the order of nanoseconds.

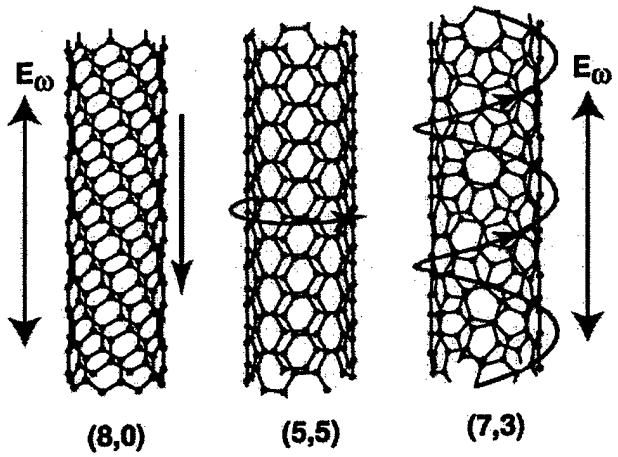

FIG. 2 (color). Electronic shift currents produced by excitation of BN nanotubes with light polarized along their axis. For the (8,0) wrapping the chiral index is $\nu = -1$, and the shift current is purely longitudinal. The (5,5) armchair wrapping has chiral index $\nu = 0$ and has zero longitudinal current and a nonzero azimuthal current which runs "counterclockwise" on the tube surface. The (7,3) wrapping has a chiral shift current with nonzero longitudinal and azimuthal components.

This formalism can be extended to study *chiral shift currents* with nonvanishing longitudinal and azimuthal components. Interestingly, the long wavelength Hamiltonian in Eq. (1) gives zero azimuthal current for *any* chiral index ν. As $Q_\pm = k \pm i\delta \to 0$ this occurs because of a cancellation of contributions from the K and K' points whose long wavelength Hamiltonians have opposite handedness. However, azimuthal currents arise due to discrete lattice effects occurring at higher orders in an expansion in $Q_\pm$. To study this, we define two unit vectors at each point in the tube surface, perpendicular to the local outward unit normal $\hat{n}$: $\hat{e}_x$ which points along the tube axis, and $\hat{e}_y = \hat{n} \times \hat{e}_x$ which points counterclockwise on the tube surface. A chiral angle θ is defined as the angle between $\hat{e}_x$ and the T_1 lattice direction as shown in Fig. 1 (with this convention armchair nanotubes have $\theta = 0$). Then the lowest nonvanishing contribution to an azimuthal (y-polarized) shift current must have the form $\cos(6\phi - 3\theta)$ where $\phi = \tan^{-1}(\delta/k)$. The dependence on 6ϕ means that azimuthal currents first occur in the continuum theory at sixth order in $|Q|$.

We can study these terms by replacing the kinetic energy terms in the Hamiltonian of Eq. (1) by the discrete lattice counterpart $iv_F(k + i\delta) = iv_F Q_+ \to t\sum_n e^{i(K+Q)\cdot\tau_n}$ where t is the hopping amplitude between sites connected by the bond vectors τ_n. A systematic expansion of the azimuthal shift current in powers of $Q_\pm$ then gives contributions with the correct lattice symmetry and shows that the ratio of the azimuthal and longitudinal in-plane current densities scales as

$$p = \frac{J_y}{J_x} = \frac{(k^2 + \delta^2)^3\tau^3}{\delta(\Delta^2 + k^2 + \delta^2)}\cos(6\phi - 3\theta). \quad (11)$$

The azimuthal current for any zigzag wrapping is zero because of the angular factor, while its longitudinal current, shown in Fig. 2, is determined by the chiral index ν. For armchair tubes and all nonzigzag tubes with chiral index $\nu = 0$, we have $\delta = 0$, so the shift current is purely azimuthal with a direction determined by the sign of the

potential Δ. These energy dependent currents vanish at the band ERROR: syntaxerror)^3. Nonzigzag tubes with chiral inde; OFFENDING COMMAND: > thus the azimuthal current is nonzero with $p \propto (\delta/\Delta)^2(\delta\tau)^3$. There the shift curre STACK: tes in a *helical pattern* on the tube surface as shown in the right panel of Fig. 2, with a chirality determine and i) creases according to $p(E) = p(0) + a(E^2 - \Delta^2)$. Thus 43 ; shown in Fig. 2, the zigzag nanotubes generate a ph 45 urrent like a wire, the armchair tubes like a coil, and 1892 3814 iral tubes can exhibit a helical current on the tube -mark- .

Alternatively, the shift current can be studied in a semiclassical model, by considering an expansion in t/Δ, where t is the nearest neighbor hopping amplitude, and Δ is the site diagonal potential. In the limit $t/\Delta \ll 1$ the tube can be regarded as a network of independent bonds whose excitations are superimposed. Here the local symmetry of the zigzag tube requires zero net azimuthal current while the armchair wrapping has a nonzero azimuthal current with its direction determined by the sign of Δ. However, it is difficult to correctly describe the physics of the *longitudinal* current using this model. This is because the longitudinal current is controlled by the quantization of the transverse momentum δ. The first terms in the semiclassical expansion that are sensitive to δ occur at order $(t/\Delta)^N$ where N is the number of bonds ($\approx$40) around the tube circumference. This reflects the fact that the longitudinal current is fundamentally a nonclassical quantity for this system.

The longitudinal shift current reduces the ground state electric polarization of the nanotube. This can lead to a *fast readjustment* of atomic positions on the tube walls. Generation of voltages by a mechanical elongation [19] of NCS nanotubes is a related effect. In both situations the response can be stronger in buckled nanotubes [20] or if different types of atoms occur in different layers, as in MoS_2, WS_2 [21], or GaSe nanotubes [22]. Recently, mechanical motions, strikingly similar to those found in some biomolecular systems [23], were observed in irradiated nanotube bundles [24]. Interesting mechanical response to an applied dc bias is observed in carbon nanotubes immersed in a solution of NaCl [25]. Here, the motion is caused by *attraction of ions* of a given polarity to the nanotube. The speed but short duration of the shift current-induced mechanical response complements the slow but steady state effect of a dc bias.

Experimental observation of the shift current in BN nanotubes would provide a striking illustration of fundamental concepts in the modern quantum theory of polarization. The effect is also promising for new applications since it couples the microscopic physics on short length scales, which can be tuned by local fields and mechanical loads, to the long distance properties of the system (polarization, photovoltage, etc.) Finally, there is a rapidly growing family of related submicron one dimensional materials to which these ideas can be applied.

P. K. acknowledges J. E. Sipe and M. Shapiro for financial support under Grant No. DE-FG02-84ER45118 (E. J. M.), by the NSF under Grant No. DMR 98-02560 (E. J. M.), and by the ONR under Grant No. N00014-99-1-0252 (D. T.).

[1] N. G. Chopra *et al.*, Science **269**, 966 (1995).
[2] Z. Weng-Sieh *et al.*, Phys. Rev. B **51**, 11 229 (1995).
[3] K. Suenaga *et al.*, Appl. Phys. A **68**, 301 (1999).
[4] B. I. Sturman and V. M. Fridkin, *The Photovoltaic and Photorefractive Effects in Noncentrosymmetric Materials* (Gordon and Breach Science Publishers, New York, 1992), and references therein.
[5] P. Král and D. Tománek, Phys. Rev. Lett. **82**, 5373 (1999).
[6] E. J. Mele, P. Král, and D. Tománek, Phys. Rev. B **61**, 7669 (2000).
[7] V. I. Belinicher, E. L. Ivchenko, and B. I. Sturman, Sov. Phys. JETP **56**, 359 (1982).
[8] J. E. Sipe and A. Shkrebtii, Phys. Rev. B **61**, 5381 (2000).
[9] P. Král, J. Phys. Condens. Matter **12**, 4851 (2000).
[10] J. Liu *et al.*, Nature (London) **385**, 780 (1997); Ph. Avouris *et al.*, Nature (London) **394**, 780 (1999).
[11] X. Blase *et al.*, Appl. Phys. Lett. **70**, 197 (1997).
[12] Y. Miyamoto, S. G. Louie, and M. L. Cohen, Phys. Rev. Lett. **76**, 2121 (1996).
[13] Y. Miyamoto, Phys. Rev. B **54**, R11 149 (1996).
[14] O. M. Yevtushenko *et al.*, Phys. Rev. Lett. **79**, 1102 (1997).
[15] C. L. Kane and E. J. Mele, Phys. Rev. Lett. **78**, 1932 (1997).
[16] E. I. Blount, in *Solid State Physics, Advances in Research and Applications*, edited by F. Seitz and D. Turnbull (Academic, New York, 1962), Vol. 13, p. 305.
[17] Equation (3) is gauge invariant if $i\delta_{\beta\alpha}\partial_k g_{m\alpha}(k)$ is generalized to the covariant derivative $[i\delta_{\beta\alpha}\partial_k + \Gamma_{\beta\alpha}(k)]g_{m\alpha}(k)$, where $\Gamma_{\beta\alpha}(k) = i\int dr\, U^*_{k\beta}(r)\partial_k U_{k\alpha}(r)$ arises from the k dependence in the basis functions $U_{k\alpha}(r)$. Our choice of basis in Bloch functions gives $\Gamma_{\alpha\beta}(k) = 0$.
[18] A. Rubio, J. Corkill, and M. L. Cohen, Phys. Rev. B **49**, 5081 (1994).
[19] J.-P. Salvetat *et al.*, Phys. Rev. Lett. **82**, 944 (1999).
[20] E. Hernández, C. Goze, P. Bernier, and A. Rubio, Phys. Rev. Lett. **80**, 4502 (1998).
[21] R. Tenne *et*

Printed on September 25, 2002

Energetics and Electronic Structure of a Polyacetylene Chain Contained in a Carbon Nanotube

G. C. McIntosh[1], D. Tománek[2] and Y. W. Park[1]

[1]*School of Physics, Seoul National University, Seoul 151-742, Korea*

[2]*Department of Physics and Astronomy and Center for Fundamental Materials Research, Michigan State University, East Lansing, Michigan 48824-1116*

(Received)

Abstract

Using density functional theory, we calculate the energy and electronic structure of a polyacetylene chain interacting with various carbon nanotubes. We find that polyacetylene chains are weakly attracted exo- or endohedrally to nanotubes. The equilibrium separation between the chain and the wall is close to 3.3 Å, suggesting an energetic preference for polyacetylene to be enclosed in nanotubes wider than the (6,6) tube. The chains are expected to be spontaneously pulled into open nanotubes by forces amounting to a fraction of a nano-Newton. Electronic structure calculations reveal the occurrence of a peak at the Fermi level in the electronic density of states, caused by the weak interaction between polyacetylene and the carbon nanotube, which may facilitate the onset of superconductivity in this system.

It was noted soon after their initial discovery[1] that carbon nanotubes (CNTs) are hollow cylindrical structures, which could make ideal containers for just a few atoms or small molecules.[2] In this regard, they have been considered for hydrogen storage[3] and as nano-sized 'test-tubes for manipulating chemical/biological molecules'.[4] Filling of carbon nanotubes with molten lead, induced by capillary action, has been demonstrated experimentally.[5] The formation of 'peapod' structures is now well established, whereby C_{60} buckyballs readily migrate into a (10,10) nanotube.[6] Further to this, if one is interested in investigating one-dimensional nano-systems, then carbon nanotubes could act as a support structure to contain the nano-system. For example, nanotubes have been considered for confining a chain of metal atoms,[7] where the interest lies in comparing the properties of the one-dimensional chain with that of the three-dimensional bulk metal.

Even in the absence of contained atoms or molecules, armchair carbon nanotubes are very interesting one-dimensional metallic systems which, for example, have been considered as prime candidates for observing a Luttinger liquid.[8] Another one-dimensional material of considerable interest is polyacetylene (PA). Unlike metallic carbon nanotubes,[9] polyacetylene succumbs to Peierls distortion that causes dimerization in pristine PA, accompanied by a band gap opening at the Fermi level. The charge carriers in lightly doped PA are the somewhat more exotic solitons, which can carry spin and no charge or charge and no spin.[10] In the bulk system, the intrinsic properties of individual PA chains may be obscured by inter-chain coupling, complicated morphology of the bulk material, or by effects coming from dopant atoms. To avoid these artifacts, we propose to use carbon nanotubes as support structures to keep PA chains straight and to isolate them. Since both nanotubes and highly doped polyacetylene are good metals, the combined nanotube/polyacetylene system may show intriguing transport behavior with widescale technological applications.

Two main issues to be addressed are finding the ideal size of a carbon nanotube to comfortably contain just a single PA chain, and to determine the degree of interaction between the carbon nanotube and the enclosed PA chain. On the one hand, a negligible interaction is desirable if the PA chain is to retain its original properties after insertion into

the carbon nanotube. On the other hand, given that both carbon nanotubes and PA are very interesting materials on their own, we are curious as to whether some new phenomena might emerge within the combined system.

In this study, we investigate for the first time the interaction energy and electronic structure of a polyacetylene chain aligned axially either exo- or endohedrally with a nanotube. We find that the polymer chains are weakly attracted towards, and may be spontaneously pulled into sufficiently wide nanotubes. The undoped polyacetylene/nanotube system is metallic. The weak interaction between the subsystems induces a peak in the electronic density of states at the Fermi level, which may facilitate the onset of superconductivity.

Our calculations are based on density functional theory (DFT) within the local density approximation (LDA) and performed using the SIESTA code.[11] Troullier-Martins pseudopotentials were used to represent the nuclei plus core electrons. We used the Perdew-Zunger form of the exchange-correlation potential in LDA.

In all cases, the axes of the PA chain and carbon nanotube were kept parallel. The structural arrangement is illustrated in the insets of Fig. 1(a) as well as in Fig. 2(a-b). To reduce computing requirements,[12] only armchair nanotubes were considered at this stage. Since the lattice structure of a PA chain and graphitic armchair nanotube are very similar, the PA lattice could be held commensurate with the nanotube lattice, thus reducing the number of atoms required per unit cell. This necessitated the unit cell length of the PA chain to be reduced slightly from 2.475 Å to 2.460 Å, at the negligible energy cost of only $\approx$1 meV per unit cell.

Depending on the size of the carbon nanotube being considered, the unit cell contained between 20 atoms (for a (4,4) nanotube) and 32 atoms (for a (7,7) nanotube). Of these, two carbon atoms and two hydrogen atoms were associated with the PA chain, as illustrated in Fig. 2(b). The unit cell size perpendicular to the carbon nanotube axis was set to at least 10 Å, so that there was no interaction between structures in adjacent cells. For total energy calculations, we sampled the irreducible wedge of the one-dimensional Brillouin zone by 4 k-points. To achieve sufficient energy convergence yielding smooth E versus d curves

in Figs. 1 and 2, the energy cutoff for plane wave expansion was set to 100 Ry. For the non-bonding interaction between the PA chain and carbon nanotube, we applied the counterpoise correction using ghost orbitals to account for basis set superposition errors.

As a test case, we have optimized the structure of an isolated PA chain. We obtained an average carbon-carbon bond length of 1.396 Å, which is close to the experimental value of 1.4 Å,[13] and a bond length alteration (BLA) of 0.051 Å. This value for the BLA is less than the experimental value of 0.08 Å, but under-estimation of the BLA has been acknowledged previously for DFT calculations.[14] Resolving this problem requires going beyond the LDA.[15] As another test, we have calculated the equilibrium separation between two graphite sheets. We obtain 3.44 Å, in close agreement with the experimental value.

In our first study, we explored the nature of the binding between a PA chain and a carbon nanotube. Figure 1(a) shows the interaction energy between a (4,4) carbon nanotube and a PA chain for the case that the PA chain is situated outside the carbon nanotube. We find a clear minimum in the E versus d curve with a binding energy of 45.4 meV. Comparing this value to kT, we conclude that the system can be bound at room temperature. The equilibrium separation of 3.34 Å turns out to be similar to that between graphite sheets. This is not too surprising, given that the nanotube can be considered as a rolled up graphite sheet and that the carbon backbone of the PA chain is almost commensurate with graphite. For the sake of comparison, in Fig. 1(b) we also show the interaction energy between a PA chain and a graphite sheet, representing a nanotube of large diameter. In this case, the binding energy is slightly increased to 59.3 meV and the associated equilibrium separation reduced to 3.30 Å. Evidently, curvature of the graphitic structure plays a role in the interaction energy, whereby having more atoms in close proximity to the PA chain increases the binding interaction. Our values for the equilibrium separation also indicate that a carbon nanotube would require a diameter of at least 6.6 Å, before an insertion of a PA chain into the nanotube would become energetically favourable.

Figure 2 shows our main result for a PA chain inside armchair carbon nanotubes of various radii R, as a function of the axial separation r. Figure 2(c) shows that on energy

grounds, PA is likely to enter nanotubes of sufficiently large diameter and free for off-axial displacements. For the PA chain inside a (4,4) nanotube the energy never becomes negative, indicating that this configuration is energetically unfavourable.[16] The same holds also for the wider (5,5) nanotube, where the insertion process is only marginally endothermic. For the (6,6) and (7,7) nanotubes, the nanotube diameter is sufficient to allow PA to be bound inside the nanotube, as seen on the exapanded energy scale in Fig. 2(d). For the (6,6) nanotube, the minimum is fairly wide so that a PA chain enclosed inside a (6,6) nanotube would still have some degree of lateral freedom. As compared to larger nanotubes, this system allows PA to interact with more atoms, thus causing further stabilization, as already suggested by the results of Fig. 1. The (7,7) nanotube, with a set of energy minima at $r > 0$, is sufficiently wide to accommodate more than one PA chain.

We next address the possible insertion process of a PA chain into a carbon nanotube, illustrated in Fig. 3(a). Given that the (6,6) nanotube has an appropriate diameter to contain just one PA chain, we consider this as a model system. The energy gain associated with the axial insertion of a PA chain into the (6,6) nanotube is depicted in Fig. 3(b). Since the translation symmetry along the axis is broken in this case, the calculations are performed for finite, hydrogen-terminated clusters representing the nanotube and PA, as shown in the inset of Fig. 3(b), and extrapolated for a semi-infinte PA chain and nanotube. For PA completely outside the nanotube, corresponding to positive z values, the total energy is that of an isolated nanotube and an isolated PA chain and taken as a reference value. We see the energy becoming lowered as the end of the PA chain moves into the carbon nanotube, indicating that the PA chain is likely to be pulled in once it is partially inserted. Of interest is that the PA chain begins to feel the attraction, when it is still $\approx$2 Å outside the carbon nanotube. This suggests that the insertion process should start spontaneously as soon as the PA chain approaches the open end of the carbon nanotube. For a semi-infinite chain entering a semi-infinite nanotube, the energy gain per segment inserted is constant and can be inferred from Fig. 2. The constant slope of the $E(z)$ curve in Fig. 3(b) corresponds to a force of 0.159 nN that pulls the PA chain in. Even though this force appears small on a

ERROR: undefined
OFFENDING COMMAND: ~ ıg it by the cross-sectional area of the nanotube yields an effective

STACK: : of 301 MPa. This large, capillarity-induced pressure will li

(
? ? ? ł ł ? ł ł
)
83
57
6861
4251
-mark-

PHYSICAL REVIEW B VOLUME 58, NUMBER 24 15 DECEMBER 1998-II

Electronic and structural properties of multiwall carbon nanotubes

Young-Kyun Kwon and David Tománek
Department of Physics and Astronomy, and Center for Fundamental Materials Research, Michigan State University, East Lansing, Michigan 48824-1116
(Received 12 October 1998)

We calculate the potential energy surface, the low-frequency vibrational modes, and the electronic structure of a (5,5)@(10,10) double-wall carbon nanotube. We find that the weak interwall interaction and changing symmetry cause four pseudogaps to open and close periodically near the Fermi level during the soft librational motion at $\nu \leq 30$ cm^{-1}. This electron-libration coupling, absent in solids composed of fullerenes and single-wall nanotubes, may yield superconductivity in multiwall nanotubes. [S0163-1829(98)51548-2]

Carbon nanotubes,[1,2] narrow seamless graphitic cylinders, show an unusual combination of a nanometer-size diameter and millimeter-size length. This topology, combined with absence of defects on a macroscopic scale, gives rise to uncommon electronic properties of individual single-wall nanotubes[3,4] which, depending on their diameter and chirality, can be either conducting or insulating.[5–7] Significant changes in conductivity of these nanowires may be induced by minute geometric distortions[8] or external fields.[9] More intriguing effects, ranging from opening of a pseudogap at E_F (Refs. 10 and 11) to orientational melting,[12] have been predicted to occur when identical metallic nanotubes are bundled to a "rope."[13] It appears that the many interesting phenomena in single-wall tubes have distracted the attention of theorists from the more abundant multiwall tubes.

Existing investigations of multiwall nanotubes have focussed primarily on their growth mechanism,[14–16] as well as changes of the band structure[17,18] and total energy[19] as the inner tube rotates about or slides along the tube axis. The interwall interaction in a multiwall tube is very similar to the interball interaction in the C_{60} solid, since these structures share the same sp^2 bonding and interwall distance of $\approx$3.4 Å found in graphite. While it is well established that C_{60} molecules rotate relatively freely in the solid at room temperature,[20] there has been little discussion of the analogous rotation in systems consisting of nanotubes. Only recently, rotations of individual nanotubes in a rope consisting of (10,10) tubes have been discussed.[11,12] Owing to the uncommon combination of a relatively small energy barrier for rotation and a large mass of macroscopically long nanotubes, individual tubes are unlikely to move as rigid objects in the rope, but rather to bend and twist locally, displacing orientational dislocations that were frozen in during the tube synthesis.

An intriguing effect, namely the formation of a pseudogap at E_F,[10,11] has been predicted to occur in ropes of metallic (10,10) nanotubes of D_{10h} symmetry due to the symmetry lowering while forming a triangular lattice. It is interesting to investigate whether the weak intertube interaction, which strongly modifies the low-frequency end of the vibrational spectrum and the density of state near E_F in an infinite three-dimensional lattice of identical nanotubes, may cause even more dramatic effects in a one-dimensional multiwall tube.

Here we show that the interwall coupling, which opens a pseudogap in bundled single-wall nanotubes due to symmetry lowering, may periodically open and close four such pseudo-gaps near E_F in a "metallic" double-wall nanotube during its librations around and vibrations normal to the tube axis. This type of electron-phonon coupling has not been observed in librating molecular crystals of C_{60} fullerenes or (10,10) nanotubes, that are orientationally frustrated. We study the intriguing interplay between geometry and electronic structure during the low-frequency motion of a double-wall nanotube. Our results indicate that the coupling of conduction electrons to soft tube librations and vibrations is caused by periodic symmetry changes, which are unique in this system and may lead to its superconducting behavior.

We focus the following investigation on the (5,5)@(10,10) double-wall nanotube, shown schematically in Fig. 1(a). The individual (5,5) and (10,10) tubes are both metallic and show the preferred "graphitic" interwall separation of 3.4 Å when nested. Assuming both tubes to be rigid cylinders with parallel axes, the double-wall tube geometry is defined uniquely by the separation of the axes Δr, the axial offset of the inner tube Δz, the orientation of the inner tube φ_{in} and the outer tube φ_{out} with respect to the plane containing the two axes, shown in Fig. 1(a).

To determine the structural and electronic properties of multiwall nanotubes, we used the parametrized tight-binding technique with parameters determined by *ab initio* calculations for simpler structures.[21] This approach has been found useful to describe minute electronic structure and total energy differences for systems with too large unit cells to handle accurately by *ab initio* techniques. Some of the problems tackled successfully by this technique are the electronic structure and superconducting properties of the doped C_{60} solid[22] and the opening of a pseudogap near the Fermi level in a rope consisting of (10,10) nanotubes.[11] The band structure energy functional is augmented by pairwise interactions describing both the closed-shell interatomic repulsion and the long-range attractive van der Waals interaction, to correctly reproduce the interlayer distance and the C_{33} modulus of graphite. The adequacy of this approach can be checked independently by realizing that the translation and rotation of individual tubes are closely related to the shear motion of graphite. We expect the energy barriers in tubes to lie close

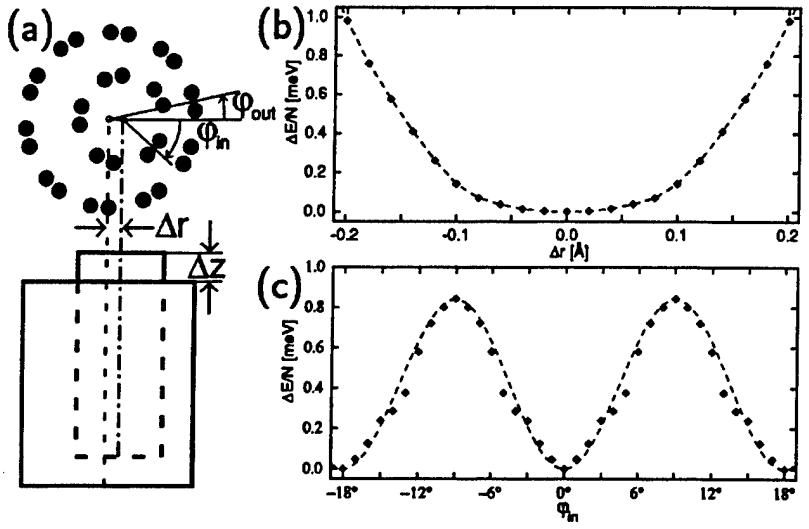

FIG. 1. (a) Schematic view of the (5,5)@(10,10) double-wall tube. The relative radial, axial, and rotational displacement of the inner with respect to the outer tube are described by Δr, Δz, φ_{in} and φ_{out}, respectively. Energy dependence on (b) the separation of the tube axes Δr (for $\Delta z=0$, $\varphi_{in}=0$, $\varphi_{out}=0$), and (c) the orientation of the inner tube φ_{in} (for $\Delta r=0$, $\Delta z=0$, $\varphi_{out}=0$). All energies are given per atom.

to the graphite value which, due to the smaller unit cell, is also easily accessible to *ab initio* calculations.[23]

We focus in our calculations on the softest vibrational modes and ignore the deformation of individual tubes from a perfectly cylindrical shape. The dependence of the total energy of the double-wall tube on the distance between the (5,5) and (10,10) tube axes is shown in Fig. 1(b). Even though our results suggest that the system is coaxial in equilibrium, the potential energy is nearly flat for $|\Delta r| \lesssim 0.1$ Å. For a perfectly straight tube, the shallow potential well would suggest a very soft radial mode to occur with $\nu = 18\ \mathrm{cm}^{-1}$. At nonzero temperatures, we do not expect the inner tube to be coaxial, but rather to form a helix inside the outer tube. Such a helix would maximize the interwall contact and also could vibrate and rotate locally about its axis. We believe that helical or similar tube distortions of $\lesssim 0.1$ Å are real, but probably are undetectable in transmission electron microscope images.

Due to the low compressibility of tubes along their axis, axial motion of individual nanotubes resembles that of a rigid body. Even though the activation barrier *per atom* for axial displacement of one tube inside the other is only 0.2 meV,[19] the activation barrier to move the entire rigid nanotube is infinitely high, thus effectively freezing in this particular degree of freedom.

Due to the relatively high symmetry of the coaxial system consisting of a D_{5d} (5,5) nanotube nested inside the D_{10h} (10,10) nanotube, the dependence of the inter-tube interaction on the tube orientation shows a periodicity of 18°. Our results in Fig. 1(c) suggest this interaction to be harmonic, with a relatively low activation barrier for tube rotation of 0.8 meV/atom. Assuming that the outer tube was pinned, the inner tube would exhibit a soft libration with a frequency $\nu_{in} \approx 31\ \mathrm{cm}^{-1}$. In the opposite case of a fixed inner tube, the heavier outer wall should librate with $\nu_{out} \approx 11\ \mathrm{cm}^{-1}$. A free double-wall tube should librate with a single frequency $\nu \approx 33\ \mathrm{cm}^{-1}$.

As in an infinite system consisting of bundled identical nanotubes, we expect also in an individual double-wall nanotube an orientational depinning and melting to occur at suf-

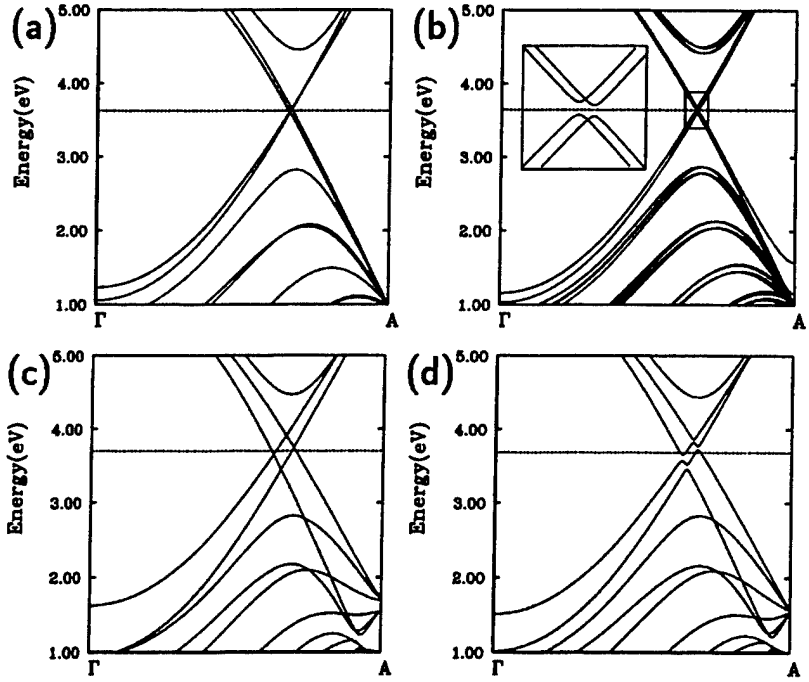

FIG. 2. Band structure of aligned nanotube pairs, along the tube axis. Near degenerate bands with no gap characterize the (5,5)@(10,10) double-wall nanotube without intertube interaction (a). Intertube interaction opens a gap in a pair of (individually metallic) (10,10) nanotubes (b). In presence of intertube interaction, depending on the mutual tube orientation, the (5,5)@(10,10) system may show zero gap in the most symmetric, stable configuration at $\varphi_{in}=0°$ (c), or four pseudogaps in a less symmetric and stable configuration at $\varphi_{in}=3°$ (d). The Fermi level is shown by the dashed line.

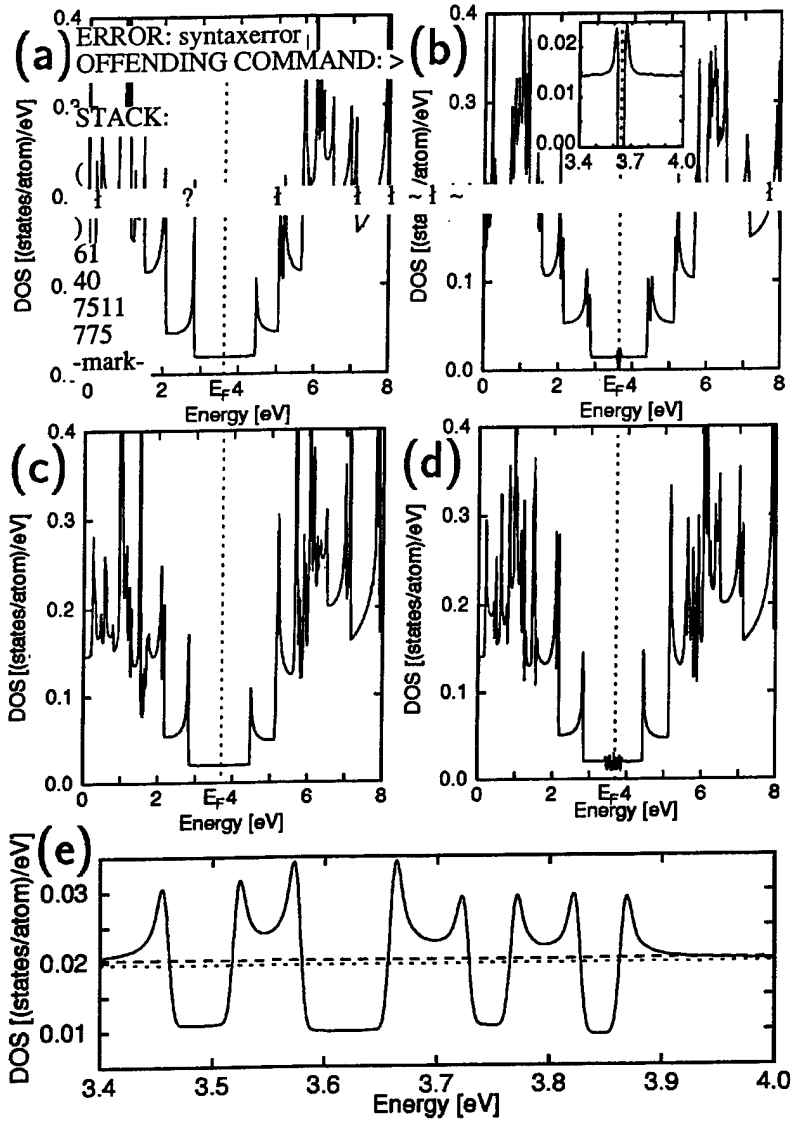

FIG. 3. Density of states of aligned nanotube pairs, corresponding to the band structures in Fig. 2: The (5,5)@(10,10) double-wall tube with no intertube interaction (a); pair of interacting (10,10) nanotubes (b); the (5,5)@(10,10) double-wall tube as a function of mutual tube orientation, for $\varphi_{in}=0°$ (c), and $\varphi_{in}=3°$ (d). The Fermi level is shown by the dashed line. The densities of states of (5,5)@(10,10) tubes near E_F are compared on an expanded energy scale in (e). Appearance of pseudogaps, shown by the solid line for $\varphi_{in}=3°$, is in stark contrast with the flat density of states for $\varphi_{in}=0°$ and $\varphi_{in}=9°$, shown by the long-dashed line. The dotted line indicates the density of states of noninteracting (5,5) and (10,10) tubes.

ficiently high temperatures. The onset of orientational melting at T_{OM} is expected to be qualitatively similar to that described for the infinite lattice of (10,10) nanotubes.[11,12] Even though the activation barrier for rotation may be small on a *per atom* basis, the relevant quantity in this case is the infinitely high barrier for the entire rigid tube that would lock it in place. In the other extreme of a straight, zero-rigidity tube composed of independent atoms, 0.8 meV/atom activation barrier for rotation would give rise to an orientational melting transition at $T_{OM}\approx 10$ K.

A more realistic estimate of the onset of orientational disorder must consider that multiwall nanotubes, when synthesized, are far from being straight over long distances. As suggested by the potential energy surface for the librational mode in Fig. 1(c), a local twist by $\varphi_{in}>9°$ results in the nanotube switching locally from one equilibrium orientation to another. Formally, by mapping the orientational coordinate φ_{in} onto the position coordinate x, this process can be described using the Frenkel-Kontorova model used to describe dislocations in strained one-dimensional lattices. Under synthesis conditions at temperatures exceeding 1000 K, we expect substantial finite twists to occur in the individual tubes. Upon forming a multiwall tube, in an attempt to optimize the interwall interaction while minimizing the torsion energy, orientational dislocations are frozen in at an energy cost of only ≈ 1.0 meV per atom in a ≈ 100 Å long strained region,[24] as compared to an optimized straight double-wall tube. Taking a straight, zero-rigidity tube as a reference, we expect T_{OM} to increase from the 10 K value with increasing rigidity. Presence of orientational dislocations, on the other hand, should lower the activation barrier for tube rotations, thus lowering T_{OM} and possibly compensating the effect of nonzero rigidity.

The weak intertube interaction not only induces new vibrational modes, but also modifies significantly the electronic structure near E_F. Individual (5,5) and (10,10) armchair nanotubes, with their respective D_{5d} and D_{10h} symmetries, are metallic. The band structure of each tube is characterized by two crossing linear bands near E_F, one for "left" and one for "right" moving electrons. The band structure of a pair of decoupled (5,5) and (10,10) nanotubes, a mere superposition of the individual band structures, is shown in Fig. 2(a). The linearity of the energy bands in between the van Hove singularities closest to E_F translates into a constant density of states in that energy region, as shown in Fig. 3(a).

It has been argued that the symmetry lowering upon bunching identical metallic (10,10) tubes to a close-packed

"Bucky Shuttle" Memory Device: Synthetic Approach and Molecular Dynamics Simulations

Young-Kyun Kwon,[1] David Tománek,[1] and Sumio Iijima[2]
[1]*Department of Physics and Astronomy, and Center for Fundamental Materials Research, Michigan State University, East Lansing, Michigan 48824-1116*
[2]*NEC Corporation, Fundamental Research Laboratories, 34 Miyukigaoka, Tsukuba, Ibaraki 3058501, Japan*
(Received 23 October 1998)

Thermal treatment is reported to convert finely dispersed diamond powder to multiwall carbon nanocapsules containing fullerenes such as C_{60}. We investigate the internal dynamics of a related model system, consisting of a $K@C_{60}^{+}$ endohedral complex enclosed in a C_{480} nanocapsule. We show this to be a tunable two-level system, where transitions between the two states can be induced by applying an electric field between the C_{480} end caps, and discuss its potential application as a nonvolatile memory element. [S0031-9007(99)08484-7]

PACS numbers: 61.48.+c, 61.50.Ah, 73.61.Wp, 81.10.Aj

Carbon nanotubes [1,2], consisting of seamless and atomically perfect graphitic cylinders a few nanometers in diameter, have been synthesized in bulk quantities [3,4]. The unusual combination of their molecular nature and micrometer-size length [5,6] gives rise to uncommon electronic properties of these systems. Electrical transport measurements for individual nanotubes indicate that these systems may behave as genuine quantum wires [7], nonlinear electronic elements [8], or transistors [9]. Potential use of nanotube-based two-level systems for permanent data storage, discussed here, would significantly extend their range of application.

Here, we present evidence that unusual multiwall nanotube structures, such as the "bucky shuttle" [10], self-assemble from elemental carbon under specific conditions. Our molecular dynamics simulations indicate that the bucky shuttle shows an unusual dynamical behavior that suggests its use as a nanometer-sized memory element. We show that a nanotube memory would combine high switching speed, high packing density, and stability with nonvolatility of the stored data.

The system described in this study was produced by thermally annealing diamond powder of an average diameter of 4–6 nm which was prepared by the detonation method (Cluster Diamond, Toron Company Ltd.). The powder was heated in a graphite crucible in inert argon atmosphere at 1800 °C for 1 hour. This treatment transforms the diamond powder into graphitic nanostructures presented in transmission electron microscope images shown in Fig. 1. A large portion of this material consists of multiwall capsules with few layers, the smallest structures being fullerenes with a diameter close to that of C_{60}. In several cases depicted in Fig. 1, the enclosed fullerenes may move rather freely inside the outer capsule, like a bucky shuttle.

An enlargement of one of such structures in Fig. 1 is displayed in Fig. 2(a). Figure 2(b) illustrates a corresponding model, consisting of a C_{60} encapsulated in a C_{480} capsule. The energetics of the $C_{60}@C_{480}$ system is shown in Fig. 2(c). The ends of the outer capsule are halves of the C_{240} fullerene, the optimum structures to hold a C_{60} molecule at an interwall distance of 3.4 Å. These end caps connect seamlessly to the cylindrical portion of the capsule, a 1.5 nm long segment of the (10, 10) nanotube [3]. The interaction between the unmodified C_{60} molecule and the enclosing capsule is similar to that found in C_{60} crystals and nanotube bundles [3]; it is dominated by a van der Waals and a weak covalent interwall interaction that is proportional to the contact area between the constituents. An additional image charge interaction,

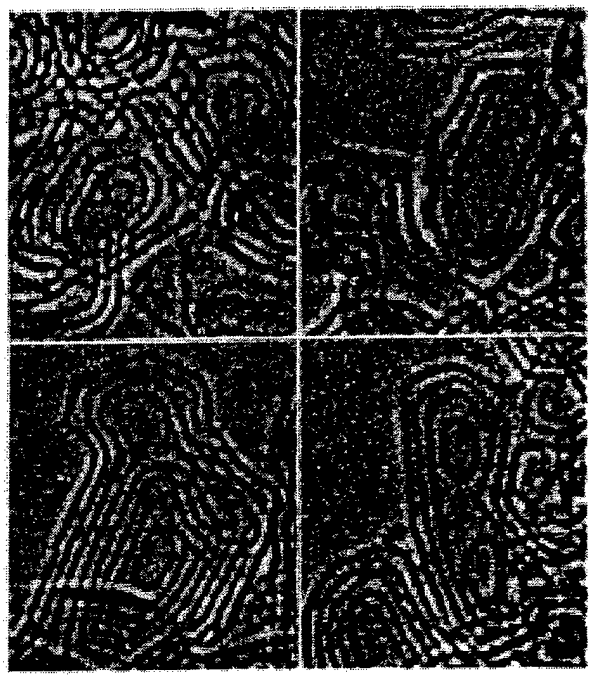

FIG. 1. Transmission electron microscope images depicting multiwall carbon structures that self-assemble during the thermal annealing of nanodiamond powder under the conditions described in this report. The smallest spherical structures are C_{60} molecules that are always found near the end of the capsule, where the attractive interwall interaction is strongest.

 0031-9007/99/82(7)/1470(4)$15.00

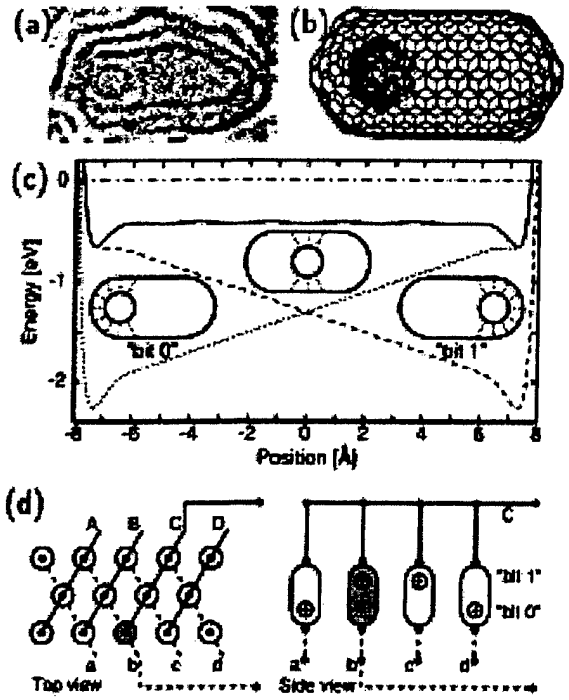

FIG. 2. (a) Enlargement of the upper-right section of the transmission electron microscope image in Fig. 1. (b) Structural model for an isolated $K@C_{60}^{+}@C_{480}$ bucky shuttle, with the $K@C_{60}^{+}$ ion in the "bit 0" position. (c) Potential energy of $K@C_{60}^{+}$ as a function of its position with respect to the outer capsule in zero field (solid line) and switching field $E_s = 0.1$ V/Å (dashed lines). The $K@C_{60}^{+}$ ion position, representing the information, can be changed by applying this switching field between the ends of the capsule. Energy zero corresponds to an isolated $K@C_{60}^{+}$ at infinite separation from the C_{480} capsule. (d) Schematic of a high-density memory board in the top and the side view. When a switching voltage is applied between conductors b and C, the corresponding bit information will be stored in the memory element bC at their intersection, shown shaded.

which is nearly independent of the C_{60} position, occurs if the C_{60} molecule carries a net positive charge, as we discuss below. Obviously, the van der Waals interaction stabilizes the C_{60} molecule at either end of the capsule, where the contact area is largest. This is reflected in the potential energy behavior in Fig. 2(c), and results in the likelihood of C_{60} being found near the ends of the capsule, as evidenced in Figs. 1 and 2(a). In the following, we will study the possibility of information storage in this two-level system.

Usefulness of this nanostructure for data storage implies the possibility to *write and read* information fast and reliably. Of equal importance is the capability to *address* the stored data efficiently, and the *nonvolatility* of the stored information.

In order to move the encapsulated C_{60} from one end of the capsule to the other (the molecular analog of writing) and to determine its position within the capsule (the molecular analog of reading) most efficiently, the C_{60} should carry a net charge. In the $K@C_{60}$ complex, which is known to form spontaneously under synthesis conditions in the presence of potassium, the valence electron of the encapsulated K atom is completely transferred to the C_{60} shell [11]. The C_{60} is likely to transfer the extra electron to the graphitic outer capsule, since the ionization potential of $K@C_{60}$ is smaller than the work function of graphite. The extra electron will likely be further transferred to the (graphitic) structure that holds this element in place. Since the enclosed K^+ ion does not modify the chemical nature of C_{60}, we will model the dynamics of the $K@C_{60}^{+}$ ion in the neutral C_{480} capsule by uniformly distributing a static charge of $+1e$ over the C_{60} shell.

The *writing process* corresponds to switching the equilibrium position of the C_{60}^{+} ion between the "bit 0" and the "bit 1" ends of the capsule in an applied electric field. This is best achieved if the connecting electrodes, supplying the bias voltage, are integral parts of the end caps, to reduce the field screening by the nanotube [12]. The energetics of C_{60}^{+} in the switching field $E_s = \pm 0.1$ V/Å, generated by applying a voltage of ≈ 1.5 V between the end caps, is displayed in Fig. 2(c). One of the local minima becomes unstable above a critical field strength, causing the C_{60}^{+} ion to move to the only stable position. The switching field $E_s = 0.1$ V/Å is small and will have no effect on the integrity of the carbon bucky shuttle, since graphitic structures disintegrate only in fields $E \gtrsim 3$ V/Å [13,14].

The information, physically stored in the position of the C_{60}^{+} ion within the capsule, can be *read nondestructively* by detecting the polarity of the capsule. An alternative *destructive read* process would involve measuring the current pulse in the connecting wires, caused by the motion of the C_{60}^{+} ion due to an applied probing voltage. The total charge transfer associated with the current pulse, which is one electron in our case, may be increased by connecting several capsules in parallel to represent one bit, and by using higher charged complexes such as $La@C_{82}^{2+}$.

When targeting high storage densities, the *addressability* of the stored information becomes important. One possible way to realize a high-density memory board is presented in Fig. 2(d). Maximum density is achieved by packing the nanotube memory elements like eggs in a carton. Rows of nanocapsules can be connected at the top and at the bottom by nanowire electrodes in such a way that a single memory element is addressed at their crossing point. Applying a switching voltage between two crossing electrodes [e.g., the bC pair in Fig. 2(d)] will generate a nonzero field only in the memory element labeled bC. As in the ferrite matrix memory, many memory elements can be addressed in parallel using such an addressing scheme. This arrangement applies both for the writing and the destructive reading processes described above, and allows for multiple bits to be written and read in parallel. In the latter case, the status of the memory element bC is inspected by applying a switching voltage between the electrode pair b, C and monitoring the current in these electrodes.

Unlike in presently used dynamic random access memory (DRAM) elements, where information has to be sustained by an external power source, the *nonvolatility of the stored information* results from a nonzero trap potential near the "bit 0" or "bit 1" end of the capsule. Thermal stability and nonvolatility of data depend on the depth of this trap potential, which in turn can be adjusted by changing the encapsulated fullerene complex. The calculated trap potential depth of ≈ 0.24 eV for the $K@C_{60}^+$ ion near the ends of the capsule in zero field suggests that stored information should be stable well beyond room temperature and require temperatures $T \gtrsim 3000$ K to be destroyed. Further improvement of the thermal stability could be achieved using higher-charged endohedral complexes containing divalent or trivalent donor atoms, such as $La@C_{82}$ discussed above.

To study the efficiency of the writing process, we performed a molecular dynamics simulation of the switching process from "bit 0" to "bit 1" in the microcanonical ensemble of the $C_{60}^+@C_{480}$ memory element. We used a parametrized linear combination of atomic orbitals (LCAO) total energy functional [15], augmented by long-range van der Waals interactions [16]. Our computationally efficient $O(N)$ approach to determine the forces on individual atoms [17] had been previously used with success to describe the disintegration dynamics of fullerenes [18] and the growth of multiwall nanotubes [19]. A time step of 5×10^{-16} s and a fifth-order Runge-Kutta interpolation scheme was used to guarantee a total energy conservation of $\Delta E/E \lesssim 10^{-10}$ between successive time steps.

The results of our simulation are shown in Fig. 3. Initially, the C_{60}^+ ion is equilibrated near the "bit 0" position. At time $t = 0$, a constant electric field of 0.1 V/Å is applied along the axis of the outer capsule. The originally stable "bit 0" configuration becomes unstable in the modified total energy surface, depicted in Fig. 2(c). The C_{60}^+ ion is subject to a constant acceleration to the right, and reaches the "bit 1" position only 4 ps later, as seen in Fig. 3(a). During this switching process, the potential energy lost by the C_{60}^+ ion is converted into kinetic energy, as seen in Fig. 3(b). Because of the small (albeit non-negligible) interaction between the encapsulated ion and the capsule, the kinetic energy gained initially occurs as rigid-body translational energy of the C_{60}^+ ion. A nearly negligible energy transfer into the internal degrees of freedom due to atomic-scale friction, manifested in a very small increase of the vibrational temperature in Fig. 3(c), is observed during this initial stage of the switching process.

The C_{60}^+ ion reaches the opposite end of the capsule, 4 ps after the switching field is applied, having gained 1.5 eV of net kinetic energy. This kinetic energy is too small to damage the capsule, as inelastic collisions involving C_{60} require energies exceeding 200 eV to occur [20]. Upon impact onto the enclosing capsule from the inside, a substantial fraction of this energy is converted into heat, thus increasing the vibrational temperature of

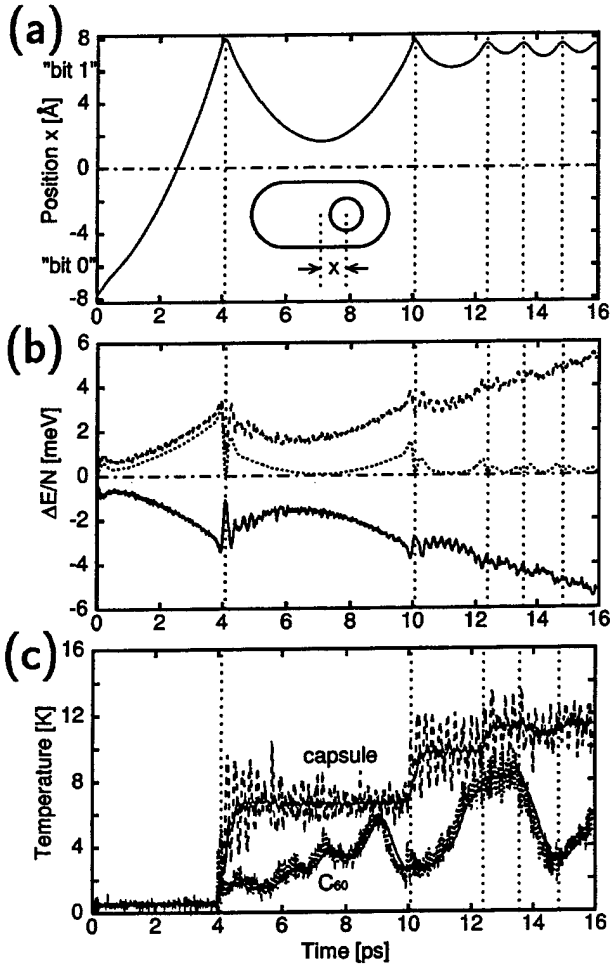

FIG. 3. Results of a molecular dynamics simulation of the switching process from "bit 0" to "bit 1", when a constant electric field of 0.1 V/Å is applied along the axis of the capsule. (a) Position of the $K@C_{60}^+$ ion with respect to the center of the enclosing C_{480} capsule as a function of time. (b) Changes in the potential energy (solid line) and kinetic energy (dashed line) in the laboratory reference frame as a function of time. The portion of the kinetic energy, corresponding to the translation of the enclosed $K@C_{60}^+$ ion with respect to the capsule (dotted line), is seen to decrease as the system temperature rises. The total energy (dash-dotted line) is conserved. All energies are given per atom. (c) Vibrational temperature of the enclosed $K@C_{60}^+$ ion (dotted line) and the enclosing capsule (dashed line) as a function of time. The solid lines are backward convolutions of the vibrational temperature values, using a Gaussian with a full-width at half maximum of 7.5×10^{-13} s.

the outer capsule by $\lesssim 10$ K and that of the C_{60}^+ ion by ≈ 2 K. Because of the high heat conductivity and melting temperature $T_M \lesssim 4,000$ K of graphitic nanostructures [18], this modest heat evolution is unlikely to cause any structural damage even at high access rates.

As seen in Fig. 3(b), the net kinetic energy of the encapsulated C_{60}^+ with respect to the outer capsule is significantly reduced during this collision. The C_{60}^+ bounces back towards the middle of the capsule, slowed down by the opposing electric field, and finally turns again towards

the "bit 1" end. Figure 3(c) indicates that thermal equilibration in the system after the collision is achieved stepwise. The step period of ≈ 1 ps results from the beats between the low-frequency quadrupolar deformation modes of the colder encapsulated C_{60}^+ ion and the hotter enclosing capsule, which have been excited during the quasielastic collision.

One or few oscillations of the C_{60}^+ ion inside the enclosing capsule, damped by transferring energy from macroscopic to internal degrees of freedom, are necessary to stabilize it in the new equilibrium "bit 1" position, with a kinetic energy not exceeding the depth of the trap potential. As seen in Fig. 3(b), this situation occurs ≈ 10 ps after the initial onset of the switching field, thus resulting in an ideal memory switching and access rate close to 0.1 THz. In the slower sequential mode, this translates into a data throughput rate of 10 Gbyte/s, 4 orders of magnitude faster than the data throughput rate of 4–5 Mbyte/s which is achieved presently in magnetic mass storage devices.

In order to further reduce the switching time, one may consider increasing the field to shorten the transfer time between the two states, keeping in mind that the damping process would be prolonged in such a case. Unlike in our model simulation, there is no need to apply a constant switching field during the entire bit flip process. A 0.5 ps pulse of a 0.1–0.5 V/Å field is found to suffice to detach the C_{60}^+ ion from its stable position and thus to change the memory state. This approach may be of particular use if an increase of the trap potential, due to a different fullerene complex, should be desirable.

Mass production of nanotube-based memory devices such as the one discussed here rely on the self-assembly of nanotubes and nanocapsules to ordered close-packed arrays. There has been encouraging evidence of such a self-assembly mechanism in the synthesis of free-standing nanotube ropes [3], aligned nanotube columns forming free-standing membranes [21], multiwall nanotube columns growing from a SiC(111) wafer [22], and most recently many C_{60} molecules inside long carbon nanotubes [23]. We also note that, since any double-wall nanocapsule with the enclosed structure shorter than the outer capsule behaves as a tunable two-level system, the functionality of the proposed nanoscale memory is basically independent of the exact size and shape of the encapsulated ion and the enclosing capsule.

In summary, we have shown that thermal treatment may convert finely dispersed diamond powder to multi-wall carbon nanocapsules containing fullerenes such as C_{60}. Using molecular dynamics simulations, we investigated the internal dynamics of a related model system, consisting of a $K@C_{60}^+$ endohedral complex enclosed in a C_{480} nanocapsule. We showed this to be a tunable two-level system, where transitions between the two states can be induced by applying an electric field between the C_{480} end caps. This system, if considered as a memory element, would offer a combination of high switching speed, high density, nonvolatility of data, and relatively easy read/write access.

D.T. and Y.K.K. acknowledge fruitful discussions with R.E. Smalley and financial support by the Office of Naval Research.

[1] S. Iijima, Nature (London) **354**, 56 (1991).
[2] M.S. Dresselhaus, G. Dresselhaus, and P.C. Eklund, *Science of Fullerenes and Carbon Nanotubes* (Academic Press, San Diego, 1996).
[3] A. Thess, R. Lee, P. Nikolaev, H. Dai, P. Petit, J. Robert, C. Xu, Y.H. Lee, S.G. Kim, D.T. Colbert, G. Scuseria, D. Tománek, J.E. Fischer, and R.E. Smalley, Science **273**, 483 (1996).
[4] T.W. Ebbesen, Annu. Rev. Mater. Sci. **24**, 235 (1994).
[5] J.W.G. Wildöer, L.C. Venema, A.G. Rinzler, R.E. Smalley, and C. Dekker, Nature (London) **391**, 59 (1998).
[6] T.W. Odom, J.-L. Huang, P. Kim, and C.M. Lieber, Nature (London) **391**, 62 (1998).
[7] S.J. Tans, Michel H. Devoret, Hongjie Dai, Andreas Thess, Richard E. Smalley, L.J. Geerligs, and Cees Dekker, Nature (London) **386**, 474 (1997).
[8] M. Bockrath, David H. Cobden, Paul L. McEuen, Nasreen G. Chopra, A. Zettl, Andreas Thess, and R.E. Smalley, Science **275**, 1922 (1997).
[9] S.J. Tans, A.R.M. Verschueren, and C. Dekker, Nature (London) **393**, 49 (1998).
[10] For a review of the field of fullerenes and nanotubes, see B.I. Yakobson and R.E. Smalley, Am. Sci. **85**, 324 (1997).
[11] Y.S. Li and D. Tománek, Chem. Phys. Lett. **221**, 453 (1994).
[12] L. Lou, P. Nordlander, and R.E. Smalley, Phys. Rev. B **52**, 1429 (1995).
[13] S.G. Kim, Y.H. Lee, P. Nordlander, and D. Tománek, Chem. Phys. Lett. **264**, 345 (1997).
[14] Y.H. Lee, S.G. Kim, and D. Tománek, Chem. Phys. Lett. **265**, 667 (1997).
[15] D. Tománek and M.A. Schluter, Phys. Rev. Lett. **67**, 2331 (1991).
[16] Y.-K. Kwon, D. Tománek, Y.H. Lee, K.H. Lee, and S. Saito, J. Mater. Res. **13**, 2363 (1998).
[17] W. Zhong, D. Tománek, and G.F. Bertsch, Solid State Commun. **86**, 607 (1993).
[18] S.G. Kim and D. Tománek, Phys. Rev. Lett. **72**, 2418 (1994).
[19] Y.-K. Kwon, Y.H. Lee, S.-G. Kim, P. Jund, D. Tománek, and R.E. Smalley, Phys. Rev. Lett. **79**, 2065 (1997).
[20] H.-G. Busmann, Th. Lill, and I.V. Hertel, Chem. Phys. Lett. **187**, 459 (1991).
[21] G. Che, B.B. Lakshmi, E.R. Fisher, and C.R. Martin, Nature (London) **393**, 346 (1998).
[22] M. Kusunoki, J. Shibata, M. Rokkaku, and T. Hirayama, Jpn. J. Appl. Phys. **37**, L605 (1998).
[23] Brian W. Smith, Marc Monthioux, and David E. Luzzi, Nature (London) **396**, 323 (1998).

Photogalvanic Effects in Heteropolar Nanotubes

Petr Král,[1] E. J. Mele,[2] and David Tománek[3]

[1]*Department of Chemical Physics, Weizmann Institute of Science, 76100 Rehovot, Israel*
[2]*Department of Physics, Laboratory for Research on the Structure of Matter, University of Pennsylvania, Philadelphia, Pennsylvania 19104*
[3]*Department of Physics and Astronomy, and Center for Fundamental Materials Research, Michigan State University, East Lansing, Michigan 48824-1116*

(Received 18 January 2000)

We show that an electrical shift current is generated when electrons are photoexcited from the valence to conduction bands on a BN nanotube. This photocurrent follows the light pulse envelope and its symmetry is controlled by the atomic structure of the nanotube. We find that the shift current has an intrinsic quantum mechanical signature in which the chiral index of the tube determines the direction of the current along the tube axis. We identify the discrete lattice effects in the tangent plane of the tube that lead to an azimuthal component of the shift current. The nanotube shift current can lead to ultrafast optoelectronic and optomechanical applications.

PACS numbers: 72.40.+w, 61.48.+c, 78.20.Jq, 85.40.Ux

Recent progress in synthesis of nanometer scale materials has led to the discovery of $B_xC_yN_z$ nanotubes. They can be formed in nearly homogeneous ordered structures [1,2] or in multiwall hybrid structures with alternating BN and C compositions [3]. These materials differ fundamentally from the structurally similar carbon nanotubes by being *noncentrosymmetric* (NCS) and *polar*. This opens the possibility for accessing a new class of photovoltaic effects at the molecular scale.

Photovoltaic effects in NCS materials are often based on an asymmetric generation of hot carriers at momenta $\pm\mathbf{k}$ leading to a so-called "ballistic photocurrent" [4–6]. In polar NCS materials, photoexcitation across the band gap with polarized light also produces the so-called electrical "shift current" [7–9]. Microscopically this originates from a net displacement of charge in the unit cell due to light induced interband transitions ($\mathbf{J}_e$), intraband relaxation ($\mathbf{J}_s$), and (radiative) transitions to the original bands ($\mathbf{J}_r$). In bulk materials, the excitation component $\mathbf{J}_e$ usually prevails.

We show that *unpolarized light* can induce a shift current $\mathbf{J}_e$ in polar NCS nanotubes, with a direction along the tube axis which is determined by the chiral index of the tube. We find that this effect has an essentially quantum mechanical origin, where the *sign* of the current along the tube axis is controlled by the phase matching of electronic Bloch waves around the tube circumference. The discrete lattice structure controls the azimuthal component of this current and thus produces a net *helical current* on the tube. These photoeffects can lead to an assortment of new optoelectronic, optomechanical, and magnetic applications, and interesting extensions to ring structures [10] and heterojunctions [11]. We should stress that the photoeffects we discuss here are found at nonlinear order in the exciting fields, and are therefore physically distinct from chiral currents tilted with respect to the tube axis, predicted in dc bias driven chiral BN nanotubes [12] or chiral stretched C nanotubes [13,14].

A flat BN sheet has a honeycomb lattice with the B and N occupying alternate sublattices as shown in Fig. 1. The physics of the shift current can be understood qualitatively by considering the response of this 2D network of bonds to normally incident polarized light. The valence states are polarized towards the N sites and the conduction states towards the B sites. For vertically polarized (y-polarized) incident light the response of the system is dominated by the bonds which produce a net y-polarized current. For horizontally (x-polarized) incident light, the bonds with a nonzero horizontal component dominate, but these also produce a net y-polarized current. Note that excitation with an unpolarized incident field *cannot* produce a net current on this lattice since it has a threefold symmetry. However, this symmetry is removed when the sheet is wrapped into a cylindrical nanotube where the physics should be dominated by excitations with the field polarized along the tube axis. Depending on the wrapped structure of the tube, we anticipate an intrinsic photocurrent which can flow along the tube, around the tube, or in a chiral pattern on the tube surface.

These ideas can be quantified by developing a quantum mechanical model which generalizes our long wavelength theory for a nonpolar carbon nanotube [15] to the heteropolar lattice. We work in a basis of Bloch orbitals $\Phi_{k\alpha}(r) = e^{ik\cdot r}\sum_n e^{-ik\cdot(r-R_n-\tau_\alpha)}\phi_{n\alpha}/\sqrt{N} = e^{ik\cdot r}U_{k\alpha}$ where $\alpha = \pm 1$ denotes the two sublattices occupying sites at τ_α in the nth unit cell. We study the states near the conduction and valence band edges at the K and K' points of the Brillouin zone shown in Fig. 1. A long wavelength Hamiltonian for these states is obtained by an expansion in small crystal momenta around these points, and yields in our two component basis ($\hbar = 1$)

 0031-9007/00/85(7)/1512(4)$15.00

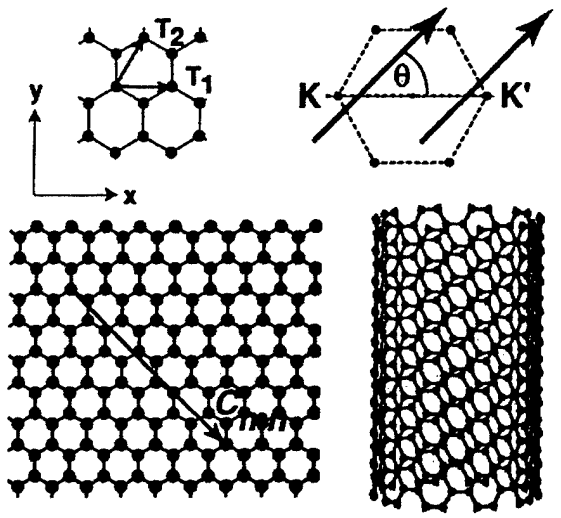

FIG. 1 (color). Planar BN forms a honeycomb lattice with B and N occupying alternate sites (upper left). A BN tube is formed by wrapping the sheet through the translation vector C_{mn} (lower left) quantizing the transverse crystal momenta. The upper right-hand panel shows two representative lines of allowed momenta for a tube with a nonzero chiral index $\nu = \mathrm{mod}(m - n, 3)$ and chiral angle θ. The lower right panel shows the structure for the nonchiral armchair (10, 10) wrapping of the BN sheet.

$$H_\lambda(\Delta, k, \delta_\lambda) = \begin{pmatrix} \Delta & \lambda v_F(k - i\delta_\lambda) \\ \lambda v_F(k + i\delta_\lambda) & -\Delta \end{pmatrix}, \tag{1}$$

where $\lambda = \pm 1$ is an index which labels an expansion around the K or K' points. The Hamiltonian in Eq. (1) is parametrized by three energies: a symmetry breaking site diagonal potential Δ, the kinetic energy $v_F k$ for motion along the tube, and the kinetic energy $v_F\delta$ due to the quantization of the transverse momentum around the circumference of the tube. On a cylindrical tube with lattice constant a and primitive lattice translation vectors in its tangent plane $T_1 = a(1, 0)$ and $T_2 = a(1/2, \sqrt{3}/2)$ (Fig. 1) it is conventional to index the lattice structure by two integers m and n which define a superlattice translation vector $C_{mn} = mT_1 + nT_2$. The transverse momenta on an (m, n) tube are quantized to the values $\delta_N = \delta_0 + 2\pi N/|C_{mn}|$ where $\delta_0 = 2\pi\,\mathrm{sgn}(\nu)/3|C_{mn}|$, depending on the sign of the chiral index of the tube, $\nu = \mathrm{mod}(n - m, 3)$. In Eq. (1) $\delta_\lambda = \lambda\delta_N$.

The eigenvectors of H in Eq. (1) are

$$g_v = \begin{pmatrix} ue^{-i\phi/2} \\ -ve^{i\phi/2} \end{pmatrix} \frac{e^{i\theta_{vk}}}{\sqrt{2}}; \qquad g_c = \begin{pmatrix} ve^{-i\phi/2} \\ ue^{i\phi/2} \end{pmatrix} \frac{e^{i\theta_{ck}}}{\sqrt{2}}, \tag{2}$$

where $E = \sqrt{v_F^2(k^2 + \delta_\lambda^2) + \Delta^2}$, $\phi = \tan^{-1}(\delta_\lambda/\lambda k)$, $u = \sqrt{(E - \Delta)/E}$, and $v = \sqrt{(E + \Delta)/E}$. In the rest of this paper we will set the Fermi velocity $v_F = 1$ so that energies and momenta are measured in the same units. Equation (2) explicitly includes a gauge function θ_{mk} since the overall phase of the Bloch function is not fixed, and our calculation will require differentiation with respect to k. The Bloch eigenfunctions of our problem are expressed as the product of three factors $\psi_{km}(r) = e^{ik\cdot r}\sum_\alpha g_{m\alpha}(k)U_{k\alpha}(r)$.

We extend the model Hamiltonian in Eq. (1) to include coupling of electrons to the oscillating optical fields $\mathbf{E}(t) = \mathbf{E}e^{-i\omega t}$ + c.c. through the dipole operator [8,9] $H_{\mathrm{int}} = -e\mathbf{E}(t)\cdot\mathbf{r}$. For a field polarized along the tube direction the matrix elements of the dipole operator between band eigenstates m and m' at crystal momenta k and k' are expressed using a formulation due to Blount [16]

$$r_{m'm}(k', k) = \langle\psi_{k'm'}|r|\psi_{km}\rangle = -i\langle\psi_{k'm'}|\partial_k|\psi_{km}\rangle + i\delta(k - k')\sum_{\alpha\beta}\delta_{\alpha\beta}g^*_{m'\beta}(k')\partial_k g_{m\alpha}(k). \tag{3}$$

The second term on the right-hand side of (3) forms the connection $\xi_{m'm} = ig^*_{m'}(k)\cdot\partial_k g_m(k)$ due to the k dependence of the eigenstates in (2) [17].

In general the shift current $\mathbf{J}$ can be expressed in terms of the band off-diagonal matrix elements of the velocity operator $\mathbf{v}_{\beta\alpha}$ ($\mathbf{v} = i[H, \mathbf{r}]$), and the band off-diagonal term in the density matrix $\rho_{\alpha\beta}$, calculated to second order in the exciting fields $\mathbf{E}$, as follows [7–9]:

$$\mathbf{J} = 2e\sum_{m\neq n}\int\frac{dk}{2\pi}\mathbf{v}_{mn}(k)\rho_{nm}(k) = \mathbf{J}_e + \mathbf{J}_s + \mathbf{J}_r. \tag{4}$$

We focus on the component of the excitation current J_e *along the tube direction.* After evaluating the sum in (4), we arrive at the transparent result

$$J_e = 2e\int\frac{dk}{2\pi}\dot{f}_{cv}(k)R_{cv}(k) \approx e\dot{n}\mathcal{R}. \tag{5}$$

Here $\dot{f}_{cv}(k)$ is the transition rate at wave vector k, and the *shift vector* $R_{cv}(k)$ is given by

$$R_{cv}(k) = \partial_k\theta_{vc}(k) + \xi_{cc}(k) - \xi_{vv}(k) \tag{6}$$

with $\xi_{vc}(k) = |\xi_{vc}(k)|e^{i\theta_{vc}(k)}$. The shift vector $R_{cv}(k)$ is invariant under the gauge transformations $\exp(i\theta_{mk})$ and we will evaluate it in a gauge with $\partial_k\theta_{mk} = 0$.

For an incident electric field polarized along the tube direction, interband excitations are allowed only between band states with the same transverse momentum δ. For transitions between the lowest two azimuthal subbands ($N = 0$) using the eigenfunctions in Eq. (2) we find

$$\xi_{vc}(k) = \frac{-1}{2}uv\left(\frac{\Delta}{E^2 - \Delta^2}\partial_k E + i\partial_k\phi\right), \tag{7}$$

which gives the off-diagonal contribution in Eq. (6)

$$\partial_k\theta_{vc} = \partial_k\tan^{-1}\left(\frac{-\delta\sqrt{\delta^2 + \Delta^2 + k^2}}{k\Delta}\right). \tag{8}$$

The diagonal elements in Eq. (6) are

$$\xi_{mm}(k) = ig^\dagger_m\cdot\partial_k g_m = \mp\frac{\Delta}{2E}\left(\frac{\delta}{\delta^2 + k^2}\right), \tag{9}$$

where the sign is negative for valence states and positive for conduction states. Combining Eqs. (8) and (9) we obtain the shift vector

$$R_{cv}(k) = \frac{2\delta\Delta}{(\delta^2 + k^2)\sqrt{\delta^2 + \Delta^2 + k^2}}. \quad (10)$$

Comparison with Eq. (9) shows that the shift current [Eq. (5)] opposes the direction of the ground state polarization of the tube.

This shift vector is odd in the symmetry breaking potential Δ and *odd in the transverse momentum* δ. Therefore, two BN tubes with nearly the same wrapped lattice structure but *opposite* chiral indices ν exhibit reversed ground state polarizations and opposite shift currents. Armchair BN nanotubes with wrapping indices (m, m) have chiral index $\nu = 0$ and do not exhibit a longitudinal shift current [as shown in the middle panel in Fig. 2 for the (5,5) tube]. Zigzag BN tubes with wrapping indices $(m, 0)$ can be grouped into three families with positive, negative, or zero shift currents distinguished by the sign of the chiral index ν [an example for the (8,0) tube with $\nu = -1$ is in the left panel of Fig. 2]. It is important to notice that an isolated flat BN sheet has a threefold symmetry axis perpendicular to the BN plane and therefore it has zero electric polarization in its tangent plane, by symmetry. Thus it has no shift current for excitations at the band edge. The nonzero shift vector in Eq. (10) when $k \to 0$ is a remarkable long wavelength quantum mechanical effect that reveals the quantization of the transverse momentum on the wrapped tube.

The shift current J_e in Eq. (5) is determined by the average shift vector $\mathcal{R}$, describing the change of polarity in the excitation, and by the carrier injection rate $\dot{n}$. The BN bond has significant ionic character with [18] $2\Delta \approx 4$ eV. This gives for excitations near the band edge, $k \to 0$, a shift vector with a magnitude $\mathcal{R} \approx 0.06$ nm for a (17,0) tube. For an incident intensity $S = 100$ kW/cm^2 we can also obtain the interband excitation rate; we estimate that $\dot{n} \approx 70\ \text{nm}^{-1}\,\mu\text{s}^{-1}$ produces a net electronic shift current of $J_e \approx 0.67$ pA. This value is slightly larger than what one obtains for excited bulk polar semiconductors. Opposing shift currents on different walls of a coaxial multiwall tube can reduce the macroscopic current, but cannot eliminate it except for rare high symmetry concentric lattice structures. We also expect that the recombination current J_r will oppose J_e since both currents rely on optical transitions with longitudinal polarization. However, this should not prevent the observation of J_e using pulsed laser excitation since the time scale for J_r is of the order of nanoseconds.

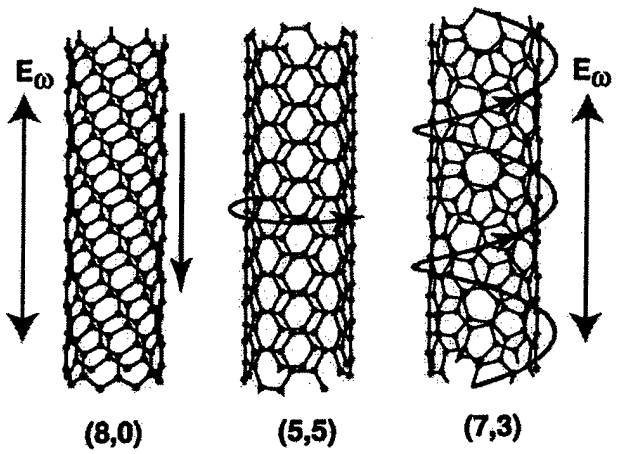

FIG. 2 (color). Electronic shift currents produced by excitation of BN nanotubes with light polarized along their axis. For the (8,0) wrapping the chiral index is $\nu = -1$, and the shift current is purely longitudinal. The (5,5) armchair wrapping has chiral index $\nu = 0$ and has zero longitudinal current and a nonzero azimuthal current which runs "counterclockwise" on the tube surface. The (7,3) wrapping has a chiral shift current with nonzero longitudinal and azimuthal components.

This formalism can be extended to study *chiral shift currents* with nonvanishing longitudinal and azimuthal components. Interestingly, the long wavelength Hamiltonian in Eq. (1) gives zero azimuthal current for *any* chiral index ν. As $Q_\pm = k \pm i\delta \to 0$ this occurs because of a cancellation of contributions from the K and K' points whose long wavelength Hamiltonians have opposite handedness. However, azimuthal currents arise due to discrete lattice effects occurring at higher orders in an expansion in $Q_\pm$. To study this, we define two unit vectors at each point in the tube surface, perpendicular to the local outward unit normal $\hat{n}$: $\hat{e}_x$ which points along the tube axis, and $\hat{e}_y = \hat{n} \times \hat{e}_x$ which points counterclockwise on the tube surface. A chiral angle θ is defined as the angle between $\hat{e}_x$ and the T_1 lattice direction as shown in Fig. 1 (with this convention armchair nanotubes have $\theta = 0$). Then the lowest nonvanishing contribution to an azimuthal (y-polarized) shift current must have the form $\cos(6\phi - 3\theta)$ where $\phi = \tan^{-1}(\delta/k)$. The dependence on 6ϕ means that azimuthal currents first occur in the continuum theory at sixth order in $|Q|$.

We can study these terms by replacing the kinetic energy terms in the Hamiltonian of Eq. (1) by the discrete lattice counterpart $iv_F(k + i\delta) = iv_F Q_+ \to t\sum_n e^{i(K+Q)\cdot\tau_n}$ where t is the hopping amplitude between sites connected by the bond vectors τ_n. A systematic expansion of the azimuthal shift current in powers of $Q_\pm$ then gives contributions with the correct lattice symmetry and shows that the ratio of the azimuthal and longitudinal in-plane current densities scales as

$$p = \frac{J_y}{J_x} = \frac{(k^2 + \delta^2)^3\tau^3}{\delta(\Delta^2 + k^2 + \delta^2)}\cos(6\phi - 3\theta). \quad (11)$$

The azimuthal current for any zigzag wrapping is zero because of the angular factor, while its longitudinal current, shown in Fig. 2, is determined by the chiral index ν. For armchair tubes and all nonzigzag tubes with chiral index $\nu = 0$, we have $\delta = 0$, so the shift current is purely azimuthal with a direction determined by the sign of the

potential Δ. These energy dependent currents vanish at the band edge as $\propto(E^2 - \Delta^2)^3$. Nonzigzag tubes with chiral index $\nu \neq 0$ have a nonzero δ and thus the azimuthal current is nonzero with $p \propto (\delta/\Delta)^2(\delta\tau)^3$. There the shift current circulates in a *helical pattern* on the tube surface as shown in the right panel of Fig. 2, with a chirality determined by the index ν. The pitch is also energy dependent and increases according to $p(E) = p(0) + a(E^2 - \Delta^2)$. Thus, as shown in Fig. 2, the zigzag nanotubes generate a photocurrent like a wire, the armchair tubes like a coil, and the chiral tubes can exhibit a helical current on the tube surface.

Alternatively, the shift current can be studied in a semiclassical model, by considering an expansion in t/Δ, where t is the nearest neighbor hopping amplitude, and Δ is the site diagonal potential. In the limit $t/\Delta \ll 1$ the tube can be regarded as a network of independent bonds whose excitations are superimposed. Here the local symmetry of the zigzag tube requires zero net azimuthal current while the armchair wrapping has a nonzero azimuthal current with its direction determined by the sign of Δ. However, it is difficult to correctly describe the physics of the *longitudinal* current using this model. This is because the longitudinal current is controlled by the quantization of the transverse momentum δ. The first terms in the semiclassical expansion that are sensitive to δ occur at order $(t/\Delta)^N$ where N is the number of bonds ($\approx$40) around the tube circumference. This reflects the fact that the longitudinal current is fundamentally a nonclassical quantity for this system.

The longitudinal shift current reduces the ground state electric polarization of the nanotube. This can lead to a *fast readjustment* of atomic positions on the tube walls. Generation of voltages by a mechanical elongation [19] of NCS nanotubes is a related effect. In both situations the response can be stronger in buckled nanotubes [20] or if different types of atoms occur in different layers, as in MoS_2, WS_2 [21], or GaSe nanotubes [22]. Recently, mechanical motions, strikingly similar to those found in some biomolecular systems [23], were observed in irradiated nanotube bundles [24]. Interesting mechanical response to an applied dc bias is observed in carbon nanotubes immersed in a solution of NaCl [25]. Here, the motion is caused by *attraction of ions* of a given polarity to the nanotube. The speed but short duration of the shift current-induced mechanical response complements the slow but steady state effect of a dc bias.

Experimental observation of the shift current in BN nanotubes would provide a striking illustration of fundamental concepts in the modern quantum theory of polarization. The effect is also promising for new applications since it couples the microscopic physics on short length scales, which can be tuned by local fields and mechanical loads, to the long distance properties of the system (polarization, photovoltage, etc.) Finally, there is a rapidly growing family of related submicron one dimensional materials to which these ideas can be applied.

P. K. acknowledges J. E. Sipe and M. Shapiro for financial support. This work was also supported by the DOE under Grant No. DE-FG02-84ER45118 (E. J. M.), by the NSF under Grant No. DMR 98-02560 (E. J. M.), and by the ONR under Grant No. N00014-99-1-0252 (D. T.).

[1] N. G. Chopra *et al.*, Science **269**, 966 (1995).
[2] Z. Weng-Sieh *et al.*, Phys. Rev. B **51**, 11 229 (1995).
[3] K. Suenaga *et al.*, Appl. Phys. A **68**, 301 (1999).
[4] B. I. Sturman and V. M. Fridkin, *The Photovoltaic and Photorefractive Effects in Noncentrosymmetric Materials* (Gordon and Breach Science Publishers, New York, 1992), and references therein.
[5] P. Král and D. Tománek, Phys. Rev. Lett. **82**, 5373 (1999).
[6] E. J. Mele, P. Král, and D. Tománek, Phys. Rev. B **61**, 7669 (2000).
[7] V. I. Belinicher, E. L. Ivchenko, and B. I. Sturman, Sov. Phys. JETP **56**, 359 (1982).
[8] J. E. Sipe and A. Shkrebtii, Phys. Rev. B **61**, 5381 (2000).
[9] P. Král, J. Phys. Condens. Matter **12**, 4851 (2000).
[10] J. Liu *et al.*, Nature (London) **385**, 780 (1997); Ph. Avouris *et al.*, Nature (London) **394**, 780 (1999).
[11] X. Blase *et al.*, Appl. Phys. Lett. **70**, 197 (1997).
[12] Y. Miyamoto, S. G. Louie, and M. L. Cohen, Phys. Rev. Lett. **76**, 2121 (1996).
[13] Y. Miyamoto, Phys. Rev. B **54**, R11 149 (1996).
[14] O. M. Yevtushenko *et al.*, Phys. Rev. Lett. **79**, 1102 (1997).
[15] C. L. Kane and E. J. Mele, Phys. Rev. Lett. **78**, 1932 (1997).
[16] E. I. Blount, in *Solid State Physics, Advances in Research and Applications*, edited by F. Seitz and D. Turnbull (Academic, New York, 1962), Vol. 13, p. 305.
[17] Equation (3) is gauge invariant if $i\delta_{\beta\alpha}\partial_k g_{m\alpha}(k)$ is generalized to the covariant derivative $[i\delta_{\beta\alpha}\partial_k + \Gamma_{\beta\alpha}(k)]g_{m\alpha}(k)$, where $\Gamma_{\beta\alpha}(k) = i\int dr\, U^*_{k\beta}(r)\partial_k U_{k\alpha}(r)$ arises from the k dependence in the basis functions $U_{k\alpha}(r)$. Our choice of basis in Bloch functions gives $\Gamma_{\alpha\beta}(k) = 0$.
[18] A. Rubio, J. Corkill, and M. L. Cohen, Phys. Rev. B **49**, 5081 (1994).
[19] J.-P. Salvetat *et al.*, Phys. Rev. Lett. **82**, 944 (1999).
[20] E. Hernández, C. Goze, P. Bernier, and A. Rubio, Phys. Rev. Lett. **80**, 4502 (1998).
[21] R. Tenne *et al.*, Nature (London) **360**, 444 (1992); L. Margulis *et al.*, Nature (London) **365**, 114 (1993).
[22] M. Côté, M. L. Cohen, and D. J. Chadi, Phys. Rev. B **58**, R4277 (1998).
[23] A. D. T. Samuel and H. C. Berg, Biophys. J. **71**, 918 (1996).
[24] Y. Zhang and S. Iijima, Phys. Rev. Lett. **82**, 3472 (1999).
[25] R. H. Baughman *et al.*, Science **284**, 1340 (1999).

Unusually High Thermal Conductivity of Carbon Nanotubes

Savas Berber, Young-Kyun Kwon,* and David Tománek

Department of Physics and Astronomy, and Center for Fundamental Materials Research, Michigan State University, East Lansing, Michigan 48824-1116

(Received 23 February 2000)

Combining equilibrium and nonequilibrium molecular dynamics simulations with accurate carbon potentials, we determine the thermal conductivity λ of carbon nanotubes and its dependence on temperature. Our results suggest an unusually high value, $\lambda \approx 6600$ W/m K, for an isolated (10, 10) nanotube at room temperature, comparable to the thermal conductivity of a hypothetical isolated graphene monolayer or diamond. Our results suggest that these high values of λ are associated with the large phonon mean free paths in these systems; substantially lower values are predicted and observed for the basal plane of bulk graphite.

PACS numbers: 61.48.+c, 63.22.+m, 66.70.+f, 68.70.+w

With the continually decreasing size of electronic and micromechanical devices, there is an increasing interest in materials that conduct heat efficiently, thus preventing structural damage. The stiff sp^3 bonds, resulting in a high speed of sound, make monocrystalline diamond one of the best thermal conductors [1]. An unusually high thermal conductance should also be expected in carbon nanotubes [2,3], which are held together by even stronger sp^2 bonds. These systems, consisting of seamless and atomically perfect graphitic cylinders a few nanometers in diameter, are self-supporting. The rigidity of these systems, combined with virtual absence of atomic defects or coupling to soft phonon modes of the embedding medium, should make isolated nanotubes very good candidates for efficient thermal conductors. This conjecture has been confirmed by experimental data that are consistent with a very high thermal conductivity for nanotubes [4].

In the following, we will present results of molecular dynamics simulations using the Tersoff potential [5], augmented by van der Waals interactions in graphite, for the temperature dependence of the thermal conductivity of nanotubes and other carbon allotropes. We will show that isolated nanotubes are at least as good of heat conductors as high-purity diamond. Our comparison with graphitic carbon shows that interlayer coupling reduces thermal conductivity of graphite within the basal plane by 1 order of magnitude with respect to the nanotube value which lies close to that for a hypothetical isolated graphene monolayer.

The thermal conductivity λ of a solid along a particular direction, taken here as the z axis, is related to the heat flowing down a long rod with a temperature gradient dT/dz by

$$\frac{1}{A}\frac{dQ}{dt} = -\lambda \frac{dT}{dz}, \tag{1}$$

where dQ is the energy transmitted across the area A in the time interval dt. In solids where the phonon contribution to the heat conductance dominates, λ is proportional to Cvl, the product of the heat capacity per unit volume C, the speed of sound v, and the phonon mean free path l. The latter quantity is limited by scattering from sample boundaries (related to grain sizes), point defects, and by umklapp processes. In the experiment, the strong dependence of the thermal conductivity λ on l translates into an unusual sensitivity to isotopic and other atomic defects. This is best illustrated by the reported thermal conductivity values in the basal plane of graphite [6] which scatter by nearly 2 orders of magnitude. As similar uncertainties may be associated with thermal conductivity measurements in "mats" of nanotubes [4], we decided to determine this quantity using molecular dynamics simulations.

The first approach used to calculate λ was based on a direct molecular dynamics simulation. Heat exchange with a periodic array of hot and cold regions along the nanotube has been achieved by velocity rescaling, following a method that had been successfully applied to the thermal conductivity of glasses [7]. Unlike glasses, however, nanotubes exhibit an unusually high degree of long-range order over hundreds of nanometers. The perturbations imposed by the heat transfer reduce the effective phonon mean free path to below the unit cell size. We found it hard to achieve convergence, since the phonon mean free path in nanotubes is significantly larger than unit cell sizes tractable in molecular dynamics simulations.

As an alternate approach to determine the thermal conductivity, we used equilibrium molecular dynamics simulations [8,9] based on the Green-Kubo expression that relates this quantity to the integral over time t of the heat flux autocorrelation function by [10]

$$\lambda = \frac{1}{3Vk_BT^2}\int_0^\infty \langle \mathbf{J}(t)\cdot\mathbf{J}(0)\rangle\, dt\,. \tag{2}$$

Here, k_B is the Boltzmann constant, V is the volume, T the temperature of the sample, and the angular brackets denote an ensemble average. The heat flux vector $\mathbf{J}(t)$ is

defined by

$$\mathbf{J}(t) = \frac{d}{dt}\sum_i \mathbf{r}_i \Delta e_i$$

$$= \sum_i \mathbf{v}_i \Delta e_i - \sum_i \sum_{j(\neq i)} \mathbf{r}_{ij}(\mathbf{f}_{ij} \cdot \mathbf{v}_i), \quad (3)$$

where $\Delta e_i = e_i - \langle e \rangle$ is the excess energy of atom i with respect to the average energy per atom $\langle e \rangle$. $\mathbf{r}_i$ is the position and $\mathbf{v}_i$ the velocity of atom i, and $\mathbf{r}_{ij} = \mathbf{r}_j - \mathbf{r}_i$. Assuming that the total potential energy $U = \sum_i u_i$ can be expressed as a sum of binding energies u_i of individual atoms, then $\mathbf{f}_{ij} = -\nabla_i u_j$, where ∇_i is the gradient with respect to the position of atom i.

In low-dimensional systems, such as nanotubes or graphene monolayers, we infer the volume from the way these systems pack in space (nanotubes form bundles and graphite a layered structure, both with an interwall separation of $\approx$3.4 Å) in order to convert thermal conductance of a system to thermal conductivity of a material.

Once $\mathbf{J}(t)$ is known, the thermal conductivity can be calculated using Eq. (2). We found, however, that these results depend sensitively on the initial conditions of each simulation, thus necessitating a large ensemble of simulations. This high computational demand was further increased by the slow convergence of the autocorrelation function, requiring long integration time periods.

These disadvantages have been shown to be strongly reduced in an alternate approach [11] that combines the Green-Kubo formula with nonequilibrium thermodynamics [12,13] in a computationally efficient manner [14]. In this approach, the thermal conductivity along the z axis is given by

$$\lambda = \lim_{\mathbf{F}_e \to 0} \lim_{t \to \infty} \frac{\langle J_z(\mathbf{F}_e, t) \rangle}{F_e T V}, \quad (4)$$

where T is the temperature of the sample, regulated by a Nosé-Hoover thermostat [15], and V is the volume of the sample. $J_z(\mathbf{F}_e, t)$ is the z component of the heat flux vector for a particular time t. $\mathbf{F}_e$ is a small fictitious "thermal force" (with a dimension of inverse length) that is applied to individual atoms. This fictitious force $\mathbf{F}_e$ and the Nosé-Hoover thermostat impose an additional force $\Delta\mathbf{F}_i$ on each atom i. This additional force modifies the gradient of the potential energy and is given by

$$\Delta\mathbf{F}_i = \Delta e_i \mathbf{F}_e - \sum_{j(\neq i)} \mathbf{f}_{ij}(\mathbf{r}_{ij} \cdot \mathbf{F}_e)$$

$$+ \frac{1}{N}\sum_j \sum_{k(\neq j)} \mathbf{f}_{jk}(\mathbf{r}_{jk} \cdot \mathbf{F}_e) - \alpha \mathbf{p}_i. \quad (5)$$

Here, α is the Nosé-Hoover thermostat multiplier acting on the momentum $\mathbf{p}_i$ of atom i. α is calculated using the time integral of the difference between the instantaneous kinetic temperature T of the system and the heat bath temperature T_{eq}, from $\dot{\alpha} = (T - T_{\text{eq}})/Q$, where Q is the thermal inertia. The third term in Eq. (5) guarantees that the net force acting on the entire N-atom system vanishes.

In Fig. 1 we present the results of our nonequilibrium molecular dynamics simulations for the thermal conductance of an isolated (10, 10) nanotube aligned along the z axis. In our calculation, we consider 400 atoms per unit cell, and use periodic boundary conditions. Each molecular dynamics simulation run consists of 50 000 time steps of 5.0×10^{-16} s. Our results for the time dependence of the heat current for the particular value $F_e = 0.2$ Å^{-1}, shown in Fig. 1(a), suggest that $J_z(t)$ converges within the first few picoseconds to its limiting value for $t \to \infty$ in the temperature range below 400 K. The same is true for the quantity $J_z(t)/T$, shown in Fig. 1(b), the average of

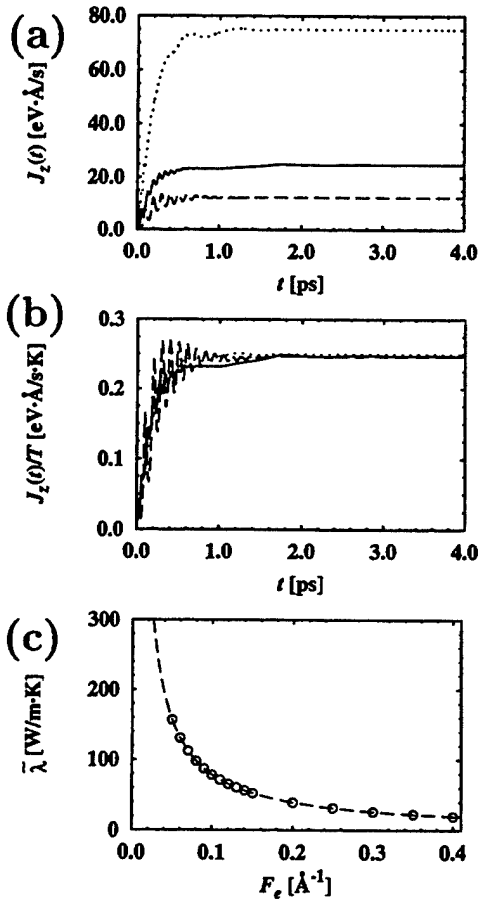

FIG. 1. (a) Time dependence of the axial heat flux $J_z(t)$ in a (10, 10) carbon nanotube. Results of nonequilibrium molecular dynamics simulation at a fixed applied thermal force $F_e = 0.2$ Å^{-1} are shown at temperatures $T = 50$ K (dashed line), 100 K (solid line), and 300 K (dotted line). (b) Time dependence of $J_z(t)/T$, a key quantity for the calculation of the thermal conductivity, for $F_e = 0.2$ Å^{-1} and the same temperature values. (c) Dependence of the heat transport on the applied heat force F_e in the simulations for $T = 100$ K. The dashed line represents an analytical expression that is used to determine the thermal conductivity λ by extrapolating the simulation data points $\tilde{\lambda}$ for $F_e \to 0$.

which is proportional to the thermal conductivity λ according to Eq. (4). Our molecular dynamics simulations have been performed for a total time length of 25 ps to well represent the long-time behavior.

In Fig. 1(c) we show the dependence of the quantity

$$\tilde{\lambda} \equiv \lim_{t\to\infty} \frac{\langle J_z(\mathbf{F}_e, t)\rangle}{F_e T V} \tag{6}$$

on F_e. We have found that direct calculations of $\tilde{\lambda}$ for very small thermal forces carry a substantial error, as they require a division of two very small numbers in Eq. (6). We base our calculations of the thermal conductivity at each temperature on 16 simulation runs, with F_e values ranging from 0.4 to 0.05 Å^{-1}. As shown in Fig. 1(c), data for $\tilde{\lambda}$ can be extrapolated analytically for $\mathbf{F}_e \to 0$ to yield the thermal conductivity λ, shown in Fig. 2.

Our results for the temperature dependence of the thermal conductivity of an isolated (10, 10) carbon nanotube, shown in Fig. 2, reflect the fact that λ is proportional to the heat capacity C and the phonon mean free path l. At low temperatures, l is nearly constant, and the temperature dependence of λ follows that of the specific heat. At high temperatures, where the specific heat is constant, λ decreases as the phonon mean free path becomes smaller due to umklapp processes. Our calculations suggest that at $T = 100$ K, carbon nanotubes show an unusually high thermal conductivity value of 37 000 W/m K. This value lies very close to the highest value observed in any solid, $\lambda = 41\,000$ W/m K, that has been reported [1] for a 99.9% pure ^{12}C crystal at 104 K. In spite of the decrease of λ above 100 K, the room temperature value of 6600 W/m K is still very high, exceeding the reported thermal conductivity value of 3320 W/m K for nearly isotopically pure diamond [16].

We found it useful to compare the thermal conductivity of a (10, 10) nanotube to that of an isolated graphene monolayer as well as bulk graphite. For the graphene monolayer, we unrolled the 400-atom large unit cell of the (10, 10) nanotube into a plane. The periodically repeated unit cell used in the bulk graphite calculation contained 720 atoms, arranged in three layers. The results of our calculations, presented in Fig. 3, suggest that an isolated nanotube shows a very similar thermal transport behavior as a hypothetical isolated graphene monolayer, in general agreement with available experimental data [17–19]. Whereas even larger thermal conductivity should be expected for a monolayer than for a nanotube, we must consider that unlike the nanotube, a graphene monolayer is not self-supporting in vacuum. For all carbon allotropes considered here, we also find that the thermal conductivity decreases with increasing temperature in the range depicted in Fig. 3.

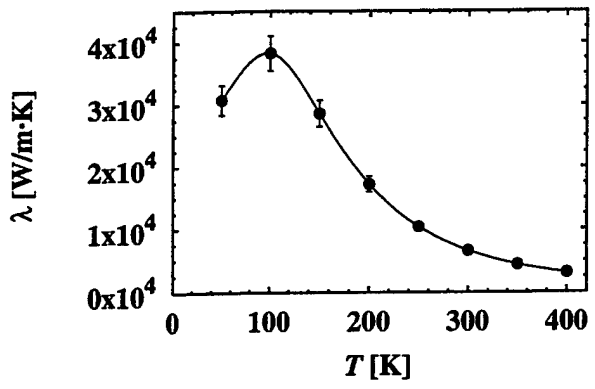

FIG. 2. Temperature dependence of the thermal conductivity λ for a (10, 10) carbon nanotube for temperatures below 400 K.

Very interesting is the fact that once graphene layers are stacked in graphite, the interlayer interactions quench the thermal conductivity of this system by nearly 1 order of magnitude. For the latter case of crystalline graphite, we also found our calculated thermal conductivity values to be confirmed by corresponding observations in the basal plane of highest-purity synthetic graphite [17–19] which are also reproduced in the figure. We would like to note that experimental data suggest that the thermal conductivity in the basal plane of graphite peaks near 100 K, similar to our nanotube results.

Based on the above described difference in the conductivity between a graphene monolayer and graphite, we should expect a similar reduction of the thermal conductivity when a nanotube is brought into contact with other systems. This should occur when nanotubes form a bundle or rope, become nested in multiwall nanotubes, or interact with other nanotubes in the "nanotube mat" of "bucky paper" and could be verified experimentally. Consistent with our conjecture is the low value of $\lambda \approx 0.7$ W/m K reported for the bulk nanotube mat at room temperature [4].

In summary, we combined results of equilibrium and nonequilibrium molecular dynamics simulations with

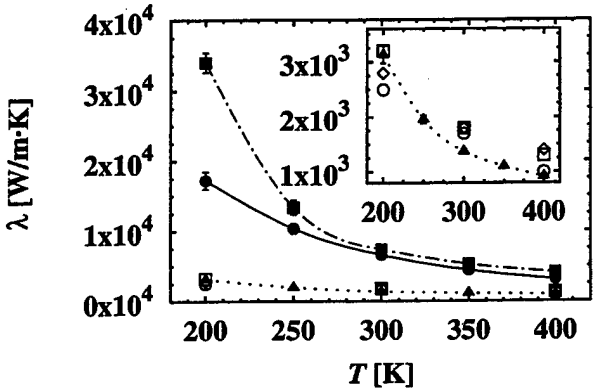

FIG. 3. Thermal conductivity λ for a (10, 10) carbon nanotube (solid line), in comparison to a constrained graphite monolayer (dash-dotted line), and the basal plane of *AA* graphite (dotted line) at temperatures between 200 and 400 K. The inset reproduces the graphite data on an expanded scale. The calculated values (solid triangles) are compared to the experimental data of Refs. [17] (open circles), [18] (open diamonds), and [19] (open squares) for graphite.

accurate carbon potentials to determine the thermal conductivity λ of carbon nanotubes and its dependence on temperature. Our results suggest an unusually high value $\lambda \approx 6600$ W/mK for an isolated (10, 10) nanotube at room temperature, comparable to the thermal conductivity of a hypothetical isolated graphene monolayer or graphite. We believe that these high values of λ are associated with the large phonon mean free paths in these systems. Our numerical data indicate that in the presence of interlayer coupling in graphite and related systems, the thermal conductivity is reduced significantly to fall into the experimentally observed value range.

This work was supported by the Office of Naval Research and DARPA under Grant No. N00014-99-1-0252. We acknowledge useful discussions with Professor Pao-Kuang Kuo and Professor Ctirad Uher.

*Present address: Department of Physics, University of California, and Materials Sciences Division, Lawrence Berkeley Laboratory, Berkeley, CA 94720.

[1] Lanhua Wei, P. K. Kuo, R. L. Thomas, T. R. Anthony, and W. F. Banholzer, Phys. Rev. Lett. **70**, 3764 (1993).
[2] S. Iijima, Nature (London) **354**, 56 (1991).
[3] M. S. Dresselhaus, G. Dresselhaus, and P. C. Eklund, *Science of Fullerenes and Carbon Nanotubes* (Academic Press, San Diego, 1996).
[4] J. Hone, M. Whitney, C. Piskoti, and A. Zettl, Phys. Rev. B **59**, R2514 (1999); J. Hone, M. Whitney, and A. Zettl, Synth. Met. **103**, 2498 (1999).
[5] J. Tersoff, Phys. Rev. B **37**, 6991 (1988).
[6] Citrad Uher, in *Numerical Data and Functional Relationships in Science and Technology,* edited by O. Madelung and G. K. White, Landolt-Börnstein, New Series, Group III, Vol. 15c (Springer-Verlag, Berlin, 1991), pp. 426–448.
[7] Philippe Jund and Rémi Jullien, Phys. Rev. B **59**, 13 707 (1999).
[8] M. Schoen and C. Hoheisel, Mol. Phys. **56**, 653 (1985).
[9] D. Levesque and L. Verlet, Mol. Phys. **61**, 143 (1987).
[10] D. A. McQuarrie, *Statistical Mechanics* (Harper & Row, London, 1976).
[11] A. Maeda and T. Munakata, Phys. Rev. E **52**, 234 (1995).
[12] D. J. Evans, Phys. Lett. **91A**, 457 (1982).
[13] D. P. Hansen and D. J. Evans, Mol. Phys. **81**, 767 (1994).
[14] D. C. Rapaport, *The Art of Molecular Dynamics Simulation* (Cambridge University Press, Cambridge, England, 1998).
[15] S. Nosé, Mol. Phys. **52**, 255 (1984); W. G. Hoover, Phys. Rev. A **31**, 1695 (1985).
[16] T. R. Anthony, W. F. Banholzer, J. F. Fleischer, Lanhua Wei, P. K. Kuo, R. L. Thomas, and R. W. Pryor, Phys. Rev. B **42**, 1104 (1990).
[17] Takeshi Nihira and Tadao Iwata, Jpn. J. Appl. Phys. **14**, 1099 (1975).
[18] M. G. Holland, C. A. Klein, and W. D. Straub, J. Phys. Chem. Solids **27**, 903 (1966).
[19] A. de Combarieu, J. Phys. (Paris) **28**, 951 (1967).

Effect of van der Waals Interactions on the Raman Modes in Single Walled Carbon Nanotubes

A. M. Rao,[1,*] J. Chen,[2,†] E. Richter,[2] U. Schlecht,[1] P. C. Eklund,[3] R. C. Haddon,[2] U. D. Venkateswaran,[4] Y.-K. Kwon,[5,‡] and D. Tománek[5]

[1]*Department of Physics and Astronomy, Clemson University, Clemson, South Carolina 29634*
[2]*Department of Chemistry, University of Kentucky, Lexington, Kentucky 40506*
[3]*Department of Physics, Pennsylvania State University, University Park, Pennsylvania 16802*
[4]*Department of Physics, Oakland University, Rochester, Michigan 48309*
[5]*Department of Physics and Astronomy and Center for Fundamental Materials Research, Michigan State University, East Lansing, Michigan 48824*

(Received 26 July 2000)

We have measured the Raman spectrum of individual single walled carbon nanotubes in solution and compare it to that obtained from the same starting material where the tubes are present in ordered bundles or ropes. Interestingly, the radial mode frequencies for the tubes in solution are found to be $\sim 10\ \mathrm{cm}^{-1}$ higher than those observed for tubes in a rope, in apparent contradiction to lattice dynamics predictions. We suggest that there is no such contradiction, and propose that the upshift is due rather to a decreased energy spacing of the Van Hove singularities in isolated tubes over the spacings in a rope, thereby allowing the same laser excitation to excite different diameter tubes in these two samples.

DOI: 10.1103/PhysRevLett.86.3895 PACS numbers: 78.30.Na

The dominant experimental technique for studying phonons in single walled carbon nanotubes (SWNTs) has been Raman spectroscopy [1–5]. Until now, almost all Raman spectra have been collected on nanotube bundles that are synthesized by the pulsed laser vaporization (PLV) [6] or the electric arc (EA) [7] methods. These bundles contain on the order of 100 well-aligned SWNTs arranged in an approximately closed-packed triangular lattice. A typical Raman spectrum of the EA-derived SWNT bundles obtained using the 1064 nm excitation wavelength exhibits two prominent features at $\omega_R \sim 160\ \mathrm{cm}^{-1}$ (radial band) and $\omega_T \sim 1590\ \mathrm{cm}^{-1}$ (tangential band). The position and the line shape of these bands have been used extensively to determine the SWNT diameter distribution and semiconducting/metallic nature of SWNTs.

The tube-tube interactions within SWNT bundles are weak, similar to the coupling between adjacent graphene planes in 3D crystalline graphite or the interball coupling found in solid C_{60}. This weak intertube coupling is dominated by the van der Waals interaction, but contains a nonzero covalent component that has been shown theoretically and experimentally to have significant influence on the vibrational [8–12] and electronic states for carbon nanotubes [13–15]. Recently, Chen *et al.* [5] reported the synthesis of soluble shortened and full-length single walled carbon nanotubes. Details of the preparation and characterization of the solubilized tubes (S-SWNTs) are described elsewhere [5]. Atomic force microscope images showed that the majority of the bundled SWNTs were separated into small bundles (2–5 nm in diameter) and isolated tubes during the solubilization process [5].

In Fig. 1, the Raman spectrum of S-SWNTs in CS_2 is compared to that obtained for bundled SWNTs, the latter in powder form. The S-SWNTs and bundled SWNTs referred to in Fig. 1 stem from the same as-prepared EA material. Three modes, previously identified with A_{1g}, E_{1g}, and E_{2g} symmetries and frequencies that are nearly independent of the tube diameter, are expected near the 1590 cm^{-1} band for achiral tubes [1]. For the chiral tubes, six modes are Raman active with A_1, E_1, and E_2 symmetries [16]. In contrast to the high frequency band at 1590 cm^{-1}, the low frequency band centered $\sim 160\ \mathrm{cm}^{-1}$ is identified with A_{1g}

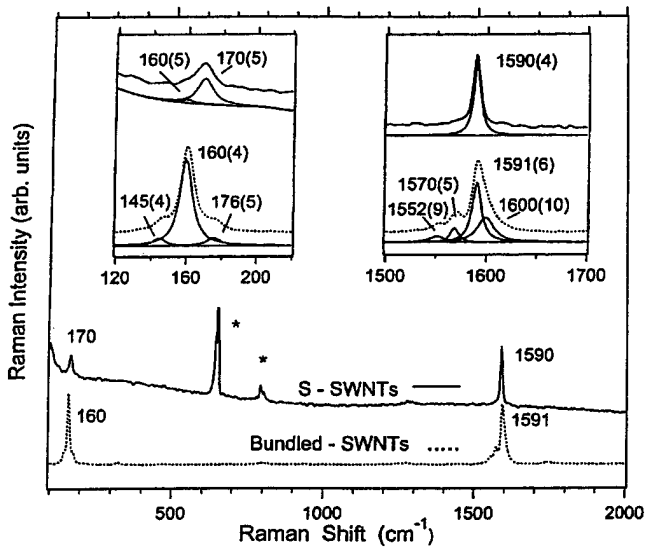

FIG. 1. Room temperature Raman spectrum of arc synthesized bundled SWNTs and solubilized SWNTs (S-SWNTs) in CS_2 (excitation wavelength = 1064 nm). The peaks identified by * are attributed to CS_2. The tangential band intensity is set to a constant peak intensity value so that the radial band intensities in the two spectra can be compared. Left- and right-hand insets show, respectively, the deconvolution of the radial and tangential bands in bundled and S-SWNTs. The vertical and horizontal axes for the two insets correspond, respectively, to the Raman intensity and shift. The numbers within parentheses refer to the full width at half maximum intensity of the Raman lines.

radial breathing modes whose frequency is strongly dependent on the tube diameter [16]. Consistent with the calculated mode frequencies and intensities, other weak Raman-active features have been observed in the intermediate phonon frequency region between ω_R and ω_T [1].

For an isolated SWNT, theoretical calculations have shown that the radial mode frequency ω_R' exhibits a particularly simple dependence on the tube diameter d' as [3]

$$\omega_R' \sim 224\ \mathrm{cm}^{-1} \cdot \mathrm{nm}/d'. \quad (1)$$

(Henceforth, primed and unprimed notation correspond, respectively, to isolated and bundled SWNTs.) Equation (1) has been widely used to determine the tube diameter distribution in samples containing both isolated and bundled nanotubes, since Raman spectroscopy provides a quick and convenient technique for sample characterization. Thus, care has to be taken to understand the origin of potential deviations from this relationship. As mentioned above, most Raman spectra have been obtained for bundled nanotubes. Because of the space restrictions imposed by the presence of neighboring tubes, tube-tube interactions within a bundle have been predicted to cause a $\sim$6–20 cm^{-1} up-shift in ω_R with respect to the corresponding value in isolated tubes, depending on particular theoretical calculations [8,9,11,15]. The effect of intertube interactions on the vibrational modes of SWNTs was first reported by Venkateswaran *et al.* [8] and has been used to interpret shifts in both ω_R and ω_T that were induced by applying external pressure. Comparing these experimental results to those obtained from a generalized tight binding calculation, which included the effects of the externally applied pressure, the simple $\omega_R' \sim 224\ \mathrm{cm}^{-1} \cdot \mathrm{nm}/d'$ relation for isolated tubes was generalized to nanotubes inside a bundle by the addition of a nearly constant upshift of $\sim$7% for tubes in the diameter range $0.7\ \mathrm{nm} < d < 1.5\ \mathrm{nm}$ [8,9]. Thus, in the case of bundled SWNTs, Eq. (1) is modified as

$$\omega_R \sim (224\ \mathrm{cm}^{-1} \cdot \mathrm{nm}/d) + \Delta\omega_R, \quad (2)$$

where $\Delta\omega_R$ is the anticipated up-shift due to tube-tube interactions which is approximately independent of the tube diameter in the restricted range of diameters.

According to Eq. (2), the observed up-shift in ω_R from bundled to S-SWNTs in Fig. 1 is anomalous, since the loss of intertube forces in S-SWNTs would be expected to soften ω_R relative to its frequency of 160 cm^{-1} observed in the Raman spectrum of bundled SWNTs. It should be noted that shifts in ω_R or ω_T have also been observed in doped nanotube bundles, where they have been related to the charge transfer between the nanotubes and the alkali metal (down-shift) or halogen dopants (up-shift) [17]. However, unlike the tube-tube coupling which affects mainly ω_R and not ω_T (see, for example, Fig. 1), charge transfer induced by doping was found to affect *both* the radial and the tangential mode frequencies to a large extent [17]. Clearly, for the spectra depicted in Fig. 1, the 10 cm^{-1} up-shift in ω_R upon forming S-SWNTs from bundled SWNTs cannot be attributed to charge transfer, since ω_T for S-SWNT exhibits an insignificant frequency shift from the value observed in bundled SWNTs.

It is also of interest to note from the right-hand inset of Fig. 1 that the loss of intertube interactions in the S-SWNTs in CS_2 leads to narrower linewidths for the tangential band relative to those observed in bundled SWNTs. A Lorenztian line shape analysis reveals at least four narrow subbands for the bundled SWNTs and a single narrow mode for S-SWNTs in CS_2. Similarly, from the left-hand inset in Fig. 1 for the radial band, a reduced number of Lorentzians is observed in the spectrum of S-SWNT sample when compared to that of the bundled SWNTs. It is not yet understood how tube-tube interactions might affect the number of tangential bands observed.

In Fig. 2, we compare the radial and tangential bands of PLV synthesized bundled SWNTs and *solid* full length PLV synthesized S-SWNTs (i.e., solubilized full length SWNTs obtained by evaporating the organic solvents). Unfortunately, the Raman spectra of S-SWNT dissolved in organic solvents (CS_2 or THF) obtained using visible laser excitations showed strong luminescence, and prevented us from detecting the radial or the tangential bands. The origin of this luminescence is not understood at present and warrants an independent study. The radial bands in solid S-SWNTs are consistently up-shifted relative to those of bundle SWNTs in all spectra depicted in Fig. 2(a). On the other hand, narrowing of the tangential band in S-SWNTs in CS_2 (see right-hand inset of Fig. 1) is absent in the tangential bands in solid S-SWNTs [Fig. 2(b)]. At least two important conclusions can be drawn from the Raman data presented in Figs. 2(a) and 2(b):

(i) Both semiconducting and metallic tubes exhibit $\sim$10 cm^{-1} up-shift as bundled tubes are solubilized. As Pimenta *et al.* [18] have argued, the 647.1 nm excitation couples predominantly to metallic tubes in the sample.

(ii) The relatively broader tangential band in solid S-SWNTs compared to that of S-SWNT in CS_2 suggests that the organic solvent-nanotube interactions have a smaller influence on the tangential mode lifetime than the tube-tube interactions in solid S-SWNTs.

Of particular importance to the discussion of the anomalous up-shift in ω_R is the electronic density of states (DOS) of isolated and bundled nanotubes with a diameter distribution representative of the sample. For the sake of simple comparison, we restrict our discussion to (8,8)–(11,11) armchair tubes, although similar calculations can be performed for zigzag and chiral tubes. A density functional formalism within the local density approximation (LDA) was used [14]. The tight-binding parametrization, based on LDA electronic structure results [19], had been used successfully to describe the effect of intertube coupling on quantum transport [20] and the opening of pseudogaps in bundled and multiwalled nanotubes [14,21]. The calculated electronic DOS of these quasi-1D systems, presented

in Fig. 3, shows sharp singularities at energies E_i, associated with the $(E - E_i)^{-1/2}$ Van Hove singularities. The electronic DOS plots show that the metallic tubes have a small, nearly constant DOS near the Fermi level (E_F). Our results indicate that intertube coupling causes an additional band dispersion of ~0.2 eV, which not only opens up a pseudogap at E_F but also broadens by the same amount the Van Hove singularities and the peak positions shift away from E_F. This leads to a net increase of the energy spacing Δ_1 between the first, and Δ_2 between the second, pair of Van Hove singularities in the electronic DOS for bundled nanotubes (Table I).

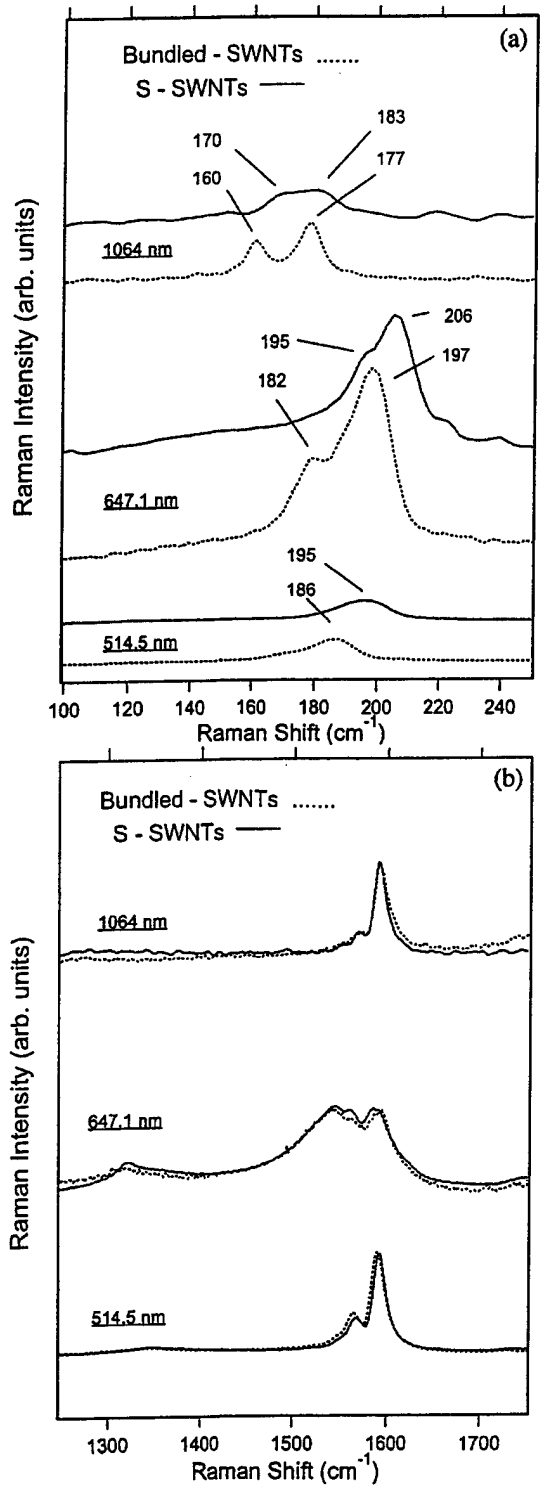

FIG. 2. Comparison of the radial (a) and tangential bands (b) in the PLV synthesized bundled and S-SWNTs for three laser excitation energies. In (b), the tangential bands for the bundled and S-SWNTs are superimposed for comparison of the linewidths.

Quantum confinement effects were observed in the Raman spectra of SWNT bundles through the resonant Raman enhancement effect between the excitation laser energy (E_{laser}) and the electronic transitions between the Van Hove singularities in the quasi-1D DOS in the valence and conduction bands of carbon nanotubes [1]. The combined scanning tunneling spectroscopy studies on PLV synthesized SWNTs [22,23] and optical transmission spectra taken from SWNTs synthesized using Ni:Y catalyst in the EA method [24] yield the approximate relations for semiconducting and metallic nanotubes, respectively:

$$\Delta_1' = \alpha/d'. \tag{3a}$$

In the above relation between Δ_1' and the tube diameter d', tight-binding theory shows that $\alpha = 2\gamma_0 d_{C\text{-}C}$ for semiconducting tubes and $\alpha = 6\gamma_0 d_{C\text{-}C}$ in metallic tubes, where γ_0 is the nearest neighbor overlap energy (or the transfer integral of a tight-binding model) and $d_{C\text{-}C}$ is the nearest neighbor distance in the hexagonal network. Amending this equation for intertube interactions, we have

$$\Delta_1 = \alpha/d + \delta\Delta_1. \tag{3b}$$

We now discuss the origin of the anomalous up-shift in ω_R in the Raman spectrum for S-SWNTs. The

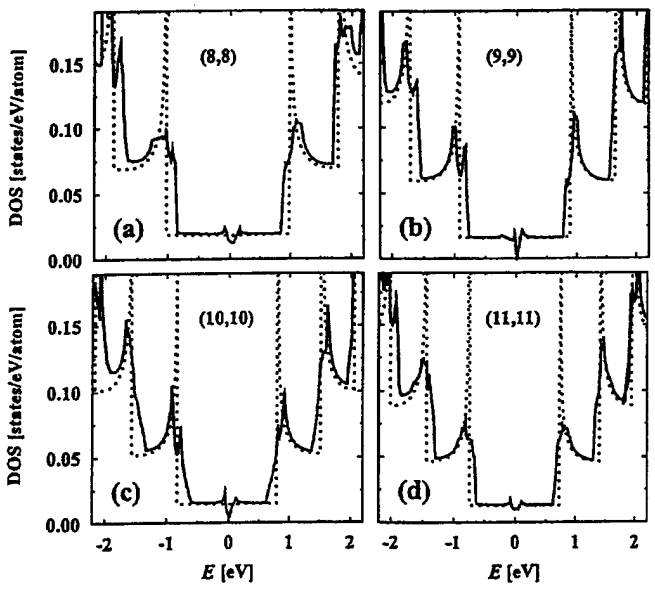

FIG. 3. Density of states of isolated (dotted lines) and bundled (solid lines) (8,8) (a), (9,9) (b), (10,10) (c), and (11,11) (d) carbon nanotubes. Clearly visible is the appearance of the pseudogap near $E_F = 0$ and the broadening of the Van Hove singularities, as isolated nanotubes bundle up into a close-packed triangular lattice. The tube indices (n, n) refer to armchair tubes (Ref. [16]).

TABLE I. Calculated energy difference, Δ_1, between the first and, Δ_2, between the second pairs of Van Hove singularities in the electronic density of states for isolated tubes and weakly interacting tubes in a bundle. The difference between the tube and bundle values is denoted by $\delta\Delta$. All energy values are in eV units.

(n,n)	Δ_1 (tube)	Δ_1 (rope)	$\delta\Delta_1$	Δ_2 (tube)	Δ_2 (rope)	$\delta\Delta_2$
(8,8)	2.03	2.23	0.20	3.69	3.89	0.20
(9,9)	1.83	1.99	0.16	3.39	3.55	0.16
(10,10)	1.64	1.84	0.20	3.12	3.29	0.17
(11,11)	1.49	1.63	0.14	2.87	2.98	0.11

$\sim 10\ \mathrm{cm}^{-1}$ up-shift can be understood and estimated numerically via Eqs. (1)–(3). Using the calculated value for $\Delta\omega_R \sim 14\ \mathrm{cm}^{-1}$ in bundled tubes in Ref. [9], Eq. (2) can be rewritten as

$$\omega_R \sim 224\ \mathrm{cm}^{-1} \cdot \mathrm{nm}/d + 14\ \mathrm{cm}^{-1}. \quad (4)$$

Because of the resonant Raman scattering process in SWNTs, at a fixed excitation laser energy ($E_{\mathrm{laser}} = \Delta_1$), it follows from Eqs. (3a) and (3b) that the following equality should be satisfied as the bundles are processed into isolated tubes:

$$\alpha/d' = \alpha/d + 0.2\ \mathrm{eV}. \quad (5)$$

For $\gamma_0 \sim 2.9$ eV [25], $d_{\mathrm{C\text{-}C}} \sim 1.42$ Å and $\omega_R' \sim 224\ \mathrm{cm}^{-1} \cdot \mathrm{nm}/d'$ it follows from Eqs. (2), (4), and (5) that $\omega_R' - \omega_R \sim 40\ \mathrm{cm}^{-1}$ for semiconducting tubes, and $\sim 4\ \mathrm{cm}^{-1}$ for metallic tubes. Furthermore, for fixed laser frequency, we see that the laser couples preferentially to isolated tubes with diameter d' and bundled tubes with diameter d, where $\Delta d = d' - d \cong -0.2d^2/\alpha$. Regardless of the tube type (semiconducting or metallic), the net result of debundling is an apparent up-shift in the Raman active radial breathing mode frequency for the S-SWNTs using the same excitation frequency. Recently, Duesberg *et al.* [26] found using the 633 nm excitation that ω_R up-shifts from $\sim 188\ \mathrm{cm}^{-1}$ in a ~ 5 nm thick SWNT bundle to $\sim 193\ \mathrm{cm}^{-1}$ in a ~ 1.5 nm bundle.

Finally, it should be mentioned that the above explanation for the observed up-shift in the radial mode frequency assumes that α remains unchanged as bundled tubes are debundled [cf. Eqs. (3a) and (3b)]. An independent study based on LDA calculations will be necessary to verify the assumption made for α in this study.

A. M. R. and R. C. H. acknowledge financial support from the NSF MRSEC Grant No. 9809686, and P. C. E. through the NSF MRSEC Grant No. 9809686 and ONR Grant No. N00014-99-1-0619. U. D. V. acknowledges partial support of this research by the Donors of The Petroleum Research Fund, administered by the American Chemical Society. Y. K. K. and D. T. acknowledge financial support by the Office of Naval Research and DARPA under Grant No. N00014-99-1-0252.

*Author to whom correspondence should be addressed. Electronic address: arao@clemson.edu
†Present address: Zyvex Corporation, Richardson, TX 75081.
‡Present address: Department of Physics, University of California–Berkeley, Berkeley, CA 94720.

[1] A. M. Rao *et al.*, Science **275**, 187 (1997).
[2] A. Kasuya *et al.*, Phys. Rev. Lett. **78**, 4434 (1998).
[3] S. Bandow *et al.*, Phys. Rev. Lett. **80**, 3779 (1998).
[4] A. G. Rinzler *et al.*, Appl. Phys. A, Mater. Sci. Process. **67**, 29–37 (1998).
[5] J. Chen *et al.*, Science **282**, 95 (1998); J. Phys. Chem. B **105**, 2525 (2001).
[6] A. Thess *et al.*, Science **273**, 483 (1996).
[7] C. Journet *et al.*, Nature (London) **388**, 756 (1997).
[8] U. D. Venkateswaran *et al.*, Phys. Rev. B **59**, 10 928 (1999).
[9] E. Richter and P. C. Eklund (unpublished).
[10] D. Kahn and J. P. Lu, Phys. Rev. B **60**, 6535 (1999).
[11] L. Henrard *et al.*, Phys. Rev. B **60**, R8521 (1999).
[12] J. Kurti *et al.*, Phys. Rev. B **58**, R8869 (1998).
[13] P. Delany *et al.*, Nature (London) **391**, 466 (1998).
[14] Y. K. Kwon *et al.*, Phys. Rev. B **58**, R13 314 (1998).
[15] L. Alvarez *et al.*, Chem. Phys. Lett. **316**, 186 (2000).
[16] R. Saito, G. Dresselhaus, and M. S. Dresselhaus, *Physical Properties of Carbon Nanotubes* (Imperial College Press, London, 1998).
[17] A. M. Rao *et al.*, Nature (London) **388**, 257 (1997).
[18] M. Pimenta *et al.*, Phys. Rev. B **58**, R16 016 (1998). Note: In Ref. [18], the line shape of the tangential band is observed to be sensitive to the excitation laser energies. It was concluded in Ref. [18] that the laser energies in the interval 1.7–2.2 eV predominantly excite metallic SWNTs in the sample.
[19] D. Tománek and Michael A. Schluter, Phys. Rev. Lett. **67**, 2331 (1991).
[20] S. Sanvito, Y.-K. Kwon, D. Tománek, and C. J. Lambert, Phys. Rev. Lett. **84**, 1974 (2000).
[21] Y.-K. Kwon and D. Tománek, Phys. Rev. B **58**, R16 001 (1998).
[22] J. W. G. Wildoer *et al.*, Nature (London) **391**, 59 (1998).
[23] T. W. Odom, J. L. Huang, P. Kim, and C. M. Lieber, Nature (London) **391**, 62 (1998).
[24] H. Kataura *et al.*, Synth. Met. **103**, 2555 (1999).
[25] G. Dresselhaus *et al.*, in *Science and Applications of Nanotubes*, edited by D. Tománek and R. J. Enbody (Kluwer Academic, New York, 2000), pp. 275–295.
[26] G. S. Duesberg *et al.*, Phys. Rev. Lett. **85**, 5436 (2000).

PERGAMON

Carbon 40 (2002) 1123–1130

CARBON

Scrolls and nested tubes in multiwall carbon nanotubes

J. Gerard Lavin[a], Shekhar Subramoney[a,*], Rodney S. Ruoff[b], Savas Berber[c], David Tománek[c]

[a]*Du Pont Central Research and Development, Experimental Station, Wilmington, DE 19880-0228, USA*
[b]*Department of Mechanical Engineering, Northwestern University, 2145 Sheridan Drive, Evanston, IL 60208-3111, USA*
[c]*Department of Physics and Astronomy, Michigan State University, East Lansing, MI 48824, USA*

Received 19 December 2001; accepted 18 January 2002

Abstract

Recent high-resolution transmission electron microscopy (HREM) studies of multiwalled carbon nanotubes (MWCNTs) reveal a class of defects analogous to edge dislocations in a crystal. These defects are believed to mark the transition from scrolls on one side to nested tubes on the other. On the tube side, layer spacing becomes irregular. Analysis of the helicity of the tubes shows a strong correlation between diameter and helicity. This suggests that the organizing principle for the tubes is not Van der Waals forces, as in the case of graphite or turbostratic carbon, but preservation of helicity. Based on these observations and total energy calculations, the authors speculate that graphene monolayers initially form scrolls and subsequently transform into multiwall nanotubes through the progression of defects. Scrolls and nested tubes thus coexist within a single MWNT. © 2002 Published by Elsevier Science Ltd.

Keywords: A. Carbon nanotubes; C. Transmission electron microscopy; D. Defects, Microstructure

1. Introduction

Multiwalled carbon nanotubes (MWCNTs) were discovered in 1991 by Iijima [1] in the plasma of a carbon arc used to make fullerenes, this time at pressures below 1 atm. Later, single-walled carbon nanotubes were discovered from a somewhat similar process [2]. Although the existence of MWCNTs formed by catalytic processes had been known for decades [3–5], the relatively defect-free structures of the MWCNTs formed in the extremely high temperatures of the arc-discharge process (about 5000 °C) have been intriguing enough to lead to a number of studies on their unique structure and properties [6–9].

From a historic perspective, the discovery of sub-micron size 'graphite whiskers', with a microstructure analogous to MWCNTs, was first reported by Bacon in 1960 [10]. These whiskers were made in a DC carbon arc, in inert gas at a pressure of 93 atm. By passing a large current through one of these 'whiskers' and exploding one of its ends, Bacon observed that they possessed a scroll-like microstructure. A very recent study on the cross-sectional structure of vanadium oxide nanotubes [11], albeit at significantly higher resolutions, illustrates the co-existence of scrolled and nested structures within individual tubes.

Analysis of the structure of MWCNTs processed by the arc-discharge method started with their discovery in 1991. Initially observed by high-resolution transmission electron microscopy (HREM), the MWCNTs were proposed to be made of carbon atom hexagonal sheets arranged in a helical fashion about the tube axis [1]. With the diameters of most arc-discharge produced carbon nanotubes approximately in the 10-nm range combined with their rather symmetrical microstructures, several theoretical predictions were made about their unique electronic and physical properties [12–14]. Considering how important the precise microstructure of individual nanotubes would be in dictating specific properties, characterizing the structure of these novel materials at the atomic level became a paramount issue for several researchers. Among various analytical techniques, HREM has clearly been the most applied technique for studying the intricate structure of MWCNTs in detail, providing information on how the tubes are stacked, the nature of defects, and the structure of internal as well as external closures [15]. Other analytical methods

*Corresponding author. Fax: +1-302-695-1351.
E-mail address: shekhar.subramoney@usa.dupont.com (S. Subramoney).

0008-6223/02/$ – see front matter
PII: S0008-6223(02)00050-7

have been also used for the structural characterization of MWCNTs: X-ray diffraction for crystallographic measurements [16], scanning probe microscopy for surface topography at the atomic scale [17], and electron diffraction to analyze the internal structure on a detailed basis [18].

Visual inspection of a large number of HREM images of MWCNTs clearly illustrates that these materials have a highly complex structure fraught with numerous defects. It is believed that the chaotic environment associated with evaporation of graphite electrodes in an arc leads to these complex structures. In this paper we discuss the structure of 'hybrid' MWCNTs composed of scrolled and nested segments, with the respective features typically separated from each other by defects such as edge dislocations.

2. Experimental

The MWCNTs analyzed in this work were prepared by the arc-discharge process involving dual graphitic electrodes, similar to those used by Ebbesen and Ajayan for large scale synthesis of MWCNTs [19]. The conditions inside the reaction vessel included a helium atmosphere at 500 Torr, and operating voltage and current at 20 V and 100 Amp, respectively. The gap between the anode and the cathode was maintained at ~1 mm by continuously translating the anode during the experiment with a motor. As outlined earlier by numerous researchers, the anode is consumed and a cylindrical growth occurs on the face of the cathode during the arc discharge process. The MWCNTs are found in the core of this cylindrical growth.

The MWCNT samples obtained from the core of the cathode following the arc-discharge process were dispersed using pure ethanol onto holey carbon coated transmission electron microscopy (TEM) grids. HREM was performed on a Philips CM-20 high-resolution TEM equipped with an Ultratwin polepiece. The microscope was operated at an accelerating voltage of 200 kV and images were recorded under conventional conditions on sheet films.

3. Theoretical

It is now well established that the strain energy involved in deforming an sp^2 bonded graphene sheet can be well described by continuum elasticity theory [20,21]. The key quantities in this formalism are the flexural rigidity of a graphene sheet, $D = 1.41$ eV, and Poisson's ratio $\alpha = 0.165$. The energy needed to bend a graphene monolayer into a cylinder of radius R is

$$\Delta E_s = \pi D\, L/R = \epsilon_{cyl} L/R \quad (1)$$

where $\epsilon_{cyl} = 4.43$ eV and L is the axial length. The corresponding strain energy for a spherical structure is independent of the radius, and is given by

$$\Delta E_s = 4\pi D\,(\alpha + 1) = 20.6\ \text{eV} \quad (2)$$

The interlayer interaction ΔE_i, which stabilizes multiwall structures, is proportional to the contact area A and given by

$$\Delta E_i = \epsilon_{vdw} A \quad (3)$$

where $\epsilon_{vdw} = 2.48$ eV/nm^2. The latter value, obtained from graphite, is based on an interlayer separation of 0.34 nm that is common to virtually all sp^2 bonded structures. Finally, there is an energy penalty ΔE_e associated with the generation of an exposed edge

$$\Delta E_e = \epsilon_e L \quad (4)$$

where $\epsilon_e = 21$ eV/nm is an average value for graphite [22] and L is the length of the exposed edge.

The reference system in all these considerations is a large graphene monolayer with no exposed (or completely saturated) edges. Formation of a scroll requires the energy to form two edges along the entire axis and the strain energy associated with rolling up the sheet. A scroll will be stable as long as the energy gain upon forming interwall interactions outweighs this energy investment. Formation of a multiwall nanotube involves the strain energy to form the individual cylindrical wall, which is compensated by a similar gain due to interlayer interactions. We observe that these two energies are comparable for multiwall systems with the same inner and outer radius, whether a scroll or a multiwall tube composed of nested cylinders. Since the scroll contains two edges along the entire length, it should be intrinsically less stable than a multiwall nanotube. As a transformation between these two structures involves bond rearrangement, the metastable scroll could in principle co-exist with the more stable multiwall system of nested cylinders.

4. Results and discussion

In this work, we use a kinematic approach for analyzing the HREM images of MWCNTs as a working hypothesis. Recently, using this approach, minute changes of the interwall spacing in MWNTs were investigated quantitatively [23]. In view of the level of detail in our analysis, extra caution is being paid to avoiding potential artifacts, such as mistaking interference fringes for graphitic layers. Even though complex structures, such as bent MWNTs, will produce intriguing diffraction patterns, it is inconceivable that artifacts such as a discontinuity in the number of walls would occur only in one and not the opposite wall of the same tube without a corresponding structural defect. While a dynamical analysis will probably give a more complete account of the scattering processes than a purely kinematic approach in such studies involving HREM, the associated complexity of the modeling calculation makes

this approach prohibitively involved for the nanotubes analyzed in this paper. The kinematic approach followed in this work is currently state-of-the-art for HREM studies of MWCNTs, and we expect our results to be confirmed by a dynamical interpretation in the future.

One of the most common defects observed in most of the MWCNTs studied in this work was the variation in thickness of the tube wall along the perimeter, as illustrated in Fig. 1. This TEM image shows essentially a longitudinal cross-section of this tubular system, showing a 'pair of thick walls' separated by the inner cavity. While the interlayer spacing of the (0002) graphene planes on the thinner of the two walls appears fairly uniform, the variation in interplanar spacings is fairly significant on the thicker wall. The number of independent (0002) interplanar spacings observed on the thicker wall considerably exceeds two singular spacings as suggested by Amelinckx et al. [7]. This anomaly was observed in most of the MWCNTs observed in this sample and it may be attributed to specific formation conditions that existed in the arc during the synthesis. Even though the interplanar spacing on the thinner wall appears fairly uniform on a visual basis, data generated in this work indicates that the graphene planes comprising the thinner wall exhibit a small but clearly significant variation in layer-to-layer spacing.

The classic variation in the interplanar spacing of the graphene sheets on the lower wall is indicated by the letter B in Fig. 1. Further examination of this MWCNT along its length reveals a previously undiscovered feature. It shows what appears to be a classic slip-plane defect, marked by the letter A. We believe that this defect marks the boundary between a scroll and a nested tube configuration within the same MWCNT. Interestingly enough, visual examination of this MWCNT for lengths of about 300 nm on either side of A indicated that the wall thickness was more or less uniform to the left, but the interplanar spacings on the lower wall became larger and larger on the right of point A, such as at point B.

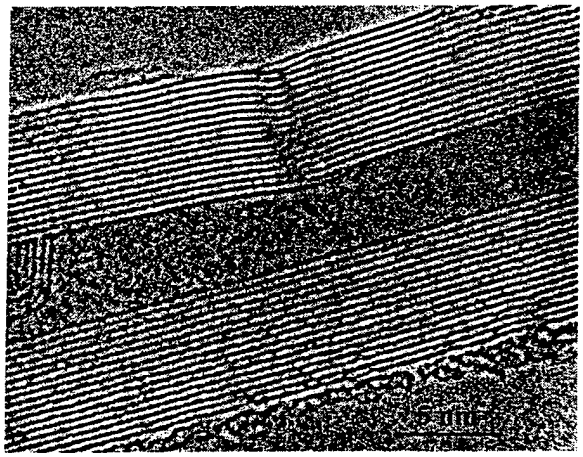

Fig. 2. Enlargement of the slip plane defect in Fig. 1, marking a junction of scroll and nested tube sections.

An enlargement of the defect (marked as A in Fig. 1) is shown in Fig. 2, and a pair of terminating (0002) lattice fringes are clearly visible in this image. This feature is associated with an edge dislocation running parallel to the axis of the MWCNT and this indicates that such an edge dislocation causes a changeover from scroll-like to a nested configuration (or vice versa) of the MWCNT. It appears that most of the MWCNTs examined in this sample flip-flopped between the scroll-like and nested structures by well-marked defects along the length of the nanotubes.

Another HREM image of a MWCNT exhibiting significant variable layer spacing in one of its walls is shown in Fig. 3. The most interesting feature of this particular tube

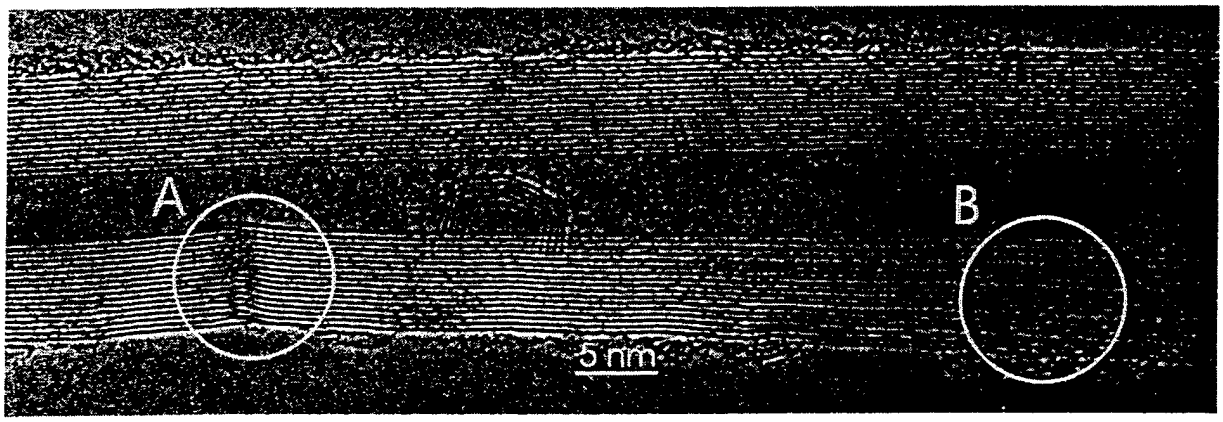

Fig. 1. Transmission electron micrograph of a multiwall carbon nanotube with a slip-plane defect and irregular layer spacing.

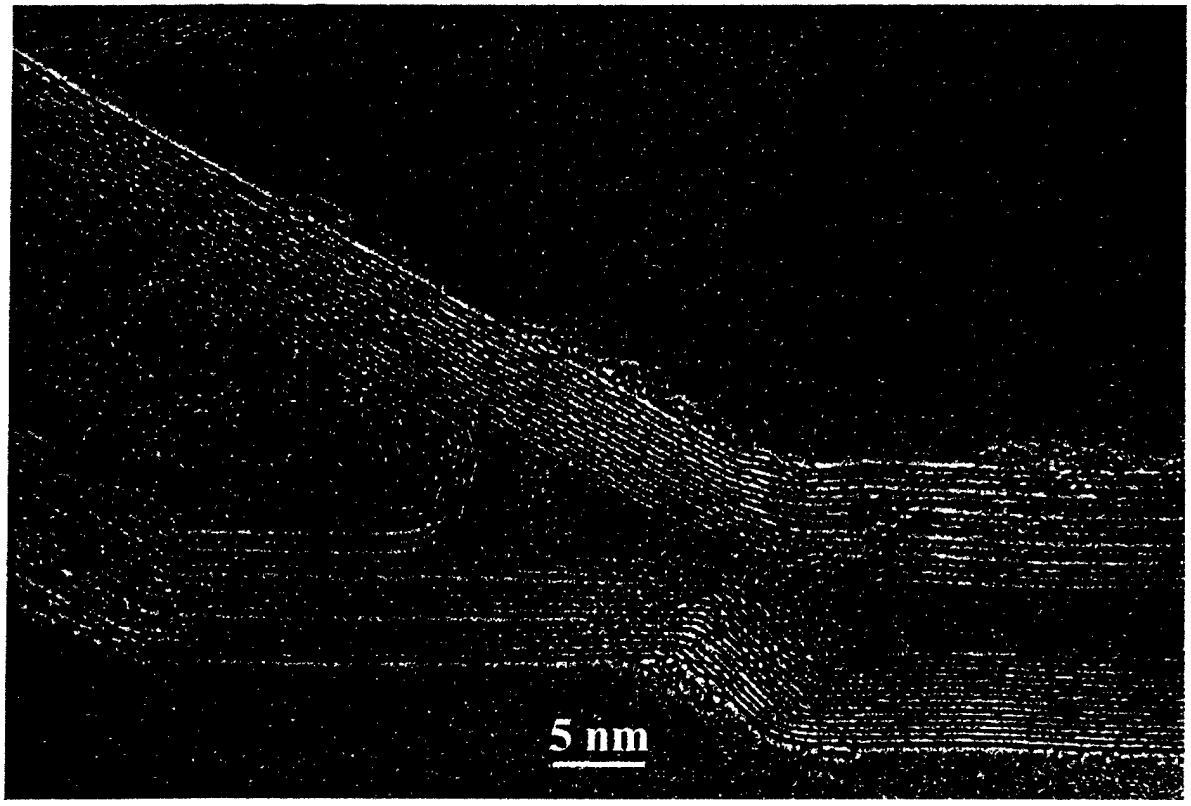

Fig. 3. Irregular layer spacing shifting from side to side and internal caps associated with irregular layer spacing.

is that a series of defect structures causes the variable layer spacing to change from one wall to the other. It appears that strategically placed lattice defects such as pentagons and heptagons can account for changing the eccentric nature of the MWCNT from one wall to the other. Analysis of several images indicates that the variable layer spacing is associated with nested eccentric tubes. Support for this belief is also observed in Fig. 3, which shows internal caps associated with variable layer spacing. The caps are inconsistent with a scroll configuration.

The defect structure that accounts for the noticeable variation in the layer spacing of the (0002) lattice fringes on one wall of the MWCNT sometimes manifests itself as an extra layer plane in the immediate vicinity of the defect site. This is clearly illustrated in the HREM image of the MWCNT shown in Fig. 4. An extra layer plane is clearly visible within the circle marked on the lower wall of the tube compared to the number of layer planes on the upper wall, which lends further credence to the co-existence of nested and scrolled structures in MWCNTs separated by defects. As observed in several other instances, a noticeable variation in the interplanar spacing is visible to the left side of the defect on the lower wall of the tube.

The mechanism responsible for variable lattice spacing was not immediately obvious. In a search for clues, nested tubes were examined for helicity utilizing image analysis via graphics software (CORELDRAW). HREM images were printed at a magnification of 1.7 million, and scanned to form digital images. Selected parts of four tubes were cropped in Corel PHOTOPAINT, and imported into CORELDRAW. This software is vector-based, and precise information is

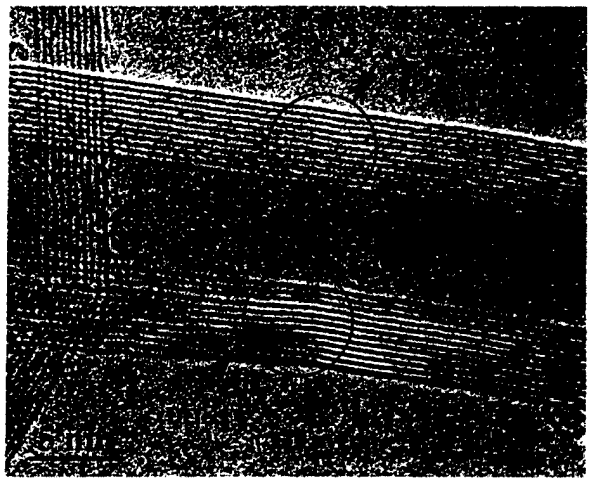

Fig. 4. Extra layer plane in the vicinity of slip-plane defect.

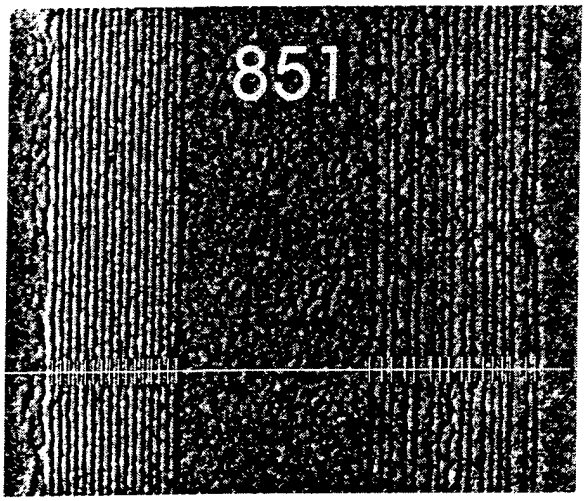

Fig. 5. Lattice spacing determination.

available on the coordinates of each line. The images were enlarged 16 or 32×, and white lines drawn in the center of the dark areas, as determined by eye (see Fig. 5). From the coordinates of the individual lines, lattice spacings and tube diameters were calculated. Minimum helicity was calculated by determining the number of repeat units (Fig. 6) contained in the tube circumference, rounded upwards to the next integer.

The helicity was calculated as the arccosine of the tube circumference divided by the number of repeat units times unit length. In this work, helicity is defined as the deviation from the armchair configuration, in contrast to the chirality defined by the conventional roll-up vector, in which the armchair configuration has an angle of 30°. The angle of the chiral vector can be determined by subtracting

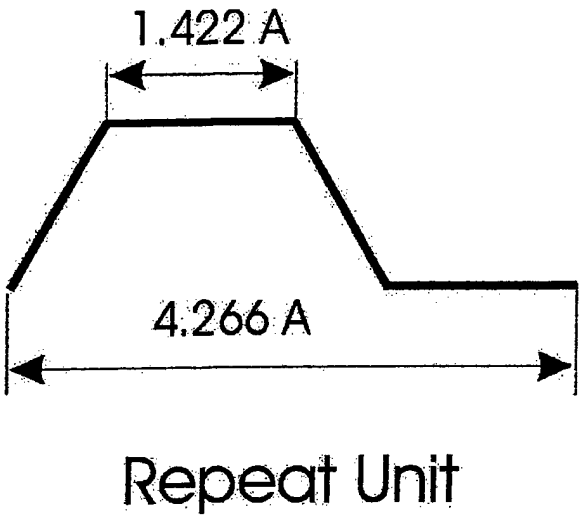

Fig. 6. Repeat unit.

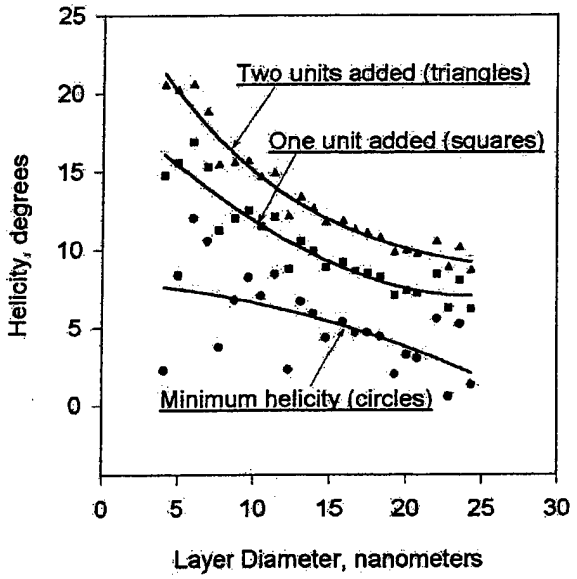

Fig. 7. Effect of excess repeat units on helicity, for nanotube from image 863.

the helicity calculated in this work from 30°. Handedness was assumed to be the same for all layers. When the minimum helicity was plotted against tube diameter, a pattern appeared of decreasing helicity with increasing diameter, but with a great deal of scatter. When an extra repeat unit was added, helicity decreased monotonically with tube diameter, and when a second repeat unit was added, scatter decreased noticeably. These data, for a single nanotube, are plotted in Fig. 7.

Lattice spacing and tube diameter data were collected on three additional tubes, of varying inside diameter and number of layers (see Table 1). Data for the four tubes, with two extra repeat units are plotted in Fig. 8. The correlation line is developed from a simple cubic equation, and the correlation coefficient is a remarkably high 0.945. The helicity of a nested tube appears to be dependent only upon its diameter! The equation for the correlation is:

Φ = helix angle, degrees: d = layer diameter, nm

$$\Phi = 29.3136 - 2.3343d + 0.1049d^2 - 0.0018d^3$$

Several observations should be made. First, a multiwall

Table 1
Characteristics of multiwall nanotubes

Tube no.	O.D. (nm)	I.D. (nm)	No. of layers
863	24.3	4.07	24
858a	15.12	3.91	14
851	22.23	8.92	16
862	18.84	5.42	17

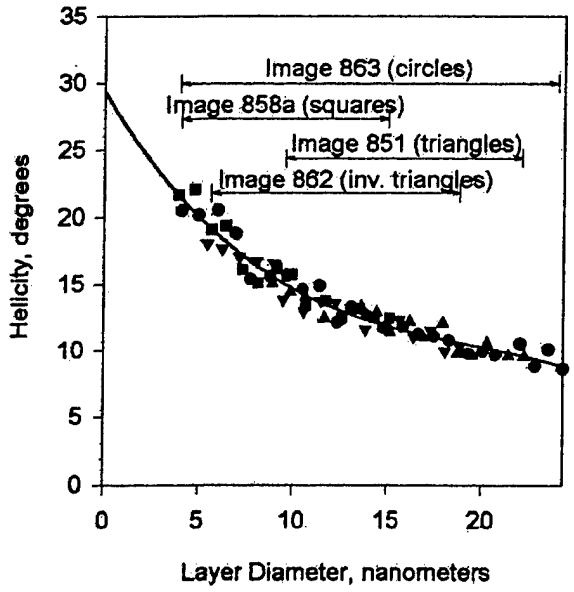

Fig. 8. Helicity vs. layer diameter, with two added repeat units.

structure is probably the lowest energy form for the nanotube, analogous to graphite heat treated at high temperatures. The rearrangements necessary at the transition between scroll and nested tube represent major defects, much more serious for nanotube strength than Stone–Wales reorganizations. Second, there is no guarantee that the nested tubes used in this analysis were imaged at their maximum diameter, although the quality of the correlation suggests that the numbers obtained are close. The simple algorithm proposed shows that a small change in helicity takes place from layer to layer, the increments being small.

The rather significant variations in (0002) interplanar spacings on one wall in MWCNTs and the possible causes for this feature are not totally novel concepts in carbon nanotube research. In the introduction to [23] Kiang et al. report average layer spacing from several workers covering the range 0.34–0.375 nm, and in their own work reported values from 0.34 to 0.39 nm, depending on diameter. Also, the co-existence of scrolled (where the helicity is conserved from layer to layer) and nested features within the same nanotube has been reported previously. High-resolution electron microscopy of ultrathin cross-sections by Dravid et al. [24] of what are believed to be MWCNTs has indicated the presence of non-terminated graphene layer planes, suggesting a localized scroll-type structure. HREM and electron diffraction studies by Liu and Cowley [25] have suggested that the tubes have a polygonized cross-section that accounts for significant variations in interplanar spacings on one wall. However, a polygonal cross-section would lead to uniformly higher-spaced planes on one wall with respect to the other, as opposed to a wall with widely varying interplanar spacings from layer to layer. The growth model as proposed by Amelinckx et al. [8,9] suggests that nested and scroll type structures would be present side by side in the lateral dimensions as well, accounting for variation in chiral angle from layer to layer as well as asymmetric (0002) lattice fringe spacings. In this paper we have shown that scrolled and nested structures can occur during the growth of a MWCNT and these features are typically separated from each other by well characterized defect structures that possibly occur due to very localized variations in the arc environment. This analysis goes hand in hand with chemical property measurements that have demonstrated the presence of regions in the tubes that are intercalatable and those that are not [10,26]. Our hypothesis is that the scroll-like features are open to intercalation and de-intercalation processes and that the nested features are not.

The energetics of the cylindrical multiwall system are discussed in Fig. 9 by plotting the required energy investment to form a scroll or a MWCNT of n nested cylinders out of a graphene strip of width W. Whereas there is only one-way to form n nested cylinders, separated by 0.34 nm, from the graphene strip, we allowed the scroll to assume its optimum geometry and readjust the inner diameter.

The system of nested cylinders behaves similar to that of nested spherical shells forming an onion [20]. Keeping the number of walls fixed while increasing W leads to a reduction of the strain energy. Beyond a critical value W_c the system gains more energy by creating an extra wall and thus increasing the interwall interaction at the cost of an

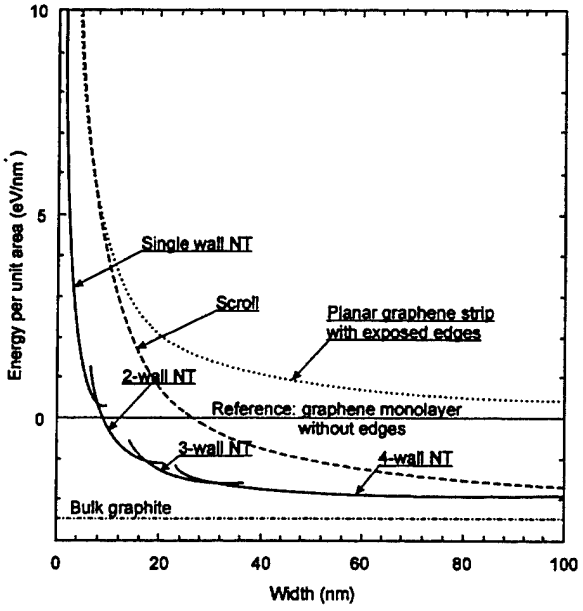

Fig. 9. Energy cost per unit area associated with the conversion of a graphene monolayer strip of width W with completely saturated edges into multiwall tubes.

increased overall strain energy. According to the results presented in Fig. 9, single-wall nanotubes are more stable only for $W < 7.7$ nm, corresponding to a tube radius of 1.2 nm. For $W > 7.7$ nm, double-wall tubes are more stable, and for $W > 17$ nm, triple-wall tubes. At each value of W, a multiwall structure consisting of nested cylinders is more stable than the optimum scroll, chiefly due to the energy penalty associated with the exposed edges. Also shown in Fig. 9 is the line denoting the relative stability with respect to a graphene strip terminated by two edges, given by $2\epsilon_e/W$. Inspection of the crossing points between this demarcation line and the energy of the individual structures indicates that for $W > 0.7$ nm, the energy gain upon eliminating two exposed edges outweighs the energy loss to form a cylinder, thus making a SWNT the preferred structure. The critical width to form a scroll is somewhat larger, with $W > 8.4$ nm. For large values of W, the energy of all multiwall structures approaches asymptotically the bulk graphite value of -2.48 eV/nm^2.

An intriguing question is, whether particular nanotubes show a preference for a conversion to a 'bamboo structure'. Let us consider a segment of a SWNT of radius R and length ΔL. If the nanotube is divided into two halves at this position, this segment is to be converted to two hemispherical domes separating and terminating the halved tubes. Since the area of the two hemispheres is $4\pi R^2$, the length of the tube segment will be $\Delta L = 4\pi R^2/2\pi R = 2R$. The strain energy stored in this segment is $2\epsilon_{cyl} = 8.9$ eV, much smaller than the energy of 20.6 eV that is needed to generate the two hemispheres. Hence, independent of the tube radius, the energy cost to subdivide a tube and close the ends by hemispherical domes is 11.7 eV.

These results suggest the following scenario for the formation of multiwall nanotubes at high temperatures. Forming graphite flakes may spontaneously roll up to form a scroll of a given helicity. During the harsh formation conditions, atomic vacancies or other defects may form that would connect the outer edge of the scroll to the neighboring wall, or any pair of adjacent walls. In this way, the topology of the scroll would be locally converted into the more stable nested cylinder structure within a MWCNT. A conversion between these structures would involve only opening and reconnecting bonds at the interface between the two structures, similar to an atomic-scale zipper. The activation energy, even though not negligible, is lower than requiring simultaneous opening of bonds along the entire length of the MWCNT. The net gain in energy upon eliminating exposed edges should drive the reaction to increase the length of the tube segments at the cost of the scroll segments.

5. Conclusions

The authors speculate that MWCNTs are complex structures composed of scroll-like and nested features existing side-by-side along their lengths, separated by well marked defects. Within the nested tubes, helicity changes little from layer to layer and depends only on layer diameter. Our proposed scenario for the formation of MWCNTs involves the formation of a scroll of a given helicity which converts, assisted by defects, into the thermodynamically more stable multiwall structure composed of nested cylinders.

Acknowledgements

The authors wish to thank Dr. Amand Lucas for useful discussions. D. Tománek, S. Berber and R.S. Ruoff were supported by the Office of Naval Research and DARPA under Grant No. N00014-99-1-0252.

References

[1] Iijima S. Helical microtubules of graphitic carbon. Nature 1991;354:56–8.
[2] Iijima S, Ichihashi T. Single-shell carbon nanotubes of 1-nm diameter. Nature 1993;363:603–5;
Bethune DS, Kiang CH, de Vries MS, Gorman G, Savoy R, Vasquez J. Cobalt-catalyzed growth of carbon nanotubes with single-atomic-layer walls. Nature 1993;363:605–7.
[3] Iley R, Riley HL. The deposition of carbon on vitreous silica, J Chem Soc 1948;Part II:1362–1366.
[4] Davis WR, Slawson RJ, Rigby GR. An unusual form of carbon. Nature 1953;171:756.
[5] Hofer LJE, Sterling E, MacCartney JT. Structure of the carbon deposited from carbon monoxide on iron, cobalt and nickel. J Phys Chem 1955;59:1153–5.
[6] Zhang XF, Zhang XB, Van Tendeloo G, Amelinckx S, Op de Beeck M, Van Landuyt J. Carbon nanotubes; their formation process and observation by electron microscopy. J Cryst Growth 1993;130:368–82.
[7] Amelinckx S, Bernaerts D, Zhang XB, Van Tendeloo G, Van Landuyt J. A structure model and growth mechanism for multishell carbon nanotubes. Science 1995;267:1334–8.
[8] Zhou O, Fleming RM, Murphy DW, Chen CH, Haddon RC, Ramirez AP, Glarum SH. Defects in carbon nanotubes. Science 1994;263:1744–7.
[9] Bretz M, Demczyk BG, Zhang L. Structural imaging of a thick-walled carbon nanotubule. J Cryst Growth 1994;141:304–9.
[10] Bacon R. Growth, structure, and properties of graphite whiskers. J Appl Phys 1960;31:283–90.
[11] Krumeich F, Muhr HJ, Niederberger M, Bieri F, Nesper R. The cross-sectional structure of vanadium oxide nanotubes studied by transmission electron microscopy and electron spectroscopic imaging. Z Anorg Allg Chem 2000;626:2208–16.
[12] Mintmire JW, Dunlap BI, White CT. Are fullerene tubes metallic? Phys Rev Lett 1992;68:631–4.
[13] Yakobson BI, Brabec CJ, Bernholc J. Nanomechanics of carbon tubes: instabilities beyond linear response. Phys Rev Lett 1996;76:2511–4.

[14] Charlier JC, Michenaud JP. Energetics of multilayered carbon tubules. Phys Rev Lett 1993;70:1858–61.
[15] Ajayan PM, Ichihashi T, Iijima S. Distribution of pentagons and shapes in carbon nano-tubes and nano-particles. Chem Phys Lett 1993;202:384–8.
[16] Reznik D, Olk CH, Neumann DA, Copley JRD. X-ray powder diffraction from carbon nanotubes and nanoparticles. Phys Rev B 1995;52:116–24.
[17] Tsang SC, de Oliviera P, Davis JJ, Green MLH, Hill HAO. The structure of the carbon nanotube and its surface topography probed by transmission electron microscopy and atomic force microscopy. Chem Phys Lett 1996;249:413–22.
[18] Zhang XB, Zhang XF, Amelinckx S, Van Tendeloo G, Van Landuyt J. The reciprocal space of carbon nanotubes: a detailed interpretation of the electron diffraction effects. Ultramicroscopy 1994;54:237–49.
[19] Ebbesen TW, Ajayan PM. Large-scale synthesis of carbon nanotubes. Nature 1992;358:220–2.
[20] Tománek D, Zhong W, Krastev E. Stability of multishell fullerenes. Phys Rev B 1993;48:15461–4.
[21] Robertson DH, Brenner DW, Mintmire JW. Energetics of nanoscale graphitic tubules. Phys Rev B 1992;45:12592–5.
[22] Thess A, Lee R, Nikolaev P, Dai H, Petit P, Robert J, Xu C, Lee YH, Kim SG, Colbert DT, Scuseria G, Tománek D, Fischer JE, Smalley RE. Crystalline ropes of metallic carbon nanotubes. Science 1996;273:483–7.
[23] Kiang CH, Endo M, Ajayan PM, Dresselhaus G, Dresselhaus MS. Size effects in carbon nanotubes. Phys Rev Lett 1998;81:1869–72.
[24] Dravid VP, Lin X, Wang Y, Wang XK, Yee A, Ketterson JB, Chang RHP. Buckytubes and derivatives: their growth and implications for buckyball formation. Science 1993;259:1601–4.
[25] Liu M, Cowley JM. Structures of the helical carbon nanotubes. Carbon 1994;32(3):393–403.
[26] Mordkovitch VZ, Baxendale M, Yoshimura S, Chang RHP. Intercalation into carbon nanotubes. Carbon 1996;34(10):1301–3.

Imaging the interlayer interactions of multiwall carbon nanotubes using scanning tunneling microscopy and spectroscopy

A. Hassanien[a)]
Nanotechnology Research Institute, National Institute of Advanced Industrial Science and Technology (AIST), 1-1-1 Umezono, Tsukuba, Ibaraki 305-8568, Japan

A. Mrzel
Jozef Stefan Institute, Jamova 39, 1000 Ljubljana, Slovenia

M. Tokumoto
Nanotechnology Research Institute, National Institute of Advanced Industrial Science and Technology (AIST), 1-1-1 Umezono, Tsukuba, Ibaraki 305-8568, Japan

D. Tománek
Department of Physics and Astronomy, Michigan State University, East Lansing, Michigan 48824-1116

(Received 4 June 2001; accepted for publication 11 October 2001)

Using atomically-resolved scanning tunneling microscopy and spectroscopy, we probe the nature of interwall interactions within multiwall carbon nanotubes at room temperature. We find that, at low bias voltages, the tunnel current depends strongly on the atomic position, introducing visibility differences between adjacent lattice sites. Since all atoms are equally visible in analogous measurements on single-wall nanotubes, we conclude that these modulations are introduced by the interwall interactions and provide unique information about the stacking nature. © *2001 American Institute of Physics.* [DOI: 10.1063/1.1427743]

Single-wall (SWCNTs) and multiwall (MWCNTs) carbon nanotubes exhibit a wealth of extraordinary properties, making them ideal candidates for device applications.[1] Particular attention has been paid to their electronic properties, since small variations in diameter or chiral angle cause profound changes in their conductance.[2–5] This unique behavior, coupled with the small diameter, large aspect ratio, and atomic perfections of carbon nanotubes has made it possible to construct new nanoscale devices, such as field effect transistors,[6] diodes, and field emitters.[7] Nevertheless, the full potential of nanotubes in high performance devices remains to be explored.

Transport measurements in MWCNTs have been performed to understand the nature of electronic conduction in these quasi-1D systems. Conductance quantization has been observed in both multiwall[8] and single-wall[9] nanotubes. Still, little is known about the effect of interlayer interactions on the nature of electronic states near the Fermi level in MWCNTs.

In this letter, we present a comparative study of structural and electronic properties of MWCNTs and SWCNTs using atomic-resolution scanning tunneling microscopy (STM) at room temperature. In order to probe the inter-wall interactions in MWCNTs, we utilize the current imaging tunneling spectroscopy (CITS) to probe locally the electronic structure at specific atomic sites along the nanotube walls. High-resolution STM scans of MWCNTs, with a previously unachievable atomic resolution at room temperature, reveal visibility differences between carbon atoms of the outer wall of the tubes. These observations find a remarkable counterpart in scanning tunneling spectroscopy (STS) measurements indicating that the current versus bias voltage characteristics depends strongly on the atomic locations. Neither effect has been observed in SWCNTs. As the measurements on SWCNTs and MWCNTs are performed under same conditions for all samples, we suggest that these visibility asymmetries have an electronic origin in the weak inter-wall interaction in MWCNTs, in analogy to a similar effect observed in pristine graphite.[10]

The SWCNT and MWCNT samples of this study were synthesized using the arc discharge method.[1] A mat of the generated soot was sonicated in ethyl alcohol for a few minutes prior to being cast onto a highly oriented pyrolytic graphite (HOPG) substrate for STM measurements. We have carried out STM measurements using a Digital Instruments Nanoscope IIIa instrument equipped with a customized vibration isolation, operated at room temperature in ambient conditions. High quality images revealing the atomic structure of MWCNTs, SWCNTSs, and of HOPG were obtained by recording the distance between the Pt-Ir tip and the substrate at constant current, with the STM operated at a typical tunnel current of 300 pA and a bias voltage of 50 mV. The images presented here have not been processed in any way. STS measurements in the CITS mode were performed by interrupting the lateral scans, as well as the feed-back loop, and measuring the current (I) as a function of the tip-sample voltage (V) at a fixed tip-sample distance. A combination of STM and STS measurements on individual nanotubes allowed us to investigate both their structural and electronic properties. We first focus in the interpretation of the atomic resolution STM images of SWNTs and MWNTs. Then, we discuss the CITS results, revealing the nature of the interwall interactions.

In Fig. 1 we show atomic resolution images of (a) a

a)Author to whom correspondence should be addressed; electronic mail: Abdou.Hassanien@aist.go.jp

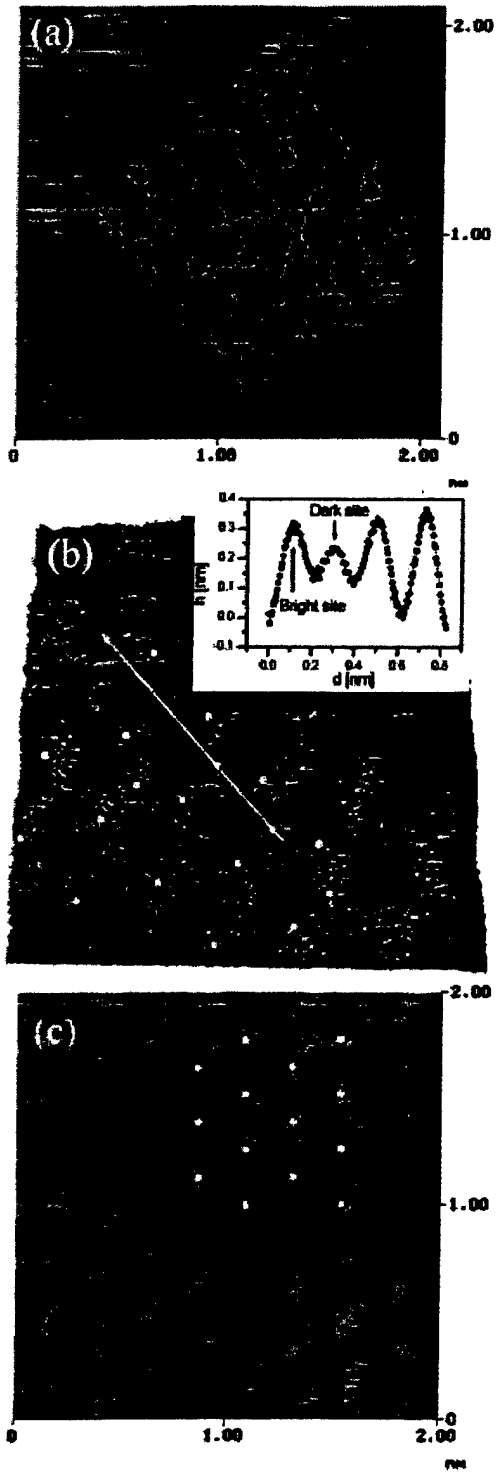

FIG. 1. (Color) Room temperature topographic STM images with true atomic-resolution of a (a) zigzag SWCNT with a diameter of 1.3 nm, a (b) zigzag MWCNT with a diameter of 2.3 nm and (c) highly oriented pyrolytic graphite (HOPG). In all cases the darkest areas correspond to centers of the carbon hexagons and brighter areas mark the location of carbon atoms. In HOPG and MWCNTs, the brightest spots indicate atoms with no neighbor in the adjacent layer below, whereas atoms with such neighbors appear darker. This asymmetry is caused by spatial variations in the local electronic density of states which occur both in MWCNTs and HOPG, but are absent in SWCNTs. The inset in (b) is a line profile taken along the highlighted line in the main image, where differences in peaks height are clearly visible.

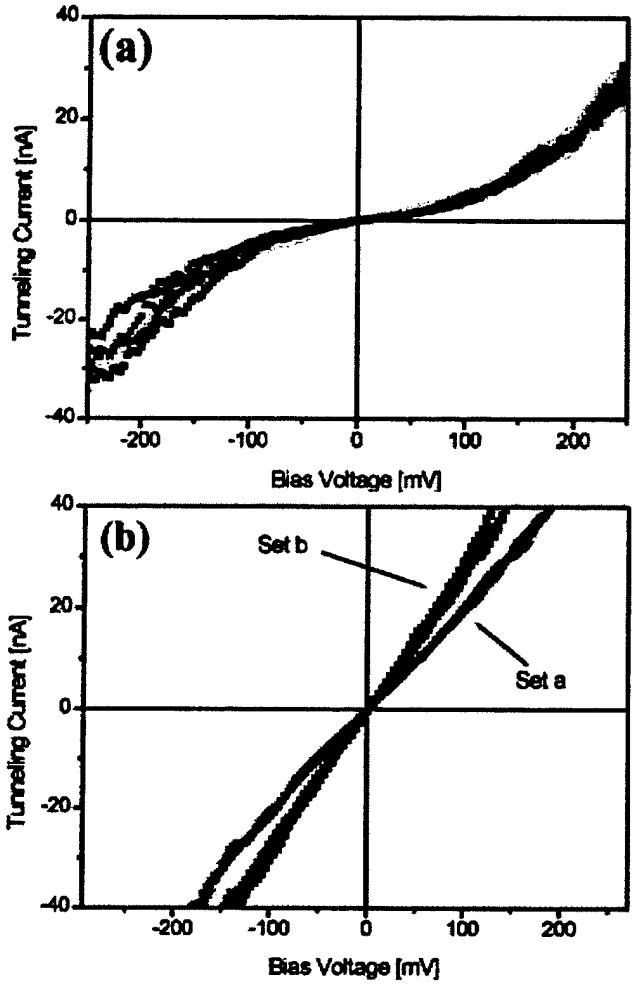

FIG. 2. (Color) Scanning tunneling spectra of carbon nanotubes. For SWCNTs (a), the current–voltage ($I-V$) curves show remarkable reproducibility, independent of the atomic site. For MWCNTs (b), two sets of $I-V$ data can be distinguished. $I-V$ spectra of "set b" are obtained at bright sites, whereas spectra of "set a" are correlated with atomic sites that appear darker.

zigzag SWNT with a diameter of 1.3 nm, and (b) a zigzag MWNT with a diameter of 2.3 nm. In both cases, the dark areas correspond to the center of the carbon hexagons, which

surface. The distance between neighboring dark spots is 0.25 nm, which compares well with that of HOPG shown in Fig. 1(c). The hexagon centers appear elongated along the tube circumference due to the geometrical distortion arising from the locally changing tip-sample arrangement due to the tube morphology.[11] The measuring conditions in (a), (b), and (c) are identical.

Next, we examined more carefully the signal intensity at different atomic sites of MWNTs in Fig. 1(b) and found that some atoms are clearly more visible than others. This effect is not seen in the case of SWNTs in Fig. 1(a), but is reminiscent of the site asymmetry in HOPG.[10] The topographic STM image of HOPG in Fig. 1(c) shows two triangular sublattices with a markedly different visibility within the honeycomb atomic lattice of the graphite layer. The origin of this effect lies in the atomic stacking nature of hexagonal graphite, which places half the atoms directly on top of each other in adjacent layers (A sites, solid circles), whereas the remaining atoms (B sites, open circles) have no such neighbors. Due to the local crystal symmetry, the only interlayer interaction due to the π states, which are imaged by the STM due to their proximity to the Fermi level, occurs normal to the

sites in pristine HOPG with a hexagonal or a rhombohedral stacking of graphene layers. The interlayer interactions cause an energy dispersion of almost 1 eV along the chains of A atoms normal to the layers, whereas the negligible interlayer interaction along the analogous chains of B atoms yields no such dispersion.[10] Consequently, one observes a sharp peak near E_F in the local density of states at the B sites, which spreads into a band at the A sites. In low biased (<50 meV) STM experiments, we therefore expect the B sites (with no neighbors in the adjacent layer below) to be more visible than the A sites. Then, the STM image will show a triangular rather than a honeycomb pattern.

The above elucidation is consistent with the fact that all atoms are equally visible within the honeycomb lattice of a SWNT, as seen in Fig. 1(a). The STM image of a MWNT, shown in Fig. 1(b), exhibits a more complex structure, with some sites considerably more visible than others. This difference in visibility even between adjacent atomic sites on the same nanotube is a consequence of spatial variations in the local density of states, originating in the inter-wall interaction. Following the previous arguments about STM images of HOPG, the discernible differences in the local electronic density of states provide information about the relative stacking (or the relative atomic arrangement) in the outermost tube walls. This means that a comparison of local intensities identifies not only those atoms which have a neighbor in the adjacent layer below, but also provides an indirect information about the chirality of the second outermost wall. Furthermore, the stability of the intensity modulation pattern provides a clear evidence that individual tubes do not rotate freely even at room temperature.

To understand the origin of the visibility difference, we have performed atomically resolved scanning tunneling spectroscopy measurements on both single- and multiwall carbon nanotubes. Data obtained from SWCNTs, presented in Fig. 2(a), do not show any site-to-site variations in the $I-V$ characteristics. Data obtained from MWCNTs, on the other hand, exhibit two very different types of $I-V$ characteristics, as shown in Fig. 2(b). "Set b" of $I-V$ curves, taken at the bright sites, is markedly different from data of "set a," taken at less visible sites on MWNTs. The larger slope of the $I-V$ curves of "set b" reflects a higher electronic density of states near the Fermi level at these sites. This is consistent with our assessment that the brighter sites, called "B sites" in HOPG, have no neighbors in the adjacent layer below. The lower slope of the $I-V$ curves of "set a" indicates a lower density of states, caused by the hybridization with atoms in the adjacent layer located directly below.

The complementarity of the information obtained using scanning tunneling microscopy and spectroscopy indicates that these techniques are unique probes of the inter-wall interaction in carbon nanotubes. Combining STM and STS measurements allows us to detect not only the atomic stacking in the outermost tube walls, but also the site-dependence of the inter-wall interaction.

One of the authors (D.T.) acknowledges financial support by the Office of Naval Research and DARPA under Grant No. N00014-99-1-0252, and the hospitality of the Tokyo Institute of Technology.

[1] M. S. Dresselhaus, G. Dresselhaus, and P. C. Eklund, Science of Fullerenes and Carbon Nanotubes (Academic, San Diego, 1996).
[2] Jeroen W. G. Wildoer, Liesbeth C. Venema, Andrew G. Rinzler, Richard E. Smalley, and Cees Dekker, Nature (London) **391**, 59 (1998).
[3] Teri Wang Odom, Jin-Lin Huang, Philip Kim, and Charles M. Lieber, Nature (London) **391**, 62 (1998).
[4] A. Hassanien, M. Tokumoto, Y. Kumazawa, H. Kataura, Y. Maniwa, S. Suzuki, and Y. Achiba, Appl. Phys. Lett. **73**, 3839 (1998).
[5] A. Hassanien, M. Tokumoto, S. Ohshima, Y. Kuriki, F. Ikazaki, K. Uchida, and M. Yumura, Appl. Phys. Lett. **75**, 2755 (1999).
[6] Y. Saito, K. Hamaguchi, S. Uemura, K. Uchida, Y. Tasaka, F. Ikazaki, Y. Yumura, A. Kasuya, and Y. Nishina, Appl. Phys. A **67**, 95 (1998).
[7] Sander J. Trans, Alwin R. M. Verschueren, and Cess Dekker, Nature (London) **393**, 49 (1998).
[8] S. Frank, P. Poncharal, Z. L. Wang, and W. A. de Heer, Science **280**, 1744 (1998).
[9] S. J. Tans, M. H. Devoret, H. J. Dai, A. Thess, R. E. Smalley, L. J. Geerligs, C. Dekker, Nature (London) **386**, 474 (1997).
[10] D. Tománek, S. G. Louie, H. J. Mamin, D. W. Abraham, R. E. Thomson, E. Ganz, and J. Clarke, Phys. Rev. B **35**, 7790 (1987); D. Tománek and S. G. Louie, Phys. Rev. B **37**, 8327 (1988).
[11] V. Meunier and Ph. Lambin, Phys. Rev. Lett. **81**, 5588 (1998).

RAPID COMMUNICATIONS

PHYSICAL REVIEW B VOLUME 62, NUMBER 4 15 JULY 2000-II

Electronic and structural properties of carbon nanohorns

Savas Berber, Young-Kyun Kwon,* and David Tománek
Department of Physics and Astronomy, and Center for Fundamental Materials Research, Michigan State University, East Lansing, Michigan 48824-1116

(Received 3 March 2000; revised manuscript received 3 May 2000)

We use a parametrized linear combination of atomic orbitals calculations to determine the stability, optimum geometry, and electronic properties of nanometer-sized capped graphitic cones, called "nanohorns." Different nanohorn morphologies are considered, which differ in the relative location of the five terminating pentagons. Simulated scanning tunneling microscopy images of the various structures at different bias voltages reflect a net electron transfer towards the pentagon vertex sites. We find that the density of states at the tip, observable by scanning tunneling spectroscopy, can be used to discriminate between different tip structures.

Since their first discovery,[1] carbon nanotubes have drawn the attention of both scientists and engineers due to the large number of interesting new phenomena they exhibit,[2–5] and due to their potential use in nanoscale devices: quantum wires,[6] nonlinear electronic elements,[7] transistors,[8] molecular memory devices,[9] and electron field emitters.[10–13] Even though nanotubes have not yet found commercially viable applications, projections indicate that this should occur in the very near future, with the advent of molecular electronics and further miniaturization of micro-electromechanical devices (MEMS). Among the most unique features of nanotubes are their electronic properties. It has been predicted that single-wall carbon nanotubes[14,15] can be either metallic or semiconducting, depending on their diameter and chirality.[16–18] Recently, the correlation between the chirality and conducting behavior of nanotubes has been confirmed by high resolution scanning tunneling microscopy (STM) studies.[19,20]

Even though these studies have demonstrated that atomic resolution can be achieved,[19–21] the precise determination of the *atomic configuration*, characterized by the chiral vector, diameter, distortion, and position of atomic defects, is still a very difficult task to achieve in nanotubes. Much of the difficulty arises from the fact that the electronic states at the Fermi level are only indirectly related to the atomic positions. Theoretical modeling of STM images has been found crucial to correctly interpret experimental data for graphite,[22,23] and has been recently applied to carbon nanotubes.[24,25] As an alternative technique, scanning tunneling spectroscopy combined with modeling has been used to investigate the effect of the terminating cap on the electronic structure of nanotubes.[26]

Among the more unusual systems that have been synthesized in the past few years are cone-shaped graphitic carbon structures.[27,28] Whereas similar structures have been observed previously near the end of multiwall nanotubes,[29] it is only recently that an unusually high production rate of up to 10 g/h has been achieved for single-walled cone-shaped structures, called "nanohorns," using the CO_2 laser ablation technique at room temperature in absence of a metal catalyst.[30] These conical nanohorns have the unique opening angle of $\approx 20°$.

We consider a microscopic understanding of the electronic and structural properties of nanohorns a crucial prerequisite for understanding the role of terminating caps in the physical behavior of contacts between nanotube-based nanodevices. So far, neither nanohorns nor other cone-shaped structures have been investigated theoretically. In the following, we study the structural stability of the various tip morphologies, and the interrelationship between the atomic arrangement and the electronic structure at the terminating cap, as well as the disintegration behavior of nanohorns at high temperatures.

Cones can be formed by cutting a wedge from planar graphite and connecting the exposed edges in a seamless manner. The opening angle of the wedge, called the disclination angle, is $n(\pi/3)$, with $0 \leq n \leq 6$. This disclination angle is related to the opening angle of the cone by $\theta = 2\sin^{-1}(1-n/6)$. Two-dimensional planar structures (e.g., a graphene sheet) are associated with $n=0$, and one-dimensional cylindrical structures, such as the nanotubes, are described by $n=6$. All other possible graphitic cone structures with $0<n<6$ have been observed in a sample generated by pyrolysis of hydrocarbons.[28] According to Euler's rule, the terminating cap of a cone with the disclination angle $n(\pi/3)$ contains n pentagon(s) that substitute for the hexagonal rings of planar graphite.

The observed cone opening angle of $\approx 20°$, corresponding to a $5\pi/3$ disclination, implies that all nanohorns contain exactly five pentagons near the tip. We classify the structure of nanohorns by distinguishing the relative positions of the carbon pentagons at the apex which determine the morphology of the terminating cap. Our study will focus on the influence of the relative position of these five pentagons on the properties of nanohorns.

The cap morphologies investigated in this study are presented in Fig. 1. Nano-horns with all five pentagons at the "shoulder" of the cone, yielding a blunt tip, are shown in Figs. 1(a)–(c). Nanohorns with a pentagon at the apex of the tip, surrounded by the other four pentagons at the shoulder, are shown in Figs. 1(d)–(f). Note that the cone angle of each nanohorn is $\approx 20°$, even though the size of the terminating cap varies with the relative position of the pentagons.

To determine the structural and electronic properties of carbon nanohorns, we used the parametrized linear combina-

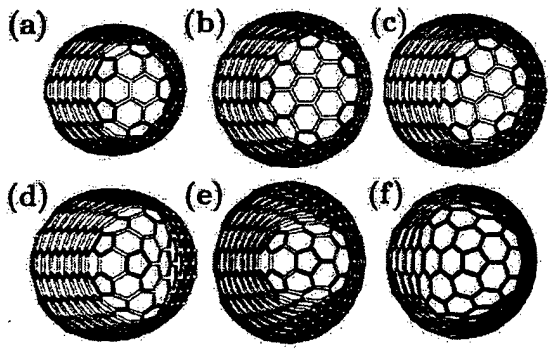

FIG. 1. Optimized carbon nanohorn structures with a total disclination angle of $5(\pi/3)$, containing five isolated pentagons at the terminating cap. Structures (a)–(c) contain all pentagons at the conical "shoulder," whereas structures (d)–(f) contain a pentagon at the apex. The pentagons are highlighted by a darker color.

tion of atomic orbitals (LCAO) technique with parameters determined by *ab initio* calculations for simpler structures.[31] This approach has been found useful to describe minute electronic structure and total energy differences for systems with unit cells that are too large to handle accurately by *ab initio* techniques.[32] Some of the problems tackled successfully by this technique are the electronic structure and superconducting properties of the doped C_{60} solid,[33] the opening of pseudogaps near the Fermi level in a (10,10) nanotubes rope,[34,35] and a (5,5)@(10,10) double-wall nanotube,[36] as well as fractional quantum conductance in nanotubes.[37] This technique, combined with the recursion technique to achieve an $O(N)$ scaling, can determine very efficiently the forces on individual atoms,[38] and had previously been used with success to describe the disintegration dynamics of fullerenes,[39] the growth of multiwall nanotubes[40] and the dynamics of a "bucky-shuttle."[9]

To investigate the structural stability and electronic properties of carbon nanohorns, we first optimized the structures with various cap morphologies, shown in Fig. 1. For the sake of an easier interpretation of our results, we distinguish the $N_{cap} \approx 40-50$ atoms at the terminating cap from those within the cone-shaped mantle, that is terminated by N_{edge} atoms at the other end. We associate the tip region of a hypothetically infinite nanohorn with all the sites excluding the edge. Structural details and the results of our stability calculations are presented in Table I. These results indicate that atoms in nanohorns are only ≈ 0.1 eV less stable than in graphite. The relative differences in $\langle E_{coh,tot} \rangle$ reflect the strain energy changes induced by the different pentagon arrangements. To minimize the effect of under-coordinated atoms at the edge on the relative stabilities, we excluded the edge atoms from the average when calculating $\langle E_{coh,tip} \rangle$. Since our results for $\langle E_{coh,tip} \rangle$ and $\langle E_{coh,tot} \rangle$ follow the same trends, we believe that the effect of edge atoms on the physical properties can be neglected for structures containing hundreds of atoms. Even though the total energy differences may appear minute on a per-atom basis, they translate into few electron-volts when related to the entire structure. Our results suggest that the under-coordinated edge atoms are all less stable than the cone mantle atoms by ≈ 0.5 eV. Also, atoms in pentagons are less stable than those in hexagons by ≈ 0.1 eV, resulting in an energy penalty of ≈ 0.5 eV to create a pentagon if the strain energy induced by bending the lattice could be ignored.

TABLE I. Structural data and stability results for carbon nanohorn structures (a)–(f), presented in Fig. 1. $N_{tot} = N_{tip} + N_{edge}$ is the total number of atoms, which are subdivided into tip and edge atoms. $\langle E_{coh,tot} \rangle$ is the average binding energy, taken over the entire structure, and $\langle E_{coh,tip} \rangle$ the corresponding value excluding the edge region. $\langle E_{coh,edge} \rangle$ is the binding energy of the edge atoms, and $\langle E_{coh,pent} \rangle$ is the average over the pentagon sites in each system.

Quantity	(a)	(b)	(c)	(d)	(e)	(f)
N_{tot}	205	272	296	290	308	217
N_{tip}	172	233	257	251	270	180
N_{edge}	33	39	39	39	38	37
$\langle E_{coh,tot} \rangle$ (eV)	−7.28	−7.29	−7.30	−7.30	−7.31	−7.28
$\langle E_{coh,tip} \rangle$ (eV)	−7.36	−7.36	−7.37	−7.36	−7.37	−7.36
$\langle E_{coh,edge} \rangle$ (eV)	−6.88	−6.88	−6.88	−6.88	−6.87	−6.89
$\langle E_{coh,pent} \rangle$ (eV)	−7.28	−7.28	−7.28	−7.28	−7.28	−7.28

When comparing the stabilities of the tip regions, described by $\langle E_{coh,tip} \rangle$, we found no large difference between blunt tips that have all the pentagons distributed along the cylinder mantle and pointed tips containing a pentagon at the apex. We found the structure shown in Fig. 1(c) to be more stable than the other blunt structures with no pentagon at the apex. Similarly, the structure shown in Fig. 1(e) is most stable among the pointed tips containing a pentagon at the apex. Equilibrium carbon-carbon bond lengths in the cap region are $d_{CC} = 1.43-1.44$ Å at the pentagonal sites and $d_{CC} = 1.39$ Å at the hexagonal sites, as compared to $d_{CC} = 1.41-1.42$ Å in the mantle. This implies that the "single bonds" found in pentagons should be weaker than the "double bonds" connecting hexagonal sites, thus confirming our results in Table I and the analogous behavior in the C_{60} molecule.

Since pentagon sites are defects in an all-hexagon structure, they may carry a net charge.[41] To characterize the nature of the defect states associated with these sites, we calculated the electronic structure at the tip of the nanohorns. The charge density associated with states near E_F, corresponding to the local density of states at that particular position and energy, is proportional to the current observed in STM experiments. To compute the local charge density associated with a given eigenstate, we projected that state onto a local atomic basis. The projection coefficients were used in conjunction with real-space atomic wave functions from density functional calculations[23] to determine the charge density corresponding to a particular level or the total charge density. To mimic a large structure, we convoluted the discrete level spectrum by a Gaussian with a full-width at half-maximum of 0.3 eV. Using this convoluted spectrum, we also determined the charge density associated with particular energy intervals corresponding to STM data for a given bias voltage.

In Fig. 2, we present such simulated STM images for the nanohorns represented in Figs. 1(c) and 1(d). We show the charge density associated with occupied states within a narrow energy interval of 0.2 eV below the Fermi level[42] as three-dimensional charge density contours, for the density value of $\rho = 1.35 \times 10^{-3}$ electrons/Å^3. Very similar results to

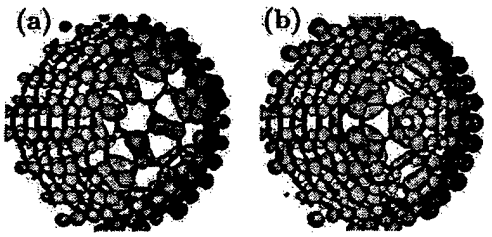

FIG. 2. Simulated STM images in the tip region for (a) the nano-horn shown in Fig. 1(c) and (b) the nanohorn shown in Fig. 1(d). These results for the occupied electronic states near the Fermi level, corresponding to the bias voltage of $V_b = 0.2$ V, are suggestive of a net electron transfer from the hexagonal to the pentagonal sites. The charge density contour displayed corresponds to the value of $\rho = 1.35 \times 10^{-3}$ electrons/Å^3. Dark lines depict the atomic bonds to guide the eye.

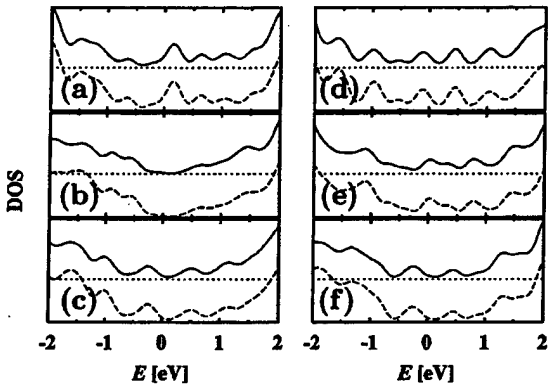

FIG. 3. Electronic densities of states, normalized per atom and shown in consistent arbitrary units, for the terminating cap of the tip (solid line) and for the pentagon sites only (dashed line) of nanohorn structures shown in Fig. 1. The similarity between the results for the entire cap and the pentagon sites necessitated a vertical offset of one set of data for an easy distinction, thus indicating that variations in the arrangement of pentagons affect the densities of states not only at the pentagonal sites, but within the entire cap region. The most marked differences are noted near the Fermi level, at $E \approx 0$ eV.

those presented in Fig. 2 were obtained at a higher bias voltage of 0.4 eV. As seen in Fig. 2, $pp\pi$ interactions dominate the spectrum near E_F. These images also show a net excess of electrons on the pentagonal sites as compared to the hexagonal sites. This extra negative charge at the apex should make pointed nanohorn structures with a pentagon at the apex better candidates for field emitters[10–13] than structures with no pentagon at the apex and a relatively blunt tip.

It has been shown previously that theoretical modeling of STM images is essential for the correct interpretation of experimental data. Atomically resolved STM images, however, are very hard to obtain, especially near the terminating caps of tubes[26] and cones, due to the large surface curvature that can not be probed efficiently using current cone-shaped STM tips. A better way to identify the tip structure may consist of scanning tunneling spectroscopy (STS) measurements in the vicinity of the tip. This approach is based on the fact that in STS experiments, the normalized conductance $(V/I)(dI/dV)$ is proportional to the density of states which, in turn, is structure sensitive. We have calculated the density of states at the terminating cap for the different nanohorn structures shown in Fig. 1. Our results are shown in Fig. 3, convoluted using a Gaussian with a full-width at half-maximum of 0.3 eV.

To investigate the effect of pentagonal sites on the electronic structure at the tip, we first calculated the density of states only at the 25 atoms contained in the five terminating pentagons. The corresponding densities of states, shown by the dashed curve in Fig. 3, are found to vary significantly from structure to structure near the Fermi level.[42] Thus, a comparison between the densities of states at $E \approx E_F$ should offer a way to discriminate between the various tip morphologies. For an easy comparison with experiments, we also calculated the density of states in the entire terminating cap, including all five pentagons and consisting of $N_{cap} \approx 40-50$ atoms, depending on the structure. The corresponding density of states, given by the solid line in Fig. 3, is vertically displaced for easier comparison. Our results show that the densities of states, both normalized per atom, are very similar. Thus, we conclude that the pentagonal sites determine all essential features of the electronic structure near the Fermi level at the tip. We note that a perturbation of the electronic structure far from defects has also been predicted in nanotubes.[43]

In summary, we used a parametrized linear combination of atomic orbitals calculations to determine the stability, optimum geometry and electronic properties of nanometer-sized capped graphitic cones, called nanohorns. We considered different nanohorn morphologies that differ in the relative location of the five terminating pentagons. We found a net electron transfer to the pentagonal sites of the cap. This negative excess charge is seen in simulated scanning tunneling microscopy images of the various structures at different bias voltages. We found that the density of states at the tip, observable by scanning tunneling spectroscopy, can be used to discriminate between different tip structures.

We thank S. Iijima for fruitful discussions on carbon nanohorns. We acknowledge financial support by the Office of Naval Research and DARPA under Grant No. N00014-99-1-0252.

*Present address: Department of Physics, University of California, and Materials Sciences Division, Lawrence Berkeley Laboratory, Berkeley, CA 94720.

[1] Sumio Iijima, Nature (London) **354**, 56 (1991).

[2] M. S. Dresselhaus, G. Dresselhaus, and P. C. Eklund, *Science of Fullerenes and Carbon Nanotubes* (Academic Press, San Diego, 1996).

[3] T. W. Ebbesen, Phys. Today **49**(6), 26 (1996).

[4] B. I. Yakobson and R. E. Smalley, Am. Sci. **85**, 324 (1997).

[5] R. Saito, G. Dresselhaus, and M. S. Dresselhaus, *Physical Properties of Carbon Nanotubes* (Imperial College Press, London, 1998).

[6] S. J. Tans, Michel H. Devoret, Hongjie Dai, Andreas Thess, Richard E. Smalley, L. J. Geerligs, and Cees Dekker, Nature (London) **386**, 474 (1997).

[7] M. Bockrath, David H. Cobden, Paul L. McEuen, Nasreen G.

Chopra, A. Zettl, Andreas Thess, and R. E. Smalley, Science **275**, 1922 (1997).

[8] S. J. Tans, A. R. M. Verschueren, and C. Dekker, Nature (London) **393**, 49 (1998).

[9] Young-Kyun Kwon, David Tománek, and Sumio Iijima, Phys. Rev. Lett. **82**, 1470 (1999).

[10] A. G. Rinzler, J. H. Hafner, P. Nikolaev, L. Lou, S. G. Kim, D. Tománek, P. Nordlander, D. T. Colbert, and R. E. Smalley, Science **269**, 1550 (1995).

[11] W. A. de Heer, A. Châtelain, and D. Ugarte, Science **270**, 1179 (1995).

[12] L. A. Chernozatonskii, Y. V. Gulyaev, Z. J. Kosakovskaja, N. I. Sinitsyn, G. V. Torgashov, Y. F. Zakharchenko, E. A. Fedorov, and V. P. Valchuk, Chem. Phys. Lett. **233**, 63 (1995).

[13] W. B. Choi, D. S. Chung, J. H. Kang, H. Y. Kim, Y. W. Jin, I. T. Han, Y. H. Lee, J. E. Jung, N. S. Lee, G. S. Park, and J. M. Kim, Appl. Phys. Lett. **75**, 3129 (1999).

[14] S. Iijima and T. Ichihashi, Nature (London) **363**, 603 (1993).

[15] D. S. Bethune, C. H. Kiang, M. S. de Vries, G. Gorman, R. Savoy, J. Vazquez, and R. Beyers, Nature (London) **363**, 605 (1993).

[16] J. W. Mintmire, B. I. Dunlap, and C. T. White, Phys. Rev. Lett. **68**, 631 (1992).

[17] R. Saito, M. Fujita, G. Dresselhaus, and M. S. Dresselhaus, Appl. Phys. Lett. **60**, 2204 (1992).

[18] N. Hamada, S. Sawada, and A. Oshiyama, Phys. Rev. Lett. **68**, 1579 (1992).

[19] J. W. G. Wildöer, L. C. Venema, A. G. Rinzler, R. E. Smalley, and C. Dekker, Nature (London) **391**, 59 (1998).

[20] T. W. Odom, J.-L. Huang, P. Kim, and C. M. Lieber, Nature (London) **391**, 62 (1998).

[21] W. Clauss, D. J. Bergeron, and A. T. Johnson, Phys. Rev. B **58**, R4266 (1998).

[22] David Tománek, Steven G. Louie, H. Jonathon Mamin, David W. Abraham, Ruth Ellen Thomson, Eric Ganz, and John Clarke, Phys. Rev. B **35**, 7790 (1987).

[23] David Tománek and Steven G. Louie, Phys. Rev. B **37**, 8327 (1988).

[24] V. Meunier and Ph. Lambin, Phys. Rev. Lett. **81**, 5588 (1998); A. Rubio, Appl. Phys. A: Mater. Sci. Process. **68A**, 275 (1999); V. Meunier, P. Senet, and Ph. Lambin, Phys. Rev. B **60**, 7792 (1999).

[25] C. L. Kane and E. J. Mele, Phys. Rev. B **59**, R12 759 (1999).

[26] D. L. Carroll, P. Redlich, P. M. Ajayan, J. C. Charlier, X. Blase, A. DeVita, and R. Car, Phys. Rev. Lett. **78**, 2811 (1997); Philip Kim, Teri W. Odom, Jin-Lin Huang, and Charles M. Lieber; *ibid.* **82**, 1225 (1999).

[27] M. Ge and K. Sattler, Chem. Phys. Lett. **220**, 192 (1994).

[28] A. Krishnan, E. Dujardin, M. M. J. Treacy, J. Hugdahl, S. Lynum, and T. W. Ebbesen, Nature (London) **388**, 451 (1997).

[29] S. Iijima, T. Ichihashi, and Y. Ando, Nature (London) **356**, 776 (1992).

[30] S. Iijima, M. Yudasaka, R. Yamada, S. Bandow, K. Suenaga, F. Kokai, and K. Takahashi, Chem. Phys. Lett. **309**, 165 (1999).

[31] D. Tománek and Michael A. Schluter, Phys. Rev. Lett. **67**, 2331 (1991).

[32] During structure optimization, we keep all sites charge neutral by modifying the diagonal elements of the Hamiltonian, to suppress structural artifacts near the edge. Once the geometry is optimized, the on-site energies are kept at the unperturbed values. Due to the absence of a Hubbard term, this procedure tends to exaggerate the net charge transfer when compared to truly self-consistent calculations.

[33] M. Schluter, M. Lannoo, M. Needels, G. A. Baraff, and D. Tománek, Phys. Rev. Lett. **68**, 526 (1992).

[34] Young-Kyun Kwon, Susumu Saito, and David Tománek, Phys. Rev. B **58**, R13 314 (1998).

[35] Young-Kyun Kwon, David Tománek, Young Hee Lee, Kee Hag Lee, and Susumu Saito, J. Mater. Res. **13**, 2363 (1998).

[36] Young-Kyun Kwon and David Tománek, Phys. Rev. B **58**, R16 001 (1998).

[37] Stefano Sanvito, Young-Kyun Kwon, David Tománek, and Colin J. Lambert, Phys. Rev. Lett. **84**, 1974 (2000).

[38] W. Zhong, D. Tománek, and G. F. Bertsch, Solid State Commun. **86**, 607 (1993).

[39] S. G. Kim and D. Tománek, Phys. Rev. Lett. **72**, 2418 (1994).

[40] Young-Kyun Kwon, Young Hee Lee, Seong Gon Kim, Philippe Jund, David Tománek, and Richard E. Smalley, Phys. Rev. Lett. **79**, 2065 (1997).

[41] Ph. Lambin, A. Fonseca, J. P. Vigneron, J. B. Nagy, and A. A. Lucas, Chem. Phys. Lett. **245**, 85 (1995); G. Treboux, P. Lapstun, and K. Silverbrook, J. Phys. Chem. B **103**, 1871 (1999).

[42] The nanohorn structures considered in our calculation are clusters containing edge atoms. We found that due to the electron transfer towards the under-coordinated atoms at the edge, the "Fermi level" of these clusters may drop by as much as $\approx$1.0–1.2 eV with respect to that of a graphene monolayer. To compensate for this artifact, we excluded the edge region from the calculated density of states and found the E_F value to lie very close to that of a graphene monolayer.

[43] V. Meunier, L. Henrard, and Ph. Lambin, Phys. Rev. B **57**, 2586 (1998).

EUROPHYSICS LETTERS 1 July 2002

Europhys. Lett., **59** (1), pp. 75-80 (2002)

Giant magneto-conductance in twisted carbon nanotubes

S. W. D. BAILEY[1], D. TOMÁNEK[2], Y.-K. KWON[2](*) and C. J. LAMBERT[1]

[1] *Department of Physics, Lancaster University - Lancaster, LA1 4YB, UK*

[2] *Department of Physics and Astronomy and Center for Fundamental Materials Research Michigan State University - East Lansing, MI 48824-1116, USA*

(received 12 December 2001; accepted in final form 4 April 2002)

PACS. 61.48.+c – Fullerenes and fullerene-related materials.
PACS. 72.80.Rj – Electronic transport: fullerenes and related materials.
PACS. 73.61.Wp – Electronic structure: fullerenes and related materials.

Abstract. – Using the Landauer-Büttiker formalism, we calculate the effect of structural twist on electron transport in conducting carbon nanotubes. We demonstrate that even a localized region of twist scatters the propagating π electrons and induces the opening of a (pseudo-) gap near the Fermi level. The subsequent conductance reduction may be compensated by an applied axial magnetic field, leading to a twist-induced, giant positive magneto-conductance in clean armchair nanotubes.

Carbon nanotubes [1-3] exhibit a range of unusual electronic properties associated with the morphology of these quasi-1D structures. Early one-electron theories successfully associated metallic or semi-conducting behaviour with the chiral vector that characterizes a given nanotube [4-6]. Further studies addressed the effect of atomic-level impurities [7-10] and inter-tube interactions [11-14] on electrical conductance, or magneto-transport [7,15-19]. In parallel with the development of such one-electron theories, intensive studies of electron-electron correlations have been undertaken. Indeed, nonlinear current-voltage (I-V) characteristics have recently been observed [20], which are reminiscent of Luttinger liquid behaviour. An intriguing question remains however, namely whether other effects may augment or even dominate such nonlinearities in the transport properties of nanotubes.

In this letter we predict that scattering of electrons from twistons may give rise to strongly nonlinear I-V characteristics. Twistons [21-23], associated with regions of axial twist in otherwise perfect nanotubes, are intrinsic defects that are frozen into nanotube bundles during their synthesis and hence cannot be ignored when discussing electron transport. Unlike ideal straight and defect-free nanotubes, which have been shown to exhibit conventional magneto-resistive behaviour [24], we find that nanotubes containing twistons may behave in a very different way. In twisted tubes, we predict the occurrence of a giant positive magneto-conductance, an unexpected effect that by far exceeds the positive magneto-conductance associated with weak localisation in disordered tubes [25].

(*) Present address: Covalent Materials, Inc. - 1295A 67th Street, Emeryville, CA 94608, USA.

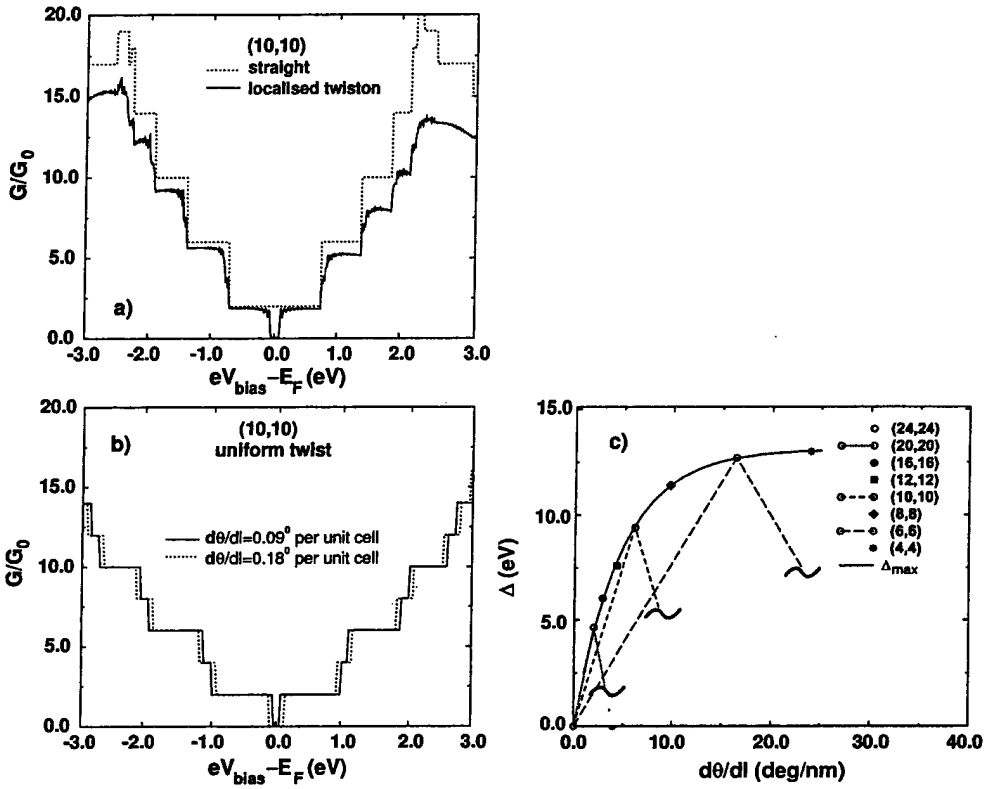

Fig. 1 –Differential conductance G of an infinite $(10,10)$ carbon nanotube as a function of the applied bias voltage $V_{\rm bias}$. (a) Results for a perfectly straight tube (dotted line) are compared to those for a $\Delta\theta = 36°$ finite twiston extending over 100 unit cells in the axial direction. For a tube with radius R, a portion of the unit cell of length L is shown in the inset. $G_0 = 2e^2/h$ is the conductance quantum. (b) Differential conductance of the $(10,10)$ nanotube subject to an infinitely long uniform twist, for different values of the twist per unit length $\mathrm{d}\theta/\mathrm{d}l$. (c) Dependence of the conductance gap Δ on the infinitely long twist $\mathrm{d}\theta/\mathrm{d}l$ for various (n,n) nanotubes.

To compute the effect of a finite scattering region on transport in an otherwise perfect (n,n) armchair nanotube, we use a parameterized four-state (s,p_x,p_y,p_z) Hamiltonian, based on a global fit to density functional results for graphite, diamond and C_2 as a function of the lattice parameter [26]. A finite twiston is treated as a scattering region connecting two semi-infinite (n,n) nanotubes. A recursive Green's function formalism is used to evaluate the transmission matrix $\boldsymbol{t}$, describing the scattering of electrons of energy E from one end of the semi-infinite nanotube to the other [27]. The differential electrical conductance at bias voltage $V_{\rm bias}$ is related to scattering properties at energy $E = E_{\rm F} - eV_{\rm bias}$ by the Landauer formula $G = G_0 \mathrm{Tr}\left\{t^\dagger t\right\}$, where $G_0 = 2e^2/h$ is the conductance quantum. A twiston is formed by introducing a small angular distortion between neighbouring axial slices within the scattering region. This is shown schematically in the inset of fig. 1(a), which displays the local shear distortion within the unit cell of length L, containing two axial slices. The perturbation to the Hamiltonian matrix enters through the scaling of the nearest-neighbour hopping integrals that follow the changes in C-C bonds r_1 and r_2.

Figure 1 shows the differential conductance for a straight and twisted $(10,10)$ nanotube. In

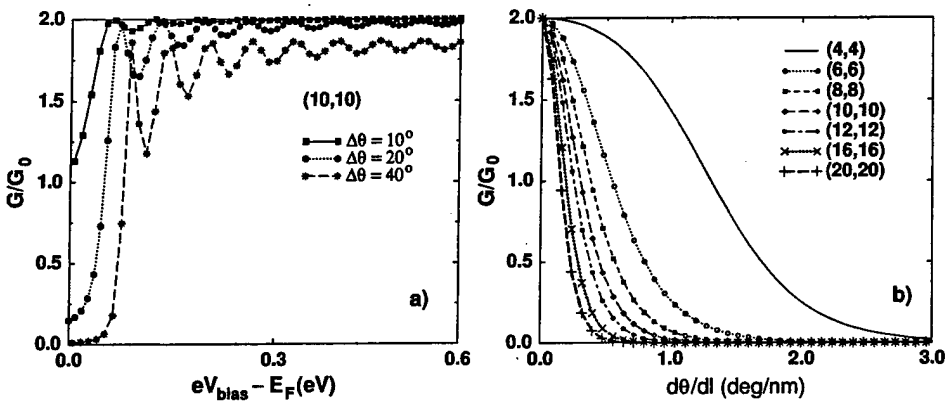

Fig. 2 – (a) Details of the differential conductance G of a $(10,10)$ carbon nanotube subject to a finite twiston, as a function of the applied bias voltage V_{bias}. (b) Differential conductance of (n,n) nanotubes at zero bias as a function of the local twist in finite twistons. In both figures, the twistons $\Delta\theta$ extend only across a finite segment of 100 unit cells in the axial direction.

the straight nanotube of fig. 1(a), the nondegenerate bands, which cross near E_{F}, open up two conductance channels at this energy. Additional conduction channels follow as an increasing number of subbands appear near $E_{\text{F}} - eV_{\text{bias}}$ at higher bias voltages. In the presence of a localized twiston, the differential conductance is suppressed at all energies, in particular near the Fermi level. This is shown in fig. 1(a) for a finite-length twiston, with a total twist of 36° extending over 100 unit cells or ≈ 24.6 nm. The occurrence of a conductance gap near E_{F} suggests that electron scattering by a finite twiston can be viewed as a tunneling phenomenon.

For comparison with fig. 1(a), fig. 1(b) shows results for a nanotube subject to an infinitely long uniform twist $\mathrm{d}\theta/\mathrm{d}l$. This shows that that a localized or infinitely long twist opens up a conductance gap Δ near E_{F}. The predicted gap in the presence of infinitely long twists is shown in fig. 1(c) and agrees with results of refs. [21] and [22].

In the following, we discuss the dependence of the conductance gap on the twist distortion $\mathrm{d}\theta/\mathrm{d}l$, the spatial extent of the twiston, and an axially applied magnetic field. As shown in fig. 1(c), we find that for a range of (n,n) tubes subject to an infinitely long twist, the magnitude of the conductance gap Δ increases linearly with increasing twist distortion to its maximum value Δ_{max}, and decreases thereafter. For an (n,n) nanotube, we find the maximum value of the conductance gap Δ_{max} to be achieved at an "optimum tube twist" value $(\mathrm{d}\theta/\mathrm{d}l)_0 \approx An^{-2}$ (with $A = 620°/\text{nm}$), which depends on the chiral index n. The dependence of Δ_{max} on the optimum tube twist $(\mathrm{d}\theta/\mathrm{d}l)_0$ corresponds to the envelope function in fig. 1(c), and is well approximated by $\Delta_{\text{max}} \approx \Delta(\mathrm{d}\theta/\mathrm{d}l)_0 \approx 1.30$ eV $(1 - e^{-0.21(\mathrm{d}\theta/\mathrm{d}l)_0})$, with $(\mathrm{d}\theta/\mathrm{d}l)_0$ in °/nm units.

Details of conductance changes due to localized twistons, such as those of fig. 1(a), are shown for small bias voltages in fig. 2(a). In the present case, we subjected a straight $(10,10)$ nanotube to finite twists $\Delta\theta$ extending over 100 unit cells. We find that the conductance pseudo-gap associated with finite twistons is accompanied by conductance oscillations at small bias voltages. A tube subject to an infinitely long twist, on the other hand, possesses a real gap with no such oscillations. The zero-bias conductance as a function of the twist angle for finite twistons extending over 100 unit cells is presented in fig. 2(b) for a range of tube sizes. This type of conductance behaviour is reminiscent of that associated with tunneling through a potential barrier, where the twist-induced gap is analogous to the height of the barrier.

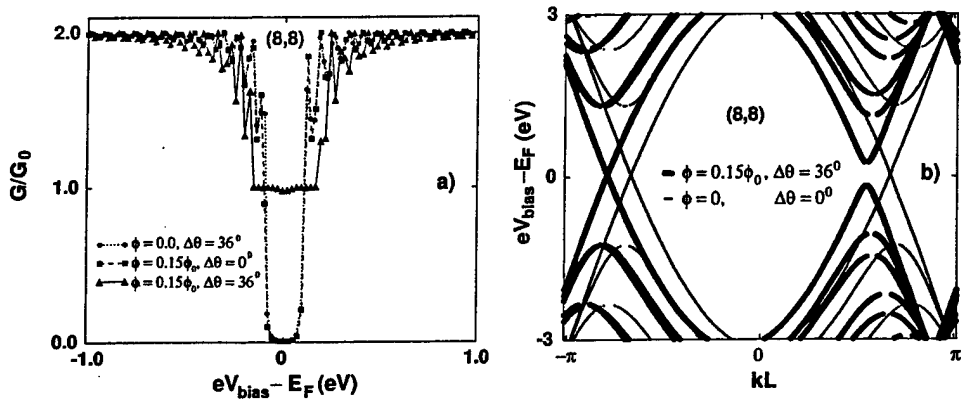

Fig. 3 – (a) Differential conductance of an $(8,8)$ carbon nanotube subject to a $\Delta\theta = 36°$ twiston extending over 100 unit cells and/or a magnetic flux $\Phi = 0.15\Phi_0$ in the axial direction. Both the twiston and the flux alone open up near-identical conductance gaps. A careful combination of nonzero flux and twist reopens a single conductance channel at small bias voltages. (b) Corresponding band structure of an infinite $(8,8)$ carbon nanotube. Results for a straight tube in zero field are compared to those for a tube subject to an infinitely long uniform twist of $\mathrm{d}\theta/\mathrm{d}l = 0.36°$ per unit cell and a magnetic flux $\Phi = 0.15\Phi_0$ in the axial direction.

These results, when combined, clearly demonstrate that finite twistons yield nonlinear I-V characteristics.

It must be stressed that the degree of twist required to open a pseudo-gap is small. For example in the finite $(10,10)$ carbon nanotube of fig. 2(a), $\Delta\theta = 20°$ over 100 unit cells is equivalent to $\mathrm{d}\theta/\mathrm{d}l \lesssim 1°/\mathrm{nm}$ only. The resulting perturbation to the Hamiltonian is therefore well within the limits of our model, where the twist is viewed as a frozen-in defect to the nanotube at low temperatures [23].

In a reasoning based on London theory, we now consider the effect of a uniform magnetic field on transport in straight and twisted nanotubes. Axially applied magnetic fields produce an Aharonov-Bohm effect in carbon nanotubes [16,17,28], which in the clean limit arises from the opening and closing of a band gap at the Fermi level. In the presence of a twiston, we now demonstrate that the reverse effect can occur, namely that an axial magnetic field can remove the twiston-induced conductance gap, resulting in a positive magneto-conductance. The effect of a combined structural twist and magnetic field on the conductance of nanotubes is discussed in fig. 3(a). These results show that a magnetic field may restore the zero-bias conductance of twisted armchair nanotubes from an essentially vanishing value to near half of the initial zero-twist value.

To understand this behaviour, we consider the roll-up process of a graphene sheet, spanned by the Bravais lattice vectors $\boldsymbol{a}_1$ and $\boldsymbol{a}_2$, to an armchair nanotube. Structural twist of the tube, depicted in the inset of fig. 1(a), is related to a shear distortion of the initial graphene sheet. Let us assume that the electronic structure near E_{F} can be attributed to the nearest-neighbour $pp\pi$ interactions. The imposed structural twist is modeled by changing the relative strength of the hopping integral γ_i along the neighbour vector $\boldsymbol{r}_i$ with respect to the undistorted reference value $\gamma_0 = 1$. Taking into account the diatomic basis of the distorted graphene sheet, we obtain a half-filled band with particle-hole symmetry and an energy gap between the valence and conduction band of

$$\Delta(\boldsymbol{k}) = \left|1 + \gamma_1 e^{i\boldsymbol{k}\cdot\boldsymbol{a}_1} + \gamma_2 e^{i\boldsymbol{k}\cdot\boldsymbol{a}_2}\right| .$$

During the initial roll-up process to an (n, n) nanotube, the two-dimensional electron momentum space of the graphene sheet collapses into a one-dimensional space with $\boldsymbol{k}$ along the tube axis. Exposing the tube to a magnetic field adds the term $e\boldsymbol{A}/\hbar$ to $\boldsymbol{k}$, where $\boldsymbol{A}$ is the vector potential, thus introducing a new phase factor [17]. Further noting that $\boldsymbol{k} \cdot \boldsymbol{a}_i = \boldsymbol{k} \cdot \boldsymbol{r}_i$, we find that the energy gap between the highest valence and lowest conduction band of a twisted tube becomes

$$\Delta(\boldsymbol{k}) = |1 + \gamma_1 e^{i\boldsymbol{k}\cdot\boldsymbol{r}_1} e^{i\phi} + \gamma_2 e^{i\boldsymbol{k}\cdot\boldsymbol{r}_2} e^{i\phi}| \,. \tag{1}$$

The phase $\phi = 2\pi\Phi/\Phi_0$ depends on the ratio between the magnetic flux Φ trapped in the tube and the fundamental unit of flux $\Phi_0 = h/e$. Note that the fundamental unit of flux used in this paper is twice the flux quantum, $\Phi_0 = h/2e$. The fundamental gap $\Delta = \Delta(\boldsymbol{k}_0)$, occurring at $\boldsymbol{k}_0$, is the minimum value found in the Brillouin zone. We also note that $\Delta = 0$ for an undistorted tube in zero field.

In view of the twisted-tube morphology defined in fig. 1(a), it is convenient to introduce the quantity $\alpha = \boldsymbol{k}\cdot\boldsymbol{r}_1 = -\boldsymbol{k}\cdot\boldsymbol{r}_2$. From eq. (1) we find that $\Delta(\boldsymbol{k}) = 0$ only if $(\sin\phi/\sin\alpha) = (\gamma_1 - \gamma_2)$ and $(\cos\phi/\cos\alpha) = (-\gamma_1 - \gamma_2)$. Combining these equations, we find that the fundamental gap closes if

$$\cos 2\phi = \frac{(\gamma_1^2 + \gamma_2^2) - (\gamma_1^2 - \gamma_2^2)^2}{2\gamma_1\gamma_2} \tag{2}$$

and

$$\cos 2\alpha = \frac{1 - \gamma_1^2 - \gamma_2^2}{2\gamma_1\gamma_2} \,. \tag{3}$$

In other words, according to eq. (2), the twist-induced fundamental gap closes again, once the (n, n) nanotube is exposed to a magnetic field B

$$B = B_c \, \arccos\left(\frac{(\gamma_1^2 + \gamma_2^2) - (\gamma_1^2 - \gamma_2^2)^2}{2\gamma_1\gamma_2}\right) \tag{4}$$

along its axis, where $B_c = 2.28{\times}10^4 \text{ T}/n^2$. According to eq. (3), the longitudinal wave vector $\boldsymbol{k}_0$, at which the fundamental gap vanishes, must satisfy the condition

$$\boldsymbol{k}_0\cdot\boldsymbol{r}_1 = \frac{1}{2} \arccos\left(\frac{1 - \gamma_1^2 - \gamma_2^2}{2\gamma_1\gamma_2}\right) \,. \tag{5}$$

The above heuristic model also demonstrates why the exact result of fig. 3(a) yields $G \approx G_0$ for the zero-bias conductance in the presence of a nonzero twist and flux, rather than the value $G = 2G_0$ for a twist-free tube in zero field. In the latter case, the two open scattering channels at E_F correspond to values of α (or wave vector $\boldsymbol{k}$) of opposite sign. For a given nonzero flux Φ and a corresponding sign of the phase ϕ, $(\sin\phi/\sin\alpha) = (\gamma_1 - \gamma_2)$ can be satisfied by only one of these channels. This is shown in fig. 3(b), where the dispersion curves in the presence of a compensating twist and flux are compared to those of a perfectly straight nanotube in zero field. As expected, reversing the sign of the twist angle switches the allowed conduction channel. Figure 3(b) also illustrates that the longitudinal Fermi wave vector $\boldsymbol{k}_0$, which marks the band crossing at E_F, is shifted from the value for the unperturbed tube, as predicted by eq. (5).

In summary, we have analyzed for the first time the scattering properties of finite-size twistons and shown that these introduce nonlinear I-V characteristics associated with the opening of a pseudo-gap at E_F, thus effectively quenching the nanotube conductance. This conductance gap can be closed in an axial magnetic field, leading to a giant positive magneto-conductance. At small bias voltages, the conductance of a twisted tube in nonzero field can reach up to half the ballistic conductance value of a straight tube in zero field.

REFERENCES

[1] IIJIMA S., *Nature*, **354** (1991) 56.
[2] DRESSELHAUS M. S., DRESSELHAUS G. and EKLUND P. C., *Science of Fullerenes and Carbon Nanotubes* (Academic Press, San Diego) 1996.
[3] SAITO R., DRESSELHAUS G. and DRESSELHAUS M. S., *Physical Properties of Carbon Nanotubes* (Imperial College London) 1998 and references therein.
[4] MINTMIRE J. W., DUNLAP B. I. and WHITE C. T., *Phys. Rev. Lett.*, **68** (1992) 631.
[5] SAITO R., FUJITA M., DRESSELHAUS G. and DRESSELHAUS M. S., *Appl. Phys. Lett.*, **60** (1992) 2204.
[6] HAMADA N., SAWADA S. and OSHIYAMA A., *Phys. Rev. Lett.*, **68** (1992) 1579.
[7] ROCHE S. and SAITO R., *Phys. Rev. B*, **59** (1999) 5242.
[8] CHOI H. J., IHM J., LOUIE S. G. and COHEN M. L., *Phys. Rev. Lett.*, **84** (2000) 2917.
[9] ROLAND C., NARDELLI M. B., WANG J. and GUO H., *Phys. Rev. Lett.*, **84** (2000) 2921.
[10] ANANTRAM M. P. and GOVINDAN T. R., *Phys. Rev. B*, **58** (1998) 4882.
[11] KWON Y.-K. and TOMÁNEK D., *Phys. Rev. B*, **58** (1998) R16001.
[12] DELANEY P., CHOI H. J., IHM J., LOUIE S. G. and COHEN M. L., *Nature*, **391** (1998) 466.
[13] KWON Y.-K., SAITO S. and TOMÁNEK D., *Phys. Rev. B*, **58** (1998) R13314.
[14] SANVITO S., KWON Y.-K., TOMAŃEK D. and LAMBERT C. J., *Phys. Rev. Lett.*, **84** (2000) 1974.
[15] SAITO R., FUJITA M., DRESSELHAUS G. and DRESSELHAUS M., *Appl. Phys. Lett.*, **60** (1992) 2204.
[16] AHARONOV Y. and BOHM D., *Phys. Rev.*, **115** (1959) 485.
[17] TIAN W. and DATTA S., *Phys. Rev. B*, **49** (1994) 5097.
[18] LIN M. F. and SHUNG K. W. K., *Phys. Rev. B*, **51** (1995) 7592.
[19] ORLIKOWSKI D. *et al.*, *Phys. Rev. B*, **63** (2001) 155412.
[20] BOCKRATH M. *et al.*, *Nature*, **397** (1999) 598.
[21] KANE C. L. and MELE E. J., *Phys. Rev. Lett.*, **78** (1997) 1932.
[22] ROCHEFORT A., AVOURIS P., LESAGE F. and SALAHUB D. R., *Phys. Rev. B*, **60** (1999) 13824.
[23] KWON Y.-K. and TOMÁNEK D., *Phys. Rev. Lett.*, **84** (2000) 1483.
[24] MAKSIMENKO A. S. and SLEPYAN G. Y., *Phys. Rev. Lett.*, **84** (2000) 362.
[25] LANGER L. *et al.*, *J. Mater. Res.*, **9** (1994) 927.
[26] TOMÁNEK D. and SCHLUTER M. A., *Phys. Rev. Lett.*, **67** (1991) 2331.
[27] SANVITO S., LAMBERT C. J. and JEFFERSON J. H., *Phys. Rev. B*, **59** (1999) 11936.
[28] BACHTOLD A. *et al.*, *Nature*, **397** (1999) 673.

Printed on September 25, 2002

Energetics and Electronic Structure of a Polyacetylene Chain Contained in a Carbon Nanotube

G. C. McIntosh[1], D. Tománek[2] and Y. W. Park[1]

[1]*School of Physics, Seoul National University, Seoul 151-742, Korea*

[2]*Department of Physics and Astronomy and Center for Fundamental Materials Research, Michigan State University, East Lansing, Michigan 48824-1116*

(Received)

Abstract

Using density functional theory, we calculate the energy and electronic structure of a polyacetylene chain interacting with various carbon nanotubes. We find that polyacetylene chains are weakly attracted exo- or endohedrally to nanotubes. The equilibrium separation between the chain and the wall is close to 3.3 Å, suggesting an energetic preference for polyacetylene to be enclosed in nanotubes wider than the (6,6) tube. The chains are expected to be spontaneously pulled into open nanotubes by forces amounting to a fraction of a nano-Newton. Electronic structure calculations reveal the occurrence of a peak at the Fermi level in the electronic density of states, caused by the weak interaction between polyacetylene and the carbon nanotube, which may facilitate the onset of superconductivity in this system.

It was noted soon after their initial discovery[1] that carbon nanotubes (CNTs) are hollow cylindrical structures, which could make ideal containers for just a few atoms or small molecules.[2] In this regard, they have been considered for hydrogen storage[3] and as nano-sized 'test-tubes for manipulating chemical/biological molecules'.[4] Filling of carbon nanotubes with molten lead, induced by capillary action, has been demonstrated experimentally.[5] The formation of 'peapod' structures is now well established, whereby C_{60} buckyballs readily migrate into a (10,10) nanotube.[6] Further to this, if one is interested in investigating one-dimensional nano-systems, then carbon nanotubes could act as a support structure to contain the nano-system. For example, nanotubes have been considered for confining a chain of metal atoms,[7] where the interest lies in comparing the properties of the one-dimensional chain with that of the three-dimensional bulk metal.

Even in the absence of contained atoms or molecules, armchair carbon nanotubes are very interesting one-dimensional metallic systems which, for example, have been considered as prime candidates for observing a Luttinger liquid.[8] Another one-dimensional material of considerable interest is polyacetylene (PA). Unlike metallic carbon nanotubes,[9] polyacetylene succumbs to Peierls distortion that causes dimerization in pristine PA, accompanied by a band gap opening at the Fermi level. The charge carriers in lightly doped PA are the somewhat more exotic solitons, which can carry spin and no charge or charge and no spin.[10] In the bulk system, the intrinsic properties of individual PA chains may be obscured by inter-chain coupling, complicated morphology of the bulk material, or by effects coming from dopant atoms. To avoid these artifacts, we propose to use carbon nanotubes as support structures to keep PA chains straight and to isolate them. Since both nanotubes and highly doped polyacetylene are good metals, the combined nanotube/polyacetylene system may show intriguing transport behavior with widescale technological applications.

Two main issues to be addressed are finding the ideal size of a carbon nanotube to comfortably contain just a single PA chain, and to determine the degree of interaction between the carbon nanotube and the enclosed PA chain. On the one hand, a negligible interaction is desirable if the PA chain is to retain its original properties after insertion into

the carbon nanotube. On the other hand, given that both carbon nanotubes and PA are very interesting materials on their own, we are curious as to whether some new phenomena might emerge within the combined system.

In this study, we investigate for the first time the interaction energy and electronic structure of a polyacetylene chain aligned axially either exo- or endohedrally with a nanotube. We find that the polymer chains are weakly attracted towards, and may be spontaneously pulled into sufficiently wide nanotubes. The undoped polyacetylene/nanotube system is metallic. The weak interaction between the subsystems induces a peak in the electronic density of states at the Fermi level, which may facilitate the onset of superconductivity.

Our calculations are based on density functional theory (DFT) within the local density approximation (LDA) and performed using the SIESTA code.[11] Troullier-Martins pseudopotentials were used to represent the nuclei plus core electrons. We used the Perdew-Zunger form of the exchange-correlation potential in LDA.

In all cases, the axes of the PA chain and carbon nanotube were kept parallel. The structural arrangement is illustrated in the insets of Fig. 1(a) as well as in Fig. 2(a-b). To reduce computing requirements,[12] only armchair nanotubes were considered at this stage. Since the lattice structure of a PA chain and graphitic armchair nanotube are very similar, the PA lattice could be held commensurate with the nanotube lattice, thus reducing the number of atoms required per unit cell. This necessitated the unit cell length of the PA chain to be reduced slightly from 2.475 Å to 2.460 Å, at the negligible energy cost of only $\approx$1 meV per unit cell.

Depending on the size of the carbon nanotube being considered, the unit cell contained between 20 atoms (for a (4,4) nanotube) and 32 atoms (for a (7,7) nanotube). Of these, two carbon atoms and two hydrogen atoms were associated with the PA chain, as illustrated in Fig. 2(b). The unit cell size perpendicular to the carbon nanotube axis was set to at least 10 Å, so that there was no interaction between structures in adjacent cells. For total energy calculations, we sampled the irreducible wedge of the one-dimensional Brillouin zone by 4 k-points. To achieve sufficient energy convergence yielding smooth E versus d curves

in Figs. 1 and 2, the energy cutoff for plane wave expansion was set to 100 Ry. For the non-bonding interaction between the PA chain and carbon nanotube, we applied the counterpoise correction using ghost orbitals to account for basis set superposition errors.

As a test case, we have optimized the structure of an isolated PA chain. We obtained an average carbon-carbon bond length of 1.396 Å, which is close to the experimental value of 1.4 Å,[13] and a bond length alteration (BLA) of 0.051 Å. This value for the BLA is less than the experimental value of 0.08 Å, but under-estimation of the BLA has been acknowledged previously for DFT calculations.[14] Resolving this problem requires going beyond the LDA.[15] As another test, we have calculated the equilibrium separation between two graphite sheets. We obtain 3.44 Å, in close agreement with the experimental value.

In our first study, we explored the nature of the binding between a PA chain and a carbon nanotube. Figure 1(a) shows the interaction energy between a (4,4) carbon nanotube and a PA chain for the case that the PA chain is situated outside the carbon nanotube. We find a clear minimum in the E versus d curve with a binding energy of 45.4 meV. Comparing this value to kT, we conclude that the system can be bound at room temperature. The equilibrium separation of 3.34 Å turns out to be similar to that between graphite sheets. This is not too surprising, given that the nanotube can be considered as a rolled up graphite sheet and that the carbon backbone of the PA chain is almost commensurate with graphite. For the sake of comparison, in Fig. 1(b) we also show the interaction energy between a PA chain and a graphite sheet, representing a nanotube of large diameter. In this case, the binding energy is slightly increased to 59.3 meV and the associated equilibrium separation reduced to 3.30 Å. Evidently, curvature of the graphitic structure plays a role in the interaction energy, whereby having more atoms in close proximity to the PA chain increases the binding interaction. Our values for the equilibrium separation also indicate that a carbon nanotube would require a diameter of at least 6.6 Å, before an insertion of a PA chain into the nanotube would become energetically favourable.

Figure 2 shows our main result for a PA chain inside armchair carbon nanotubes of various radii R, as a function of the axial separation r. Figure 2(c) shows that on energy

grounds, PA is likely to enter nanotubes of sufficiently large diameter and free for off-axial displacements. For the PA chain inside a (4,4) nanotube the energy never becomes negative, indicating that this configuration is energetically unfavourable.[16] The same holds also for the wider (5,5) nanotube, where the insertion process is only marginally endothermic. For the (6,6) and (7,7) nanotubes, the nanotube diameter is sufficient to allow PA to be bound inside the nanotube, as seen on the exapanded energy scale in Fig. 2(d). For the (6,6) nanotube, the minimum is fairly wide so that a PA chain enclosed inside a (6,6) nanotube would still have some degree of lateral freedom. As compared to larger nanotubes, this system allows PA to interact with more atoms, thus causing further stabilization, as already suggested by the results of Fig. 1. The (7,7) nanotube, with a set of energy minima at $r > 0$, is sufficiently wide to accommodate more than one PA chain.

We next address the possible insertion process of a PA chain into a carbon nanotube, illustrated in Fig. 3(a). Given that the (6,6) nanotube has an appropriate diameter to contain just one PA chain, we consider this as a model system. The energy gain associated with the axial insertion of a PA chain into the (6,6) nanotube is depicted in Fig. 3(b). Since the translation symmetry along the axis is broken in this case, the calculations are performed for finite, hydrogen-terminated clusters representing the nanotube and PA, as shown in the inset of Fig. 3(b), and extrapolated for a semi-infinte PA chain and nanotube. For PA completely outside the nanotube, corresponding to positive z values, the total energy is that of an isolated nanotube and an isolated PA chain and taken as a reference value. We see the energy becoming lowered as the end of the PA chain moves into the carbon nanotube, indicating that the PA chain is likely to be pulled in once it is partially inserted. Of interest is that the PA chain begins to feel the attraction, when it is still $\approx$2 Å outside the carbon nanotube. This suggests that the insertion process should start spontaneously as soon as the PA chain approaches the open end of the carbon nanotube. For a semi-infinite chain entering a semi-infinite nanotube, the energy gain per segment inserted is constant and can be inferred from Fig. 2. The constant slope of the $E(z)$ curve in Fig. 3(b) corresponds to a force of 0.159 nN that pulls the PA chain in. Even though this force appears small on a

macroscopic scale, dividing it by the cross-sectional area of the nanotube yields an effective pressure of 301 MPa. This large, capillarity-induced pressure will likely cause an efficient filling of the available volume by polyacetylene.

We next investigate the degree of electronic interaction between the carbon nanotube and enclosed PA chain. Our model system in this case is the (7,7) nanotube containing a polyacetylene chain, which has been displaced off the tube axis close to its equilibrium position. The electronic density of states of the (7,7) nanotube is shown in Fig. 4(a), that of an isolated PA chain[17] in Fig. 4(b), and that of the combined system in Fig. 4(c). We find the density of states of the combined system to differ from the superposition of its components, indicating some degree of electronic interaction between the valence systems of the two structures. Comparison between Figs. 4(b) and (c) indicates that the presence of PA does not affect the van Hove singularities in the DOS of the nanotube. The most pronounced change occurs in the metallic region in-between the first van Hove singularities of the nanotube, close to E_F. There, we can see a signature of the van Hove singularities of PA, which have been upshifted by the crystal potential. Of particular interest is the fact that one of these PA-induced peaks in the DOS coincides with the Fermi level. Should the nanotube/PA system exhibit superconducting behavior, similar to pristine nanotubes[18], such an increase in the DOS at the Fermi level could enhance the superconducting transition temperature. This can be seen from the weak coupled BCS theory, where the transition temperature is given by the McMillan formula as $T_c \sim \hbar\omega_D \exp(-1/\lambda)$, with $\lambda = N(E_F)V_0$ being the electron-phonon interaction. Here, $N(E_F)$ is the DOS at the Fermi level and V_0 is the Bardeen-Pines interaction. Since $N(E_F)$ appears in the exponent, even a minute peak in the DOS at the Fermi level should increase T_c significantly. This mechanism for T_c enhancement has been proposed previously for the high-T_c cuprates[19], where band structure calculations revealed a van Hove singularity in the DOS close to the Fermi level. Since superconductivity has been observed in ropes of single-walled carbon nanotubes at temperatures below 0.55 K only,[18] the insertion of a PA chain could results in an increase of T_c.

Figure 4(e) shows the charge distribution through a cross section of the combined (7,7)

nanotube/PA system, in a plane defined by Fig. 4(d). To find out the effect of nanotube-PA interaction on the charge distribution, we subtract from the total charge density the superposition of the charge densities of the isolated (7,7) nanotube and PA chain, and present the results in Fig. 4(f). Even though the perturbation is relatively small, reflecting the weak interaction, we can clearly discern a region of increased charge density between the chain and the nanotube wall within the PA-nanotube interaction range. Since this charge stems predominantly from the nanotube, we can talk about PA-induced hole-doing of the nanotube. This effect has also been predicted previously for double-walled carbon nanotubes.[20] We conclude that due to the nonvanishing interaction, armchair carbon nanotubes do not act as "perfectly inert" containers for polyacetylene. A possible alternative in this respect would be boron-nitride nanotubes,[7] which show a much larger fundamental gap than insulting carbon nanotubes and thus should not intereact with the valence electron system of the PA chain.

In summary, we have performed density functional calculations to investigate the interaction between polyacetylene chains and armchair carbon nanotubes. We find that polyacetylene chains are weakly attracted exo- or endohedrally to nanotubes at an equilibrium separation between the chain and the wall close to 3.3 Å, suggesting the energetic preference for enclosure in sufficiently wide nanotubes. We find the (4,4) nanotube too narrow, but the (6,6) nanotube nearly ideal to contain a single PA chain. Larger nanotubes, such as the (10,10) nanotube, may contain more than one PA chain. We expect PA chains to be pulled spontaneously into open nanotubes by forces amounting to a fraction of a nano-Newton. Electronic structure calculations reveal the occurrence of a peak at the Fermi level in the electronic density of states, caused by the weak interaction between a PA chain and a carbon nanotube. This peak should occur both for polyacetylene chains attached from outside or enclosed inside nanotubes, and may facilitate the onset of superconductivity in this system.

One of the authors (GCM) would like to thank the following people for helpful discussions: S. H. Jhang, M. Yoon, Z. X. Jin, D. S. Suh, and A. Kaiser. We acknowledge the Korean IMT-2000 "Molecular Logic Devices" program and the BK21 project of the Ministry of Education (MOE), Korea, for providing financial support.

REFERENCES

[1] S. Iijima, Nature **354**, 56 (1991).

[2] Mark R. Pederson and Jeremy Q. Broughton, Phys. Rev. Lett. **69**, 2689 (1992).

[3] Andrea Quintel, AIP Conf. Proc. **544**, 537 (2000).

[4] Fei Zhang, J. Chem. Phys. **111**, 9082 (1999).

[5] P. M. Ajayan and Sumio Iijima, Nature **361**, 333 (1993).

[6] Susumu Okada, Susumu Saito and Atsushi Oshiyama, Phys. Rev. Lett. **86**, 3835 (2001).

[7] Angel Rubio, Yoshiyuki Miyamoto, X. Blase, Marvin L. Cohen and Steven G. Louie, Phys. Rev. B **53**, 4023 (1996).

[8] Marc Bockrath, David H. Cobden, Jia Lu, Andrew G. Rinzler, Richard E. Smalley, Leon Balents and Paul L. McEuen, Nature **397**, 598 (1999).

[9] J. W. Mintmire, B. I. Dunlap and C. T. White, Phys. Rev. Lett. **68**, 631 (1992).

[10] Siegmar Roth, *One-dimensional metals: Physics and materials science*, Weinheim : VCH (1995).

[11] P. Ordejón, E. Artacho and J. M. Soler, Phys. Rev. B **53**, R10441 (2000); D. Sánchez-Portal, P. Ordejón, E. Artacho and J. M. Soler, Int. J. Quantum Chem. **65**, 453 (1997).

[12] Calculations were carried out on a 1.7 GHz Pentium 4 computer.

[13] C. R. Fincher, Jr., C.-E. Chen, A. J. Heeger, A. G. MacDiarmid and J. B. Hastings, Phys. Rev. Lett. **48**, 100 (1982).

[14] Konstantin N. Kudin and Gustavo E. Scuseria, Phys. Rev. B **61**, 16440 (2000).

[15] M. van Faassen, P. L. de Boeij, R. van Leeuwen, J. A. Berger and J. G. Snijders, Phys. Rev. Lett. **88**, 186401 (2002).

[16] Asymmetry at $r = 0$ in the $E(r)$ curve for PA inside the narrow (4,4) nanotube is due to the strong perturbation of the cylindrical symmetry near the axis by the potential of the tube atoms.

[17] The fundamental band gap of polyacetylene is under-estimated in our calculations, a well-documented deficiency of the LDA.

[18] M. Kociak, A. Yu. Kasumov, S. Guéron, B. Reulet, I. I. Khodos, Yu. B. Gorbatov, V. T. Volkov, L. Vaccarini and H. Bouchiat, Phys. Rev. Lett. **86**, 2416 (2001).

[19] R. S. Markiewicz, J. Phys. Chem. Solids **58**, 1179 (1997).

[20] Yoshiyuki Miyamoto, Susumu Saito and David Tománek, Phys. Rev. B **65**, 041402 (2001).

FIGURES

FIG. 1. Interaction energy between a PA chain and (a) a (4,4) carbon nanotube and (b) a graphite monolayer, representing an extremely wide tube. The schematic geometry, including the definition of the distance d between the chain axis and the graphitic wall, is given in the insets. Energies are given per unit cell, containing two carbon and two hydrogen atoms of the polyacetylene. The equilibrium separations are indicated by arrows.

FIG. 2. Interaction between polyacetylene and armchair nanotubes of different diameters. (a) Schematic perspectivic view of the system. (b) Unit cell geometry, defining the nanotube radius R and the axial separation r. (c) Interaction energy between a PA chain and various (n, n) nanotubes as a function of the axial separation r. (d) Details of the interaction energy, given on an expanded scale. Energies are given per unit cell, illustrated in Fig. 2(b). Vertical arrows for $R(n, n)$ indicate the position of the respective nanotube walls.

FIG. 3. Energetics of a polyacetylene chain entering a (6,6) nanotube. (a) Schematic diagram, defining the distance z between the ends of the tube and the chain. (b) Energy change associated with a semi-infinite PA chain being pulled into a semi-infinite (6,6) nanotube. The solid curve, based on calculations for the finite cluster shown in the inset, highlights the behaviour as the PA chain approaches the open end of the carbon nanotube. The data points $(*)$ at $z < 0$ values, as well as the connecting dashed line, are based on the interaction energy for the infinite system, presented in Fig. 2. The horizontal spacing of these data points corresponds to the unit cell size, and their energy is set as a multiple of the interaction energy per unit cell.

FIG. 4. Electronic structure of a polyacetylene chain interacting with a (7,7) nanotube. The electronic density of states near the Fermi level is shown for (a) an isolated (7,7) nanotube, (b) an isolated PA chain, and (c) for the combined system. (e) Charge distribution for the combined PA@(7,7) nanotube system within the cross-section plane indicated in (d). (f) Charge redistribution induced by the nanotube-polyacetylene interaction, obtained after the charge distributions from the individual (7,7) nanotube and PA chain are subtracted off the total charge density in (e). The white circle indicates the position of the (7,7) nanotube wall.

Figure 1

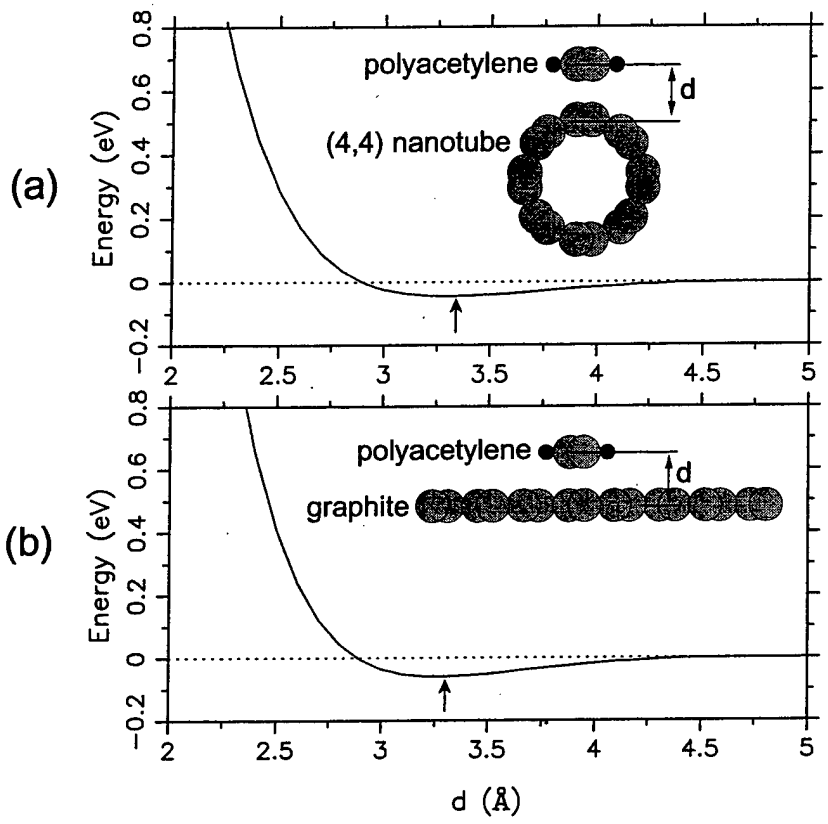
(a)
Energy (eV)
0.8
0.6
0.4
0.2
0
−0.2
polyacetylene
d
(4,4) nanotube
2
2.5
3
3.5
4
4.5
5
(b)
Energy (eV)
polyacetylene
d
graphite
d (Å)

Figure 2

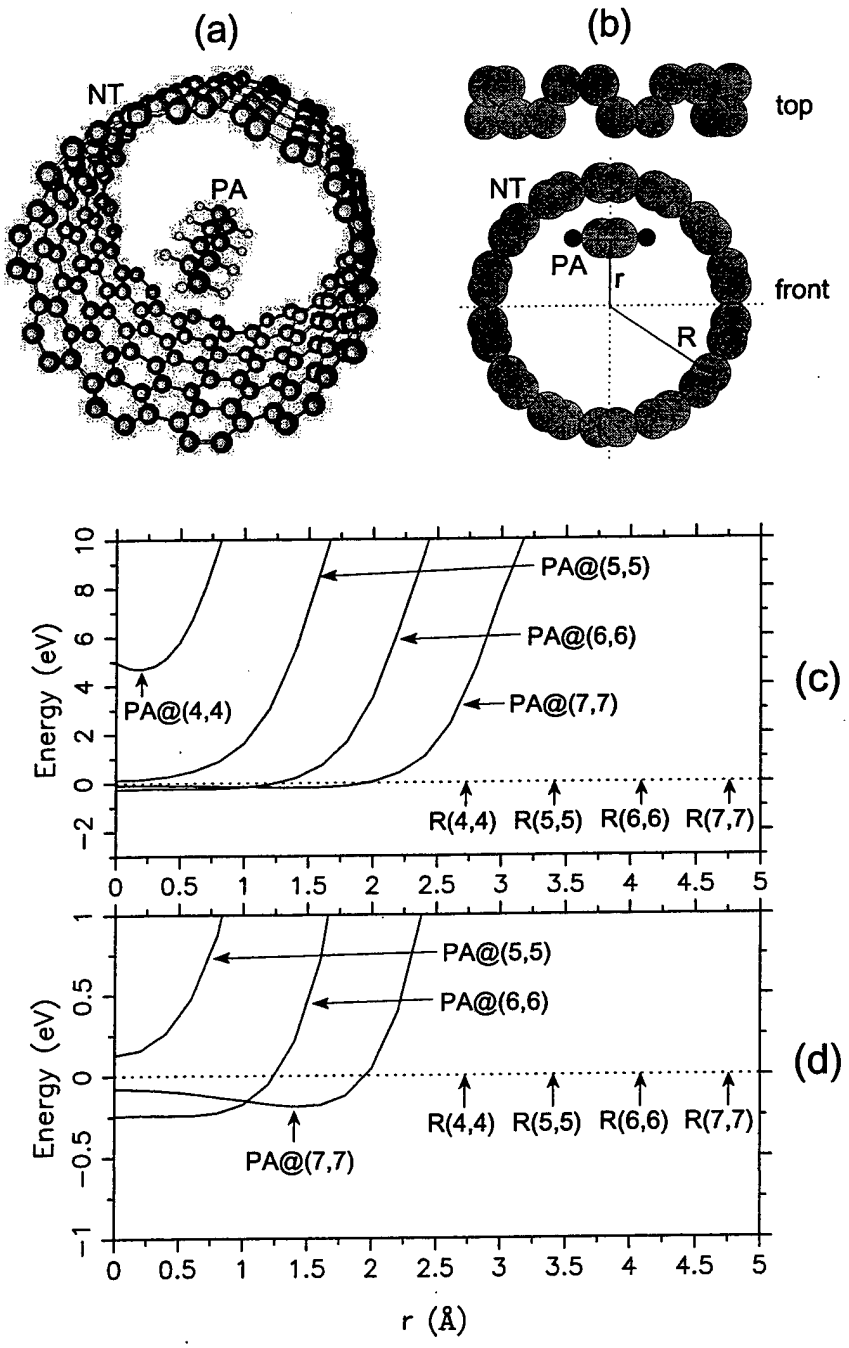
(a)
NT
PA
(b)
top
NT
PA
r
front
R
Energy (eV)
PA@(5,5)
PA@(6,6)
PA@(7,7)
PA@(4,4)
R(4,4) R(5,5) R(6,6) R(7,7)
(c)
Energy (eV)
PA@(5,5)
PA@(6,6)
PA@(7,7)
R(4,4) R(5,5) R(6,6) R(7,7)
(d)
r (Å)

Figure 3

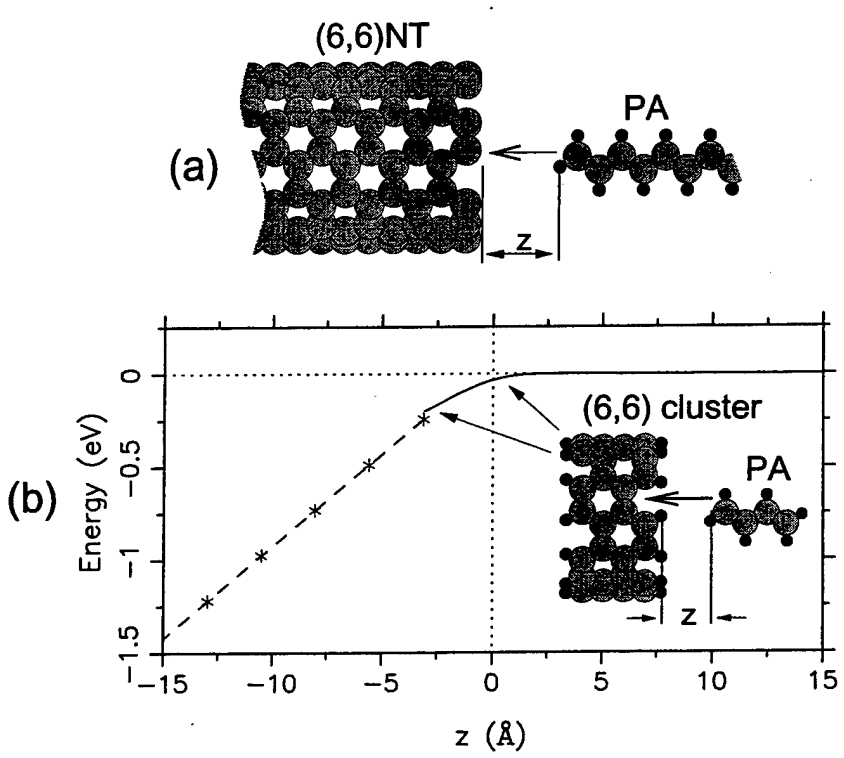

Figure 4

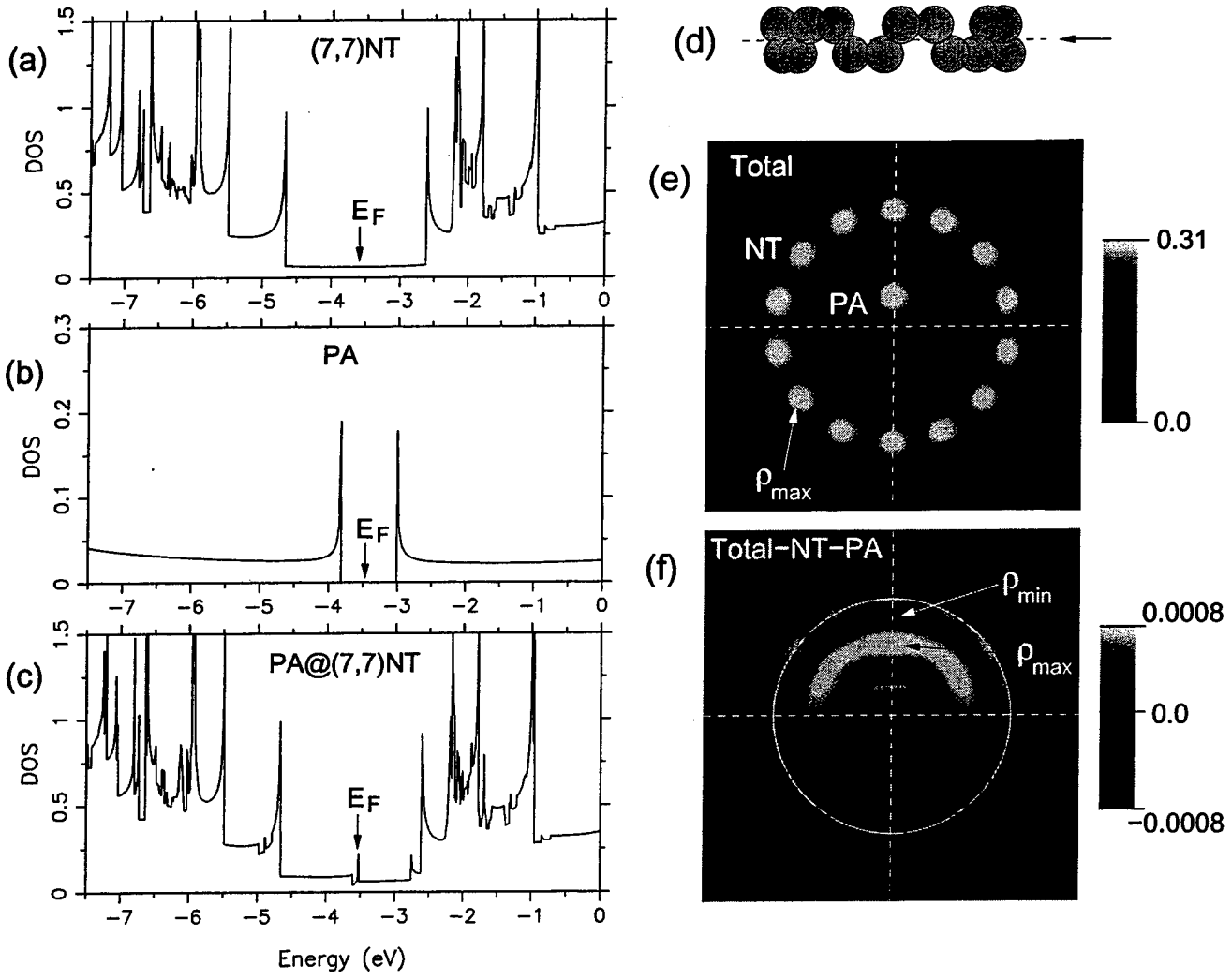
(a)
(7,7)NT
DOS
E_F
(b)
PA
DOS
E_F
(c)
PA@(7,7)NT
DOS
E_F
Energy (eV)
(d)
(e)
Total
NT
PA
ρ_{max}
0.31
0.0
(f)
Total-NT-PA
ρ_{min}
ρ_{max}
0.0008
0.0
-0.0008

Fractional Quantum Conductance in Carbon Nanotubes

Stefano Sanvito,[1,2,3,*] Young-Kyun Kwon,[3] David Tománek,[3] and Colin J. Lambert[1]

[1]*School of Physics and Chemistry, Lancaster University, Lancaster LA1 4YB, United Kingdom*

[2]*DERA, Electronics Sector, Malvern, Worcestershire WR14 3PS, United Kingdom*

[3]*Department of Physics and Astronomy and Center for Fundamental Materials Research, Michigan State University, East Lansing, Michigan 48824-1116*

(Received 4 August 1999)

Using a scattering technique based on a parametrized linear combination of atomic orbitals Hamiltonian, we calculate the ballistic quantum conductance of multiwall carbon nanotubes. We find that interwall interactions not only block some of the quantum conductance channels, but also redistribute the current nonuniformly over individual tubes across the structure. Our results provide a natural explanation for the unexpected integer and noninteger conductance values reported for multiwall nanotubes by Stefan Frank *et al.* [Stefan Frank *et al.*, Science **280**, 1744 (1998)].

PACS numbers: 72.80.Rj, 61.48.+c, 73.50.–h, 73.61.Wp

Carbon nanotubes [1,2] are narrow seamless graphitic cylinders, which show an unusual combination of nanometer-size diameter and millimeter-size length. This topology, combined with the absence of defects on a macroscopic scale, gives rise to uncommon electronic properties of individual single-wall nanotubes [3,4], which—depending on their diameter and chirality—can be either conducting or insulating [5–7]. Significant changes in conductivity of these nanowires may be induced by minute geometric distortions [8] or external fields [9]. More intriguing effects, ranging from the opening of a pseudogap at E_F [10,11] to orientational melting [12], have been predicted to occur when identical metallic nanotubes are bundled together in the form of a "rope" [13].

Electron transport in nanotubes is believed to be ballistic in nature, implying the absence of inelastic scattering [14]. Recent conductance measurements of multiwall carbon nanotubes [14] have raised a significant controversy due to the observation of unexpected conductance values in apparent disagreement with theoretical predictions. In these experiments, multiwall carbon nanotubes, when brought into contact with liquid mercury, exhibit not only even, but also odd multiples of the conductance quantum $G_0 = 2e^2/h \approx (12.9\ \mathrm{k}\Omega)^{-1}$, whereas the conductance of individual tubes has been predicted to be exactly $2G_0$ [15]. An even bigger surprise was the observation of noninteger quantum conductance values, such as $G \approx 0.5G_0$, since conductance is believed to be quantized in units of G_0 [16].

In this Letter, we demonstrate that the unexpected conductance behavior can arise from the interwall interaction in multiwall or in bundled nanotubes. This interaction may not only block some of the quantum conductance channels, but also redistribute the current nonuniformly over the individual tubes. We show that under the experimental conditions described in Ref. [14], this effect may reduce the conductance of the whole system to well below the expected value of $2G_0$.

The electronic band structure of single-wall [5–7] and multiwall carbon nanotubes [17–19], as well as single-wall nanotube ropes [10,11], is now well documented. More recently, it has been shown that interwall coupling leads to the formation of pseudogaps near the Fermi level in multiwall nanotubes [19] and single-wall nanotube ropes [10,11]. These studies have described infinite periodic structures, the conductance of which is quantized in units of $2G_0$. In what follows, we study the effect of interwall coupling on the transport in *finite* structures.

To determine the conductance of finite multiwall nanotubes, we combine a linear combination of atomic orbitals (LCAO) Hamiltonian with a scattering technique developed recently for magnetic multilayers [20,21]. The parametrization of the LCAO matrix elements, based on *ab initio* results for simpler structures [22], has been used successfully to describe electronic structure details and total energy differences in large systems that were untreatable by *ab initio* techniques. This electronic Hamiltonian had been used previously to explain the electronic structure and superconducting properties of the doped C_{60} solid [23], the opening of a pseudogap near the Fermi level in bundled and multiwall nanotubes [11,19].

The scattering technique, which has recently been employed in studies of the giant magnetoresistance [20,21], determines the quantum-mechanical scattering matrix S of a phase-coherent "defective" region that is connected to "ideal" external reservoirs [20]. At zero temperature, the energy-dependent electrical conductance is given by the Landauer-Büttiker formula [24] $G(E) = (2e^2/h)T(E)$, where $T(E)$ is the total transmission coefficient evaluated at the energy E which, in the case of small bias, is the Fermi energy E_F [25].

For a homogeneous system, $T(E)$ assumes integer values corresponding to the total number of open scattering channels at the energy E. For individual (n, n) "armchair" tubes, this integer is further predicted to be even [15], with a conductance $G = 2G_0$ near the Fermi level. As a reference to previous results [15], the density of states and the calculated conductance of an isolated (10, 10) nanotube is shown in Fig. 1.

 0031-9007/00/84(9)/1974(4)$15.00

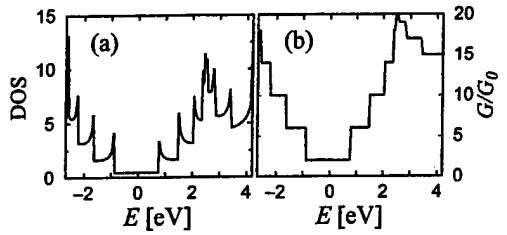

FIG. 1. Electronic density of states (DOS) (a) and conductance G (b) of an isolated single-wall (10, 10) carbon nanotube. The DOS is given in arbitrary units, and G is given in units of the conductance quantum $G_0 = 2e^2/h \approx (12.9\ \mathrm{k}\Omega)^{-1}$.

The corresponding results for the (10, 10)@(15, 15) double-wall nanotube [19] and the (5, 5)@(10, 10)@(15, 15) triple-wall nanotube, where the interwall interaction significantly modifies the electronic states near the Fermi level, are shown in Fig. 2. The conductance results suggest that some of the conduction channels have been blocked close to E_F. The interwall interaction, which is responsible for this behavior, also leads to a redistribution of the total conduction current over the individual tube walls. The partial conductances of the tube walls are defined accordingly as projections of the total conductance and shown in Fig. 3. We notice that the partial conductance is strongly nonuniform within the pseudogaps, where the effects of intertube interactions are stronger.

The experimental setup of Ref. [14], shown schematically in Fig. 4(a), consists of a multiwall nanotube that is attached to a gold tip of a scanning tunneling microscope (STM) and used as an electrode. The STM allows the tube to be immersed at calibrated depth intervals into liquid mercury, acting as a counterelectrode. This arrangement allows precise conduction measurements to be performed on an isolated tube. The experimental data of Ref. [14]

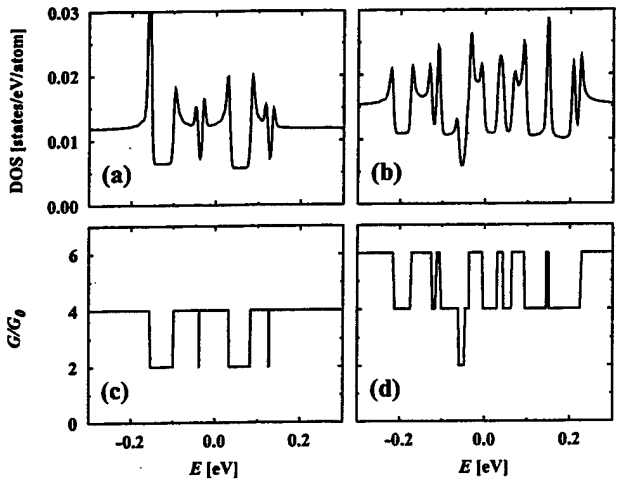

FIG. 2. Electronic density of states and conductance of a double-wall (10, 10)@(15, 15) nanotube [(a) and (c), respectively] and a triple-wall (5, 5)@(10, 10)@(15, 15) nanotube [(b) and (d), respectively].

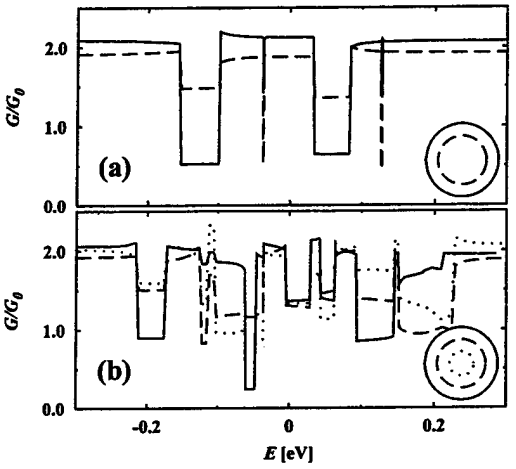

FIG. 3. Partial conductance of the constituent tubes of (a) a double-wall (10, 10)@(15, 15) nanotube and (b) a triple-wall (5, 5)@(10, 10)@(15, 15) nanotube. Values for the outermost (15, 15) tube are given by the solid line, for the (10, 10) tube by the dashed line, and for the innermost (5, 5) tube by the dotted line.

for the conductance G as a function of the immersion depth z of the tube, reproduced in Fig. 5, suggest that in a finite-length multiwall nanotube, the conductance may achieve values as small as $0.5G_0$ or $1G_0$.

The key problem in explaining these experimental data is that nothing is known about the internal structure of the multiwall nanotube or the nature of the contact between the tube and the Au and Hg electrodes. We have considered a number of different scenarios and have concluded that

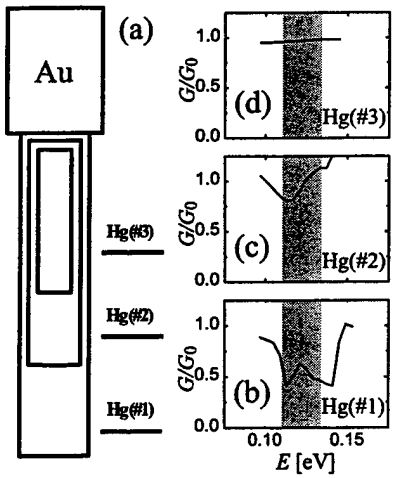

FIG. 4. (a) Schematic geometry of a multiwall nanotube that is being immersed into mercury up to different depths labeled Hg(#1), Hg(#2), and Hg(#3). Only the outermost tube is considered to be in contact with the gold STM tip on which it is suspended. The conductance of this system is given in (b) for the immersion depth Hg(#1), in (c) for Hg(#2), and in (d) for Hg(#3) as a function of the position of E_F. The Fermi level may shift with changing immersion depth within a narrow range indicated by the shaded region.

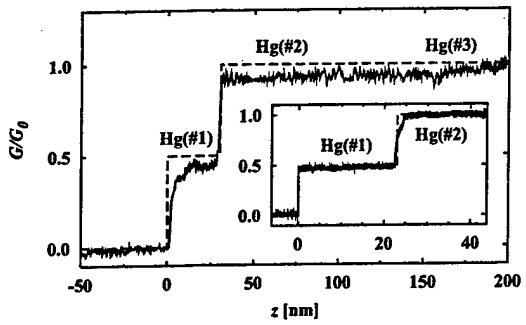

FIG. 5. Conductance G of a multiwall nanotube as a function of immersion depth z in mercury. Results predicted for the multiwall nanotube discussed in Fig. 4, given by the dashed line, are superimposed on the experimental data of Ref. [14]. The main figure and the inset show data for two nanotube samples, which in our interpretation differ only in the length of the terminating single-wall segment.

the experimental data can be explained only by assuming that (i) current injection from the gold electrode occurs only into the outermost tube wall, and that (ii) the chemical potential equals that of mercury, shifted by a contact potential [26], only within the submersed portion of the tube. In other words, the number of tube walls in contact with mercury depends on the immersion depth. The first assumption implies that the electrical contact between the tube and the gold electrode involves only the outermost wall, as illustrated in Fig. 4(a). The validity of the second assumption—in spite of the fact that mercury only wets the outer tubes—is justified by the presence of the interwall interaction. The main origin of the anomalous conductance reduction, to be discussed below, is the backscattering of carriers at the interface of two regions with different numbers of walls due to a discontinuous change of the conduction current distribution.

The conductance calculation is then reduced to a scattering problem involving a semi-infinite single-wall nanotube (the one in direct contact with gold) in contact with a scattering region consisting of an *inhomogeneous* multiwall tube and the Hg reservoir as the counterelectrode. Depending on the immersion depth, denoted by Hg(#1), Hg(#2), and Hg(#3) in Fig. 4(a), portions of the single-wall, the double-wall, and even the triple-wall sections of the tube are submersed into mercury. Our calculations are performed within the linear-response regime and assume that the entire submersed portion of the tube is in "direct contact," i.e., equipotential with the mercury [26]. Increasing the immersion depth from Hg(#1) to Hg(#2) and Hg(#3), an increasing number of walls achieve direct contact with mercury, thereby changing the total conductance $G(E)$, as shown in Figs. 4(b)–4(d) and Fig. 5. We also notice that the conductance of the inhomogeneous multiwall structure of Fig. 4(a) cannot exceed that of a single-wall nanotube, which is the only tube in electrical contact with the gold electrode.

The calculation underlying Fig. 4(b) for the submersion depth Hg(#1) considers a scattering region consisting of a finite-length (5,5)@(10,10)@(15,15) nanotube connected to another finite segment of a (10,10)@(15,15) nanotube. This scattering region is then connected to external semi-infinite leads consisting of (15,15) nanotubes. The calculation for the submersion depth Hg(#2), shown in Fig. 4(c), considers a scattering region formed of a finite-length (5,5)@(10,10)@(15,15) nanotube segment that is attached to a (15,15) nanotube lead on one end and to a (10,10)@(15,15) nanotube lead on the other end. Results in Fig. 4(d) for the submersion depth Hg(#3) represent the conductance of a (5,5)@(10,10)@(15,15) nanotube lead in contact with a (15,15) nanotube lead. The calculated conductances depend on the position of the Fermi level within the tube. Assuming that the Fermi level lies within the narrow energy window of $\approx$0.05 eV, indicated by the shaded region in Figs. 4(b)–4(d), we expect the conductance to increase in discrete steps from $G \approx 0.5G_0$ for Hg(#1) to $G \approx 1G_0$ for Hg(#2) and Hg(#3). This is in excellent agreement with the recent experimental data of Ref. [14], presented in Fig. 5.

It is essential to point out that from our calculations we expect a conductance value $G \approx 0.5G_0$ only when a single tube wall is in direct contact with mercury. In the case that a single-wall region is long, we expect this small conductance value to extend over a large range of immersion depths [14]. Should such a single-wall segment be absent, or should E_F lie outside the grey-shaded region in Fig. 4(b), we expect for the conductance only values of $1G_0$ and above. We believe that the anomalous sample-to-sample variation of the observed conductance [14], which shows the $G \approx 1.0G_0$ value in all cases and the $G \approx 0.5G_0$ value only for particular samples, is related to the structural properties of the nanotube and not to defects which are believed to play only a minor role in transport [27].

We also want to point out that a very different conductance behavior is expected when more than one tube is in direct contact with the Au electrode. As a possible scenario, we consider an inhomogeneous nanotube similar to that in Fig. 4(a), where now all of the three tube walls are in direct contact with the gold electrode. With two conduction channels per tube wall, the conductance has an upper bound of $6G_0$. Calculations analogous to those presented in Fig. 4 suggest a minimum conductance value $G \approx 1G_0$ to occur for a finite-length (10,10)@(15,15) tube segment sandwiched between (15,15) and (5,5)@(10,10)@(15,15) nanotube leads, representing the smallest submersion depth Hg(#1), with mercury in direct contact with only the single-wall portion of the tube. The conductance value $G \approx 2G_0$ is obtained for a (10,10)@(15,15) nanotube lead in contact with a (5,5)@(10,10)@(15,15) nanotube lead, representing submersion depth Hg(#2), with mercury in direct contact with a double-wall tube segment. Finally, depending on the

position of E_F, the conductance of a triple-wall nanotube submersed in mercury, modeled by an infinite (5,5)@(10,10)@(15,15) tube, may achieve conductance values of $4G_0$ or $6G_0$. Even though the interwall interaction leads to a significant suppression of the conductance, the predicted increase in the conductance from $1G_0$ to $2G_0$ and $4G_0$–$6G_0$ with increasing submersion depth is much larger than in the scenario of Fig. 4. Also the predicted conductance values are very different from the experimental data of Ref. [14], thus suggesting that only the outermost tube is in electrical contact with the gold electrode.

In summary, we have shown that fractional quantum conductance may occur in multiwall nanotubes due to interwall interactions that modify the density of states near the Fermi level, and due to tube inhomogeneities, such as a varying number of walls along the tube. We found that the interwall interaction not only blocks certain conduction channels, but also redistributes the current nonuniformly across the walls. We have shown that experiments of Ref. [14] can be interpreted quantitatively for a particular double- and triple-wall tube. An anomalous conductance behavior is also expected to occur in more complex systems not treated here, such as "bucky-bamboo," multichiral tubes, or inhomogeneous tube bundles that are in contact with a metal electrode. Fundamental questions still remain open regarding the nature of the nanotube/metal contact. We hope that our work will stimulate further theoretical and experimental studies on this intriguing topic.

We acknowledge fruitful discussions with Walt de Heer. This work has been done in collaboration with the group of J. H. Jefferson at DERA. S. S. acknowledges financial support by the DERA and the MSU-CMPT visitor fund. Y. K. K. and D. T. acknowledge financial support by the Office of Naval Research and DARPA under Grant No. N00014-99-1-0252.

*Present address: Materials Department, University of California, Santa Barbara, CA 93106.
Email address: ssanvito@mrl.ucsb.edu

[1] S. Iijima, Nature (London) **354**, 56 (1991).
[2] M. S. Dresselhaus, G. Dresselhaus, and P. C. Eklund, *Science of Fullerenes and Carbon Nanotubes* (Academic Press Inc., San Diego, 1996), and references therein.
[3] S. Iijima and T. Ichihashi, Nature (London) **363**, 603 (1993).
[4] D. S. Bethune, C. H. Kiang, M. S. de Vries, G. Gorman, R. Savoy, J. Vazquez, and R. Beyers, Nature (London) **363**, 605 (1993).
[5] J. W. Mintmire, B. I. Dunlap, and C. T. White, Phys. Rev. Lett. **68**, 631 (1992).
[6] R. Saito, M. Fujita, G. Dresselhaus, and M. S. Dresselhaus, Appl. Phys. Lett. **60**, 2204 (1992).
[7] N. Hamada, S. Sawada, and A. Oshiyama, Phys. Rev. Lett. **68**, 1579 (1992).
[8] C. L. Kane and E. J. Mele, Phys. Rev. Lett. **78**, 1932 (1997); A. Rochefort, D. Salahub, and P. Avouris, Chem. Phys. Lett. **297**, 45 (1998).
[9] S. J. Tans, A. R. M. Verschueren, and C. Dekker, Nature (London) **393**, 49 (1998).
[10] P. Delaney, H. J. Choi, J. Ihm, S. G. Louie, and M. L. Cohen, Nature (London) **391**, 466 (1998).
[11] Y.-K. Kwon, S. Saito, and D. Tománek, Phys. Rev. B **58**, R13 314 (1998).
[12] Y.-K. Kwon, D. Tománek, Y. H. Lee, K. H. Lee, and S. Saito, J. Mater. Res. **13**, 2363 (1998).
[13] A. Thess, R. Lee, P. Nikolaev, H. Dai, P. Petit, J. Robert, C. Xu, Y. H. Lee, S. G. Kim, D. T. Colbert, G. Scuseria, D. Tománek, J. E. Fischer, and R. E. Smalley, Science **273**, 483 (1996).
[14] S. Frank, P. Poncharal, Z. L. Wang, and W. A. de Heer, Science **280**, 1744 (1998).
[15] L. Chico, L. X. Benedict, S. G. Louie, and M. L. Cohen, Phys. Rev. B **54**, 2600 (1996); W. Tian and S. Datta, *ibid.* **49**, 5097 (1994); M. F. Lin and K. W.-K. Shung, *ibid.* **51**, 7592 (1995).
[16] R. Landauer, Philos. Mag. **21**, 863 (1970).
[17] R. Saito, G. Dresselhaus, and M. S. Dresselhaus, J. Appl. Phys. **73**, 494 (1993).
[18] Ph. Lambin, L. Philippe, J. C. Charlier, and J. P. Michenaud, Comput. Mater. Sci. **2**, 350 (1994).
[19] Y.-K. Kwon and D. Tománek, Phys. Rev. B **58**, R16 001 (1998).
[20] S. Sanvito, C. J. Lambert, J. H. Jefferson, and A. M. Bratkovsky, Phys. Rev. B **59**, 11 936 (1999).
[21] S. Sanvito, C. J. Lambert, J. H. Jefferson, and A. M. Bratkovsky, J. Phys. C **10**, L691 (1998).
[22] D. Tománek and M. A. Schluter, Phys. Rev. Lett. **67**, 2331 (1991).
[23] M. Schluter, M. Lannoo, M. Needels, G. A. Baraff, and D. Tománek, Phys. Rev. Lett. **68**, 526 (1992).
[24] M. Büttiker, Y. Imry, R. Landauer, and S. Pinhas, Phys. Rev. B **31**, 6207 (1985).
[25] When calculating the S matrix of a doubly infinite nanotube, comprising a scattering region connected to two semi-infinite single- and multiwall nanotube leads, we note that the unit cell in each segment consists of two atomic planes along the nanotube axis. Since the hopping matrix between adjacent unit cells (H_1 in Ref. [20]) is singular in this case, we first project out the noncoupled degrees of freedom before calculating the scattering channels.
[26] In an unbiased system, the Fermi level position should depend on the work function of the graphitic nanotube, ϕ_{gr} = 5.0 eV, which lies in between the values ϕ_{Hg} = 4.5 eV for mercury and ϕ_{Au} = 5.1–5.5 eV for gold. Consequently, due to the contact with Hg and Au and in view of the screening within the nanotube, we expect a small up-shift of E_F by much less than 0.5 eV in the tube, as indicated in Fig. 4.
[27] T. Ando and T. Nakanishi, J. Phys. Soc. Jpn. **67**, 1704 (1998); T. Ando, T. Nakanishi, and R. Saito, *ibid.* **67**, 2857 (1998).

The Potential of Carbon-based Memory Systems[1]

Mark Brehob and Richard Enbody
Department of Computer Science and Engineering

Young-Kyun Kwon and David Tománek
Department of Physics and Astronomy

Michigan State University, East Lansing, MI
{brehob, enbody, kwonyou1, tomanek}@msu.edu

Abstract

It seems likely that density concerns will force the DRAM community to consider using radically different schemes for the implementation of memory devices. We propose using nano-scale carbon structures as the basis for a memory device. A single-wall carbon nanotube would contain a charged buckyball. That buckyball will stick tightly to one end of the tube or the other. We assign the bit value of the device depending on which side of the tube the ball is. The result is a high-speed, non-volatile bit of memory. We propose a number of schemes for the interconnection of these devices and examine some of the known electrical issues.

1. Introduction

If the DRAM industry is to continue with its exponential rate of density improvement, it seems likely that there will need to be a radical change in the construction of memory devices at some point. Certainly quantum-dot [1] devices have possibilities in this role and significant R&D effort has been put forward to develop it. A different possibility is in the construction of a nanometer-sized memory device based on the self-assembly of buckyballs inside of carbon nanotubes. This "bucky shuttle" [2] memory offers nonvolatility and terahertz switching speeds. Also, each bit could require as little as two square nanometers. Extrapolating from the density needs laid out in "The National Technology Roadmap for Semiconductors" [3] this density would be sufficient well past 2030.

Our goal in this paper is to familiarize the reader with the basic issues involved in building a RAM out of carbon nano-structures. We start by discussing the carbon structures used. Next we describe the nanomemory device, followed by a discussion of possible interconnection schemes. Finally, we mention a few of the issues we are currently attempting to resolve.

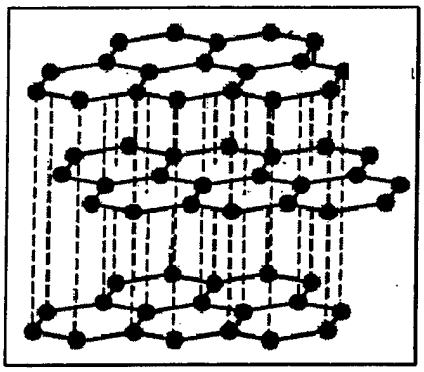

Figure 1 The atomic structure of graphite. The dashed lines indicate the weak connection between the planes of graphite.

1.1. Fullerine nanotubes

Carbon atoms can form a number of very different structures, two of the better known are diamond and graphite. A new carbon structure, the buckyball, was discovered in 1985. Soon after, the nanotube was discovered. These carbon structures, collectively known as fullerines, have been of great interest to the physics and chemistry communities. In the remainder of this section we will give a brief overview of these structures. Readers looking for additional details about fullerines are directed to an excellent overview article found in *American Scientist* [4].

Graphite consists of sheets of carbon atoms in a hexagonal arrangement (see Figure 1). The sheets are very loosely connected to each other. Now imagine taking a single sheet of graphite and cutting a long narrow strip. If that strip is rolled into a long, narrow tube, it would be a nanotube. The ends of the tubes usually form caps, as the dangling atoms will be receptive to forming bonds with their neighbors. The resulting structure is shown in Figure 2. The electrical properties of the newly created nanotube depend upon the exact angle at which the

[1] This research is supported by the Office of Naval Research, Grant # N00014-99-1-0252

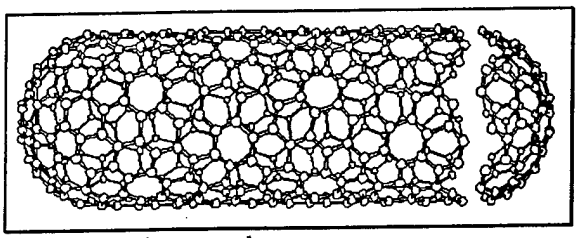

Figure 2 A carbon nanotube

graphite was cut. A cut along one of the edges of the hexagons would result in a conductive "armchair" nanotube. Other angles would result in semi-conductors and even insulators. This *chiral angle* can range from 0° and 30°.

A buckyball can be thought of as the smallest of the nanotubes. It is simply the connection of the two caps with no "tube" in between, and consists of exactly 60 carbon atoms (see Figure 3). Its combination of hexagons and pentagons is exactly the same as that found on a soccer ball. For historical reasons very short nanotubes with 70, or even 80 atoms are sometimes also called buckyballs. In this paper we will use the term only to describe C_{60}.

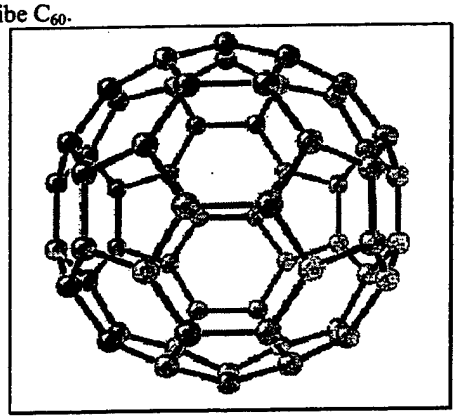

Figure 3 A buckyball

2. The Nanomemory Device

Our proposed nanomemory device (NMD) consists of two parts: the "capsule" which holds the much smaller, charged "shuttle." In Figure 4 we show an example where the capsule is a C_{240} nanotube while the shuttle is a buckyball. The buckyball contains a potassium ion (K^+) which gives the shuttle its charge. (The potassium ion is not shown in the figure.) The outer dimensions of this capsule would be about 1.4nm in diameter and about 2.0nm in length. This K^+ inside of a C_{60} inside of a C_{240} ($K^+@C_{60}@C_{240}$) structure is the smallest and simplest device we have considered. However we are also examining other options such as longer capsules which use other nanotubes as shuttles, as well as having many charged shuttles inside of each NMD.

The state of the memory device is determined by the location of the shuttle: if it is on one side of the capsule, we treat it as a '1'; on the other we treat it as a '0'. The Van der Waals forces between the tube and the shuttle will tightly bind the shuttle to one end of the tube or the other. There is an unstable equilibrium point when the shuttle is in the exact middle of the capsule, but our proposed scheme for writing to the device would prevent the shuttle from ever coming to rest there.

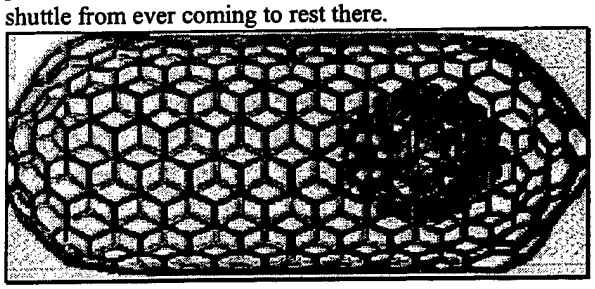

Figure 4 An example nanomemory device

2.1. Writing to the NMD

Figure 5 shows the potential energy of the shuttle at various locations in the NMD. The solid line indicates the potential energy curve when no electric field is applied. Notice that the two potential energy wells are found when the shuttle is on one side of the capsule or the other. These wells keep the shuttle bound to either side of the capsule.

The other two lines display the potential energy when a two-volt potential difference is applied. When such a voltage is applied there exists only one local minimum, and the shuttle will move to that side of the tube. It is with this two-volt potential difference that we can write to the NMD. In general the amount of voltage which needs to be applied depends upon the length of the capsule. A field of 0.1 volts/Å is sufficient to move the shuttle from one side of the tube to the other.

One important issue is how long it takes to perform a write to the NMD. Because of a bouncing effect observable in Figure 6 we have to wait for the buckyball to come to a stop. As the figure shows the time to settle will be about 20 picoseconds.

2.2. Reading from the NMD

Writing to the nanomemory devices is the easy part; reading from them is much more challenging. Somehow the state of the device must be sensed. We have proposed a number of ways to perform a read. The first requires three wires to be connected to the capsule: one on each end, and one in the middle. The position of the

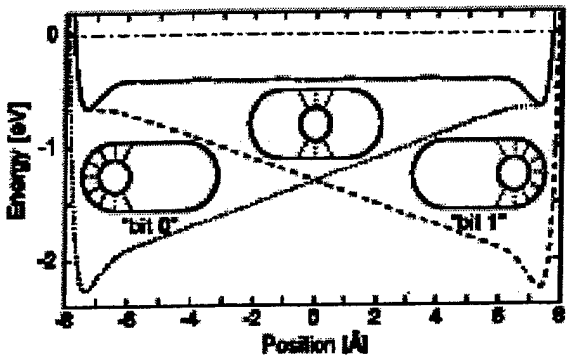

Figure 5 Potential energy of the shuttle at different locations in the capsule. The solid line is when no electric field is applied. The dashed lines are the potential energy when the two-volt potential difference is applied. [2]

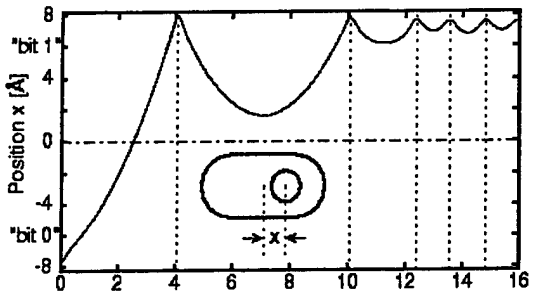

Figure 6 Location vs. time of the shuttle as a write is preformed. Time is in picoseconds. [2]

buckyball is detected by examining the resistance between the middle wire of the nanotube and the ends. A lower resistance will be found on the end that has the shuttle. This three-wire solution has a number of problems, not the least of which is that making a connection to the middle of a nanotube seems difficult. However, a long capsule and shuttle would perhaps make this solution viable.

A device without the middle wire would be easier to fabricate. The notion of a destructive read could be applied here. A read would then be performed in the same way as a write. During that write some current will flow if the shuttle moves from one side of the nanotube to the other. The total current that will flow is limited by the amount of charge held in the shuttles. It is for this type of a read that we would use many shuttles in our capsule to attempt to increase the amount of the current flow. Neither of these reading schemes is particularly satisfactory. We are currently working on other read schemes that appear to be more workable.

3. From NMD to RAM

Once the memory device is fabricated it will still be a challenge to integrate the devices into a large RAM cell. We currently foresee two possible implementations which we call "metal-wired" and "nano-wired." We view the metal-wired approach as the most viable implementation in the near term. However, it is equally useful as a stepping stone on the path to the nano-wired device which offers tremendous density improvements.

3.1. Metal-wired

The easiest device to fabricate would replace the traditional DRAM capacitor/transistor memory cell with a large number of nanomemory devices. We believe current VLSI fabrication techniques could be used, but with the addition of a layer of nano-devices. A "forest" of nanotubes has been already built [5], and a similar technique could be used to create a forest of memory devices between two conducting layers. Figure 7a is a representation of a 4-bit nanomemory device. Figure 7b shows a more detailed view of a single bit. Notice that a number of nanomemory devices are used to make up a single bit of memory. The number of devices per bit will depend upon the minimum line size of the lithography process used. With a 70nm wire width there could be nearly 1,000 nanomemory devices per bit.

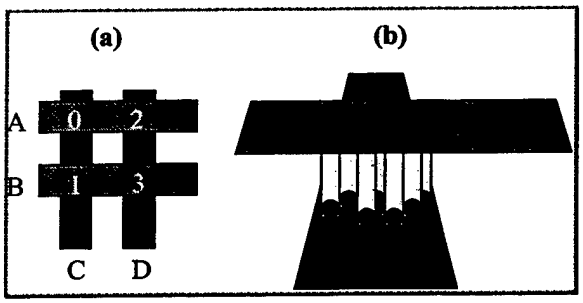

Figure 7 (a) 4-bit nanomemory device with wires A, B, C, and D. (b) a single-bit using forest of NMDs.

Consider how a write to the memory device in Figure 7 would work. Assume that a voltage differential of 2.0 volts will move the shuttles from one side of the capsule to the other. In order to write a '0' to bit three we would have to apply a +1.0 volt potential to wire B while we apply a -1.0 volt potential to wire D. If all the other wires are held at ground, only at the addressed bit will there be a strong enough electrical field to the shuttles. We would write a '1' by reversing the voltages. Writing to an entire row (or column) would be a two-stage process as the 1's and the 0's would have to be written at different times.

Now, consider a destructive read with a forest of nanotubes. Our forest of nanotubes would move a large number of charged ions. We should be able to detect if those ions moved or not. Clearly we will have destroyed the data in the process of doing the read. However, we can write it back later, much as it is handled in a traditional DRAM.

This metal-wired carbon nanomemory device has a number of useful features. It is non-volatile, the device itself switches very quickly, and it would seem to be just as buildable using 70nm lithography as it is using 350nm lithography.

3.2. Nano-wired

In this scheme, the memory array could be made entirely out of nanomemory devices and carbon nanowires. The metal wires would be replaced by conducting nanotubes. Each bit of memory would now use only a single NMD. The logic, sense-amps and pads would likely be made using traditional devices. (However, it should be noted that transistors can be built from nanotubes [4].) It would otherwise be similar to the metal-wired proposal. Nano-wires would allow for *very* high densities, with each bit fitting in about two square nanometers. Laying out this network of carbon would require self-assembly techniques well beyond anything we can do today. We believe that work in the area of carbon self-assembly is progressing well enough that this solution may be viable in 15 to 20 years.

4. Questions

***Q:* How much heat is generated by the collision of the shuttle into the capsule?**

A: We aren't really sure yet. As shown in Figure 8, simulations at 0° Kelvin show an increase in temperature of 10 to 12 degrees. At room temperatures we expect a little more heat to be generated. However, nanotubes are excellent conductors of heat, and we expect to be able to dissipate that heat quickly.

***Q:* Won't the nanotube act as a Faraday cage thus preventing an electric field from entering the nanotube?**

A: Yes. This means that we need an electrical connection to the capsule. Such a connection would greatly reduce or eliminate the screening effects.

***Q:* Just how conductive are nanotubes?**

A: This is currently an issue under a great deal of study. As noted above, the conductivity depends upon the chiral angle of the nanotube. Measured resistivities of nanotubes have ranged from greater than 5 Ωcm to less than 5.1×10^{-6} Ωcm [6]. However, resistivity may be an irrelevant measure of a nanotube. Nanotubes have been experimentally shown to be quantum conductors [7]. Further, there is some early evidence that ballistic transport occurs along nanotubes. This would seem to indicate that resistance is independent of the length of the nanotube. In all honesty this result is a little difficult for those of us that are engineers to accept, but we recognize that quantum physics can lead to counter-intuitive results.

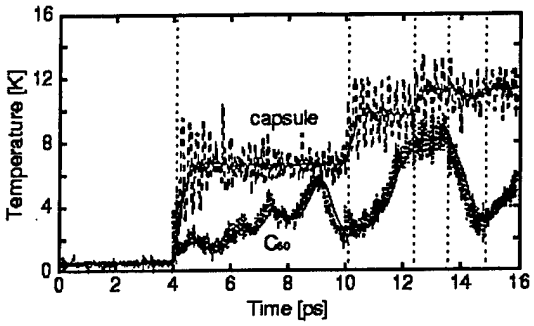

Figure 8 The heat generated by the shuttle slamming into the capsule during a write. [2]

5. Conclusion

Our proposed nanomemory device is one candidate for carrying memory devices beyond the limits of current DRAM technology. It has three important characteristics: it is small, non-volatile, and fast. At this point the carbon nanomemory has been simulated and buckyballs inside of nanotubes have been created, but a working memory device does not exist. Building it will be a challenge, but self-assembling carbon nanotechnology is an active research area with continuous and promising advances. The feasibility of our device improves daily.

[1] K. Yano, "A 128Mb early prototype for gigascale single-electron memories," in *International Solid-State Circuits Conference (ISSCC)*, 1998.

[2] Y-K. Kwon, D. Tománek, and S. Iijima, "'Bucky shuttle' memory device: synthetic approach and molecular dynamics simulations," *Physical Review Letters*, vol. 82, pp. 1470-1473, 15 Feb 1999.

[3] Semiconductor Industry Association, *National Technology Roadmap for Semiconductors: Technology Needs*, 1997, http://notes.sematech.org/ntrs/PublNTRS.nsf.

[4] B. I. Yakobson and Richard E. Smalley, "Fullerene nanotubes: $C_{1,000,000}$ and Beyond," *American Scientist*, vol. 85, pp. 324-337, July-August 1997.

[5] M. Kusunoki, J. Shibata, M. Rokkaku, and T. Hirayama, "Aligned carbon nanotube film self-organized on a SiC wafer," *Japanese Journal of Applied Physics Part 2 - Letters*, vol. 37, Issue 5B, pp. L605-L606, 1998.

[6] T.W. Ebbensen, H.J. Lezec, H. Hiura, J.W. Bennett, H.F. Ghamemi and T. Thio., "Electrical conductivity of individual carbon nanotubes," *Nature*, vol. 382, pp. 54-56, 4 July 1996.

[7] S. Frank, P. Poncharal, Z.L. Wang, and W. A. de Heer, "Carbon nanotube quantum resistors," *Science*, vol. 280, pp. 1744-1746, 12 June 1998.